nature

THE INTERNATIONAL WEEKLY JOURNAL OF SCIENCE

HIDDEN STRENGTH

Nonlinear failure of spider silk is secret of its success PAGE 72

NUTRITION

SWEET SORROW

Should sugar join tobacco and alcohol on restricted list?

PAGE 27

LITERATURE

THE OLD CURIOSITY

Science and imagination in the world of Charles Dickens

PAGE 32

MICROBIOLOGY

RESISTANCE FIGHTERS

The rocky road to an MRSA vaccine

PAGE 23

NATURE.COM/NATURE

2 February 2012 £10

Vol. 482, No. 7383

05

9 770028 083095

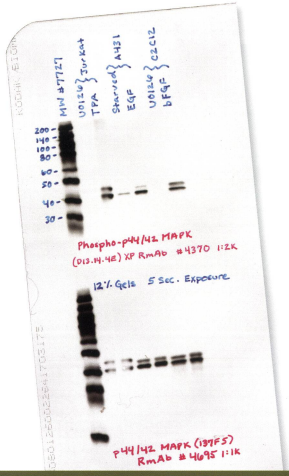

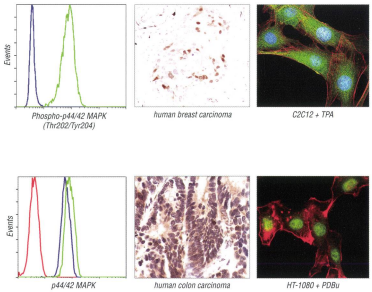

Phospho-p44/42 MAPK (Erk1/2) (Thr202/Tyr204) (D13.14.4E) XP® Rabbit mAb #4370 *(top) and* ***p44/42 MAPK (Erk1/2) (137F5) Rabbit mAb #4695*** *(bottom).*

For full validation details see www.cellsignal.com

The Highest Quality MAPK Antibodies

are from Cell Signaling Technology

Unparalleled product quality, validation, and technical support

Over 30 thoroughly validated MAPK Antibodies available

Cell Signaling Technology (CST™) offers the widest range of phospho and total protein MAPK antibodies. These reagents are the most thoroughly validated, widely used, and highly cited MAPK antibodies available.

- CST™ phospho and total protein MAPK antibodies offer **unsurpassed specificity, sensitivity, and performance**.
- **Extensive in-house validation** in a wide range of applications means that optimization is not left up to you, the user.
- **Technical support is provided by scientists** who produce the products and know them best.

WINNER! Life Science Industry Awards®
Best Antibodies :: *Best Breakthrough Products for Cancer Research*

for quality products you can trust...

www.cellsignal.com

Cell Signaling TECHNOLOGY®

Orders (toll-free) 1-877-616-CELL (2355) orders@cellsignal.com | **Fax ordering** 1-978-867-2488 | **Technical support** (toll-free) 1-877-678-TECH (8324) support@cellsignal.com | **Inquiries** info@cellsignal.com

© 2011 Cell Signaling Technology, Inc.
Cell Signaling Technology, CST and XP are trademarks of Cell Signaling Technology, Inc. Phospho-specific antibodies are exclusively licensed from Cell Signaling Technology, Inc. U.S. Pat. Nos. 7,257,486 and 7,393,630.

CONTENTS

2 February 2012 / Vol 482 / Issue No 7383

THIS WEEK

EDITORIALS

5 NUCLEAR SAFETY
The low-level nuclear threat
Europe's cooperative approach to low-dose radiation research should go global

5 INTERNATIONAL TREATIES
Poles apart
With interest in Arctic wealth raising political tension, it's time to look south

6 MATERIALS SCIENCE
Damage limitation
The power of spider silk

WORLD VIEW

7 **Global health hits crisis point**
Laurie Garrett
The shortfall at the Global Fund must be addressed

RESEARCH HIGHLIGHTS

8 SELECTIONS FROM THE SCIENTIFIC LITERATURE
Seeing is believing / Specialized diets make for big animals / Towards gene therapy for eye repair / Wetlands in retreat / What does body hair do?

SEVEN DAYS

10 THE NEWS IN BRIEF
On the trail of nanotech risks / Mars rover marks eighth anniversary / UK faces flooding risk / Roche's bid for Illumina rallies market / Kepler bags more planets

CAREERS

121 COLUMN
Global collaboration
Andrew Fung
Cultural and linguistic differences add spice to international collaborations

123 TURNING POINT
Bioinformatics can be fun, says Ewan Birney

123 CAREER BRIEFS

NEWS IN FOCUS

13 ENVIRONMENT
Scramble for Arctic oil renews conservationists' concerns

14 PSYCHIATRY
Controversial new guidelines could lead to overdiagnosis of mental illness

15 FUNDING
California stem-cell research institute faces budget reduction

16 MEDICINE
Call for better information to be provided to clinical trial participants

17 PHYSICS
Particle physicists in pursuit of neutron charge measurement despite setbacks

18 RESEARCH POLICY
Lack of support for genomics prompts top Japanese geneticist to take US post

19 RESEARCH POLICY
Researchers criticize plan to merge Japan's science funding bodies

FEATURES

23 HEALTH
Man vs MRSA
The struggle to find a vaccine against antibiotic-resistant *Staphylococcus*

COMMENT

27 NUTRITION
The toxic truth about sugar
Robert H Lustig, Laura A Schmidt & Claire D Brindis
Sugar is bad for you and should be treated like tobacco and alcohol

30 CONSERVATION
Bring elephants to Australia?
David Bowman
Feral animals and wildfires are causing havoc in the outback: call in the cavalry

BOOKS & ARTS

Q&A

Lab notes

Gary Marcus finds complexity in how the mind handles music PAGE 34

31 NEUROSCIENCE
The connected self
Christof Koch

32 LITERATURE
Wonders and ologies
Alice Jenkins

CORRESPONDENCE

35 Kampo medicine / Safety of traditional cures / Testing nanotechnologies

OBITUARY

36 **Philip D Lawley (1927–2011)**
Stanley Venitt & David H Philips

FUTURES

126 **Words and music**
Ronald D Ferguson

Instruments that are music to your hands.

FINE SURGICAL INSTRUMENTS FOR RESEARCH™

SHIPPING GLOBALLY SINCE 1974

Request a catalog at finescience.com or call 1-800-521-2109.

F · S · T®

FINE SCIENCE TOOLS

CONTENTS

2 February 2012 / Vol 482 / Issue No 7383

RESEARCH

NEW ONLINE

37 Papers published this week at nature.com

NEWS & VIEWS

38 VOLCANOLOGY
Greek inflation circa 1600 BC
Petrology study of the Bronze Age 'Minoan' eruption on Santorini
Jon Blundy & Alison Rust SEE LETTER P.77

39 NEUROSCIENCE
Reward alters specific connections
Synchronous activity marks neuronal synapses for later modulation
Timothy E Holy SEE ARTICLE P.47

41 SURFACE CHEMISTRY
Crystal cuts on the nanoscale
Shape control in nanoparticle synthesis
Peidong Yang

42 PLANT BIOLOGY
Equal-parenting policy
Zygotic genome switches on faster in plants than in animals
Christopher J Hale & Steven E Jacobsen SEE LETTER P.94

44 MOLECULAR MOTORS
A staggering giant
The funny walk of dynein on microtubules
Wilhelm J Walter & Stefan Diez

45 PRECISION MEASUREMENT
A comb in the extreme ultraviolet
Pushing frequency combs to the extreme-ultraviolet spectral range
Linda Young SEE LETTER P.68

ARTICLES

47 NEUROSCIENCE **Conditional modulation of spike-timing-dependent plasticity for olfactory learning**
S Cassenaer & G Laurent SEE N&V P.39

53 CELL BIOLOGY **DNA breaks and chromosome pulverization from errors in mitosis**
K Crasta et al.

LETTERS

59 PHYSICS **Creation and diagnosis of a solid-density plasma with an X-ray free-electron laser**
S M Vinko et al.

63 PHYSICS **Quantum-coherent coupling of a mechanical oscillator to an optical cavity mode**
E Verhagen, S Deléglise, S Weis, A Schliesser & T J Kippenberg

68 PHYSICS **Direct frequency comb spectroscopy in the extreme ultraviolet**
A Cingöz et al. SEE N&V P.45

72 MATERIALS SCIENCE **Nonlinear material behaviour of spider silk yields robust webs**
S W Cranford, A Tarakanova, N M Pugno & M J Buehler

77 EARTH SCIENCES **Decadal to monthly timescales of magma transfer and reservoir growth at a caldera volcano**
T H Druitt, F Costa, E Deloule, M Dungan & B Scaillet SEE N&V P.38

81 GENOMICS **Serial translocation by means of circular intermediates underlies colour sidedness in cattle**
K Durkin et al.

85 NEUROSCIENCE **Neuron-type-specific signals for reward and punishment in the ventral tegmental area**
J Y Cohen, S Haesler, L Vong, B B Lowell & N Uchida

89 IMMUNOLOGY **Vaccine protection against acquisition of neutralization-resistant SIV challenges in rhesus monkeys**
D H Barouch et al.

94 PLANT SCIENCES **Maternal and paternal genomes contribute equally to the transcriptome of early plant embryos**
M D Nodine & D P Bartel SEE N&V P.42

98 GENETICS **Mutations in kelch-like 3 and cullin 3 cause hypertension and electrolyte abnormalities**
L M Boyden et al.

103 PLANT SCIENCES **A novel sensor to map auxin response and distribution at high spatio-temporal resolution**
G Brunoud et al.

107 MICROBIOLOGY **Adenylylation control by intra- or intermolecular active-site obstruction in Fic proteins**
P Engel et al.

111 IMMUNOLOGY **Cysteinyl leukotriene type I receptor desensitization sustains Ca^{2+}-dependent gene expression**
S-W Ng et al.

116 STRUCTURAL BIOLOGY **Structures of cytochrome P450 17A1 with prostate cancer drugs abiraterone and TOK-001**
N M DeVore & E E Scott

120 CORRIGENDUM **The unusual γ-ray burst GRB 101225A from a helium star/neutron star merger at redshift 0.33**
C C Thöne et al.

120 CORRIGENDUM **A reserve stem cell population in small intestine renders Lgr5-positive cells dispensable**
H Tian et al.

ON THE COVER
On the web
Spider silk's remarkable properties include high extensibility and steel-like strength. But the resilience of a web requires another ingredient — a nonlinear stress response. Thanks to this, a web keeps its shape when the wind blows and suffers only minor damage during strong local deformations. PAGE 72

S CRANFORD & M J BUEHLER/MIT; DICKENS M I BSB/REX

GENOMICS

Side order

Complex chromosomal choreography produces 'colour-sided' cows. PAGE 81

nature

2 February 2012 / Vol 482 / Issue No. 7383

EDITORIAL

LONDON, MUNICH, WASHINGTON DC, NEW YORK, BOSTON, PARIS, SAN FRANCISCO, TOKYO nature@nature.com

EDITOR-IN-CHIEF: Philip Campbell
MANAGING EDITOR: Nick Campbell
PUBLISHING EXECUTIVE EDITOR: Maxine Clarke **EXECUTIVE EDITOR:** Véronique Kiermer
CHIEF MAGAZINE EDITOR: Tim Appenzeller
THIS WEEK/NEWS/FEATURES: Alison Abbott, David Adam, Ananyo Bhattacharya, Geoff Brumfiel, Declan Butler, Ewen Callaway, Erika Check Hayden, Daniel Cressey, David Cyranoski, Natasha Gilbert, Eric Hand, Heidi Ledford, Corie Lok, Brendan Maher, Emma Marris, Richard Monastersky, Brian Owens, Helen Pearson, Mark Peplow, Eugenie Samuel Reich, Ivan Semeniuk, Quirin Schiermeier, Jeff Tollefson, Richard Van Noorden, Meredith Wadman, M Mitchell Waldrop **COMMENT:** Sara Abdulla, Joanne Baker, Rosalind Cotter, Barbara Kiser, Alison McCook, Lucy Odling-Smee, Sarah Tomlin **NATURE PODCAST/VIDEO:** Adam Rutherford, Eric Olson, Kerri Smith, Charlotte Stoddart **NEWS AND VIEWS:** Sadaf Shadan, Ana Lopes, Andrew Mitchinson, Cesar Sanchez, Marian Turner **RESEARCH:** Ritu Dhand, Karl Ziemelis, Francesca Cesari, I-han Chou, Tanguy Chouard, Rosamund Daw, Alex Eccleston, Angela Eggleston, Joshua Finkelstein, Henry Gee, Patrick Goymer, Noah Gray, Marie-Thérèse Heemels, Magdalena Helmer, Karen Howell, Claudia Lupp, Barbara Marte, Andrew Mitchinson, Juliane Mössinger, Deepa Nath, Leslie Sage, Magdalena Skipper, Clare Thomas, John VanDecar, Liesbeth Venema, Ursula Weiss, Michael White **INSIGHTS/REVIEWS/PERSPECTIVES:** Ursula Weiss **CAREERS:** Gene Russo, Karen Kaplan **TECHNOLOGY FEATURES:** Monya Baker **FUTURES:** Henry Gee **SUPPLEMENTS:** Herb Brody, Michelle Grayson, Tony Scully **SUBEDITORS:** Colin Sullivan, Sarah Archibald, Nicola Bailey, Anne Blewett, Nicolas Fanget, Isobel Flanagan, Paul Fletcher, Afsaneh Gray, Dinah Loon, Anna Novitzky, Yukie Ozawa, Katherine Perry, David Price, Jenny Rooke, Chris Simms, David Winters, Anna York **PRODUCTION:** Jenny Henderson, Leonora Dawson-Bowling, Dan Foley, Stewart Fraser, Susan Gray, Simon Gribbin, James McQuat, Emilia Orivas, Yvonne Strong, Robert Sullivan, Roberta Tarran, Charles Wenz **ART AND DESIGN:** Kelly Buckheit Krause, Wesley Fernandes, Madeline Hutchinson, Barbara Izdebska, Paul Jackman, Jasiek Krzysztofiak, Annthea Lewis, Nik Spencer, Claire Weich, Mark Wood **JAPAN EDITION:** Mika Nakano, Akemi Tanaka, Mitsuyo Utsugi **PRESS OFFICE:** Ruth Francis, Neda Afsarmanesh, Lisa Boucher, Rachel Twinn, Rebecca Walton **ADMINISTRATION:** Paul Sng, Liz Bankes, Roseann Campbell, Phion Cleverley, Faye Fornasier, Amy Invernizzi, Diane Kempinski, Hazel Mayhew, Katie McGoldrick, Jenny Meyer, Rina Nozawa, Kenneth Simpson, Claire Smith

PUBLISHING

LONDON feedback@nature.com

MANAGING DIRECTOR & PUBLISHER: Steven Inchcoombe
ASSOCIATE PUBLISHER: Arash Hejazi
PUBLISHING PROJECT MANAGER: Christian Manco

TOKYO feedback@natureasia.com

PUBLISHING DIRECTOR — ASIA-PACIFIC: David Swinbanks
ASSOCIATE DIRECTOR — ASIA-PACIFIC: Antoine E Bocquet

DISPLAY ADVERTISING, SPONSORSHIP & NATUREJOBS

GLOBAL HEAD: Andrew Douglas a.douglas@nature.com
DISPLAY ADVERTISING AND SPONSORSHIP
GLOBAL HEAD: Gerard Preston g.preston@nature.com
ASSISTANT SPONSORSHIP MANAGER: Reya Silao Tel: +44 (0)20 7843 4977 (rsilao@nature.com))
EUROPE/REST OF WORLD display@nature.com Tel: +44 (0)20 7843 4960
GERMANY/SWITZERLAND/AUSTRIA: Sabine Hugi-Fürst Tel: +41 52761 3386
UK/IRELAND/SCANDINAVIA/SPAIN/PORTUGAL: Evelina Rubio Hakansson Tel: +44 (0)20 7843 4079
FRANCE/BELGIUM/THE NETHERLANDS/LUXEMBOURG/ITALY/OTHER EUROPE: Nicola Wright Tel: +44 (0)20 7843 4959
NORTH AMERICA display@natureny.com
NEW ENGLAND/ EASTERN CANADA: Sheila Reardon Tel: +1 617 494 4900
NEW YORK/MID-ATLANTIC/SOUTHEAST: Jim Breault Tel: +1 212 726 9334
MIDWEST: Mike Rossi Tel: +1 212 726 9255
WEST COAST/ WESTERN CANADA: George Lui Tel: +1 415 781 3804
WEST COAST NORTH: Kayla McCutchan Tel: +1 415 403 9038
ASIA-PACIFIC display@natureasia.com
ASIA-PACIFIC HEAD: Kate Yoneyama
JAPAN: Ken Mikami Tel: +81 3 3267 8765
GREATER CHINA/SINGAPORE: Gloria To Tel: +852 2811 7191
INDIA: Vikas Chawla Tel: +91 124 288 1057
SPONSORSHIP
BUSINESS DEVELOPMENT MANAGER: David Bagshaw Tel: +1 212 726 9215
BUSINESS DEVELOPMENT MANAGER: Patrick Murphy Tel: +1 617 475 9216
NATUREJOBS naturejobs@nature.com
EUROPEAN HEAD OFFICE, LONDON: Tel: +44 (0)20 7843 4961
EUROPEAN SALES MANAGER: Nils Moeller (n.moeller@nature.com) **BUSINESS DEVELOPMENT MANAGER, MIDDLE EAST:** Jon Giuliani (j.giuliani@nature.com) **ADVERTISING PRODUCTION MANAGER:** Stephen Russell **NATUREJOBS ONLINE PRODUCTION:** Dennis Chu
US HEAD OFFICE, NEW YORK: naturejobs@natureny.com **US SALES MANAGER:** Ken Finnegan
JAPAN HEAD OFFICE, TOKYO: Tel: +81 3 3267 8765 **ASIA-PACIFIC HEAD:** Kate Yoneyama
ASIA-PACIFIC SALES & BUSINESS DEVELOPMENT MANAGER: Yuki Fujiwara **BUSINESS DEVELOPMENT MANAGER, GREATER CHINA, SINGAPORE:** Gloria To Tel: +852 2811 7191
INDIA: Vikas Chawla Tel: +91 1242881057 (v.chawla@nature.com)

MARKETING & SUBSCRIPTIONS

USA/CANADA/LATIN AMERICA subscriptions@us.nature.com
Tel: (USA/Canada)+1 866 363 7860; (outside USA/Canada) +1 212 726 9223
MARKETING: Sara Girard **FULFILMENT:** Karen Dawson

JAPAN/CHINA/KOREA subscriptions@natureasia.com
Tel: +81 3 3267 8751 **MARKETING/PRODUCTION:** Keiko Ikeda, Takesh Murakami

EUROPE/REST OF WORLD subscriptions@nature.com
Tel: +44 (0)1256 329242
MARKETING: Elena Woodstock, Marcus Parker, Hannah Phipps **FULFILMENT:** Jean Burrows

INDIA npgindia@nature.com
Tel: +91 124 2881053/54
HEAD OF BUSINESS DEVELOPMENT, INDIA: Debashish Brahmachari **MARKETING:** Harpal Singh Gill

ANNUAL SUBSCRIPTIONS (UK/Europe, including post and packing)
FULL RATE: £1,400
PERSONAL RATES: UK £135; Europe €209; Rest of World £210
STUDENT RATES: UK £79; Europe €122; Rest of World £125
Individual rates apply to payments by personal cheque or credit card. Back issues: £20.00.

ANNUAL SUBSCRIPTIONS (USA, including post and packing)
INSTITUTIONAL/CORPORATE RATE: $2,730 ; **PERSONAL RATE:** $199; **STUDENT RATE:** $99;
POSTDOC RATE: $119
Printed in USA. Individual rates available only to subscribers paying by personal check or credit card. Orders for student/postdoc subscriptions must be accompanied by a copy of student ID. Rates apply to USA, Canada, Mexico/Central & South America. Add 7% GST tax in Canada (Canadian GST number 140911595). **BACK ISSUES:** US$20.00.

ANNUAL SUBSCRIPTIONS (Asia, including post and packing)
JAPAN: 年間購読料金： *Nature* のみ 437,800 円 +21,890 円 (消費税) =459,690 円 (合計)
Nature + *Nature Digest* 466,550 円 +23,328 円 (消費税) =489,878 (合計)
お問い合わせ 日本出版貿易株式会社 国内営業 1 部
〒101-0064 東京都千代田区猿楽町1-2-1 Tel: 03-3292-3767 Fax: 03-3292-8766
個人/学生購読について
NPG ネイチャー アジア・パシフィック フルフィルメント & カスタマーサービス
〒162-0843 東京都新宿区市谷田町2-37 千代田ビル Tel: 03-3267-8759Fax: 03-3267-8752
CHINA: www.nature.com/cn/ch subscribe; **KOREA:** www.natureasia.com/korea/subscribe

NATURE ONLINE

WWW.NATURE.COM/NATURE
CHIEF TECHNOLOGY OFFICER: Howard Ratner **ASSOCIATE DIRECTOR, NATURE.COM:** Daniel Pollock
PLATFORM DEVELOPMENT: Jeremy Macdonald **WEB PRODUCTION:** Alexander Thurrell, Deborah Anthony **WEB DESIGN:** Juan-Carlos Sobrino, Luke Stavenhagen **PLATFORM INTERFACES:** Amanda Ward

SITE LICENCES, FULFILMENT & CUSTOMER SERVICES

SITE LICENCES: npg.nature.com feedback@nature.com
CHIEF OPERATIONS OFFICER: John Carroll **ASSOCIATE DIRECTOR OF OPERATIONS:** Dominic Pettit
CUSTOMER SERVICE: Gerald Coppin **ORDER PROCESSING OPERATIONS:** Steve Poulter

NATURE PUBLISHING GROUP OFFICES

LONDON: The Macmillan Building, 4 Crinan Street, London N1 9XW Tel: +44 (0)20 7833 4000 Fax: +44 (0)20 7843 4596/7
BASINGSTOKE: Nature Publishing Group, Subscriptions, Brunel Road, Basingstoke, Hants RG21 6XS, UK Tel: +44 (0)1256 329242
WASHINGTON DC: 968 National Press Building, 529 14th St NW, Washington DC 20045-1938 Tel: +1 202 737 2355
NEW YORK: 75 Varick St, 9th Floor, New York, NY 10013-1917 Tel: +1 212 726 9200
BOSTON: 25 First Street, Suite 104, Cambridge, MA 02141 Tel: +1 617 475 9275
SAN FRANCISCO: 225 Bush Street, Suite 1453, San Francisco, CA 94104 Tel: +1 415 403 9027
MUNICH: Nymphenburger Strasse 14, D-80335 München Tel: +49 89 549057-13
PARIS: Maison de Malicorne, Sainte Maure de Touraine, Paris 37800 Tel: +33 2 47 35 72 15
TOKYO: Chiyoda Building, 2-37 Ichigaya Tamachi, Shinjuku-ku, Tokyo 162-0843 Tel: +81 3 3267 8751
INDIA: Nature Publishing Group, 3A, 4th Floor, DLF Corporate Park, Gurgaon 122002 Tel: +91 124 2881053/54

Nature® (ISSN 0028-0836) is published by Nature Publishing Group, a division of Macmillan Publishers Ltd (The Macmillan Building, 4 Crinan Street, London N19XW). Registered as a newspaper at the British Post Office. North and South American orders to subscriptions@nature.com (Tel: +1 866 363 7860). Other orders to subscriptions@nature.com (Tel: +44 (0)1256 329242; Fax +44 (0)1256 812358). Authorization to photocopy material for internal or personal use, or internal or personal use of specific clients, is granted by *Nature* to libraries and others registered with the Copyright Clearance Center (CCC) Transactional Reporting Service, provided the relevant copyright fee is paid direct to CCC, 222 Rosewood Drive, Danvers MA 01923, USA. Identification code for *Nature*: 0028-0836/03. CPC PUB AGREEMENT #40032744. In the US, *Nature* (ISSN 0028-0836) is published weekly on Thursday, except the last week in December by Nature Publishing Group, 75 Varick St, 9th Fl, New York NY 10013-1917, USA. US Periodicals postage paid at New York NY, and additional mailing post offices. US POSTMASTER: send address changes to *Nature*, Subscription Dept, 75 Varick St, 9th Fl, New York NY 10013-1917, USA. Published in Japan by NPG Nature Asia-Pacific, Chiyoda Building, 2-37 Ichigayatamachi, Shinjuku-ku, Tokyo 162-0843, Japan. ® 2012 Macmillan Publishers Limited. All rights reserved.

nature MIDDLE EAST

Emerging science in the Arab world

A FREE resource for scientists and clinicians from the world's premier science publishers

- Latest scientific research
- Breaking science news
- In-depth features and commentaries
- Local job listings and events
- Hand-picked premium content

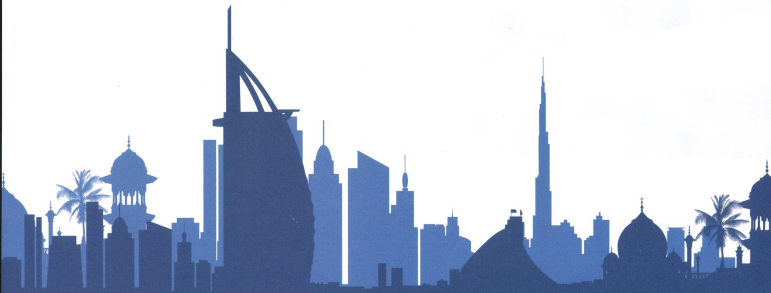

Connect, network and exchange information and ideas in the ***Nature Middle East*** **forum** and **House of Wisdom** blog.

twitter facebook

Sign up to the FREE e-alert

nature.com/nmiddleeast

Sponsored by

nature publishing group npg

Now available:
Adaptors & Primers
for Illumina®

NEW ENGLAND
BioLabs Inc.
enabling technologies in the life sciences

Take the next step.

Library Prep Reagents for Next Gen Sequencing

Isn't it time to break away from the constraints of standard workflows for NGS sample prep? With NEBNext® reagents for DNA and RNA, take advantage of multiple product formats and custom options to tailor solutions for your specific needs.

Available for the leading sequencing platforms, NEBNext reagents allow you to take the next step in designing the workflow that works for you.

www.NEBNext.com

Scan this code to learn more about how NEBNext reagents deliver flexibility to your sample prep workflow

Need a code reader? Go to 2dscan.com from your mobile browser, search for 'ScanLife' in your app store or text SCAN to 43588

Illumina® is a registered trademark of Illumina, Inc.

THIS WEEK

EDITORIALS

SPIDERS The amazing webs and weaving of our eight-legged friends **p.6**

WORLD VIEW The row over the Global Fund could spell disaster **p.7**

ILLUSION Perceived brightness is in the eye of the beholder **p.8**

The low-level nuclear threat

Europe is making a good start on learning about the health risks of low-dose radiation with a programme to share cold-war data and set research priorities. But the effort needs to be global.

Fear of the effects of an atomic strike haunted the politicians and scientists of the cold war. For years, researchers around the world worked on massive and systematic programmes to understand how ionizing radiation might affect survivors of a blast. Almost half a billion animals in the United States, the Soviet Union, Europe and Japan — mostly rats and mice, but also thousands of dogs and some rabbits and monkeys — were deliberately irradiated. These experiments were well designed and worked to identify the pathological consequences of doses of various types of radiation, delivered at different rates and by different routes, including inhalation or ingestion. Results were documented in detail and tissue samples were kept.

The political thaw of 1989 changed priorities, and these experiments and their results were largely forgotten. So were the scientists. But concern about ionizing radiation didn't fade entirely: instead, it was transferred increasingly to worries about low-level occupational exposure in the nuclear (and other) industries, and about exposure during medical diagnosis and treatment. The meltdown of the nuclear reactor in Chernobyl, now in Ukraine, in 1986 gave rise to new concern and political pressure, which was exacerbated by the Fukushima accident in Japan last year.

Science hasn't yet provided all the answers that governments need to respond to these concerns. Epidemiological studies, backed by animal experiments, have established beyond doubt that exposure to radiation levels above 100 millisieverts increases the risk of cancer in a predictable, dose-dependent way. But the risk to health at lower exposure levels is harder to pin down. In Germany, for example, the dose limit for occupational exposure is 20 millisieverts per year. But even when this limit is respected, there are more than 70,000 reports of suspected health damage among exposed workers each year, more than double the number in 1960. Some epidemiological studies suggest that low doses of radiation — as few as 10 millisieverts in children — may increase cancer risk in susceptible individuals, and may be associated with other conditions, such as heart disease and stroke. People living close to Fukushima are anticipated to receive around 10 millisieverts of accumulated radiation exposure each over the next decade.

Radiation-protection agencies want to check whether the weak associations between low-dose radiation and diseases are real. If they are, agencies need to understand the biological mechanisms behind them.

In 2008, the German Federal Office for Radiation Protection led an initiative with agencies from four other European countries and the European Commission to sketch out a rational, systematic plan to crack the low-dose problem. Their report was published in January 2009. It spawned the Multidisciplinary European Low Dose Initiative (MELODI), a platform of 15 European agencies and institutes that will develop and coordinate scientific policies. It also produced a 6-year, €13-million (US$17.2-million) European Commission Network of Excellence to help to set up the platform and address some of its questions. Keen to maintain the musical theme, the network calls itself Low Dose Research Towards Multidisciplinary Integration, or DoReMi.

Epidemiology has an important role in radiation research, but only when the dose received by an individual can be calculated with confidence, as in medical exposure. There must also be research on animals, posing questions not so different from those asked by radiobiologists during the cold war. Modern scientists won't be able to do animal experiments on the scale of those carried out before 1989, which would not be considered ethically justifiable by current standards. But they don't need to. Already, some scientists have started to analyse the cold-war data and materials, and have found that many of them should be usable.

"Agencies want to check whether the associations between low-dose radiation and diseases are real."

In Rome last week, biologists from radiation-protection agencies and research institutes around the world who have taken up the challenge of low-dose radiation research met to discuss how to share contemporary information, and how to make the vast archives of historical data available to all.

It will involve a mammoth digitization and curation effort — expensive even before new experiments to plug gaps are factored in. Some members of MELODI estimate that it could cost up to €1 billion to understand the full biological effects of low-dose radiation. Yet the problem needs more than just money: it needs lobbying to attract biologists from other disciplines, who tend to dismiss radiobiology as old-fashioned.

MELODI has made a fine start on structuring a European scientific approach to a serious social problem. It now needs to orchestrate itself as a global platform — an unchained MELODI, if you like. ■

Poles apart

Protecting the Arctic from pollution requires a binding agreement like the Antarctic Treaty.

Last month's centenary of the ill-fated arrival of Robert Scott at the South Pole prompted a swell of events and publicity. Yet there is another noteworthy anniversary from the far south this month. Sixty years ago, Antarctica — perhaps for the first and only time — echoed to the sound of hostile gunfire. In what became known as the 1952 Hope Bay Incident, Argentinian soldiers fired a machine gun over the heads of a British landing party that was attempting to re-establish and supply an Antarctic base that had burnt down several years earlier. In response, the British despatched armed marines from the Falkland Islands, who forced the Argentinians to retreat

and offered naval protection for the reconstruction of the base. The incident was quickly brushed off as a misunderstanding, but relations had been strained. Less than a decade later, the international Antarctic Treaty set aside the territorial disputes that fuelled such skirmishes, and effectively handed the continent over to science.

Such lessons from history are a useful reminder that Antarctica has not always been the research utopia that it is now, and that it took the resolution of real tensions and difficulties to render the incident at Hope Bay a curious historical footnote rather than a sign of things to come. There are also lessons here for the Arctic; specifically, how to manage the region as tensions rise over its oil and gas reserves that are driving greater exploration as the sea ice dwindles.

As we report on page 13, the drive to locate and exploit fossil-fuel resources in the Arctic continues apace. At a meeting in the Norwegian city of Tromsø last week, executives from oil and gas firms queued up to boast of the riches the region could offer to their companies and shareholders.

Politicians can see the potential too. Ola Borten Moe, Norway's minister of petroleum and energy, last month awarded 26 new production licences for mature offshore oil areas in the Norwegian Sea and Barents Sea. New oil and gas development is under way off Norway, Greenland, Alaska and the northern coast of Russia. According to a much-quoted 2008 estimate from the US Geological Society, about 13% of the world's remaining technically recoverable oil, and up to 30% of its gas, is in the Arctic — most of it under the Arctic Ocean.

Yet, in the wake of the April 2010 Deepwater Horizon oil spill in the Gulf of Mexico, the environmental risks of such a dirty industry expanding into a pristine environment are obvious. Two environmentalists who envisaged the impact of a spill in the Arctic called it "A frozen hell" in a *Nature* article published on the first anniversary of the Deepwater Horizon disaster (J. Short and S. Murray *Nature* **472,** 162–163; 2011).

Such an accident would be a global catastrophe. What can be done, on a worldwide scale, to prevent an Arctic spill from happening, and to ensure a rapid and coordinated response to mitigate the impact if it did? How can scientists contribute?

Common wisdom at this point tends to highlight the difficulties of political collaboration and governance in the Arctic, given the overlapping territorial claims and the lack of an agreement similar to the Antarctic Treaty. It is true that the Arctic Council — which represents the nations and people of the Arctic Circle — has so far done little to answer critics who dismiss it as a toothless talking shop.

Formed in its present state only in 1996, the council did, however, produce its first legally binding agreement between nations last year, which sets out the responsibilities of its members to contribute to search-and-rescue activities. And it has now set up a task force to explore whether a similar agreement could be reached on how to prevent, prepare for and respond to Arctic oil pollution.

"The high north is no longer a place of interest to only a select few."

That process could yet be controversial — Greenland has suggested it should include a formal liability and compensation scheme — and it is in its early stages. The group held only its second meeting in St Petersburg, Russia, in December, but it is scheduled to report back on the various options next year.

If the council is serious about the exercise — which it should be, given that its members will be on the front line of any Arctic spill — then it could offer a timely and useful contribution. To achieve this potential, it should open up the process as widely as possible, and follow through on plans to involve in its discussions experts from scientific and environmental fields, as well as representatives from the offshore oil and gas industry. It should aim high, and look to create a binding agreement that is legally enforceable.

If that means the council going beyond its comfort zone, then it could seek wider international support for such a move. Several non-Arctic nations, including China and India, are already eyeing the region and its opportunities, and have asked for representation on the council.

Their requests have triggered debate and some resistance, but they surely have merit. Like the far south, the high north is no longer a place of interest to only a select few. Nations in the Arctic Circle will rightly insist on having the biggest say, but all interested countries should at least be offered a voice. And to avoid polluting the Arctic is a cause behind which everyone can surely unite. ■

Damage limitation

Spider webs are designed to cope with stress and disruption, favouring repair over rebuilding.

With a proposed referendum on Scottish independence likely to happen in 2014, some 700 years after the Scots army triumphed over English forces at the symbolic Battle of Bannockburn, one tale that seems certain to be told in the build-up is the story of Scotland's King Robert the Bruce and the spider. According to legend, Bruce was hiding in a cave in the wake of several defeats when he was inspired to fight again after watching a spider persevere, and eventually succeed, in its repeated attempts to spin a web.

As Bruce — who led the Scots to victory at Bannockburn — discovered, failure does not come easily to a spider. And although the amazing properties of spider silk have fascinated us for generations, the secrets of their webs have remained elusive.

In a paper on page 72 of this issue, Markus Buehler at the Massachusetts Institute of Technology in Cambridge and his colleagues report on perhaps the most impressive design feature of a spider's web: its structural and mechanical strength. In research that both modelled webs and investigated those spun *in situ* by local garden spiders, the authors found that the strands of silk adapt to the amount of stress they experience, and how that stress is loaded onto them.

Under a light stress, a gentle highland breeze perhaps, the silk softens and extends, so allowing the web to retain its structure. But when a larger and more disruptive force strikes — such as a hand groping for a light switch in a dark attic — the silk strands first extend, then the most stretched of those strands become suddenly rigid and so break. This sacrifice of a strand or two localizes the damage, and keeps the rest of the web intact. Once the disturbance has passed, the spider can scurry out to repair the web, rather than being forced to rebuild. As Bruce — who exploited heavily wooded areas to conceal his preparations for the decisive battle — discovered, it is easier to persevere, and to succeed, when nature is on your side.

These are heady times for arachnophiles. Last month, a stunning shawl and cape woven from spider silk went on display at London's Victoria and Albert Museum. The two garments, which took eight years to create, contain silk produced by more than one million female Madagascan golden orb-weaver spiders, amassed by a team of 80 people. They used long poles to collect the spiders from their webs each day, and harvested their silk before returning them to the wild. The garments are the first textiles to be made from spider silk since a set of bed hangings displayed at the 1900 Paris Exhibition. It is another achievement for the power of perseverance. Or perhaps, as those set to campaign in 2014 for Scotland to remain part of the United Kingdom might stress, it marks a triumph of, and a tribute to, sticking together. ■

NATURE.COM
To comment online, click on Editorials at:
go.nature.com/xhunqv

MACMILLAN
SCIENTIFIC COMMUNICATIONS

Scientific **Editing**

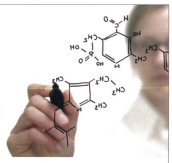

Publishing help now available

MSC's Scientific Editing Service goes far beyond regular language editing and provides you with:

- in-depth **developmental editing** by ***Nature*-standard editors**
- **feedback** and suggestions on your manuscript's content, organisation and presentation by an expert in your field
- **advice on suitable journals** for your manuscript
- **language editing** by Nature Publishing Group Language Editing

Submit your manuscript today!

www.mscediting.com

'Nature Publishing Group editorial and publishing decisions are independent of MSC services.

Exclusive partner of Nature Publishing Group, publisher of Nature *and* Scientific American

CUSTOM MONOCLONAL ANTIBODIES
Rat mAb ◦ Mouse mAb ◦ Ascites

CUSTOM PROTEIN EXPRESSION
HEK293 ◦ Baculovirus ◦ *E. coli*

Superior Quality • Unriveled Expertise
866.339.0871
www.promab.com | info@promab.com
ProMab Biotechnologies, Inc.

nature jobs

Scientists stay informed of the latest:

- **Hot jobs**
- **Career news**
- **Announcements**

Sign-up to our **FREE** jobseeker newsletter:
www.naturejobs.com/newsletter

SCIENTIFIC AMERICAN™

Publishing the latest in science and technology for more than 165 years

A site license provides online access to *Scientific American*, *Scientific American Mind* and Special Issues

Recommend site license access to your library today:
www.nature.com/libraries/scientificamerican

nature publishing group npg

™ Scientific American, Inc.

sysmex

Prospective Protein Provider

ProCube

Evolution comes, suddenly.

Bringing unprecedented efficiency to pharmaceutical development:
Introducing ProCube, a service that assists the analysis of protein interactions.

You want to outsource search and quality control processes. But you need the work done quickly, and you want to keep a lid on costs. ProCube is designed to meet the demands of this type of development environment. We offer high-quality, ready-to-use analytical tools based on proprietary specimen testing technology and protein production technology that uses silkworms. This approach streamlines business processes from search to quality control. The evolution of the pharmaceutical development environment starts with Sysmex.

Features of ProCube

- Validation data

We provide peace of mind and earn customers' trust by centralizing immobilization work and including interaction analysis results.

- Multi-variety, high-volume samples

We can accommodate a broad range of applications using silkworm technology.

www.procube.sysmex.co.jp

Sysmex Corporation

V. FLORESCU

Global health hits crisis point

The Global Fund's drive to ensure sustainability and efficiency means that it may not be able to meet its commitments to combat disease, says **Laurie Garrett**.

Last week, Michel Kazatchkine tendered his resignation as executive director of the Global Fund to Fight AIDS, Tuberculosis and Malaria. Regardless of whether you've heard of the French AIDS scientist, or even of the fund, you should keep reading. This is a crucial, dangerous moment for global health.

Kazatchkine made clear the political struggle that forced his resignation. "The Global Fund has helped to spearhead an entirely new framework of international development partnership," he wrote in his resignation letter. But under stress during the world economic crisis, with radically declining support from donors, a battle developed. "Today, the Global Fund stands at a cross-road. In the international political economy, power-balances are shifting and new alignments of countries and decision-making institutions are emerging or will have to be developed to achieve global goals. Within the area of global health, the emergency approaches of the past decade are giving way to concerns about how to ensure long-term sustainability, while at the same time, efficiency is becoming a dominant measure of success," he wrote.

It is almost possible to hear Kazatchkine spitting out the words 'sustainability' and 'efficiency'. Since the financial crisis of November 2008, a storm has been brewing over these concepts, one that affects everything from humanitarian responses to projects that distribute malaria bed nets. It is a fight, and on one side are those who believe that crises in general, and the AIDS pandemic and allied diseases in particular, constitute global 'emergencies' that must be tackled with full force, mistakes be damned. On the other are those who feel that AIDS is now a chronic disease that can be managed with medication and therefore requires investment in permanent infrastructure of care and treatment that can eventually be operated and funded by the countries themselves.

It is a classic battle of titans, pitting urgency against long-term sustainability. In his resignation letter, Kazatchkine essentially conceded victory to the forces for sustainability. Charitable urgency didn't stand a chance once the donor states started cinching their domestic budget belts so tightly that they had to punch new buckle holes.

The fund was established ten years ago as a unique mechanism to move billions of dollars from rich countries to poorer ones, to combat and treat three infectious diseases: HIV, malaria and tuberculosis. It acts as a granting agency, accepting applications from governments and health organizations, and convenes regular replenishment meetings to tell donors — mostly the governments of the United States, United Kingdom, France and Germany — how much money is needed for the next round.

By the end of 2009, the fund was disbursing US$2.7 billion a year, and was underwriting almost half of all HIV treatment in poor countries, about two-thirds of all malaria prevention and treatment in the world and about 65% of all tuberculosis efforts. The fund's most marked impact has been on malaria. At the end of 2011, the World Health Organization estimated that the number of malaria deaths had fallen by one-quarter between 2000 and 2010.

But Global-Fund cash has spawned dependency and expectation among its recipients. Should it disappear, or radically diminish, countries would be hard-pressed to finance malaria and tuberculosis efforts.

Indeed, the great diminishment has commenced. In October 2010, the fund asked donors for $20 billion for five years' worth of disbursements. The donors were indignant and committed just over half that. In response, the fund's flabbergasted leadership cancelled the next grant round, and it will now not distribute new grants until 2014.

Donor scrutiny increased and a high-level independent review panel set up by the fund's governing board, which includes representatives of United Nations agencies and the World Bank, released a scathing report, citing a litany of problems, including fraud, theft and inconsistent decision-making by grant reviewers.

At a meeting in Accra, Ghana, on 21 November, the board members expressed shock at the problems identified by the high-level panel, and by reports commissioned on the situation on the ground in some countries. Some African leaders described riots and demonstrations at the lack of vital medicines, especially for HIV. The board's own investigation showed that the fund had committed assets of $10 billion for 2011–13, but had only about $4 billion in its bank accounts.

GLOBAL-FUND CASH HAS SPAWNED DEPENDENCY AND EXPECTATION AMONG ITS RECIPIENTS.

The board called for ways to stretch available resources and eliminate inefficiencies. Key to that would be the appointment of a general manager to oversee all spending, pushing Kazatchkine aside. Stepping into that position is Colombian banker Gabriel Jaramillo.

To try to give Jaramillo a running start, in Davos, Switzerland, last week, Bill Gates handed over some $750 million, redeemable by the fund in full during 2012, or spread out over time. And the Saudi Arabian government announced a $25-million donation. As generous as these millions may be, the fund needs billions just to stay alive and fulfil country grants, let alone to grow. Right now we have no idea where that money will come from. Should the fund collapse, the consequences will be severe. Progress against tuberculosis and malaria will stall, and more than a million people living with HIV could be left without treatment. ■

➲ **NATURE.COM**
Discuss this article online at:
go.nature.com/ge9til

Laurie Garrett *is senior fellow for global health at the Council on Foreign Relations in New York, recipient of the 1996 Pulitzer Prize in Journalism and author most recently of* I Heard The Sirens Scream: How Americans Responded to the 9/11 and Anthrax Attacks.
e-mail: lgarrett@cfr.org

RESEARCH HIGHLIGHTS

Selections from the scientific literature

CANCER GENETICS

Genome shatters in brain cancer

Cancer is usually attributed to a slow accumulation of genomic changes, but a few cancers result instead from a single catastrophic event that causes massive reshuffling of the genome. Researchers have discovered these major changes, called chromothripsis, in a type of medulloblastoma — a common childhood brain cancer — and have linked the disease to mutations in the tumour-suppressor gene *TP53*, which encodes the protein p53.

Jan Korbel at the European Molecular Biology Laboratory in Heidelberg, Germany, and his colleagues sequenced the genome of one patient with medulloblastoma and mutated *TP53*, and found many large genomic rearrangements. By analysing the genomes of 98 other patients with the brain cancer, they uncovered a strong association between mutant *TP53* and chromothripsis in one subtype of the cancer.

The authors propose that the protein p53 is involved in either initiating this massive genomic storm or keeping the cells alive afterwards.

Cell 148, **59–71 (2012)**

PSYCHOLOGY

'Brightness' fools the eye

The pupils of the human eye shrink in response to brightness, even when the glow is merely an optical illusion.

Bruno Laeng and Tor Endestad at the University of Oslo used infrared eye trackers to monitor the pupils of participants looking at illusions of lightness or brightness. These graphic designs give the impression of having brighter or whiter components (**pictured right**) than similar images of equal luminance (**left**). The pupils rapidly constricted when people glanced at the 'brighter' image, then slowly readjusted to the picture's true light intensity.

The authors suggest that the physical response to the illusions may be an adaptation designed to protect the eye's sensitive light-absorbing cells from potentially damaging levels of light.

Proc. Natl Acad. Sci. USA **http://dx.doi.org/10.1073/pnas.1118298109 (2012)**

BILL HUBICK

RESTORATION ECOLOGY

New wetlands don't measure up

Wetland restoration may be falling short of its goals, with restored or created wetlands lagging behind reference ones in terms of carbon storage and native species richness and abundance.

In many parts of the world, humans have destroyed more than half of the wetlands and efforts to restore them (pictured) stretch back 60 years. David Moreno-Mateos at the University of California, Berkeley, and his colleagues analysed 621 restored or created wetlands. They found that carbon storage in such wetlands was just half that of reference wetlands even two decades after restoration. Moreover, restored and created wetlands showed only a 74% recovery in a measure of 'biological structure' that combined several measures of the number and richness of native species.

PLoS Biol. 10, **e1001247 (2012)**

EVOLUTION

Why animals get bigger over time

In palaeontology, Cope's rule holds that species evolve larger body sizes over geological time. One possible explanation has been that competition favours bigger bodies. To test this, Pasquale Raia at the University of Naples Federico II in Italy and his colleagues compiled a species tree of 554 extinct mammals across the past 60 million years, and analysed size evolution within lineages.

They found that body size tends to increase as animals develop more specialized diets confined to particular habitats. Moreover, the origination of larger sizes coincided with periods of global cooling, and came at the cost of increased extinction risk.

Am. Nat. **http://dx.doi.org/10.1086/664081 (2012)**

GENE THERAPY

An eye for gene repair

Gene therapy in dogs can reverse retinal defects that lead to blindness in humans.

William Beltran and Gustavo Aguirre at the University of Pennsylvania in Philadelphia

US NATL ACAD. SCI.

and their group targeted a form of retinitis pigmentosa. This is a common cause of blindness in which mutations in the gene *RPGR* lead to the death of light-sensing photoreceptors in the retina. The authors tested their gene-therapy approach in four dogs with mutations that model a form of the disorder. After injecting a virus carrying human *RPGR* into one eye of each animal, the authors found that the photoreceptors' structure appeared normal, and that their light-responsiveness had improved in three of the four treated eyes. In the untreated eyes, the cells were shrunken, fewer in number and less responsive to light.

The authors say that their findings open the door to gene therapy in humans for certain kinds of retinitis pigmentosa.

Proc. Natl Acad. Sci. USA **http://dx.doi.org/10.1073/pnas.1118847109 (2012)**

PHYSICS

Quantum motion captured

Even if cooled to a temperature of absolute zero, all objects will retain a fundamental jitter in their physical positions due to quantum 'zero-point' fluctuations. Oskar Painter and his colleagues at the California Institute of Technology in Pasadena have, for the first time, detected this motion in a tangible object and measured an asymmetric property that arises from it.

The researchers patterned a one-micrometre-wide silicon beam to allow for a strong interaction between laser light sent into the beam and the motion of the beam. As the beam was cooled to below 1 Kelvin, a striking asymmetry emerged. The energy of the laser photons increased the motion of the beam, but, as per the laws of quantum mechanics, the beam's fundamental jitter could not add to the energy of the laser photons.

Phys. Rev. Lett. 108, **033602 (2012)**

GENOMIC MEDICINE

Sequencing diagnoses disease

In a study that shows both its promise and limitations in the clinic, researchers have used genomic sequencing to diagnose the genetic cause of disease in individual children — but succeeded in only a small proportion of them.

A team led by David Thorburn at the Murdoch Childrens Research Institute in Melbourne, Australia, and Vamsi Mootha at Harvard Medical School in Boston, Massachusetts, sequenced DNA from 42 unrelated children with symptoms of inherited disorders of the mitochondria — the cell's energy-producing organelles. The authors sequenced the mitochondrial DNA, as well as the coding regions of more than 1,000 nuclear genes that encode mitochondrial proteins. They found mutations in known or possible disease-causing genes in 23 of the children, and 10 received a firm diagnosis.

In the other cases, the causative gene may fall outside the sequenced regions, or the disease may be caused by weak interactions between several mutated genes, the authors say.

Sci. Transl. Med. 4, **118ra10 (2012)**

CANCER

Drug drives cancer stem cells

Cancer drugs that attack tumour-sustaining blood vessels may spur proliferation of the stem cells that contribute to the disease.

One such drug, bevacizumab, fails to prolong the survival of patients with advanced breast cancers, and studies have shown that patients on similar drugs often relapse. To find out why, Max Wicha and his team at the University of Michigan in Ann Arbor implanted human breast tumours into mice and treated them with bevacizumab and another blood-vessel-blocking drug, sunitinib. Treated tumours produced more cancer stem cells than untreated ones. The low-oxygen environment that the drugs create in tumours switches on a molecular pathway that encourages cancer stem cells to divide.

Combining these drugs with others that target cancer stem cells could yield a better outcome, the authors suggest.

Proc. Natl Acad. Sci. USA **http://dx.doi.org/10.1073/pnas.1018866109 (2012)**

COMMUNITY CHOICE

The most viewed papers in science

ANIMAL BEHAVIOUR

Hair defence against bed bugs

HIGHLY READ on http://royalsocietypublishing.org in December

Hirsute individuals are better able to sense blood-sucking bed bugs crawling on their skin than are their less hairy counterparts.

Isabelle Dean and Michael Siva-Jothy at the University of Sheffield, UK, tested the ability of 29 volunteers to detect the presence of bed bugs (*Cimex lectularius*) on a shaved and an unshaved arm. The volunteers detected the insects more frequently with their unshaved arm than their shaved one, and unshaved arms with a greater density of hair were more sensitive to the insects. Hairier skin also upped the time bed bugs took to find a feeding location.

Humans may have evolved less body hair to make parasites easier to see and remove, but the authors suggest that fine body hair has been maintained to enhance their detection.

Biol. Lett. **http://dx.doi.org/10.1098/rsbl.2011.0987 (2011)**

GEOLOGY

Explosion in Death Valley

The volcanic eruption responsible for the giant Ubehebe Crater in California's Death Valley may have occurred more recently than previously thought. This could mean that the risk of similar explosions happening today is higher than anticipated.

When magma encounters groundwater, distinctive explosions, such as those of Ubehebe, ensue. But how this could have happened in Death Valley, the driest area in North America, has been unclear. Brent Goehring at Purdue University in West Lafayette, Indiana, and his colleagues dated the crater (**pictured**) using the rate of accumulation of beryllium-10 isotopes in rocks exposed by the eruption. They conclude that the crater probably appeared 800–2,100 years ago, during a period in which Death Valley underwent prolonged drought.

The authors suggest that there may be enough permanent groundwater to drive further explosive eruptions in Death Valley.

Geophys. Res. Lett. **http://dx.doi.org/10.1029/2011gl050130 (2012)**

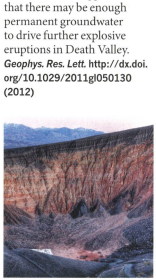

OCEAN/CORBIS

NATURE.COM

For the latest research published by *Nature* visit:

www.nature.com/latestresearch

SEVEN DAYS *The news in brief*

POLICY

Global Fund turmoil

The executive director of the Global Fund to Fight AIDS, Tuberculosis and Malaria, Michel Kazatchkine, has resigned after five years in charge. Kazatchkine, a French clinical immunologist, said on 24 January that he couldn't continue after the fund's board created the position of general manager, part of a restructuring plan agreed after the fund found corruption affecting some US$39 million of its grants (see *Nature* **470,** 6; 2011). Based in Geneva, Switzerland, the fund is struggling to raise cash and has frozen the funding of new grants until 2014. But on 26 January, it received a $750-million bonus pledge from the Bill & Melinda Gates Foundation. See page 7 for more.

Russian restraints

Physicists at one of Russia's leading research institutes have mounted an Internet campaign to draw attention to strict new budgetary and security policies that they say are hindering their work. Last year, Russia's government moved the Institute for Theoretical and Experimental Physics (ITEP) in Moscow, and two other institutions, out of the state-owned nuclear corporation Rosatom and into the jurisdiction of the Kurchatov Institute in Moscow. The new administration has restricted trips abroad for scientists, and blocked visits from foreign researchers, ITEP physicists say. See go.nature.com/getmp7 for more.

JOURNALISM AWARD

Nature reporter Ewen Callaway last week won a UK Medical Journalists' Association award for 'Fighting for a cause', a News Feature on chronic fatigue syndrome and viruses (*Nature* **471,** 282–285; 2011).

K. LEVESQUE/ARCTICNET

Engine trouble scuppers Arctic work

Canada's Arctic research vessel the *CCGS Amundsen* (pictured) has been put out of action while cracks in four of its six engines are repaired, forcing researchers to cancel the ship's research programme for 2012. The *Amundsen* can be used for science for up to 152 days a year, but only two six-week legs had been planned for this year. "If it had to happen, this was a good year for it," says Martin Fortier, executive director of ArcticNet, a research network based at Laval University in Quebec City, Canada, that provides funding and logistics for Arctic research in Canada. See go.nature.com/7dqkt1 for more.

Nanotech risks

The US National Research Council has added its voice to calls for high-quality research into the risks of nanotechnology. A report released on 25 January urges a more coordinated research strategy to cover questions such as how many nanoparticles of different kinds are being released into the environment, and who is being exposed to them. It also criticizes the dual role of the US National Nanotechnology Initiative: promotional activities should be separate from the oversight of research into risks, the report says. See go.nature.com/8zospl for more.

Indian space fracas

The former chairman of the Indian Space Research Organisation (ISRO) in Bangalore and three of his former ISRO colleagues have been barred from holding any government job. Gopalan Madhavan Nair was sanctioned after an investigation into a satellite deal between Antrix, the ISRO's commercial arm, and Bangalore-based telecommunications company, Devas Multimedia. The 2005 deal was well below market value, and the government scrapped it in February 2011. Nair and others deny wrongdoing; Nair blames his troubles on his successor at the ISRO, Koppilli Radhakrishnan. See go.nature.com/wl5avm for more.

Yucca's successor

The United States should create a programme to identify permanent and interim storage systems for nuclear waste, according to a 26 January report by a White House commission. In its final report, the commission — established in January 2010 after the administration of President Barack Obama halted work on the controversial proposed repository at Yucca Mountain

in Nevada — recommended setting up a new agency with dedicated funding. It also proposed a "consent-based approach" to nuclear storage, which involves finding communities that are willing to host waste.

Japanese merger

Japan's government is planning to cut costs by merging five prominent research organizations. Plans announced on 20 January would create one body to oversee the RIKEN network of basic-research laboratories; the National Institute for Materials Science; the Japan Agency for Marine-Earth Science and Technology; the National Research Institute for Earth Science and Disaster Prevention; and the Japan Science and Technology Agency, the national funding body. See page 19 for more.

RESEARCH

Eight years on Mars

NASA's Mars rover Opportunity marked its eighth anniversary on the red planet on 25 January, perched on an outcrop called Greeley Haven (a view from which is **pictured**), on the rim of a massive crater named Endeavour. The rover, heading into its fifth Martian winter, has driven 34.4 kilometres so far. Its instruments are

NASA/JPL-CALTECH/CORNELL/ARIZONA STATE UNIV.

fading: the decay of a cobalt-57 radiation source in the rover's Mössbauer spectrometer, for example, means that measurements of iron-containing minerals that used to take less than an hour now require weeks of work.

Planetary plethora

NASA's Kepler mission announced the discovery of 26 planets on 26 January, bringing the number of planets verified by the space probe to 61. Around 2,300 candidate planets still await confirmation. The latest findings are scattered across 11 planetary systems. See go.nature.com/hn3icx for more.

Top climate risks

Severe flooding is the United Kingdom's most pressing climate-change risk, according to an assessment of the nation's threats and opportunities under various climate scenarios. The study, which was published on 25 January, has been lauded for its innovative methodology, although it acknowledges that its confidence in many of the findings is 'low' or 'medium'. Britain will decide what actions to take when it publishes a national adaptation plan in 2013. See go.nature.com/7smiq5 for more.

PEOPLE

Chief scientist gap

The post of chief scientist at the US National Oceanic and Atmospheric Administration in Washington DC is to remain vacant after the administration of President Barack Obama withdrew its nomination of marine geochemist Scott Doney on 24 January — almost 18 months after Doney was put forward for the role. US Senator David Vitter (Republican, Louisiana) had put a hold on the confirmation process in protest at the administration's decision to issue a drilling moratorium after the April 2010 Deepwater Horizon oil spill in the Gulf of Mexico. The agency has not had a chief scientist since 1996.

FUNDING

Neglected diseases

Drug companies, philanthropists, national governments and the World Health Organization (WHO) are coordinating to tackle neglected tropical diseases (NTDs) such as sleeping sickness, Chagas disease, leprosy and river blindness. In a joint announcement on 30 January, the WHO laid out a road map to control or eliminate ten NTDs by 2020, and drug companies announced expansions and extensions to drug-donation programmes amounting to 1.4 billion treatments a year. The Bill & Melinda Gates Foundation says that it will give US$363 million over five years for NTD research. See go.nature.com/kscbg for more.

COMING UP

9 FEBRUARY

The maiden voyage of Europe's Vega rocket, a launcher for small satellites including research missions, begins. See go.nature.com/yd27mv for more.

BUSINESS

Illumina bid

A US$5.7-billion takeover bid for the dominant company in the DNA-sequencing industry spurred a rally in genome-technology stocks last week. On 25 January, the drug giant Roche, based in Basel, Switzerland, announced its intention to buy Illumina in San Diego, California. Roche is betting that the sequencing market will soon lead to clinical applications in diagnostics and drug discovery. Illumina's board of directors is still considering the proposal but has said it may offer investors cheap shares in the event that Roche starts to gain too much stock, in an effort to make a takeover more expensive. See go.nature.com/2vmedh for more.

TREND WATCH

Venture-capital biotechnology funding in the United States grew by 22% from 2010 to reach US$4.7 billion last year, according to a 20 January report. Venture-capital funding rose by 22% overall (see chart), with clean technology up 12%. But investors are sticking to established firms: the number of biotech and medical-device firms raising their first round of venture-capital reached a 15-year low, says Jonathan Leff, managing director of private-equity firm Warburg Pincus in New York.

VENTURE CAPITAL'S RECOVERY

Investment in young US firms is nearing pre-recession levels, with the biotechnology and clean-technology sectors tracking the overall rise.

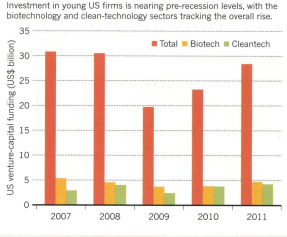

SOURCE: PRICEWATERHOUSECOOPERS/NVCA/THOMSON REUTERS

NATURE.COM

For daily news updates see:
www.nature.com/news

Welcome to the PCR Revolution.

PrimeSTAR®

GXL and Max

PrimeSTAR GXL DNA Polymerase is a revolutionary PCR enzyme with a **novel elongation factor** to dramatically increase performance for standard and challenging situations alike, including GC-rich templates. It's the enzyme of choice for most DNA templates.

PrimeSTAR Max DNA Polymerase is a unique **high-performance** DNA polymerase premix with the fastest extension speed available. Extremely accurate, sensitive, and specific. When fidelity is critical, use PrimeSTAR Max.

- **Extremely Accurate:**
  GXL: 30 errors/486,923 bp* (0.0062%)
  Max: 12 errors/542,580 bp* (0.0022%)
  *tested on ~500 bp GC-rich amplicons from *Thermus thermophilus*
- **Speed:** unsurpassed by any other commercially available PCR enzymes – amplify faster
- **PCR That Works:** success without the stress of extensive PCR optimization
- **Longer Products:** amplify products ≤ 30 kb with exceptionally high fidelity (PrimeSTAR GXL)

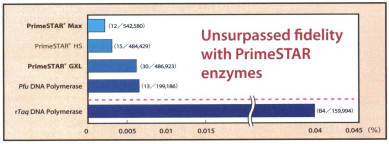

Try a FREE Sample
Samples Now Available....
Try Them While Supplies Last!!

SAMPLE Available

Ordering Information

Product Name.	Catalog #	Quantity
PrimeSTAR® GXL DNA Polymerase	R050A	250 Units
PrimeSTAR® Max DNA Polymerase	R045A	100 Rxns

Notice to Purchaser. Your use of these products and technologies is subject to compliance with any applicable licensing requirements described on the product's web page at http://www.clontech.com/takara. It is your responsibility to review, understand and adhere to any restrictions imposed by such statements. PrimeSTAR® is a registered trademark of TAKARA BIO INC. The TaKaRa logo is a trademark of TAKARA HOLDINGS, Kyoto, Japan. Unless otherwise specified, other trade names are also the trademarks or registered trademarks of various companies.

TaKaRa

TAKARA BIO INC.
800-662-2566

PCR That Works

www.clontech.com/takara

NEWS IN FOCUS

EMBRYONIC STEM CELLS Future of Californian funding agency is in doubt **p.15**

PHYSICS Subtle properties of the neutron could hold clues to a new theory **p.17**

JAPAN Leading geneticist fires parting shots as he quits his native country **p.18**

VACCINES A man with a plan to vanquish killer *Staphylococcus* **p.23**

B&C ALEXANDER/ARCTICPHOTO

Spills from pipes or rigs in icy areas such as those in Alaska are particularly challenging to clean up.

ENVIRONMENT

The great Arctic oil race begins

Conservationists fear spills in icy waters as Norway awards oil-production licences.

BY QUIRIN SCHIERMEIER IN TROMSØ, NORWAY

"The race is on for positions in the new oil provinces." That starting-gun quote was fired last week by Tim Dodson, executive vice-president of the Norwegian oil and gas company Statoil. The 'new oil provinces' are in the Arctic, which brims with untapped resources amounting to 90 billion barrels of oil, up to 50 trillion cubic metres of natural gas and 44 billion barrels of natural gas liquids, according to a 2008 estimate by the US Geological Survey. That's about 13% of the world's technically recoverable oil, and up to 30% of its gas — and most of it is offshore.

Oil companies see an opportunity to sate the world's demand for fossil fuels. Green groups and many scientists, however, are horrified by the prospect of drilling and production in remote, often ice-choked waters, where spills would be harder to control and clean up than in warmer regions. Memories of the devastating environmental impact of the *Exxon Valdez* accident in 1989 in Alaska's Prince William Sound are still all too fresh — like the oil that can still be found in the area's beaches (see *Nature* http://doi.org/d3gqd2; 2010).

At last week's Arctic Frontiers conference in Tromsø, Norway, the oil industry insisted that it will be cautious and responsible in extracting oil and gas in the region, and it rolled out an initiative to develop ways of coping with any accidents. Dodson told the meeting that "technology will be there to clean it up".

Statoil already operates the world's most northerly liquefied natural-gas production facility near Hammerfest, which draws gas equivalent to about 48,000 barrels of oil a day from the Snøhvit field in the Arctic waters off Norway. By 2020, the company hopes to extract one million barrels of oil equivalent a day from new wells in the Arctic. It is planning exploratory drilling later this year, for example, in the Skrugard and Havis gas fields that were discovered in the Barents Sea last year.

The Norwegian government is happy with Statoil's bold plans. Norway is currently the world's second-largest gas exporter, with production continuing to rise, but it is looking to the Arctic to offset a one-third decline in production at its oil fields farther south since 2000. "If we don't invest, we might lose another third within the next decade," says Ola Borten Moe, Norway's minister of petroleum and energy.

On 17 January, Moe awarded 26 production licences for developed offshore oil areas in the Norwegian and Barents Sea to companies including Statoil, Total, ExxonMobil and ConocoPhillips. And the settlement in 2010 of a long-running row between Norway and Russia over their Arctic maritime boundary will allow more exploration in formerly disputed parts of the Barents Sea (see 'Frozen fuels'). "There's an ocean of new opportunities that we will grasp with both hands," says Moe.

The resource rush is alarming critics. A group of 573 scientists, for example, wrote last week to US President Barack Obama, urging caution in authorizing new oil and gas activity in the Arctic Ocean north of Alaska. The open letter, coordinated by the Pew Environment Group, a conservation organization headquartered in Washington DC, argues that more research is needed to assess the potential impact on the region's environment and ecosystems before going ahead with more drilling.

NATURE.COM
Read more at *Nature*'s Arctic special:
ge.nature.com/s5w2pr

The industry holds that Arctic oil and gas development can be done in an environmentally ▶

sustainable manner despite the challenges. "We realize that there are huge issues when working in the cold and darkness and in the presence of sea ice in areas at great distance from any infrastructure," says Joseph Mullin, a London-based programme manager at the International Association of Oil and Gas Producers. Mullin will oversee a four-year, US$20-million research programme to address those issues, launched at the Tromsø conference by nine major oil companies.

The initiative, which is open to academic collaborators, will include research on the environmental effects of Arctic oil spills, spill trajectory modelling and remote sensing, and oil recovery techniques in sea-ice areas. It will also test Arctic clean-up technologies in a number of controlled oil releases. "You'd like to have a variety of spill-response options in the tool box before you venture out there," says Mullin.

The leading Russian oil and gas companies, Gazprom and Rosneft, have so far stayed clear of the initiative, adding to concerns about their compliance with national and international safety standards.

In December 2011, for example, at least 37 people were killed when an oil rig under contract to Gazprom capsized off Sakhalin Island in Russia's Arctic Ocean, resulting in a fine for the company.

And according to Vladimir Chuprov, a Moscow-based energy expert who works for Greenpeace, emergency contingency plans for the Prirazlomnoye oil platform in the Russian Barents Sea, where commercial drilling is to start this year, have not been publicly released, despite being required by Russian regulators.

But even companies with better safety records should avoid the Arctic, say Chuprov and other environmentalists. "In our view no company is ready for offshore oil projects in the Arctic Ocean," he says. ■

FROZEN FUELS

A 2010 Norwegian–Russian border agreement has opened up the Barents Sea to oil companies eager to exploit resources.

Oil and gas facilities: ● Planned ● Operational

Oil and gas reserves

PSYCHIATRY

Diagnostics tome comes under fire

Field tests of new criteria are flawed, critics argue.

BY HEIDI LEDFORD

Diagnoses of certain mental illnesses could rise significantly from next year, say some mental-health experts — but not because of any real changes in prevalence. Instead, the critics blame what they say is a flawed approach to testing the latest version of the *Diagnostic and Statistical Manual of Mental Disorders* (*DSM*), the standard reference used by researchers and mental-health professionals in the United States and many other countries to assess patients, inform treatment, design studies and guide health insurers.

Changes to the diagnostic criteria in the fifth edition of the manual, *DSM-5*, due to be published in May 2013 by the American Psychiatric Association (APA) in Arlington, Virginia, have raised concerns that some disorders will be overdiagnosed (see table). Critics say that the analysis of field tests of the new criteria won't settle those concerns.

Trials of *DSM-5* conducted at 11 academic centres were completed last October. In a Commentary published in the *American Journal of Psychiatry* (H. C. Kraemer *et al. Am. J. Psychiatry* **169,** 13–15; 2012), members of the task force explained that the aim was not to focus on the frequency of a given diagnosis under the proposed *DSM-5* criteria compared with that under the previous criteria. Because there is no accepted prevalence for most psychiatric disorders, they argued, it would be impossible to tell whether a rise in diagnoses reflects a true increase in the sensitivity of the revised criteria or simply a rise in the number of false positives.

That raised the hackles of some researchers, who say that without such comparisons it will be impossible to flag up the possibility that some categories will show an increased prevalence. "It's a real step back," says Thomas Widiger, a psychologist at the University of Kentucky in Lexington, who notes that trials of *DSM-IV* were careful to compare old and new diagnostic criteria to see which performed better.

Allen Frances, emeritus professor of psychiatry at Duke University in Durham, North Carolina, led the 1994 *DSM-IV* revision and is an outspoken critic of *DSM-5*. Frances

CONTENTIOUS PROPOSALS FOR *DSM-5*

Changes to diagnoses of some mental illnesses are causing disquiet about the consequences for patients.

Disorder	Change	Rationale	Reason for controversy
Autism spectrum disorder	Combines multiple *DSM-IV* diagnoses into one; changes number of criteria needed for diagnosis	Improved specificity of diagnosis	Concerns about underdiagnosis, loss of eligibility for state support
Attenuated psychosis syndrome	New diagnosis	To identify young people at risk for later manifestation of psychotic disorder	Concerns about overdiagnosis/ overmedication
Major depressive episode	Removes "bereavement" exclusion	Evidence does not support separating loss of loved one from other stressors	Concerns about overdiagnosis/ overmedication
Mild neurocognitive disorder	New diagnosis	To facilitate earlier intervention for individuals in early stages of neurocognitive disorders	Concerns about overdiagnosis/ overmedication

acknowledges that the field trials for *DSM-IV* were far from perfect. For example, his trials failed to identify the dramatic surge in diagnoses of attention-deficit/hyperactivity disorder that followed changes made in *DSM-IV*. The trials suggested that there would be an increase of about 15% in the disorder. Instead, says Frances, the diagnosis rose threefold. "We missed the boat," he says. "But at least we had some sense that there would be an increase."

Results from the *DSM-5* academic field trials have yet to be presented, but early calculations suggest that, in general, there will be no big differences in the frequency of diagnoses, says Darrel Regier, vice-chair of the *DSM-5* task force and APA director of research. That claim has done little to alleviate concerns, however, because the trials enrolled patients who were initially diagnosed under *DSM-IV* standards. This leaves untested the possibility that the *DSM-5* criteria will capture many more patients who were previously deemed healthy, notes Widiger.

Observers are also alarmed by the statistical thresholds that the trials used to assess reliability, or the likelihood that two or more clinicians would arrive at the same diagnosis using the proposed criteria. This likelihood is often expressed as a statistical term called 'Cohen's kappa'. A kappa of 0 means that there is no agreement between the clinicians; a value of 1 means that the clinicians agree totally.

Researchers in the field often strive to reach a kappa of 0.6–0.8, indicating that the independent diagnoses agree more often than not. But in the Commentary, lead author Helena Kraemer, an emeritus statistician at Stanford School of Medicine in California, argued that a kappa of 0.2–0.4 could sometimes be acceptable. Kraemer later elaborated to *Nature* that the task force was largely aiming for a kappa of 0.4–0.6, but that it wanted to prepare the field for seeing values as low as 0.2 in particularly rare diagnoses or in those without biological markers.

Unlike tests on the previous edition, the reliability tests on *DSM-5* were performed on separate occasions, so that the clinicians involved were unaware of each other's diagnoses. Widiger says that he supports the more rigorous approach, but that accepting a value as low as 0.2 gives him pause. "I've never seen anybody argue that a kappa of 0.2 is acceptable," he says. "You just can't get much lower than that."

Not everyone is worried about a surge in diagnoses. Thomas Frazier, a paediatric psychologist at the Cleveland Clinic in Ohio, has carried out his own study of *DSM-5* criteria for autism spectrum disorder. His results, published online last year (T. W. Frazier *et al. J. Am. Acad. Child Adolesc. Psychiatry* **51**, 28–40; 2012), suggested that the new definition would omit some patients with autism, but that this could be easily corrected by requiring one less symptom to meet the threshold for a positive diagnosis. "Unfortunately, the *DSM* committees are not systematically doing these kinds of studies," he says. ■

FUNDING

Stem-cell agency faces budget dilemma

The California Institute for Regenerative Medicine plans for a future without state support.

BY ERIKA CHECK HAYDEN

Halfway through its initial ten-year mandate, the California Institute for Regenerative Medicine (CIRM) in San Francisco is confronting a topic familiar to anyone at middle age: its own mortality.

The publicly funded institute, one of the world's largest supporters of stem-cell research, was born from a state referendum in 2004. Endorsements from celebrities such as then-state governor Arnold Schwarzenegger and the late actor Christopher Reeve, who had been paralysed by a spinal injury, helped to garner voter support for a public bond to underwrite the institute. But with half of the US$3 billion that it received from the state now spent and the rest expected to run out by 2021, CIRM is now actively planning for a future that may not include any further state support.

"It would be premature to even consider another bond measure at this time," wrote Jonathan Thomas, CIRM's chairman, in a draft of a transition plan requested by the state legislature. Thomas outlined the plan on 24 January at a public hearing held in San Francisco by the US Institute of Medicine, which CIRM has asked to review its operations.

Given that California is facing severe budget shortfalls, several billion dollars more for stem-cell science may strike residents as a luxury that they can ill afford. It may also prove difficult for CIRM's supporters to point to any treatments that have emerged from the state's investment. So far, the agency has funded only one clinical trial using embryonic stem cells, and that was halted by its sponsor, Geron of Menlo Park, California, last November.

Yet the institute has spent just over $1 billion on new buildings and labs, basic research, training and translational research, often for projects that scientists say are crucial and would be difficult to get funded any other way. So the prospect of a future without CIRM is provoking unease. "It would be a very different landscape if CIRM were not around," says Howard Chang, a dermatologist and genome scientist at Stanford University in California.

➲ **NATURE.COM**
Read more about CIRM's history and impact:
go.nature.com/bpedms

"It would be a very different landscape if CIRM were not around."

Chang has a CIRM grant to examine epigenetics in human embryonic stem cells, and is part of another CIRM-funded team that is preparing a developmental regulatory protein for use as a regenerative therapy. Both projects would be difficult to continue without the agency, he says. Federal funding for research using human embryonic stem cells remains controversial, and could dry up altogether after the next presidential election (see *Nature* **481**, 421–423; 2012). And neither of Chang's other funders — the US National Institutes of Health (NIH) and the Howard Hughes Medical Institute in Chevy Chase, Maryland — supports his interdisciplinary translational work. Irina Conboy, a stem-cell engineer at the University of California, Berkeley, who draws half of her lab's funding from CIRM, agrees that in supporting work that has specific clinical goals, the agency occupies a niche that will not easily be filled by basic-research funders. "The NIH might say that the work does not have a strong theoretical component, so you're not learning anything new," she says.

CIRM is developing plans to help its grantees to continue their work if the agency closes. One option is a non-profit 'venture philanthropy' fund that would raise money from private sources to support stem-cell research. The agency is also writing a strategic plan for the rest of its ten-year mandate that focuses on translating research into the clinic, acknowledging that CIRM's best shot at survival — and at sustaining future funding for stem-cell researchers — could come from a clinical success.

As CIRM board member Claire Pomeroy, chief executive of the University of California, Davis, Health System in Sacramento, noted at the agency's board meeting on 17 January: "If you asked the public what they would define as success, they would say a patient benefited." ■

MEDICINE

Informed consent on trial

Lengthy, complicated documents leave many clinical-trial participants in the dark about the risks they face.

BY DANIEL CRESSEY IN BRUSSELS

Informing clinical-trial participants of the risks they face is a cornerstone of modern medical research, and it is enshrined as a human right in international codes of ethics. But an influential group of ethicists and medical researchers warned at a meeting in Brussels last week that the process has become a box-ticking exercise focused more on offering legal protection to a trial's organizer than actually protecting patients.

"We clearly identified there is an urgent need to do informed consent better," says Ingrid Klingmann, chairman of the European Forum for Good Clinical Practice, a think tank based in Brussels and the organizer of the meeting. "The pressure is really huge on all those involved to better enable patients to understand the implications of their study participation, their benefits, risks and obligations."

The European Clinical Trials Directive, which sets minimum standards for clinical trials conducted in the European Union's member states, says that trial participants must be duly informed of the "nature, significance, implications and risks" of the clinical trial. Yet delegates at the meeting detailed a host of ways in which the system fails to meet those criteria.

Denis Lacombe, director of the Brussels headquarters of the European Organisation for Research and Treatment of Cancer, presented data showing that the median length of consent forms used in the organization's trials tripled between 1995 and 2009 (see 'Fatter forms'). In many cases "the informed consent is 20 pages of nothing", says Harry Bleiberg, an oncologist formerly at the Jules Bordet Institute in Brussels who is now a medical consultant for the pharmaceutical industry.

Other speakers showed that warnings of possible side effects are often vague, and jumble potentially serious problems among minor concerns. Details of the prognosis of the disease and the likely outcome of the treatment are often scarce.

Long, jargony forms mean that many patients have little idea what they are actually signing up to, says Dominique Sprumont, a health lawyer at the University of Neuchâtel in Switzerland. In a study of about 200 patients involved in cancer clinical trials in the United States who responded to a questionnaire, 63% were unaware of the additional risk associated with participating, and 70% did not realize that the treatments being offered were unproven (S. Joffe *et al. Lancet* **358,** 1772–1777; 2001).

FATTER FORMS

Europe's cancer-trial consent forms are much longer — but are they more informative?

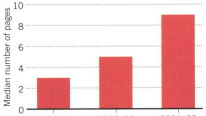

Data from protocols of 248 trials run by the European Organisation for Research and Treatment of Cancer.

One solution presented at the meeting was to base forms on those used in Norway, where a short summary of the main aspects of a trial precedes more detailed information. And many delegates advocated a greater use of graphics and charts. "We will certainly work on a proposal for a template that includes a one- or two-page summary," says Klingmann, who hopes to circulate the document to clinical-trial organizers around the world.

Some ethicists advocate digital consent forms, delivered by computer or smart phone. Interactive forms could lead participants through the consent process, and keep them more informed during the trial. They could also make it easier for researchers to obtain new consent if they need to change a study once it is under way.

GLOBAL ISSUE

Concern over the issue is not unique to Europe. Trials are increasingly 'off-shored' to less-developed countries, and several investigations have found poor consent procedures there. Last month, for example, GlaxoSmithKline was fined in Argentina over what the company describes as "administrative irregularities in the process of obtaining informed consent from a small proportion of patients" in a trial in which 14 children had died (the company is appealing the ruling).

The US Department of Health and Human Services is currently consulting about revising clinical-trial regulations, and looks likely to demand shorter, more understandable consent forms, although there is no specific deadline for a decision. "Our effort is to enable a patient who is contemplating enrolling in a clinical trial to have clear and full information to use in making a decision," says Ann Bradley, a spokeswoman for the department's Office for Human Research Protections. A number of US medical groups are backing the effort: the American Society of Hematology in Washington DC, for example, says that in addition to making the process less burdensome for researchers, shorter forms could help to increase the number of patients recruited to clinical trials.

Sprumont argues that the scientists involved in clinical trials should also work to improve the system. "Scientists must assume more responsibility," he says. ■

MORE ONLINE

TOP STORY

From mouse to elephant in a few (million) generations go.nature.com/fijfto

MORE NEWS

- Cancer drugs affect mouse genomes for generations go.nature.com/rdmmhy
- Spiders dodge cannibalism with remote copulation go.nature.com/6egqxl
- Visiting Iranian scientist falls foul of US authorities go.nature.com/lp71fw

PODCAST

The dangers of sugar, predicting supervolcanoes and bringing elephants to Australia go.nature.com/xuyueb

DLILLC/CORBIS

SOURCE: A. KNECHT

LOWERING THE BAR

The standard model of particle physics predicts a small electric dipole moment (EDM) for the neutron, well below the sensitivity of previous experiments. A larger dipole, predicted by some versions of supersymmetry, should lie within the range of three current experiments.

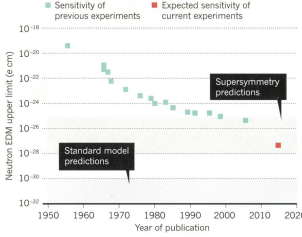

If the internal structure of the neutron creates an electric dipole (d), its orientation with respect to magnetic spin (μ) would change under a reversal of charge and parity (CP), thus violating CP symmetry.

PHYSICS

Dipole hunt stuck in neutral

Physicists admit to delays as attempts to measure the neutron's charge are plagued by difficulties.

BY EUGENIE SAMUEL REICH

Discovered 80 years ago this month, the neutron is famous for what it lacks: electric charge. Yet this is a simplification of a deeper truth. Each neutron is made of charged quarks: two down quarks that each carry a negative charge one-third as strong as an electron's; and an up quark that carries a two-thirds positive charge.

In theory, this arrangement could create an electric dipole moment (EDM) — an offset between the centres of positive and negative charge. Measuring the EDM could reveal clues to physics as profound as that sought at the Large Hadron Collider (LHC) at CERN, Europe's particle-physics lab near Geneva, Switzerland. Unlike the LHC experiments, which rely on sheer energy, dipole measurements are so subtle and easily foiled that the three leading efforts are woefully behind schedule.

This week, a US team that is developing a neutron EDM experiment at the Oak Ridge National Laboratory in Tennessee is awaiting feedback from a technical-review committee after delays forced the group to update its research plans. A team at the Laue-Langevin Institute in Grenoble, France, had intended to begin taking data in 2009, but is still running tests on its apparatus. A third group, based in Switzerland, is aiming to collect its first batch of data later this year after problems prevented it from beginning its run in 2011.

"The experiments have all taken a lot longer than any of us thought they would," says Philip Harris, a physicist at the University of Sussex, UK, and spokesman for the Grenoble-based effort.

The stakes are high. An EDM for the neutron would violate charge–parity symmetry, which dictates that particle interactions are unchanged when particles are replaced by their antimatter counterparts and by their mirror images. The standard model of particle physics predicts subtle violations of charge–parity symmetry and proposes an EDM that is below the sensitivity of any currently achievable experiment. But a larger neutron EDM, possibly detectable by the latest efforts, could point to physics beyond the standard model (see 'Lowering the bar'). One popular theory, called supersymmetry — which predicts a zoo of undiscovered particles and interactions — includes the possibility that a process known as electroweak baryogenesis took place in the early Universe, producing more matter than antimatter and breaking the symmetry between charge and parity.

Physicists at the LHC are also seeking hints of supersymmetry. Yet as the US$6.5-billion LHC has forged ahead, the neutron EDM experiments, with modest budgets of tens of millions of dollars, have hit a wall. The Swiss-based experiment at the Paul Scherrer Institute in Villigen aims to measure the dipole moment by comparing the movement of neutrons in a strong electric field to that of mercury atoms in the same field. But the experiment has been sidetracked by contamination from an unknown source that destroyed the polarization of the mercury atoms. Researchers have had to replace several parts of the apparatus to solve the problem, says project spokesman Klaus Kirch, a physicist at the Swiss Federal Institute of Technology in Zurich.

The Grenoble-based experiment has run into different problems. It uses liquid helium to cool neutrons to almost absolute zero, then observes whether their behaviour changes in an electric field. But the researchers have been stymied because the liquid helium boils and begins to break down as stronger electric fields are applied.

The US experiment, co-funded by the Department of Energy and the National Science Foundation, has had a similar problem. It aims to detect the neutron's presumed EDM by looking for changes in the light emitted when cold neutrons interact with helium-3 nuclei in the presence of an electric field, a process that is subtly altered if the neutron has an EDM. The project's co-spokesman, Paul Huffman of North Carolina State University in Raleigh, says that trial runs on a test apparatus ran into problems when bubbles began to form on its electrodes. He says that the group is now searching for alternative electrode coatings and is considering increasing the pressure in the experiment, which might prevent the bubbling.

The US agencies funding that project are tracking the problem. Last year, the Department of Energy delayed a decision on whether to approve the experiment by two years to allow for more exploratory research and development. "What we basically did was to move the goalposts," says Peter Jacobs, a senior scientist at the Lawrence Berkeley National Lab in California, who was involved in the review. Now, a second technical-review committee is assessing the latest research plans for the experiment.

"The experiments have all taken a lot longer than any of us thought they would."

Despite the problems, nuclear and particle physicists continue to express broad support for the neutron EDM studies, which they say are a unique complement to the LHC work. "It's a constellation of experiments that is critical," says Michael Ramsey-Musolf, a theoretical physicist at the University of Wisconsin-Madison. ■

RESEARCH POLICY

Genomics ace quits Japan

Yusuke Nakamura blames government inertia for his move to the United States.

BY DAVID CYRANOSKI IN TOKYO

As 2011 dawned, leading Japanese geneticist Yusuke Nakamura was launching a cabinet-level innovation office that he hoped would spur the country's stagnant biomedical industry. By the year's end he was preparing to leave for the University of Chicago in Illinois, frustrated by Japan's lack of support for genomics and doubtful that the country would ever take a global lead in medicine.

Nakamura has been a major force in Japanese science, with more than 1,150 publications to his name. He is one of the country's best-funded researchers and has led some of Japan's biggest science projects. In addition, he is a successful biotechnology entrepreneur, having established the company OncoTherapy Science, based in Kawasaki City.

But he has also been the target of criticism, both from opponents of 'big science' and from those who thought that his cancer-genetics research at the University of Tokyo put clinical science ahead of participants' rights[1] — a charge he rejects.

Some argue that Japanese science can shrug off Nakamura's departure. "He's not the only one that can do genomics," says Yuko Ito, a molecular biologist and science-policy researcher at the National Institute of Science and Technology Policy in Tokyo. "Genomics has gone far in many directions, been incorporated in so many other fields. It doesn't depend on one person."

But Tatsuhiro Shibata, head of genomics at the National Cancer Center Research Institute in Tokyo, says he is "very worried" by the move, adding that Japan has lost a strong lobbyist for the field. Without Nakamura's leadership, Shibata fears that Japan will fall further behind countries that are pressing ahead in genomics, such as China[2].

Some biologists still feel ashamed that Japan contributed only 6% of the human genome sequence published in 2001 (by contrast, the United States provided 59%). The country rebounded, largely as a result of Nakamura's efforts, by contributing about one-quarter of the International HapMap Project in 2005, which compared variations between human genomes[3]. But since then, money for genomics research in Japan has dried up. The country is leading just 1 of 50 projects under the International Cancer Genome Consortium, for example, compared with the United States' 20 and Mexico's 3.

Shibata says that genomics has lost out because of Japan's shift to post-genomic research, which saw large-scale projects launched to investigate subjects such as protein structure[4]. Nakamura blames a more general rejection of "big science" and clinical applications by the "basic scientists" involved in science policy-making. "It's obvious that support for genomics is not there," he says.

"By moving to the United States, I might be able to bring something back."

Speaking to *Nature* from his office at the University of Tokyo, Nakamura says that the loss of government support for genomics accounts for 20% of his decision to leave. The opportunities at Chicago, which recently opened a Center for Personalized Therapeutics that will incorporate genetic information into routine clinical practice, contributed another 30%. And 10% came from a tussle with the newspaper *Asahi Shimbun* over the way a story linked him with a cancer-vaccine clinical trial in which a participant experienced an adverse reaction, he says. He is suing the paper and two journalists.

But the remaining 40% — the biggest single factor — is that he felt powerless at the government's new Office of Medical Innovation. A year ago, he hoped to resuscitate Japan's moribund pharmaceutical and medical-device industries, and redirect its ballooning health-care outlays from foreign pharmaceutical coffers to domestic companies. Nakamura laments that none of the cancer drugs approved by the US Food and Drug Administration in the past decade came from Japan, and he has pushed for innovations such as a national high-throughput drug-screening facility[5]. He has also tried to persuade the government to integrate his plans into the economic stimulus programme that followed last year's earthquake and tsunami. But, he says, flatly, "my proposals were not taken".

He acknowledges that the government is investing in biomedicine as part of its quake-recovery plan. A ten-year, ¥64-billion (US$835 million) initiative launched in November — tentatively named the Tohoku Medical Megabank — aims to create the world's largest collection of biological samples at Tohoku University, which is in the quake region. But Nakamura says he was left out of the planning. "The innovation office plays no role. I had nothing to do." To add to Nakamura's frustration, it is unclear how Megabank will link to the existing BioBank Japan, a project he initiated that now holds about 200,000 samples (see 'Japan plans another huge tissue repository').

University of Tokyo vice-president Yoichiro Matsumoto, a mechanical engineer who will take over Nakamura's role at the innovation office, shares his sense of crisis. "If we don't create an innovation system now, we'll be sunk," he says. He hopes to make the office useful

BIOBANK, MEET MEGABANK

Japan plans another huge tissue repository

Japan is moving to establish a massive patient-sample bank — the Tohoku Medical Megabank — using stimulus money provided to boost the economy and replace infrastructure in the northeastern region devastated by a tsunami last March.

Masayuki Yamamoto, a cancer biologist at Tohoku University who is expected to lead the programme, says that in the first three years samples will be gathered from 70,000 healthy people from about 10,000 three-generation families; and from another 80,000 unrelated people. This will provide a resource for studying the relationship between genes and lifestyle factors in disease. The third cohort, to follow several years later, will target patients with specific diseases. How the Megabank will link in with the country's current repository, BioBank, remains to be seen.

The Megabank will be supported by medical facilities in the Tohoku region, where reconstruction plans include an electronic medical records system, which will help with the sharing of genetic and other data. Launched with ¥15.8 billion (US$207 billion) from a supplementary budget passed in November, the Megabank is expected to receive roughly ¥5 billion per year for the next decade. D.C.

by creating networks of researchers to support national projects such as the Megabank. Although he credits Nakamura as a brilliant scientist, he adds that his strengths lie more in research than administration and networking.

Atsushi Sunami, a science-policy researcher at the National Graduate Institute for Policy Studies in Tokyo, blames Nakamura's departure on bureaucracy and a lack of political leadership, rather than a fundamental problem with medical innovation. "I think he just couldn't handle the system" of Japanese government, Sunami says.

When Nakamura returned to Japan in 1989 from a position at the Howard Hughes Medical Institute at the University of Utah in Salt Lake City, he says, his ambition "was to make drugs in Japan and provide them to Japanese patients". But now, he says, "if I stay, I wouldn't be able to make anything. By moving to the United States, I might be able to bring something back." ■

1. Cyranoski, D. *Nature* **424,** 359 (2003).
2. Cyranoski, D. *Nature* **464,** 22–24 (2010).
3. The International HapMap Consortium *Nature* **437,** 1299–1320 (2005).
4. Cyranoski, D. *Nature* **443,** 382 (2006).
5. Cyranoski, D. *Nature* **474,** 136 (2011).

JIJI PRESS/AFP/GETTY IMAGES

RIKEN, home to the world's fastest supercomputer (above), may be overseen by a new body.

RESEARCH POLICY

Japan plans to merge major science bodies

Drive to save money could increase bureaucracy.

BY ICHIKO FUYUNO

In its battle against a sluggish economy, Japan's government is gearing up to make cost savings through a root-and-branch reform of the country's science system, merging some of its most prominent research organizations.

Plans approved by the government's cabinet on 20 January would consolidate the RIKEN network of basic-research laboratories with the National Institute for Materials Science (NIMS), the Japan Agency for Marine-Earth Science and Technology (JAMSTEC), the National Research Institute for Earth Science and Disaster Prevention (NIED) and the Japan Science and Technology Agency (JST) — the national funding body.

"This is the result of our aim to create the world's leading science and technology while slashing wasteful spending and making the organization as compact as possible," said Tenzo Okumura, a senior vice-minister of the education and science ministry, at a press conference last week. The policy would probably create an overarching body to supervise all five institutions, which would share more of their research and administrative resources, and lose some of their executive directors.

But with few details about the timing, potential cost savings or full implications of the change, many researchers are concerned that it could be a recipe for harsh funding cuts and even greater bureaucracy.

"The plan isn't intended to improve the research system," says Tasuku Honjo, a molecular biologist at Kyoto University and a former member of the Council for Science and Technology Policy, the government's top science advisory body. "Each of the institutes has fundamentally different characteristics, so I feel they would be very difficult to integrate effectively."

JST president Michiharu Nakamura, however, is optimistic about the change. "The new organization will be expected to play the main part in leading the national innovation," he says. "We will work hard to keep the independence of our fund-distribution process after the integration, as well as to strengthen the cooperation between stakeholders such as the academic community and industries." The plan would also merge the National Institute of Radiological Sciences (NIRS) with the Japan Atomic Energy Agency. The government says that this will speed up and strengthen its commitment to mitigating the Fukushima accident, and help to improve nuclear safety measures.

The news comes as the government scrambles to gain public support for tax hikes while cutting public spending. Since the Democratic Party of Japan took power in 2009, the Government Revitalization Unit (GRU), a budget watchdog chaired by the prime minister, has been reviewing government-funded projects and organizations to find savings (see *Nature* http://doi.org/bs75dv; 2010).

"The GRU rapidly came up with the plan a month ago and pushed forward without much discussion," says Atsushi Sunami, a science-policy specialist at the National Graduate Institute for Policy Studies (GRIPS) in Tokyo. Legislation to enact the overhaul will be submitted to Japan's parliament, the Diet, in the coming months. If passed, the changes would take effect in April 2014. More institutes may be added to the integration plan during discussions in the Diet, say policy experts.

The government also intends to set up a third-party audit system to evaluate administration and performance more strictly. The idea of more governance worries Sukekatsu Ushioda, president of NIMS. "Currently, the NIMS president has sufficient authority, so the decision-making process is fast. We at NIMS can often take new actions shortly after a board meeting," he says. "But if a higher management is added above NIMS, the decision-making would be slower and it would be difficult to take dynamic approaches." ■

➲ NATURE.COM
For more from this region, see Nature Japan: natureasia.com/japan

ATTACK OF THE BLOBS

Jellyfish will bloom as ocean health declines, warn biologists. Are they already taking over?

BY MARK SCHROPE

Blooms of giant Nomura's jellyfish (*Nemopilema nomurai*) have troubled Japanese fishing crews.

KYODO/NEWSCOM

Last summer, intrepid surfers flocked to Florida's east coast to ride the pounding swells spawned by a string of offshore hurricanes. But they were not prepared for a different kind of hazard washing towards shore — an invasion of stinging moon jellyfish, some of which reached the size of bicycle wheels. The swarms of gelatinous monsters grew so thick that they forced a Florida nuclear power plant to shut down temporarily out of concern that the jellies would clog its water-intake pipes.

Earlier in the year, similar invasions had forced shut downs at power plants in Israel, Scotland and Japan. The gargantuan Nomura's jellyfish (*Nemopilema nomurai*) found in Japanese waters can weigh up to 200 kilograms and has plagued the region repeatedly in recent years, hampering fishing crews and even causing one boat to capsize. Jellyfish have destroyed stocks at fish farms in Tunisia and Ireland. And in the Mediterranean Sea and elsewhere, officials have built nets to keep out jelly swarms.

The jellyfish blooms seem to bear out warnings from some scientists and conservationists, who argue that humans are knocking marine ecosystems off balance, causing a massive increase in the global population of jellyfish — a catch-all term that covers some 2,000 species of true cnidarian jellyfish, ctenophores (or comb jellies) and other floating creatures called tunicates. But many marine biologists are now questioning the idea that jellyfish have started to overrun the oceans.

This week, a group of researchers published preliminary results from what will be the most comprehensive review of jellyfish population data[1]. They say that there is not yet enough evidence to support any conclusions about a global upswing in jellyfish populations. "We are not at a point to make these claims," says Robert Condon, a marine scientist at the Dauphin Island Sea Lab in Alabama, who leads the group. "If you look at how that paradigm formed, it's not based on data or rigorous analyses."

The main problem, say the scientists, is that jellyfish are notoriously difficult to study, so they have historically received scant attention from marine biologists. There are remarkably few data about their life cycles, populations and responses to natural oceanographic cycles. But the creatures could serve as key indicators for the health of the oceans, so scientists are now building a database of jellyfish research and exploring new ways to keep track of them.

Monty Graham, chairman of the department of marine science at the University of Southern Mississippi in Diamondhead, is part of the review team now questioning the idea of a rise in jellyfish numbers, but more than a decade ago he was sounding the alarm. In

1996, he took a position at the Dauphin Island Sea Lab, where he found that the US National Oceanic and Atmospheric Administration had years of mostly unprocessed population data on moon jellyfish (*Aurelia aurita*) and Atlantic sea nettles (*Chrysaora quinquecirrha*) in the Gulf of Mexico. These data were a rare treasure; only a handful of similar long-term records exist.

Graham discovered that from 1985 to 1997, the jellies had grown substantially more widespread and abundant in several parts of the Gulf, and he suggested that human changes to the ecosystem might be the cause[2].

Similar findings supported the notion. In the Bering Sea, one of the handful of locations with a monitoring record longer than a few years, jelly numbers had also risen through the 1990s. That matched predictions made by ocean scientists, who had warned that as humans degrade the oceans they are shifting ecosystems, reducing numbers of larger fish and promoting populations of organisms from lower down the food chain[3,4]. Among the beneficiaries would be algae, toxic plankton and jellyfish — in other words, there would be a sea of slime.

BOOM AND BUST

The link between ocean degradation and jellyfish makes biological sense. Nutrient pollution can increase food supplies for jellyfish; overfishing can reduce their competition; and warmer temperatures are thought to trigger reproduction in some jellyfish species.

But as the slime paradigm gained traction in the literature, something odd was happening in the Gulf of Mexico. One of Graham's graduate students, Kelly Robinson, found that jellyfish numbers in the northern Gulf had declined for several years after 1997, and then rebounded. Her work has not yet been published.

Researchers studying jellyfish in the Gulf of Mexico and the Bering Sea now think that long-term natural climate cycles have an important role in controlling populations there. "Just seeing a lot of jellyfish does not say anything," says Graham now. "People say, 'Oh my God, the world is going to hell,' but jellies form blooms. That's what they're supposed to do." The challenge for researchers lies in separating normal fluctuations from those for which humans might deserve some of the blame.

Graham and others decided to take a scientific step back. In 2009, the National Center for Ecological Analysis and Synthesis at the University of California, Santa Barbara, funded Graham, Condon and Carlos Duarte, a marine ecologist at the Mediterranean Institute for Advanced Studies on Majorca, Spain, to establish the working group that has just published its findings. Made up of dozens of researchers, it compiled all the scientific data available on jellies worldwide. After a preliminary examination, the group said[1] that it could not support the conclusion that jellyfish numbers are increasing globally, because only a few places have been monitored carefully and even there the data are limited.

Researchers have tended to ignore or avoid jellyfish, in part because they are such a nightmare to deal with. Typical nets shred them, and collecting them intact can require heroic efforts. Shin-ichi Uye, a marine ecologist at Hiroshima University in Japan, says that because some jellyfish are heavier than sumo

J. GUEZ/AFP/GETTY

Jellyfish plagued an Israeli power plant in 2011.

wrestlers, marine biologists must carefully balance their small research boats to avoid capsizing when retrieving a single specimen.

To make matters worse, many jellyfish groups have complex life cycles. Several species, including moon jellyfish, reproduce sexually to form larvae that settle on the sea floor and develop into anemone-like growths called polyps. If conditions are favourable, a single polyp can bud to form 20 floating jellies. But in hard times, polyps can produce more polyps or retreat into a tough cyst. Then, when the environment improves, the waiting polyps can fuel a massive bloom of jellyfish that might seem like an invasion from nowhere.

With very few exceptions, the polyp colonies that cause large jellyfish blooms are "really hard to find", says Claudia Mills, a jellyfish specialist at the University of Washington's Friday Harbor Laboratories, who was part of the jellyfish review group and was one of the first to examine the possibility of a global rise. Bloom triggers seem to be tied to seasonal temperature changes, she says. And that raises the possibility that warming of the oceans could indeed cause populations to mushroom[5].

Most of the researchers who have questioned the idea of a jellyfish explosion say they cannot rule out the possibility that blooms are becoming more prevalent or that humans are at least partly responsible[6]. In Japan, for example, long-term records suggest that blooms happened only every 40 years or so before 2000, but have come nearly every year since[7]. Moreover, the blooms seem to originate in Chinese waters, where overfishing has severely depleted the Japanese jellyfishes' main competitors.

In most other cases, however, the trends are not so clear cut. So in 2010, the biologists on the task force began a Jellyfish Database Initiative (JEDI), compiling every scientific jellyfish record they could find, and they expect to continue expanding this resource. Some researchers are also teaming up with the public. The Monterey Bay Aquarium Research Institute in California has launched a website called Jellywatch.org, through which scientists and citizens can report jellyfish sightings to help fill out the JEDI database. The intergovernmental Mediterranean Science Commission in Monaco has started a similar programme for that sea.

HIDDEN DATA

Despite the lack of long-term studies, some scientists think that there is enough evidence to answer some important questions. In a paper due out later this month, Lucas Brotz, a graduate student in fisheries biology at the University of British Columbia in Vancouver, Canada, and his adviser, Daniel Pauly, analysed media reports and other non-scientific data about bloom patterns since 1950, such as interviews with locals and scientists. The researchers used fuzzy logic, a ranking system that incorporates the reliability and abundance of information, to identify trends in less-than-ideal data sets. They found that jellyfish populations were increasing in 31 of the 45 ocean regions that they studied.

"Our study says you can actually pierce through the confusing fog of press reports and anecdotes and scientific data to establish whether increases are occurring," says Pauly.

Graham and other researchers praise the approach, but they contend that such information just isn't adequate. The jellyfish review team will begin to analyse the full JEDI database later this month, encouraged by the growth of programmes in places such as Peru and Japan, where scientists work with fishermen to monitor jellyfish populations. But even so, the researchers caution that they will need to establish many more monitoring programmes to complete a global picture.

With such programmes in place, researchers could use the comprehensive jellyfish data sets to track how the oceans are changing. These creatures make ideal environmental sentinels because humans mostly leave them alone, says Graham. "Jellyfish are the great bystanders of the oceans and the oceans' health." ■

Mark Schrope *is a freeland writer in Melbourne, Florida.*

1. Condon, R. H. *et al. BioScience* **62**, 160–169 (2012).
2. Graham, W. M. *Hydrobiologia* **451**, 97–111 (2001).
3. Pauly, D., Christensen, V., Dalsgaard, J., Froese, R. & Torres, F. Jr *Science* **279**, 860–863 (1998).
4. Jackson, J. B. C. *Proc. Natl Acad. Sci. USA* **105**, 11458–11465 (2008).
5. Mills, C. E. *Hydrobiologia* **451**, 55–68 (2001).
6. Purcell, J. E. *Annu. Rev. Mar. Sci.* **4**, 209–235 (2012).
7. Uye, S. *Plankton Benthos Res.* **3**, S125–S131 (2008).

Cell Research

Special Issue and Web Focus

Cell Signaling, Disease and Stem Cells

The January special issue of *Cell Research* on Cell Signaling, Disease and Stem Cells brings together the latest reviews and articles in the field. The current understanding, as well as the recent advances in various aspects of cell signaling, stem cell biology, and their relevance to disease pathogenesis, is presented. Further background information on this important topic is available through the accompanying web focus which links to related articles from across Nature Publishing Group.

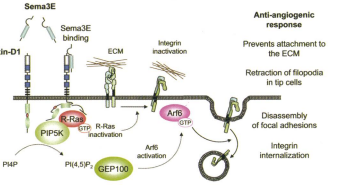

Featured articles include:

Semaphorin signaling in angiogenesis, lymphangiogenesis and cancer
Atsuko Sakurai, Colleen Doci and J Silvio Gutkind

Signal control through Raf: in sickness and in health
Jihan K Osborne, Elma Zaganjor and Melanie H Cobb

Autophagy: for better or for worse
Ellen Wirawan, Tom Vanden Berghe, Saskia Lippens, Patrizia Agostinis and Peter Vandenabeele

To access the Special Issue and Web Focus on Cell Signaling, Disease and Stem Cells visit:

www.nature.com/cr/focus/csdsc

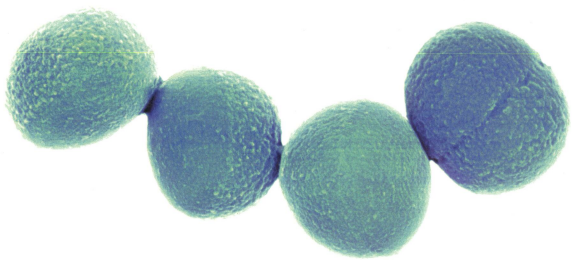

Man vs MRSA

For decades, Robert Daum has studied the havoc wreaked by methicillin-resistant Staphylococcus aureus. *Now he thinks he can stop it for good.*

BY MARYN MCKENNA

Over the years, Robert Daum has learned to respect his adversary. In 1995, he and his co-workers at the University of Chicago children's hospital in Illinois were investigating infections that had affected two dozen children in their emergency department. Three children had fast-moving pneumonia. A fourth had an abscess the size of his fist buried in the muscle of one buttock. In a fifth, the bacterium had infiltrated the bones of one foot. The infections were resistant to many common antibiotics, including methicillin. To Daum's surprise, the culprit was MRSA — methicillin-resistant *Staphylococcus aureus* — a bacterium that was thought to spread only among hospital inpatients. But none of these kids had been to the hospital for months before becoming ill.

Few researchers were willing to accept the implications. Daum wrangled for 18 months with editors at the *Journal of the American Medical Association* over a paper reporting the cases and showing that this strain was dangerous, acquired in the community and differed genetically from hospital strains. His article[1] was eventually published in 1998 and is now widely considered to be the early warning of an epidemic that currently results in millions of visits to doctors and hospitals a year[2].

Daum, a paediatric infectious-disease physician and founder of the University of Chicago's MRSA Research Center, is still raising the alarm about the epidemic. He sees the fight as more urgent than ever, and now thinks he knows how to win it. A few days before Christmas, he and Brad Spellberg, a physician who conducts vaccine research at the University of California, Los Angeles, published an article[3] calling for a vaccine that would vanquish *S. aureus*. "We can't treat this," Daum says. "We have to prevent it."

This time, Daum's views have more support. Over the past 10 years, as MRSA has become resistant even to last-resort antibiotics, several pharmaceutical companies have launched research programmes for vaccines, some with Daum's input. But Daum contends that they underestimate the enemy by relying on the standard immunological approach of triggering the production of protective antibodies. Instead, he advocates a strategy that stimulates T cells, part of a different branch of the immune system. It is an ambitious proposal and not all infectious-disease specialists are convinced that it will work.

The MRSA bacterium (pictured) is resistant to almost all antibiotics. SPL

"It is a provocative idea," says Gerald Pier, a microbiologist at Harvard Medical School in Boston, Massachusetts, who also works on *S. aureus* vaccines. "But it is still too early to know how applicable this component of immunity would be to vaccine development."

EVIDENCE FOR AN EPIDEMIC

It took a while for the field to agree with Daum that a new epidemic had begun. Attitudes began to shift around 18 months after his seminal paper, when investigators for the Centers for Disease Control and Prevention (CDC) in Atlanta, Georgia, reported that four children in Minnesota and North Dakota had died from infections similar to those in Daum's hospital. After that, the CDC and hospitals found clusters of community-associated infections in jails and prisons, then in sports teams, then in unusually high numbers of patients in emergency departments. Physicians, too, were reporting unexpected cases of grave illness — necrotizing pneumonia and flesh-eating disease — all caused by the community-associated strain.

From there, the epidemic grew. By one estimate, community-acquired MRSA accounts for half of the more than 14 million skin and soft-tissue infections that send people to doctors and emergency departments in the United States every year[2]. MRSA also causes around

➲ NATURE.COM
Read *Nature*'s special issue on vaccines:
go.nature.com/a3nzqx

100,000 serious blood infections and more than 15,000 deaths a year. Meanwhile, pharmaceutical manufacturers are backing away from making new antibiotics, arguing that resistance is undermining compounds too quickly for them to recoup their costs.

A study by staff at the CDC's Division of Healthcare Quality Promotion estimates that an *S. aureus* vaccine given to vulnerable groups could reduce the number of serious MRSA infections by 24,000–34,000 cases per year[4]. Researchers familiar with vaccine development say that manufacturers have recognized the potential market. "You can see it within the industry now. They are all interested," says Jean Lee, an *S. aureus* vaccine researcher at Harvard Medical School. "Ten years ago, that wasn't the case." But getting from interest to a viable formula is proving a formidable challenge.

SHOT IN A DIFFERENT ARM

Since Edward Jenner first scratched cowpox virus into a boy's arm 216 years ago, vaccination has mostly proceeded along variations of one strategy: introducing into the body an antigen, such as a weakened disease organism or a fragment of an organism. The immune system responds by producing an antibody, a protein that recognizes the antigen and triggers an immune attack on the organism. For years, the presence of antibodies has been taken as a sign that a person will be immune to later infection.

The first attempt at making a *S. aureus* vaccine was modelled on successful vaccines for *Streptococcus pneumoniae* and *Haemophilus influenzae*. Like them, it used antigens consisting of carbohydrate molecules from the sticky capsule surrounding the bacterium, attached to a protein produced by another bacterium. But the formula, called StaphVax and developed by Nabi Biopharmaceuticals in the late 1990s, was unsuccessful. When the company tested it in 1998–99 in a phase III trial[5], the recipients made antibodies, but then developed *S. aureus* infections in their blood at the same rate as those who received placebo. The programme was suspended in 2005 and sold to GlaxoSmithKline in 2009. Merck, meanwhile, created a formula that used a cell-surface protein involved in the bacterium's ability to take up iron. It cancelled late-phase clinical trials in June last year because of negative results.

In retrospect, Daum says, no one should have expected an *S. aureus* vaccine to be that easy. "This organism has multiple strategies for accomplishing all its tasks, from invading the blood stream to elaborating toxins to causing local skin abscesses," he says. "Targeting a vaccine against just one of them merely eggs the bug on."

Unlike most pathogens, *S. aureus* is a commensal organism; it lives on the skin and in the nostrils of up to one-third of humans, mostly without causing disease. This benign but continual occupation means that much of the population already has antibodies to the bacterium. And unlike many infections, having it once is no guarantee of protection; roughly one in four people who have one *S. aureus* infection will go on to develop another. So vaccine developers don't really know what characterizes an immune individual. "We're working without any information as to what constitutes high-level immunity to *S. aureus* infection," says Pier.

Still, some companies are attempting to build immunity using an all-out antibody attack: Pfizer, Novartis and GlaxoSmithKline are testing formulas packed with four or five antigens, hoping to elicit an array of antibodies that will overwhelm the bacterium's defences. Several other companies are trying passive immunization — delivering antibodies harvested from people — but none has yet achieved results better than placebo.

> *"This is a universal epidemic, and there should be a universal vaccine."*

The team that may have edged closest to success is actually on Daum's own campus. Microbiologist Olaf Schneewind, who is not affiliated with Daum's group, has developed a formula that incorporates a mutated version of a cell-wall component of *S. aureus* called protein A. Under normal circumstances, protein A binds to antibodies, protecting the bacterium from attack by the immune system; the mutant version, however, is unable to bind. So far, the formula has been tested only in mice[6].

Daum is familiar with the failed-vaccine landscape, not just from his consulting work with pharmaceutical companies, but also from serving on the US Food and Drug Administration's Vaccine and Related Biological Products Advisory Committee. At the same time, his research into how *S. aureus* is able to cause disease in so many tissues and its bristling array of defences against the immune system convinced him that a new approach was needed.

When Daum discusses *S. aureus*, he is blunt about the challenges and impatient to move ahead. "I don't think multiple antigens are enough," he says, sitting in the old hospital building where he spotted the first community-acquired MRSA cases, now transformed into overcrowded offices stacked with piles of journals. "I think we need multiple immunological mechanisms. And I think the central one should be something that has been considered heresy up to now."

LUCKY BREAK

The heretical approach was inspired, in part, by a patient. As part of an ongoing project to root out the causes of recurring infections, in 2009 two of Daum's team members went to the home of a toddler who had recently been in the emergency department. But the girl wasn't there; she was in the hospital's intensive-care unit with a new infection. When Daum tracked her down, he noticed something odd in her records. She had had unusually frequent abscesses and repeated bouts of pneumonia.

Acting on a hunch, Daum teamed up with Steven Holland, chief of the clinical infectious diseases laboratory at the National Institute of Allergy and Infectious Diseases in Bethesda, Maryland, to carry out a detailed genetic analysis. Daum's hunch was right: the girl had a mutation that Holland had recently linked to a rare immunodeficiency called Job's syndrome[7]. People with the syndrome have persistent, smouldering *S. aureus* infections, owing to an inability to make a type of lymphocyte, or immune cell, called a T_H17 cell.

These cells, which make a proinflammatory protein called interleukin-17, have become a hot topic in vaccine research. They are produced by a different branch of the immune system from the one that makes antibodies, yet they still seem to be involved in the body's memory of exposures to pathogens.

Daum believes that T_H17 cells are the key to an *S. aureus* vaccine. "It looks like T cells are very important in staphylococcal immunity," he says. Spellberg demonstrated in 2009 that a vaccine that stimulated production of interleukin 17 could protect mice against infections of *S. aureus* and *Candida albicans*[8]. (That vaccine is now being developed by NovaDigm Therapeutics as NDV3.)

Daum and Spellberg have now joined forces and formed a cross-disciplinary team to see whether boosting the activity of T_H17 cells can prevent *S. aureus* infections in humans. The team includes an intensive-care specialist who has developed animal models to study these infections; an epidemiologist; two immunologists; and a biomedical engineer.

They have begun by selecting current and former patients with MRSA from the University of Chicago's hospitals and comparing

JIM NEWBERRY FOR NATURE

Robert Daum has shown that MRSA is not confined to hospitals — and is determined to find a vaccine that will fight the bacterium.

their immunological activity with that of people who have never had MRSA. In a second phase, they will test how lymphocytes harvested from the patients react to a number of infectious organisms, including MRSA.

The project will face significant challenges, Spellberg points out. "One of the reasons the vaccine world has always been so focused on antibodies is because it's so easy to measure antibodies," he says. "There is no high-throughput T-cell assay. It takes a lot of work."

FAR FROM FINAL

If the team can succeed in boosting T-cell activity, it will still be only part of a solution. The group has to consider whether to include a traditional antibody-stimulating antigen in a vaccine, and whether to add a third component, such as protein A. The researchers must also work out whether one vaccine formula can stop *S. aureus* from invading many types of tissue. "We want a vaccine that prevents invasive disease, we want a vaccine that prevents pneumonia and we want a vaccine that prevents skin infections," Daum says. "Can one vaccine solve three separate clinical problems?"

The researchers will have to manoeuvre around *S. aureus*'s dual role as pathogen and commensal bacterium. If they wipe out the body's benign staph occupiers, a more harmful organism might take their place.

Daum and his collaborators will also have to face down scepticism from other staph researchers, who view the T_H17 idea as intriguing but impractical. Schneewind points out that the US Food and Drug Administration's rules require a vaccine to demonstrate antibody production to win licensure. "I am not aware of any vaccine licence where the correlate of protective immunity is IL-17 response," he says. But given the surge of interest in T_H17 cells, he adds, "people will try it, and we'll see how far they get".

Perhaps the most difficult question to answer is: who should get an *S. aureus* vaccine? Because community-acquired MRSA is so widespread, the maximum benefits might come only if the vaccine is administered to everyone. But with a great deal of suspicion of vaccines in the United States and elsewhere, an addition to the routine immunization schedule is likely to be met with resistance.

Mention these concerns to Daum, and the trademark impatience break through. "This is a universal epidemic, and there should be a universal vaccine," he says. "I think we should put this into the paediatric vaccine schedule in the first year of life. And if it happened to work on all MRSA syndromes, like the skin infections that flood our emergency room, then we would have something wonderful on our hands." ■

Maryn McKenna *is a science journalist in Atlanta, Georgia, and author of the book* Superbug: the Fatal Menace of MRSA.

1. Herold, B. C. *et al. J. Am. Med. Assoc.* **279,** 593–598 (1998).
2. Hersh, A. L. Chambers, H. F., Maselli, J. H. & Gonzales, R. *Arch. Intern. Med.* **168,** 1585–1591 (2008).
3. Daum, R. S. & Spellberg, B. *Clin. Infect. Dis.* http://dx.doi.org/10.1093/cid/cir828 (2011).
4. Lucero, C. A. *et al. Vaccine* **27,** 5061–5068 (2009).
5. Shinefield, H. *et al. N. Engl. J. Med.* **346,** 491–496 (2002).
6. Kim, H. K., Cheng, A. G., Kim, H.-Y., Missiakas, D. M. & Schneewind, O. *J. Exp. Med.* **207,** 1863–1870 (2010).
7. Holland, S. M. *et al. N. Engl. J. Med.* **357,** 1608–1619 (2007).
8. Lin, L. *et al. PLoS Pathog.* **5,** e1000703 (2009).

antibodypedia | nature

Finding the right antibody for the right application just got easier!

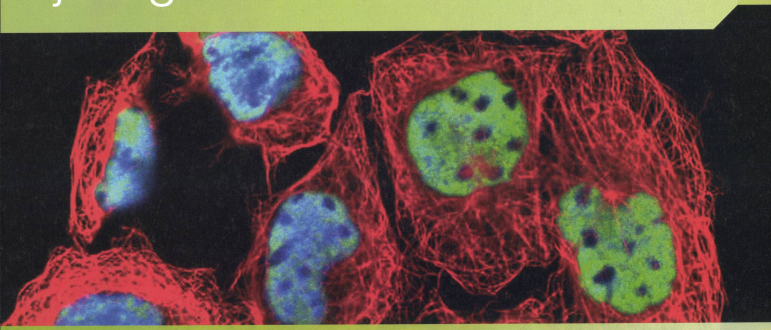

Antibodypedia is a free resource that helps you find the right antibody for the right application. Independent, with data curated with the assistance of an international advisory board, *Antibodypedia* lets you:

- Search for antibodies that have proved themselves effective for specific applications
- Discover published research employing particular antibodies
- Submit antibody validation data from your own experiments

Find the right antibody for the right application by visiting:

www.antibodypedia.com

nature publishing group npg

COMMENT

ECOLOGY How elephants could reduce fire risk in Australia **p.30**

NEUROSCIENCE The source of the self in the brain's wiring **p.31**

LITERATURE How Charles Dickens drew on science, but left room for wonder **p.32**

OBITUARY Philip Lawley and the discovery that DNA damage can cause cancer **p.36**

ILLUSTRATION BY MARK SMITH

The toxic truth about sugar

Added sweeteners pose dangers to health that justify controlling them like alcohol, argue **Robert H. Lustig**, **Laura A. Schmidt** and **Claire D. Brindis**.

SUMMARY

- Sugar consumption is linked to a rise in non-communicable disease
- Sugar's effects on the body can be similar to those of alcohol
- Regulation could include tax, limiting sales during school hours and placing age limits on purchase

Last September, the United Nations declared that, for the first time in human history, chronic non-communicable diseases such as heart disease, cancer and diabetes pose a greater health burden worldwide than do infectious diseases, contributing to 35 million deaths annually.

This is not just a problem of the developed world. Every country that has adopted the Western diet — one dominated by low-cost, highly processed food — has witnessed rising rates of obesity and related diseases. There are now 30% more people who are obese than who are undernourished. Economic development means that the populations of low- and middle-income countries are living longer, and therefore are more susceptible to non-communicable diseases; 80% of deaths attributable to them occur in these countries.

Many people think that obesity is the root cause of these diseases. But 20% of obese people have normal metabolism and will have a normal lifespan. Conversely, up to 40% of normal-weight people develop the diseases that constitute the metabolic syndrome: diabetes, hypertension, lipid problems, cardiovascular disease and non-alcoholic fatty liver disease. Obesity is not the cause; rather, it is a marker for metabolic dysfunction, which is even more prevalent.

The UN announcement targets tobacco, alcohol and diet as the central risk factors in non-communicable disease. Two of these three — tobacco and alcohol — are regulated by governments to protect public health, leaving one of the primary culprits behind this worldwide health crisis unchecked. Of course, regulating food is more ▶

complicated — food is required, whereas tobacco and alcohol are non-essential consumables. The key question is: what aspects of the Western diet should be the focus of intervention?

In October 2011, Denmark chose to tax foods high in saturated fat, despite the fact that most medical professionals no longer believe that fat is the primary culprit. But now, the country is considering taxing sugar as well — a more plausible and defensible step. Indeed, rather than focusing on fat and salt — the current dietary 'bogeymen' of the US Department of Agriculture (USDA) and the European Food Safety Authority — we believe that attention should be turned to 'added sugar', defined as any sweetener containing the molecule fructose that is added to food in processing.

Over the past 50 years, consumption of sugar has tripled worldwide. In the United States, there is fierce controversy over the pervasive use of one particular added sugar — high-fructose corn syrup (HFCS). It is manufactured from corn syrup (glucose), processed to yield a roughly equal mixture of glucose and fructose. Most other developed countries eschew HFCS, relying on naturally occurring sucrose as an added sugar, which also consists of equal parts glucose and fructose.

Authorities consider sugar as 'empty calories' — but there is nothing empty about these calories. A growing body of scientific evidence is showing that fructose can trigger processes that lead to liver toxicity and a host of other chronic diseases[1]. A little is not a problem, but a lot kills — slowly (see 'Deadly effect'). If international bodies are truly concerned about public health, they must consider limiting fructose — and its main delivery vehicles, the added sugars HFCS and sucrose — which pose dangers to individuals and to society as a whole.

NO ORDINARY COMMODITY

In 2003, social psychologist Thomas Babor and his colleagues published a landmark book called *Alcohol: No Ordinary Commodity*, in which they established four criteria, now largely accepted by the public-health community, that justify the regulation of alcohol — unavoidability (or pervasiveness throughout society), toxicity, potential for abuse and negative impact on society[2]. Sugar meets the same criteria, and we believe that it similarly warrants some form of societal intervention.

First, consider unavoidability. Evolutionarily, sugar was available to our ancestors as fruit for only a few months a year (at harvest time), or as honey, which was guarded by bees. But in recent years, sugar has been added to nearly all processed foods, limiting consumer choice[3]. Nature made sugar hard to get; man made it easy. In many parts of the world, people are consuming an average of more than 500 calories per day from added sugar alone (see 'The global sugar glut').

Now, let's consider toxicity. A growing body of epidemiological and mechanistic evidence argues that excessive sugar consumption affects human health beyond simply adding calories[4]. Importantly, sugar induces all of the diseases associated with metabolic syndrome[1,5]. This includes: hypertension (fructose increases uric acid, which raises blood pressure); high triglycerides and insulin resistance through synthesis of fat in the liver; diabetes from increased liver glucose production combined with insulin resistance; and the ageing process, caused by damage to lipids, proteins and DNA through non-enzymatic binding of fructose to these molecules. It can also be argued that fructose exerts toxic effects on the liver that are similar to those of alcohol[1]. This is no surprise, because alcohol is derived from the fermentation of sugar. Some early studies have also linked sugar consumption to human cancer and cognitive decline.

"Sugar is cheap, sugar tastes good and sugar sells, so companies have little incentive to change."

Sugar also has clear potential for abuse. Like tobacco and alcohol, it acts on the brain to encourage subsequent intake. There are now numerous studies examining the dependence-producing properties of sugar in humans[6]. Specifically, sugar dampens the suppression of the hormone ghrelin, which signals hunger to the brain. It also interferes with the normal transport and signalling of the hormone leptin, which helps to produce the feeling of satiety. And it reduces dopamine signalling in the brain's reward centre, thereby decreasing the pleasure derived from food and compelling the individual to consume more[1,6].

Finally, consider the negative effects of sugar on society. Passive smoking and drink-driving fatalities provided strong arguments for tobacco and alcohol control, respectively. The long-term economic, health-care and human costs of metabolic syndrome place sugar overconsumption in the same category[7]. The United States spends $65 billion in lost productivity and $150 billion on health-care resources annually for morbidities associated with metabolic syndrome. Seventy-five per cent of all US health-care dollars are now spent on treating these diseases and their resultant disabilities. Because about 25% of military applicants are now rejected for obesity-related reasons, the past three US surgeons general and the chairman of the US Joint Chiefs of Staff have declared obesity a "threat to national security".

HOW TO INTERVENE

How can we reduce sugar consumption? After all, sugar is natural. Sugar is a nutrient. Sugar is pleasure. So too is alcohol, but in both cases, too much of a good thing is toxic. It may be helpful to look to the many generations of international experience with alcohol and tobacco to find models that work[8,9]. So far, evidence shows that individually focused approaches, such as school-based interventions that teach children about diet and exercise, demonstrate little efficacy. Conversely, for both alcohol and tobacco, there is robust evidence that gentle 'supply side' control strategies which stop far short of all-out prohibition — taxation, distribution controls, age limits — lower both consumption of the product and the accompanying health harms. Successful interventions share a common end-point: curbing availability[2,8,9].

Taxing alcohol and tobacco products — in the form of special excise duties, value-added taxes and sales taxes — are the most popular and effective ways to

DEADLY EFFECT

Excessive consumption of fructose can cause many of the same health problems as alcohol.

Chronic ethanol exposure	Chronic fructose exposure
Haematological disorders	
Electrolyte abnormalities	
Hypertension	Hypertension (uric acid)
Cardiac dilatation	
Cardiomyopathy	Myocardial infarction (dyslipidaemia, insulin resistance)
Dyslipidaemia	Dyslipidaemia (*de novo* lipogenesis)
Pancreatitis	Pancreatitis (hypertriglyceridaemia)
Obesity (insulin resistance)	Obesity (insulin resistance)
Malnutrition	Malnutrition (obesity)
Hepatic dysfunction (alcoholic steatohepatitis)	Hepatic dysfunction (non-alcoholic steatohepatitis)
Fetal alcohol syndrome	
Addiction	Habituation, if not addiction

Source: ref. 1

SOURCE: FAO

THE GLOBAL SUGAR GLUT

Global sugar supply (in the form of sugar and sugar crops, excluding fruit and wine) expressed as calories per person per day, for the year 2007.

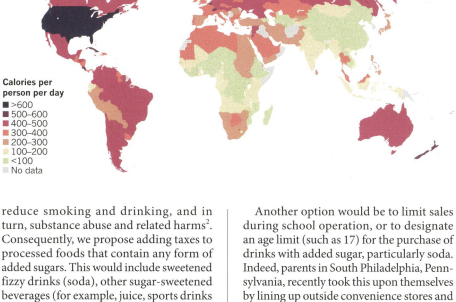

reduce smoking and drinking, and in turn, substance abuse and related harms[2]. Consequently, we propose adding taxes to processed foods that contain any form of added sugars. This would include sweetened fizzy drinks (soda), other sugar-sweetened beverages (for example, juice, sports drinks and chocolate milk) and sugared cereal. Already, Canada and some European countries impose small additional taxes on some sweetened foods. The United States is currently considering a penny-per-ounce soda tax (about 34 cents per litre), which would raise the price of a can by 10–12 cents. Currently, a US citizen consumes an average of 216 litres of soda per year, of which 58% contains sugar. Taxing at a penny an ounce could provide annual revenue in excess of $45 per capita (roughly $14 billion per year); however, this would be unlikely to reduce total consumption. Statistical modelling suggests that the price would have to double to significantly reduce soda consumption — so a $1 can should cost $2 (ref. 10).

Other successful tobacco- and alcohol-control strategies limit availability, such as reducing the hours that retailers are open, controlling the location and density of retail markets and limiting who can legally purchase the products[2,9]. A reasonable parallel for sugar would tighten licensing requirements on vending machines and snack bars that sell sugary products in schools and workplaces. Many schools have removed unhealthy fizzy drinks and candy from vending machines, but often replaced them with juice and sports drinks, which also contain added sugar. States could apply zoning ordinances to control the number of fast-food outlets and convenience stores in low-income communities, and especially around schools, while providing incentives for the establishment of grocery stores and farmer's markets.

Another option would be to limit sales during school operation, or to designate an age limit (such as 17) for the purchase of drinks with added sugar, particularly soda. Indeed, parents in South Philadelphia, Pennsylvania, recently took this upon themselves by lining up outside convenience stores and blocking children from entering them after school. Why couldn't a public-health directive do the same?

THE POSSIBLE DREAM

Government-imposed regulations on the marketing of alcohol to young people have been quite effective, but there is no such approach to sugar-laden products. Even so, the city of San Francisco, California, recently banned the inclusion of toys with unhealthy meals such as some types of fast food. A limit — or, ideally, ban — on television commercials for products with added sugars could further protect children's health.

Reduced fructose consumption could also be fostered through changes in subsidization. Promotion of healthy foods in US low-income programmes, such as the Special Supplemental Nutrition Program for Women, Infants and Children and the Supplemental Nutrition Assistance Program (also known as the food-stamps programme) is an obvious place to start. Unfortunately, the petition by New York City to remove soft drinks from the food-stamp programme was denied by the USDA.

Ultimately, food producers and distributors must reduce the amount of sugar added to foods. But sugar is cheap, sugar tastes good and sugar sells, so companies have little incentive to change. Although one institution alone can't turn this juggernaut around, the US Food and Drug Administration could "set the table" for change[8]. To start, it should consider removing fructose from the Generally Regarded as Safe (GRAS) list, which allows food manufacturers to add unlimited amounts to any food. Opponents will argue that other nutrients on the GRAS list, such as iron and vitamins A and D, can also be toxic when over-consumed. However, unlike sugar, these substances have no abuse potential. Removal from the GRAS list would send a powerful signal to the European Food Safety Authority and the rest of the world.

Regulating sugar will not be easy — particularly in the 'emerging markets' of developing countries where soft drinks are often cheaper than potable water or milk. We recognize that societal intervention to reduce the supply and demand for sugar faces an uphill political battle against a powerful sugar lobby, and will require active engagement from all stakeholders. Still, the food industry knows that it has a problem — even vigorous lobbying by fast-food companies couldn't defeat the toy ban in San Francisco. With enough clamour for change, tectonic shifts in policy become possible. Take, for instance, bans on smoking in public places and the use of designated drivers, not to mention airbags in cars and condom dispensers in public bathrooms. These simple measures — which have all been on the battleground of American politics — are now taken for granted as essential tools for our public health and well-being. It's time to turn our attention to sugar. ■

Robert H. Lustig *is in the Department of Pediatrics and the Center for Obesity Assessment, Study and Treatment at the University of California, San Francisco, California 94143, USA.* **Laura A. Schmidt** *and* **Claire D. Brindis** *are at the Clinical and Translational Science Institute and the Philip R. Lee Institute for Health Policy Studies, University of California, San Francisco, California 94118, USA.*
e-mail: rlustig@peds.ucsf.edu

1. Lustig, R. H. *J. Am. Diet. Assoc.* **110,** 1307–1321 (2010).
2. Babor, T. *et al. Alcohol: No Ordinary Commodity: Research and Public Policy* (Oxford Univ. Press, 2003).
3. Vio, F. & Uauy, R. in *Food Policy for Developing Countries: Case Studies* (eds Pinstrup-Andersen, P. & Cheng, F.) No. 9-5 (2007); available at http://go.nature.com/prjsk4
4. Joint WHO/FAO Expert Consultation. *Diet, Nutrition and the Prevention of Chronic Diseases* WHO Technical Report Series 916 (WHO; 2003).
5. Tappy, L., Lê, K. A., Tran, C. & Paquot, N. *Nutrition* **26,** 1044–1049 (2010).
6. Garber, A. K. & Lustig, R. H. *Curr. Drug Abuse Rev.* **4,** 146–162 (2011).
7. Finkelstein, E. A., Fiebelkorn, I. C. & Wang, G. *Health Aff.* **W3** (suppl.), 219–226 (2003).
8. Engelhard, C. L., Garson, A. Jr & Dorn, S. *Reducing Obesity: Policy Strategies from the Tobacco Wars* (Urban Institute, 2009); available at http://go.nature.com/w4o5uk
9. Room, R., Schmidt, L. A., Rehm, J. & Mäkela P. *Br. Med. J.* **337,** a2364 (2008).
10. Sturm, R., Powell L. M., Chriqui, J. F. & Chaloupka, F. J. *Health Aff.* **29,** 1052–1058 (2010).

Bring elephants to Australia?

There's a solution to the continent's rampant fires and feral animals, says **David Bowman** — introduce large mammals and increase hunting pressure.

Three years ago this week, Australia was burning. On 7 February 2009 — now known as Black Saturday — a massive firestorm consumed more than 400,000 hectares in southern Australia. At least 173 people died trying to outrun the fires, defend their homes or seek shelter.

That blaze was unusually fierce, but fires are a constant source of anxiety for Australia. The continent is extremely fire-prone, with a distinctive signature of oscillating fire activity that begins in the north during the winter, then moves south during the summer. Lately, the fires have been more intense and widespread, perhaps as a result of climate change — last year, around 5% of the continent was burnt.

If only fires were Australia's sole environmental concern. The continent is also overrun by invasive species. They fill holes created by a mass extinction event that occurred around 50,000 years ago during the Pleistocene, when the arrival of the first Australians coincided with a collapse in the continent's megafauna, namely giant marsupials (some as large as hippopotamuses), reptiles and birds[1]. The precise causes of that event are unclear, but the resulting gap in the food web has been filled by populations of pigs, goats, cattle, horses, donkeys, camels, buffalo and deer[2]. These animals are reconstructing ecosystems, a trend amplified by the introduction of alien plants, particularly ultra-competitive grasses[3].

So far, Australia and other regions dealing with similar environmental crises have responded by spending millions on piecemeal control programmes that target one problem at a time. For instance, Australians have tried attaching radio collars to buffalo and then following them in helicopters to find and kill others in the herd[3]. Such approaches cost millions, and are ultimately ineffectual — for every buffalo hunted, another is born to replace it.

I think that another, more holistic approach can address Australia's ecological problems. Specifically, we must restabilize food webs (now out of balance because of the Pleistocene extinctions), the loss of the Aboriginal traditions of patch burning and hunting, and the ad hoc release of non-native animals and plants. We must introduce and manage predators to control the feral animals, and bring in herbivore species to graze the flammable grasses — which we can better control using small fires as 'über-herbivores'[4].

I accept that this is a radical way of thinking; we would have to weigh the various options. For example, we could stop poisoning the Australian wolf (dingo). Poisoning disrupts their social structure, and research suggests that dingoes in packs act as top predators of smaller predators such as introduced foxes[5]. More dingoes could also help to control other feral animals, such as

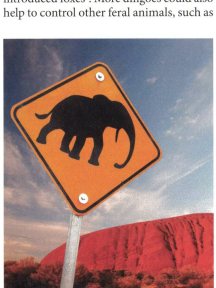

A. BRAMWELL/ALAMY

pigs. Alternatively, we could introduce predators such as the Komodo dragon, which would fill the niche of the giant lizards that once thrived in Australia[6].

But, because such predators can pose threats to humans and livestock, it might be more realistic to employ Aboriginal hunters, who could help to control feral animals and restore the traditional practice of patch burning. Indeed, existing ranger programmes that enable indigenous people to return to their roots — by hunting buffalo or managing natural resources — have been shown to have social and health benefits for this disadvantaged sector of the Australian community[7].

A major source of fuel for wildfires in the monsoon tropics is gamba grass, a giant African grass that has invaded north Australia's savannas[8]. It is too big for marsupial grazers (kangaroos) and for cattle and buffalo, the largest feral mammals. But gamba grass is a great meal for elephants or rhinoceroses. The idea of introducing elephants may seem absurd, but the only other methods likely to control gamba grass involve using chemicals or physically clearing the land, which would destroy the habitat. Using mega-herbivores may ultimately be more practical and cost-effective, and it would help to conserve animals that are threatened by poaching in their native environments. This potential solution is not limited to Australia — it has been suggested that elephants could be used as part of a project to 'rewild', or return North American ecosystems to their prehuman state[9].

I realize that there are major risks associated with what I am proposing. It would be essential to proceed cautiously, with well-designed studies to monitor the effects. The greatest challenge would be managing the density of herbivore populations so that their demand on resources does not degrade the ecosystem. Here, we could adopt management methods from game parks and reserves, such as building fences, regulating the availability of water and food, and controlling breeding and hunting.

Of course, introducing large mammals cannot solve all of Australia's ecological-management conundrums. And I am mindful that the proposal could be used to justify commercial grazing in fragile ecosystems, an ongoing controversy[10]. But the usual approaches to managing these issues aren't working. The full spectrum of options needs to be canvassed in an open and honest way. ■

David Bowman *is professor of environmental change biology at the School for Plant Science, University of Tasmania, Private Bag 55 Hobart, Tasmania 7001, Australia.*
e-mail: david.bowman@utas.edu.au

1. Johnson, C. *Australia's Mammal Extinctions: A 50,000-Year History* (Cambridge Univ. Press, 2006).
2. Low, T. *Feral Future: The Untold Story of Australia's Exotic Invaders* (Univ. Chicago Press, 1999).
3. Finlayson, C. M., Storrs, M. J. & Lindner, G. *Wetlands Ecol. Manage.* **5**, 19–36 (1997).
4. Bond, W. J. & Keeley, J. E. *Trends Ecol. Evol.* **20,** 387–394 (2005).
5. Johnson, C. N., Isaac, J. L. & Fisher, D. O. *Proc. R. Soc. B* **274,** 341–346 (2007).
6. Flannery, T. *The Future Eaters: An Ecological History of the Australasian Lands and People* (Reed Books, 1994).
7. Burgess, C. P. *et al. Med. J. Australia* **190,** 567–572 (2009).
8. Setterfield, S. A. *et al. Divers. Distrib.* **16,** 854–861 (2010).
9. Donlan, J. *et al. Nature* **436,** 913–914 (2005).
10. Williams, R. J., Wahren, C-H., Bradstock, R. A. & Müller, W. J. *Austral. Ecol.* **31,** 925–936 (2006).

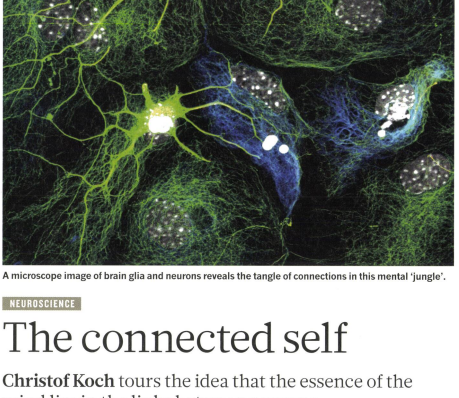

U. KÖNETZKO, UNIV. ZURICH/B. BOLLMANN, *NEURAL ARCHITECTURES*

A microscope image of brain glia and neurons reveals the tangle of connections in this mental 'jungle'.

NEUROSCIENCE

The connected self

Christof Koch tours the idea that the essence of the mind lies in the links between neurons.

We moderns believe that our momentary, subjective experience is intimately linked to events in the brain. One set of neurons fires, and we perceive an apple's colour, while a different population of cells gives rise to its taste. Yet the self is also stable: turn the brain off, as happens during heart surgery when the body is cooled to frigid temperatures, and on recovery, the patient's character, personality, habits and long-term memories remain intact. It is these stable aspects of the self, rather than the ebb and flow of our thoughts and percepts, that physicist-turned-neuroscientist Sebastian Seung seeks to explain in *Connectome*.

Seung argues intelligently and powerfully that the self lies in the totality of the brain's wiring — the eponymous 'connectome', the word used by neuroscientists to denote all the fibre bundles (the white matter) of the human brain. These insulated nerve axons have a total length of around 150,000 kilometres. Seung hails a new science, 'connectomics', as the key to understanding the brain and its pathologies.

This view is grounded in a older doctrine known as connectionism, which postulates that neurons are simple devices and that their connections determine their functions. Cataloguing the links among neurons therefore charts the mind.

➲ NATURE.COM
For *Nature*'s special issue on autism:
go.nature.com/ypa9f8

The heart of *Connectome* deals with how nervous systems can be reconstructed using electron microscopy. To do this, neural tissue is cut into slices 40–50 nanometres thick, and then imaged to a resolution of a few nanometres. Imaging 1 cubic millimetre of cortex generates 1 petabyte of data, or about a billion photo images from a typical digital camera.

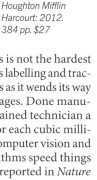

Connectome: How the Brain's Wiring Makes Us Who We Are
SEBASTIAN SEUNG
Houghton Mifflin Harcourt: 2012. 384 pp. $27

Yet taking the pictures is not the hardest part. Far more daunting is labelling and tracing each neuronal process as it wends its way through the stack of images. Done manually, this would take a trained technician a million working years for each cubic millimetre of brain; luckily, computer vision and machine-learning algorithms speed things up. Last year, two teams reported in *Nature* partial reconstructions of small volumes in the mouse retina and cortex.

Seung's companion through the neural labyrinth is Hollywood star Jennifer Aniston. In 2005, my group, collaborating with neurosurgeon Itzhak Fried, discovered individual neurons that respond selectively to the image or the name of familiar or famous individuals, such as your grandmother or Aniston. Seung reasons that such neurons must receive input from many less specific cells that respond to eye and hair colour and so on. These in turn connect to neurons responding to even more elementary stimuli, such as vertical lines. The essence of a person's concept of a celebrity lies, then, not with the individual neuron, but in its wiring. And this, in Seung's view, is why reconstructing connections is the key to understanding the mind.

Not even Aniston's agent would think that people are born with neurons that recognize her. Rather, the neural networks that feed into these highly selective cells have wired themselves up to respond in this way. Seung discusses what we know about such plasticity, describing how mammalian nervous systems rewire themselves to adapt to the environment, balance the competing demands of plasticity and stability (so new memories don't displace old ones) and compensate for damage by rerouting information.

Treating the connectome as the be-all and end-all of brain function has its problems. Seung, for example, rebrands autism and schizophrenia as 'connectopathies' — diseases in which the brain's wiring goes awry. Yet plenty of other things are wrong in brains with these disorders besides their connectivity.

Faults in synaptic transmission and in processes inside neurons and the glial cells that support them have all been implicated in mental illness and brain disease. Neurons are intricate devices with elaborate input structures that show complex, time-dependent and nonlinear processing. They have various characteristic, and often tortuous, morphologies. Connectionism treats all this as irrelevant. Even though we have known the connectome of the nematode worm for 25 years, we are far from reading its mind. We don't yet understand how its nerve cells work.

The book is well illustrated and sourced, with an ending that is both engaging and idiosyncratic. The last two chapters are predicated on the idea that "you are your connectome", as Seung quips. One deals with technologies to freeze and pickle dead brains long term, in the hope of one day reviving their minds. The final chapter looks at the possibility of simulating the entire human brain on a future supercomputer, allowing you to upload yourself and live on as a software construct. This is the dream of the singularity that Ray Kurzweil and other technologists are hoping will render them immortal: the rapture for nerds. ■

Christof Koch *is chief scientific officer at the Allen Institute for Brain Science, Seattle, Washington, USA, and a professor of biology and engineering at the California Institute of Technology, Pasadena, California, USA. e-mail: koch@klab.caltech.edu*

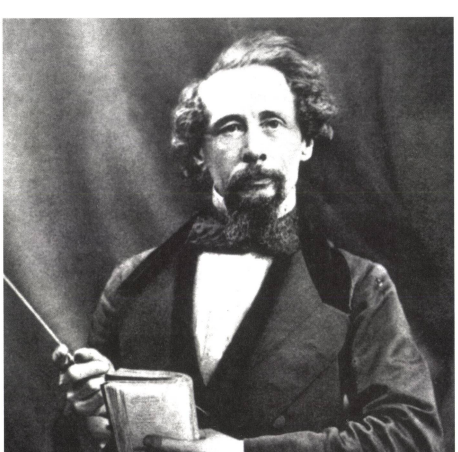

REX FEATURES

Novelist Charles Dickens delighted in scientific revelations, but deplored sterile reductionism.

LITERATURE

Wonders and ologies

In the week of the Dickens bicentennial, **Alice Jenkins** explores the literary giant's conflicted take on science.

"Go and be somethingological directly," Mrs Gradgrind orders her children in Charles Dickens's *Hard Times* (1854). The children are brought up on their father's strict utilitarian principles — or rather, on Dickens's ferocious satire of them. So they have "a little conchological cabinet, and a little metallurgical cabinet, and a little mineralogical cabinet; and all the specimens were all arranged and labelled", but they have no fairy tales or nursery rhymes — nothing that might encourage fancy or wonder.

Not surprisingly, the children come to bad ends. On her deathbed, Mrs Gradgrind tells her daughter: "There is something — not an Ology at all — that your father has missed, or forgotten."

Science, in Dickens's view, does immense good — moral, social and intellectual — but only when it works hand in hand with imagination and reverence. Relations between science and Christianity in the nineteenth century were often more harmonious than we might imagine, if we focus only on the challenges that natural selection posed to some kinds of religious belief. Dickens is an interesting case study.

He was a Protestant Christian, but had no strong affiliation to any particular sect, and did not see science as a threat to religious faith. On the contrary, he argued, learning the true nature of forces or objects brings us closer to their creator. In a speech he gave in 1869 at the Birmingham and Midland Institute, he speculated that Jesus might have taught scientific truths about the "wonders on every hand", but chose not to because "the people of that time could not bear them".

It is characteristic of Dickens's undogmatic attitude to both science and religion that he was largely unfazed by Charles Darwin's *On the Origin of Species* (John Murray, 1859). He published a review of the *Origin* in his magazine, *All the Year Round*, in 1860. Although not wholly persuaded by Darwin, the author did acknowledge that the theory "entails the vastest consequences", and quoted Darwin at length. Darwin in turn was a long-time fan of Dickens's novels, and literary critic Gillian Beer has suggested that Darwin drew on Dickens in writing the *Origin*. In *Darwin's Plots* (Cambridge University Press; 2000) Beer highlights the shared concerns of these two eminent men — among them, the relationship between the extraordinary profusion of people and things, and the many-layered interconnections between entities.

SCIENCE WITH FEELING

Dickens's objection in *Hard Times* was not to science itself, but to the reductionist principle that imposes stultifying order and leaves no room for emotion or imagination. Plenty of Victorian scientific writers would have agreed with him. Michael Faraday, for example, taught that "in the pursuit of physical science, the imagination should be taught to present the subject investigated in all possible, and even in impossible views". And, in a passage that became a touchstone for Victorian science writing, geologist Adam Sedgwick wrote in 1831 that if geology were to cause "the imagination, the feelings" to be "blunted and impaired", then the subject would become "little better than a moral sepulchre".

Dickens was appalled by people whose scientific knowledge was not connected to imagination or feelings. As soon as we meet Bradley Headstone, the teacher in *Our Mutual Friend* (1865), we know that he will prove a villain, because his mind is

NATURE.COM
Gillian Beer's essay on time in Lewis Carroll's Alice books:
go.nature.com/p8kq1d

rule-bound and sterile: "From his earliest childhood up, his mind had been a place of mechanical stowage … astronomy to the right, political economy to the left — natural history, the physical sciences, figures, music, the lower mathematics, and what not, all in their several places." The same tidy-mindedness that indicates the barrenness of the little Gradgrinds' natural specimens foretells Headstone's descent into criminal insanity.

What excited Dickens most about science was its ability to reveal an unimagined world behind ordinary objects. "The facts of science are at least as full of poetry, as the most poetical fancies," he wrote in an 1848 review of Robert Hunt's *The Poetry of Science*. By revealing the wonder of everyday things, science compensates us for the beloved but ignorant beliefs it destroys. "When [science] has freed us from a harmless superstition," Dickens wrote in the same review, "she offers to our contemplation something better and more beautiful, something which, rightly considered, is more elevating to the soul, nobler and more stimulating to the soaring fancy." Dinosaurs, he went on, are really far more impressive than dragons, and coral reefs more so than mermaids.

Accordingly, Dickens championed writers who used science to show the world as spectacular, magical or astonishing. Among his close friends were mathematician and father of the computer Charles Babbage, and Richard Owen, the comparative anatomist who coined the word dinosaur. Owen was enthralled by Dickens's novels, following them avidly as they came out in instalments. Science historian Gowan Dawson has argued that there are strong similarities between Owen's palaeontological studies

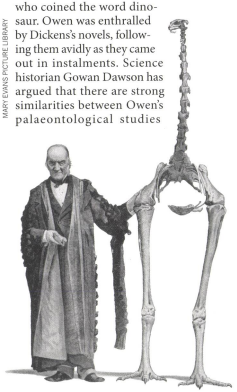

MARY EVANS PICTURE LIBRARY

Palaeontology pioneer Richard Owen (with a moa skeleton) was one of Dickens's close friends.

CHARLES DICKENS MUSEUM, LONDON

Dickens wove science into *Our Mutual Friend*, basing taxidermist Mr Venus on anatomist Richard Owen.

— which followed the principles of French naturalist Georges Cuvier to reconstruct entire extinct animals from a single fossil bone — and the way Victorian novel readers tackled serially published novels.

Both Owen and Babbage seem to have made their way into Dickens's novels — Owen as the taxidermist Mr Venus in *Our Mutual Friend* (1865), and Babbage as one of the models for Daniel Doyce, the gifted inventor in *Little Dorrit* (1857). Dickens uses his satire of the 'Circumlocution Office' in this novel to protest against the sluggish government bureaucracy that was delaying Babbage's progress with his Difference Engine.

HOUSEHOLD NAMES

Scientists also appeared in Dickens's journalism. As editor of the popular family magazine *Household Words* (1850–59), Dickens sought out writers who he thought were sympathetic to his view that science should make us see our everyday surroundings imaginatively. In 1850, for instance, he asked Percival Leigh, a physician-turned-writer, to rework Faraday's notes for his lectures on the candle and domestic chemical philosophy as articles for the magazine.

Leigh turned Faraday's notes into narratives, inventing a family, the Wilkinsons, whose young son regaled his family at tea-time with information he had acquired from the scientist's lectures at the Royal Institution. This format meant that the science could be broken up into conversational chunks, and lightened with mild domestic comedy.

Even though Dickens was happy to endorse contemporary science when he judged it to be supporting religion, feeding the imagination and telling stories, he was not above flouting scientific law for the sake of sensation. In *Bleak House* (1853), for example, two men in search of a crucial lost bundle of letters visit Krook's rag-and-bottle shop, only to find that "a smouldering suffocating vapour", "a dark greasy coating on the walls and ceiling", and a thing that looks like a small burnt log are all that remain of Krook: he has been the victim of "Spontaneous Combustion".

The controversy that followed the publication of this unscientific episode is well known. Reproached in print by science writer George Henry Lewes for perpetuating a "vulgar error … peculiarly adapted to the avid credulity of unscientific minds", Dickens responded with a list of apparent real-world cases of spontaneous combustion and a defiant preface defending them as authentic, even though they had been thoroughly discredited by Lewes and others.

Aware that this was not enough to regain credibility, Dickens concluded his preface with an appeal to the imagination: "In *Bleak House*, I have purposely dwelt upon the romantic side of familiar things."

It was the same argument that he had always made: that everyday things, and ordinary people, contain the potential for astonishing transformation. In the past he had championed science as a way of revealing this "romantic side", but this time, backed into a corner, he used it to defend a belief that no man of science could countenance.

For Dickens, science was compelling when it could be domesticated, moralized and made into an updated version of the old fairy tales, a way of telling poetical and magical tales about the world. But when science conflicted with a good story — he combusted it. ■

Alice Jenkins *is a professor of Victorian literature and culture at the University of Glasgow, UK, and author of* Space and the 'March of Mind': Literature and the Physical Sciences in Britain, 1815–1850. *e-mail: alice.jenkins@glasgow.ac.uk*

R. FRIEDMAN

Q&A Gary Marcus
The instrumentalist

Cognitive psychologist Gary Marcus researches language acquisition and the evolution of the brain at New York University. On the release of his latest book, Guitar Zero *— a personal yet scientific investigation of how people become musical — he explains how a love of music and a computer game helped him to overcome a lack of rhythm and learn to play the guitar.*

What were your early experiences of music?
As a child, I got kicked out of music class when I couldn't play *Mary Had a Little Lamb* on my recorder. Years later, Daniel Levitin, author of *This is Your Brain on Music* [Atlantic, 2007], tried to teach me the guitar, but discovered that I was so rhythmically impaired that I couldn't even follow a metronome. Then I discovered the computer game *Guitar Hero*. I was terrible at first, but luckily computers are patient. I got better at it, and for the first time felt the barest inkling of rhythm. Coupled with a love of listening to music, I was inspired to try playing the guitar for real.

How did you progress?
I taught myself to begin with, playing for an hour or two every day. After learning simple chords, I discovered the pentatonic scale, a set of notes that sound good in any order. I read every guitar book I could, worked with ear-training apps and experimented with music-creation software to get a sense of composition and arrangement. I tried to make up for limitations in my ears and fingers by developing a basic understanding of music theory. After six months I began to study with a teacher. Observant teachers target your weakest skills, as Swedish psychologist Anders Ericsson recommends. Incremental learning is key, especially for adults.

Guitar Zero: The New Musician and the Science of Learning
GARY MARCUS
Penguin Press: 2012. 274 pp. $25.95

How did you improve your sense of rhythm?
I practised a lot with a drum machine, and wrote an iPhone app called Chatternome that counts each beat out loud. That really helped me to internalize a sense of rhythm.

What are your musical goals?
To discover the underlying logic of music, to improvise rather than memorize. Our brains are set up to like new information; the reward I get from learning chord progressions and techniques has kept me going.

Why is the guitar so hard to learn?
It is partly because of the demands it places on memory. Because each pitch appears in multiple places on the fretboard, and our brains don't have the kind of database memory computers do, novices are easily confused. Playing each note requires coordination between the left and right hands. One hand has to be agile and strong to play chords, the other precise enough to play complex fingerpicking patterns. You also have to overcome the brain's natural tendency to get sloppy as you go faster.

Does your academic research involve music?
With neurobiologist Ofer Tchernichovski of Hunter College in New York, I'm researching how songbirds learn musical syntax, and comparing that to how children learn language. I am also looking at how people understand music in time, and how children learn the implicit underpinnings of music theory — the latter using a game I've written for the iPad, and hope to release for free later in 2012. And, with friends, I am building a nylon-string guitar that can safely be played in a magnetic resonance imaging (MRI) machine. We know something about how people's brains function when playing the piano, but much less about what happens when someone plays the guitar.

Name a favourite music experiment.
Psychologists Bruno Repp at Haskins Laboratories in New Haven, Connecticut, and Peter Keller at the Max Planck Institute for Human Cognitive and Brain Sciences in Leipzig, Germany, asked skilled pianists to sight-read classical compositions on completely muted electronic keyboards. Later, the pianists were able to pick out their own renditions from audio playbacks of a number of performances. This highlights the exquisite way in which experts align the neural representations of their fingers, ears and brain.

Is music the product of natural selection?
I am doubtful. Proponents like to give anecdotes about how famous musicians have more children, but rarely mention all the oboe teachers who dine alone. When you look at the brain, there is no 'music module' as there is for face recognition. Music is spread throughout the brain and implemented by many regions, such as Broca's area and the amygdala, that mainly serve other functions such as language and emotion. Music is a kind of technology that has developed over time, rather than something that is built into our minds.

What's more important, talent or practice?
Neither. If you look at the data, only about half of the variance in musical skill is accounted for by the time spent practising. Some people just learn faster and reach higher peaks. Many genes have indirect effects on music, including genes that influence auditory processing, extroversion and dexterity. All of these contribute to talent. To be truly great, you need both talent and practice. To be merely good — like me — you can get away with just practice. ■

INTERVIEW BY JASCHA HOFFMAN

Correspondence

Asian medicine: Japan's paradigm

The international medical community could benefit from the wide range of therapeutic options that traditional Japanese Kampo medicine can offer. Its integration into modern medicine has already been realized in Japan (*Nature* **480,** S96; 2011), where it is available as a 5-year specialization for physicians already trained in Western medicine.

Kampo and traditional Chinese medicine have common roots, but Kampo uses additional diagnostic techniques and more rigorously controls the quality of herbal preparations.

It would be a major loss for both Western and traditional medicines if political or financial factors were to cause the "sun to set" on Kampo.

Silke Cameron *University Medicine Göttingen, Germany. silke.cameron@med.uni-goettingen.de*
Heidrun Reissenweber *Clinic for Japanese Medicine, Munich, Germany.*
Kenji Watanabe *Center for Kampo Medicine, Keio University School of Medicine, Tokyo, Japan.*

Asian medicine: a fungus in decline

Estimates of wildlife trade for traditional Asian medicine should include that of the caterpillar fungus *Ophiocordyceps sinensis* (*Nature* **480,** S101–S103; 2011).

The fungus, used to treat asthma and other diseases, is legally harvested on a huge scale in Tibet and the Himalayas, and is one of the world's most expensive natural medical resources. Some 85–185 tonnes are collected annually by the local population for a global market worth between US$5 billion and $11 billion.

Large increases in the price (up by 900% from 1997 to 2008) and trade of caterpillar fungus have encouraged more intensive harvesting. My informal survey of harvesters in the Himalayas reveals that caterpillar fungus abundance is dwindling: the average harvest per collector dropped by around half between 2006 and 2010. Harvesters are extending their range as a result, risking overexploitation of a pristine landscape and more ecosystem degradation.

Conservation efforts must be initiated to halt the decline of this species, which is causing a loss of biodiversity and threatening local livelihoods.

Uttam Babu Shrestha *University of Massachusetts, Boston, USA. ubshrestha@yahoo.com*

Asian medicine: many unique types

The different branches of traditional Asian medicine are frequently confused (*Nature* **480,** S81–S103; 2011). Now could be the time to revive the centuries-old term 'Eastern medicine' to avoid such inaccuracies and to complement descriptions of Western medicine.

'Oriental' and 'Asian' medicine collectively describe the range of traditional treatments used in many Asian countries. Traditional Chinese medicine is more specific. Although practised mainly in China, it influenced the development of traditional medicines unique to Japan, Korea and Vietnam in the past few hundred years. Lumping all of these together as 'traditional Chinese medicine' is therefore incorrect.

The term 'Eastern medicine' was first coined in 1613 by a court physician in Korea, Heo Jun, in his book *Donguibogam* ('Principles and Practice of Eastern Medicine'). The book is still used in clinics and, in 2009, was added to the United Nations Educational, Scientific and Cultural Organization's World Documentary Heritage list.

Hoyun Lee *Health Sciences North, Sudbury, Ontario, Canada. mhlee@hsnsudbury.ca*

Asian medicine: call for more safety data

Marketing of traditional Chinese medicines is developing rapidly worldwide (*Nature* **480,** S81–S103; 2011). So much so that the European Union (EU) issued a directive in 2004 that all herbal preparations should be subject to the same screening procedures as pharmaceuticals by 2011. But by April last year, no Chinese herbal medicines had met the directive's requirements. Many have therefore been withheld from sale in the EU.

If these traditional remedies are to be accepted, their quality needs to be standardized and rigorous scientific data must be supplied on their efficacy and safety. The mystique surrounding such treatments must give way to verification and a proper understanding of concepts and applications. Only then can traditional Chinese medicine be integrated into a global health-care system.

Juncai Xu, Min Liu *Shanghai Clinical Research Center, Shanghai, China.*
Zhijie Xia *Shanghai Huashan Hospital, Fudan University, China. janexia2006@126.com*

Asian medicine: protect rare plants

As the global market in traditional Chinese medicines expands, many wild plants are on the brink of extinction (see also *Nature* **481,** 265; 2012). Urgent measures must be taken to ensure that these rare plants are harvested sustainably.

Some 11,000 plant species are listed in the Chinese pharmacopoeia, medicinal botany textbooks and ancient Chinese medical texts such as the *Compendium of Materia Medica* and Shennong's *Classic of Materia Medica*.

Examples of critically depleted natural populations include *Herba epimedii*, a herb used as an aphrodisiac, tonic and antirheumatic in China, Korea and Japan; *Panax ginseng*, a tonic and sleep-inducer; *Euchresta japonica*, for anti-tumour activity; *Dysosma versipellis*, a cleanser of toxins; and *Aconitum brachypodum*, an anti-inflammatory.

Hua-Feng Zhang *Shaanxi Normal University, Xi'an, Shaanxi, China.*
Xiao-Hua Yang *Xi'an Jiaotong University, Xi'an, Shaanxi, China; and Moscow State University, Russia. yxh@bk.ru*

Safety-test initiatives for nanomaterials

Your report on the need to establish safety regulations for nanomaterials focuses largely on US initiatives (*Nature* **480,** 160–161; 2011). Other initiatives are also making important contributions.

The Organisation for Economic Co-operation and Development (OECD) provides guidance on what parameters should be used for reporting the safety testing of nanomaterials (see go.nature.com/yiaxnd). Projects set up to aid implementation of Europe's REACH (for 'registration, evaluation, authorisation and restriction of chemicals') legislation advise on how to review information on nanomaterials.

The European Food Safety Authority published guidance last year on risk assessment of nanotechnologies in the food chain (see go.nature.com/7131fo). The European Commission's Joint Research Centre has also set up a repository of representative nanomaterials samples.

Juan Riego-Sintes *European Commission Joint Research Centre, Institute for Health and Consumer Protection, Ispra, Italy. juan.riego-sintes@ec.europa.eu*

Philip D. Lawley

(1927–2011)

Chemist who discovered that cancer is caused by damage to DNA.

Philip Lawley laid the foundation for the idea that cancer is a genetic disease. He provided the first convincing evidence that DNA is the key target for chemicals that cause cancer, and identified a major DNA-repair mechanism that counteracts the assault of carcinogens on DNA.

Lawley, who died on 18 December 2011, was born in 1927 in the village of Abbots Bromley in Staffordshire, UK, to two teachers. He obtained a degree in chemistry in 1949 at the University of Oxford and moved to the University of Nottingham, where he studied the physicochemical properties of DNA (before its double-helical structure was revealed by James Watson and Francis Crick). His graduate work included the first investigation of what later became known as DNA denaturation (the separation of the macromolecule into two strands).

After gaining a PhD in 1953, Lawley took up a post at the Chester Beatty Research Institute (now the Institute of Cancer Research) in London, where he investigated the interaction of anticancer drugs with DNA. By 1957, he had demonstrated that alkylating agents could bond covalently with DNA to produce stable products (adducts), a radical idea at a time when it was believed that such interactions were weak or reversible and that proteins were the crucial target of carcinogens.

In the late 1950s, with chemist Peter Brookes, Lawley carried out seminal studies on the binding of mutagens and carcinogens to DNA in living organisms. The Radiochemical Centre in Amersham had just begun producing radioactively labelled chemicals, including mustard gas, which had been used as a chemical weapon in the First World War. Ironically, Lawley's father had been exposed to it while serving in the trenches. Mustard gas was already known to be a mutagen and it was later found to cause lung cancer. It was the archetype of difunctional (having two chemically reactive sites) anticancer drugs, such as melphalan and chlorambucil, which were developed during the 1950s at the Chester Beatty.

To conduct these potentially hazardous studies, Lawley and Brookes moved out of London to the institute's Pollards Wood Research Station, which was set in 24 hectares of woodland and conveniently close to the Radiochemical Centre. In these leafy and peaceful surroundings, they produced their seminal work on the binding of mutagens and carcinogens to DNA. In 1960, they reported that mustard gas formed adducts with guanine in DNA, in viruses, bacteria, cultured mouse cancer cells and cancers in mice.

The adduct hindered DNA replication and cell division by crosslinking the strands of the DNA helix, thus explaining mustard gas's extraordinary toxicity to cells. They demonstrated that bacteria resistant to mustard gas used enzymes to remove those crosslinks, but sensitive bacteria did not. This was the first convincing evidence for the repair of DNA adducts in a living organism. It is now clear, 50 years on, that many of the genes mutated in human cancer are involved in DNA repair.

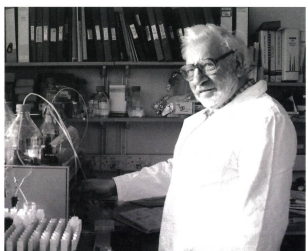

F. L. MARTIN

In a second landmark paper in 1964, Lawley and Brookes reported in *Nature* a correlation between carcinogenicity and DNA binding, using radioactively labelled polycyclic aromatic hydrocarbons (PAHs) applied to mouse skin. These ubiquitous products of incomplete combustion (found, for example, in tobacco smoke) are chemically inert, but many are potent carcinogens when metabolically activated. Lawley and Brooks found that the amount of binding to DNA, but not to protein or RNA, increased with the carcinogenic potency of the PAHs. This discovery overturned the prevailing view that proteins were the critical cellular targets for carcinogens and it changed the course of cancer research.

Lawley went on to show how point mutations are induced when potent alkylating mutagens (such as *N*-methyl-*N*-nitrosourea) react with those atoms in DNA that determine base-pairing during DNA replication. Point mutations are now known to occur frequently in a variety of human cancer genes. He also discovered the 6-*O*-methylguanine-DNA methyltransferase DNA-repair system that selectively removes such modified DNA bases.

Outwardly shy, Lawley had a wry sense of humour, liberal views and enormous integrity. He did not follow scientific fashion and was happiest working at the bench. He took extraordinary pleasure in conversation, which was enriched by his passions for books, jazz, art, dogs and old trams. He often engaged in protracted and sometimes heated debate with whoever happened to be around — usually a scientific colleague, but occasionally an innocent bystander — sometimes losing track of time. At Pollards Wood, these conversations would often continue al fresco in the coppiced beech woods, sometimes in the company of Lawley's whippet.

Lawley retired in 1992, but continued to work in the Institute of Cancer Research laboratories at Sutton in south London for many more years, enhancing the lives of those who worked alongside him with his knowledge, congeniality and wit. Fittingly, in January 2003, the institute honoured Brookes and Lawley by naming a £21-million (US$32-million) laboratory in Sutton after them. ■

Stanley Venitt *is honorary associate and* **David H. Phillips** *is professor of environmental carcinogenesis in the Analytical and Environmental Sciences Division, King's College, London SE1 9NH, UK. Both were colleagues of Philip Lawley at the Institute of Cancer Research.*
e-mail: stan.venitt@kcl.ac.uk

RESEARCH

NEW ONLINE

Papers published this week at Nature.com/nature

NEWS & VIEWS The staggering gait of the ubiquitous motor protein dynein **p.44**

LETTER A quantum interface to link a mechanical oscillator to optical photons **p.63**

LETTER Field research reveals a new structural genomic variation **p.81**

29 JANUARY 2012

STRUCTURAL BIOLOGY

GPCR modulation by an antibody

G-protein-coupled receptors (GPCRs) are the largest class of cell-surface receptor, and many of them are considered drug targets. The crystal structure of the human A_{2A} adenosine receptor in complex with a mouse antibody fragment has now been determined. The structure includes intracellular loop 3, which is crucial for G-protein binding. The use of an antibody fragment to stabilize the receptor in an inactive conformation suggest a new strategy for modulating the activity of GPCRs.

G-protein-coupled receptor inactivation by an allosteric inverse-agonist antibody
T Hino *et al.*
doi:10.1038/nature10750

EVOLUTION

Evolution by numbers

In eukaryotic cells, the chaperone protein Hsp90 facilitates the accumulation of genetic variation under non-stressful conditions by buffering the effects of mutations on many important regulatory and structural proteins. Here, Rong Li and colleagues study the role of stress-induced genome plasticity in promoting adaptive evolution in budding yeast. They show that aneuploidy, in which a cell contains an abnormal, uneven number of chromosomes, can be rapidly induced by pleiotropic stresses leading to stress adaptation. These results point to a role for Hsp90 as a guardian of chromosomal stability during adaptive evolution, with inhibition of Hsp90 a possible trigger for rapid adaptation through aneuploidy.

Hsp90 stress potentiates rapid cellular adaptation through induction of aneuploidy
G Chen *et al.*
doi:10.1038/nature10795

CANCER

Drug targets in glioblastoma

Exome sequencing of 48 childhood glioblastoma samples has identified somatic mutations in the H3.3-ATRX-DAXX chromatin remodelling pathway in 44% of tumours. Mutations in *H3F3A*, which encodes the replication-independent histone 3 variant H3.3, were found in 31% of tumours, the first indication that this gene is linked to tumorigenesis. These mutations are shown to be specific to glioblastoma and highly prevalent in children and young adults, suggesting that defects of the chromatin architecture may underlie the condition. Childhood glioblastoma is fatal and resistant to therapy, so the discovery of possible drug targets is an important advance.

Driver mutations in histone H3.3 and chromatin remodelling genes in paediatric glioblastoma
J Schwartzentruber *et al.*
doi:10.1038/nature10833

STRUCTURAL BIOLOGY

Structural and functional conservation of key domains in $InsP_3$ and ryanodine receptors
M-D Seo *et al.*
doi:10.1038/nature10751

1 FEBRUARY 2012

QUANTUM COMPUTING

Putting qubits to rights

Efforts to harness the power of quantum computers are complicated by the fact that quantum computers are more prone to errors than classical ones. Such errors can be detected and corrected without affecting computational capability by using quantum error correcting codes, the simplest of which are three-qubit codes. This paper reports the implementation of three-qubit quantum error correction using superconducting circuits. Phase- and bit-flip errors are corrected with high fidelity using a Toffoli gate — a logic gate that makes universal reversible classical computation possible. The work establishes the conceptual components of a more complex device that could correct arbitrary single-qubit errors.

Realization of three-qubit quantum error correction with superconducting circuits
M D Reed *et al.*
doi:10.1038/nature10786

IMMUNOLOGY

Inflammasome link to gut flora

Using a mouse model, Richard Flavell and co-workers study the inflammatory processes associated with progression of non-alcoholic fatty liver disease, the leading cause of chronic liver disease in developed countries, to non-alcoholic steatohepatitis, which often leads to cirrhosis and hepatocellular carcinoma. They find that alterations in the intestinal microbiota associated with the NLRP6 and NLRP3 inflammasomes enhance disease in mice with diet-induced non-alcoholic fatty liver disease. These findings highlight the pivotal role of the microbiota in the development of autoinflammatory and metabolic disorders and point to the manipulation of host–microflora interactions as a focus for new therapies.

Inflammasome-mediated dysbiosis regulates progression of NAFLD and obesity
J Henao-Mejia *et al.*
doi:10.1038/nature10809

DEVELOPMENTAL BIOLOGY

Enhancer decommissioning by LSD1 during embryonic stem cell differentiation
W A Whyte *et al.*
doi:10.1038/nature10805

NATURE PODCAST

This week, a discussion on the proposal (see Comment page 27) that the use of sugars, like tobacco and alcohol, should be regulated for our own good. And there's more on the captivating idea that the release of elephants into the Australian bush would reduce the risk of fires. **nature.com/nature/podcast**

VOLCANOLOGY

Greek inflation circa 1600 BC

A petrology study of the Bronze Age 'Minoan' eruption on the Greek island of Santorini finds that the sub-volcanic magma reservoir was recharged in spurts during the decades to months that preceded the eruption. SEE LETTER P.77

JON BLUNDY & ALISON RUST

The most powerful volcanic eruptions release so much magma that a large surface depression, or caldera, forms above the evacuated underground magma reservoir. We know from geological records that caldera-forming eruptions can discharge hundreds or even thousands of cubic kilometres of magma. A period of volcanic unrest must precede these eruptions, but the nature and duration of the warning signs are unknown because this type of eruption is so infrequent. Druitt *et al.*[1] (page 77 of this issue) show that igneous petrology, the study of once-molten rocks, can help to elucidate the likely precursory activity for these large, catastrophic eruptions.

The authors studied pumice rocks from a major volcanic event — the caldera-forming 'Minoan' eruption that occurred on the Aegean island of Santorini (Fig. 1) in around 1600 BC and which had a magma output of 40–60 cubic kilometres. Their study revealed that the magma reservoir that fuelled the eruption experienced huge incursions of hot magma between a century and just a few months (or possibly much less) before eruption. The results raise questions about the nature and timing of warning signs that may presage such large volcanic eruptions, the likes of which have never been witnessed in the modern scientific age.

Igneous petrology is a forensic enterprise: we can interrogate volcanic products only after an eruption has happened. In effect, the volcano petrologist becomes a pathologist, dissecting the cadavers of past eruptions. Those who monitor volcanoes, meanwhile, are the figurative health-care professionals, recording the volcanic equivalents of body mass and pulse rate. In medicine, the link between a patient's evolving vital signs and their ultimate demise is not a simple one. Luckily for geologists, advances in petrological tools — including high-spatial-resolution chemical analysis using electron, X-ray, laser and ion microbeams — and in satellite-based monitoring techniques[2] are closing the gap between the observation and interpretation of restless volcanoes. The challenge is to use petrology to model, retrospectively, the likely manifestations of underground magmatic processes at Earth's surface. It is hoped that this will yield a better understanding of the probable warning signs and so improve our ability to forecast large, infrequent eruptions.

SONOBAN/WIKIPEDIA

Figure 1 | Santorini's caldera. Druitt and colleagues' study[1] of pumices from the *c.*1600 BC 'Minoan' eruption, which produced the large caldera seen at the centre of this image, shows that the magma reservoir that fuelled the eruption was flooded with hot magma between a century and just a few months before eruption. The largest island is Thera; the Kameni islands in the centre of the photograph were built by lava eruptions following formation of the caldera. The most recent such eruption was in 1950.

In their study, Druitt and colleagues[1] applied an approach known as diffusion chronometry to crystals of the mineral feldspar in volcanic ejecta of the Minoan eruption. Most volcanic crystals are chemically zoned (that is, they consist of concentric zones of differing chemical composition) owing to perturbations of the magma that they grew from. The perturbations arise, for instance, from mixing with hotter magma or the release of gas. Abrupt perturbations generate sharp chemical discontinuities in the crystal. Over time, these are smoothed out by chemical diffusion at the relatively high temperatures in the magma reservoir (about 855 °C for the Minoan rhydodacite magma). The extent of smoothing can be used as a diffusive clock that records the time elapsed between the moment the system was abruptly perturbed and the instant of eruption, when rapid cooling of the magma arrests any further diffusion and stops the clock.

Crystals in natural volcanic rocks contain a slew of trace elements, present at concentrations of a few thousand parts per million at most. Each of these trace elements diffuses through the crystal at a different rate, meaning that diffusion chronometry can be used to investigate magmatic processes over a huge range of timescales, depending on which trace

element is studied. Druitt and co-workers[1] measured the chemical gradients of magnesium across individual zones in feldspar crystals. Magnesium diffuses distances of about 10 micrometres a year at temperatures of 855 °C, and so is ideal for investigating processes that happen on timescales of centuries or less. The authors used the chemical gradients of the very slow-diffusing trace elements strontium and titanium to establish that the crystal zones they studied have a thermal origin, resulting from the addition of hotter magmas to the reservoir. They propose that a significant volume of this hot magma was added in one or more spurts during the decades or months that preceded the Minoan eruption. Each spurt would have generated vigorous seismic activity and considerable inflation of the island's surface, probably serving as harbingers of catastrophe for Santorini's Minoan inhabitants[3].

This short timescale between recharge of the reservoir with hot magma and subsequent eruption, compared with the 18,000-year period of dormancy between the Minoan eruption and the previous caldera-forming eruption at Santorini, echoes the short lead-in time previously calculated[4] for the much smaller 1925–28 lava eruptions on Nea Kameni island in the centre of Santorini's caldera (Fig. 1). The net pre-Minoan influx rate of hot magma calculated by Druitt *et al.*[1] is in excess of 0.05 $km^3\ yr^{-1}$, some 50 times greater than the long-term average rate at Santorini. This is consistent with an emerging consensus that assembly of magma reservoirs is piecemeal and pulsatory, and may accelerate before eruption. These pulses can potentially be modelled from real-time ground deformation[2]. The magnitude of deformation depends on the depth and shape of the magma reservoir, the size of the pulses, and how the heated rocks above the magma reservoir deform.

Santorini seems to be a volcano of habit. The island has seen two major cycles of magmatic activity, each lasting about 180,000 years and culminating in two large caldera-forming eruptions of silica-rich rhyodacite magma about 20,000 years apart; the Minoan is the most recent of these[5]. The early stages of volcanic activity in each cycle were marked by much smaller eruptions of magma that was more silica-poor (dacites, andesites and basalts). Since at least 197 BC, Santorini's caldera has been refilling with dacite lavas and the products of associated minor explosive eruptions[5]; the most recent lava eruption was on Nea Kameni in 1950. These lavas bear chemical similarities to the hotter magmas that flooded the magma reservoir before the Minoan eruption[1]. It is not clear whether they herald the start of a new eruptive cycle on Santorini or are vestiges of the last one.

Since early 2011, there have been increasing numbers of small earthquakes beneath the floor of the Santorini caldera[6], several centimetres of surface uplift[7] and increased release of magmatic carbon dioxide from the ground[8]. So far it is not certain whether these are the signs of an impending eruption — which would probably produce a dacite lava flow similar to the small, post-Minoan eruptions on Nea Kameni — or the usual restlessness that characterizes many dormant volcanoes. The difficult task facing those charged with monitoring Santorini[6] is interpreting the ongoing signs of unrest in the context of the most likely magmatic and tectonic processes responsible and the long-term behaviour of the volcano. Applications of diffusion chronometry to volcanic rocks from Santorini[3,4] provide valuable insight into the magnitude and timing of subterranean magmatic events that preceded previous eruptions both large and small. ■

Jon Blundy *and* **Alison Rust** *are at the School of Earth Sciences, University of Bristol, Bristol BS8 1RJ, UK.*
e-mail: jon.blundy@bris.ac.uk

1. Druitt, T. H., Costa, F., Deloule, E., Dungan, M. & Scaillet, B. *Nature* **482,** 77–80 (2012).
2. Sparks, R. S. J. *Earth Planet. Sci. Lett.* **210,** 1–15 (2003).
3. Cioni, R., Gurioli, L., Sbrana, A. & Vougioukalakis, G. *Phys. Chem. Earth A* **25,** 719–724 (2000).
4. Martin, V. M. *et al. Science* **321,** 1178 (2008).
5. Druitt, T. H. *et al. Santorini Volcano* Geol. Soc. Lond. Mem. 19 (1999).
6. http://ismosav.santorini.net
7. Newman, A. V. *et al. Eos Trans. AGU* **92,** Fall Meet. Suppl. Abstr. V53C-2643 (2011).
8. Parks, M. *et al. Eos Trans. AGU* **92,** Fall Meet. Suppl. Abstr. V53E-2679 (2011).

NEUROSCIENCE

Reward alters specific connections

How does the brain couple a fleeting sensory input to a delayed reward during learning? A study in locusts shows that coincident firing of neurons can 'mark' a neuronal connection for later modulation. SEE ARTICLE P.47

TIMOTHY E. HOLY

A whiff of food followed by a tasty meal can trigger a specific learned association. In the quest to explain learning mechanistically, a long-standing hypothesis known as Hebb's rule[1,2] posits that the pairing of stimulus and reward causes their respective neurons to be simultaneously active, and that this synchronous activity then changes the strength of the connections — synapses — between the neurons. But when stimulus and reward are not simultaneous, how does the brain pick the right synapses to modify? On page 47 of this issue, Cassenaer and Laurent[3] report that correlated neuronal activity, when followed by delivery of a neurotransmitter molecule known to be released by reward, changes synapses in distinctive ways in the locust olfactory system. Moreover, the authors observed these changes in live insects and using natural stimuli (odours).

The relevance of Hebb's rule in associative learning received significant experimental support with the discovery of long-term potentiation[4], in which coincident firing of two interconnected neurons results in a stronger connection between them. However, perhaps the clearest correlate of associative learning came much later, with the discovery of spike-timing-dependent plasticity (STDP)[5]. In this process, the firing (voltage spikes) of the pre- and postsynaptic neurons must occur within a few tens of milliseconds for synaptic change (plasticity) to occur.

STDP has been extensively studied and is widespread in the brain. However, any attempt to explicitly relate this cellular phenomenon to behavioural learning faces numerous obstacles. A simplistic view specifies that the presynaptic neurons should be stimulus responsive, and the postsynaptic neurons reward responsive. However, one must acknowledge that a dizzyingly large number of arbitrary stimuli can be associated with a tiny number of intrinsic rewards. Moreover, Hebb's rule requires that all possible connections are initially present so that they might be strengthened or weakened through experience. The result might be a 'reward bottleneck', in which numerous stimulus-responsive neurons compete with each other for wiring space and/or influence over a few reward-responsive neurons.

A second obstacle arises because neurons in the brain display ongoing 'spontaneous' activity, and accidental coincidences between the spikes of pre- and postsynaptic neurons would also trigger plasticity. So, the robustness of synaptic change must be considered in light of this 'noise' problem. The narrow time window for STDP reduces the likelihood of accidental coincidence, but the sheer number of connections made by typical presynaptic

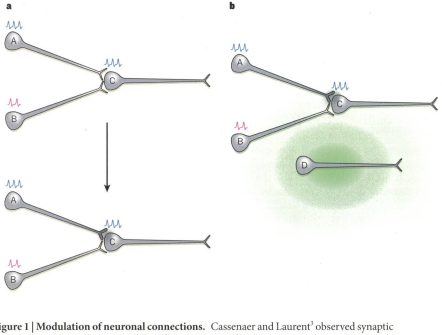

Figure 1 | Modulation of neuronal connections. Cassenaer and Laurent[3] observed synaptic modulation in a specific circuit of the olfactory system of live locusts. A and B represent neurons known as Kenyon cells, and C is a neuron from another part of the brain, the β-lobe. **a**, The strength of the synaptic connection between A and C changes when both cells fire repeatedly (blue spikes) within tens of milliseconds of each other. This process, known as spike-timing-dependent plasticity (STDP), may underlie some forms of associative learning in other systems, especially if stimulus and reward are simultaneous and are sensed by neurons such as A and C. The connection between B and C, by contrast, is not altered because they do not fire coincidently (red and blue spikes). **b**, STDP alone, however, cannot explain how stimulus and reward are connected when they occur hundreds of milliseconds apart. A possible missing link may be neuromodulatory transmitters (green) that are secreted by certain neurons (such as the reward-responsive neuron D) throughout the brain. The authors[3] show that one of these molecules, octopamine, can specifically weaken the synapses (such as the A–C synapse) that had been 'marked' 1 second earlier by STDP.

neurons seems to suggest[6] that random events are too common for reliable and stable learning through STDP alone.

A third problem is that the time window of STDP is too short to explain the seconds-long delays between stimulus and reward in typical associative-learning experiments. In some cases, sustained activity of presynaptic neurons[7] may circumvent this delay issue, but there are examples for which this does not seem to be the case. A particularly relevant example is found in the insect olfactory system, in which a group of neurons called Kenyon cells, residing in a part of the brain known as the mushroom body, respond to odours too transiently for their response to coincide with the delayed delivery of reward[8].

For the above and other reasons, researchers have focused on additional factors that regulate synaptic plasticity. Among the most prominent examples are neuromodulatory transmitters, such as acetylcholine, serotonin, dopamine, noradrenaline and octopamine. These molecules can increase or decrease the strength of synapses, and are therefore attractive candidates for mediating plasticity and learning. In both vertebrates and invertebrates, a modest number of modulatory neurons release these transmitters throughout the brain. By making reward-coupled signals widely available without the requirement for direct synapses onto reward-activated neurons, this architecture seems to relieve the reward bottleneck. However, it also implies that neuromodulators themselves cannot encode specific experiences. An attractive solution would be an interaction between neuromodulators and a synapse-specific process such as STDP. Indeed, numerous *in vitro* studies have revealed that the two do interact[9], but data on the relevance of these interactions *in vivo*, using natural sensory input, seem to be scarce.

Enter Cassenaer and Laurent[3]. Using live locusts as model organisms, they studied the synapses between the Kenyon cells and a small collection of neurons located in another part of the brain, the β-lobe. Unlike the sparsely firing Kenyon cells, β-lobe neurons fire in response to nearly every odour presented to the insect. By inserting tiny wires into the locust brain, the authors could stimulate different Kenyon cells with precise timing and record the corresponding inputs received by particular β-lobe neurons. Those synapses in which the inputs paired with the spikes of the β-lobe neuron became stronger or weaker in a typical STDP fashion (Fig. 1a).

In insects, the most well-studied mediator of reward is octopamine, and receptors for this neurotransmitter are abundant in the β-lobe[10,11]. To mimic associative-learning experiments (in which there is a delay between stimulus and reward), the authors[3] delivered a brief injection of octopamine one second after spike pairing. They found that this neurotransmitter dramatically changed how STDP worked: the synapse invariably became weaker, even under conditions in which it would normally have grown stronger. That is, plasticity still depended on precise temporal pairing of pre- and postsynaptic activity, but the addition of octopamine altered the outcome (Fig. 1b). The researchers obtained similar results when they used odour delivery, instead of electrical stimulation, to stimulate Kenyon cells.

These changes can be considered associative only if they are specific to the particular sensory experience paired with reward. In a beautiful final experiment, Cassenaer and Laurent[3] presented different odours sequentially to the locust, occasionally pairing one of them with octopamine injection. Whereas the neuronal responses to unpaired odours were scarcely affected by the neurotransmitter, the response to the paired odour was markedly decreased. Consequently, plasticity depended on the conjunction of odour-triggered activity and octopamine. It is worth noting that noradrenaline, an octopamine-related molecule, also changes olfactory circuitry in mammals and can trigger learning when paired with an odour[12,13]. Cassenaer and Laurent reveal the interaction of synapse-specific coincident firing and nonspecific neuromodulation — a combination that may help to resolve some major challenges to Hebbian plasticity, especially the delay problem.

Given the inherent complexities in relating brain-circuit processes to behavioural learning, many questions remain. One fundamental issue is whether octopamine resolves the noise problem of accidental coincidence. Indeed, over the short timescales of Cassenaer and Laurent's experiments[3], octopamine-modulated STDP was not obviously stronger, more quickly induced or more persistent than classical STDP. How, then, does (rare) neuromodulatory STDP overcome or overwhelm (common) ongoing STDP? The authors argue that, under normal conditions, ongoing STDP is balanced by mutually inhibitory activities of postsynaptic neurons, and so it requires new conditions — such as the presence of octopamine — to produce changes in neuronal firing. However, in the face of ongoing STDP, can such changes persist for long? These and similar questions will surely be tackled in future chapters of the long and complex story of memory. ■

Timothy E. Holy *is in the Department of Anatomy and Neurobiology, Washington University School of Medicine in St. Louis, St. Louis, Missouri 63110, USA.*
e-mail: holy@wustl.edu

1. Bain, A. *Mind and Body* (Appleton, 1877; reformatted Univ. Michigan Library, 2006).
2. Hebb, D. O. *The Organization of Behavior* (Psychology Press, 2002).
3. Cassenaer, S. & Laurent, G. *Nature* **482,** 47–52 (2012).
4. Bliss, T. V. P. & Lømo, T. *J. Physiol. (Lond.)* **232,** 331–356 (1973).
5. Markram, H., Gerstner, W. & Sjöström, P. J. *Front. Synaptic Neurosci.* **3,** 4 (2011).
6. Morrison, A., Aertsen, A. & Diesmann, M. *Neural Comput.* **19,** 1437–1467 (2007).
7. Drew, P. J. & Abbott, L. F. *Proc. Natl Acad. Sci. USA* **103,** 8876–8881 (2006).
8. Ito, I., Ong, R. C., Raman, B. & Stopfer, M. *Commun. Integr. Biol.* **1,** 170–171 (2008).
9. Pawlak, V., Wickens, J. R., Kirkwood, A. & Kerr, J. N. *Front. Synaptic Neurosci.* **2,** 146 (2010).
10. Degen, J., Gewecke, M. & Roeder, T. *Br. J. Pharmacol.* **130,** 587–594 (2000).
11. Sinakevitch, I., Mustard, J. A. & Smith, B. H. *PLoS ONE* **6,** e14536 (2011).
12. Linster, C., Nai, Q. & Ennis, M. *J. Neurophysiol.* **105,** 1432–1443 (2011).
13. Shea, S. D., Katz, L. C. & Mooney, R. *J. Neurosci.* **28,** 10711–10719 (2008).

SURFACE CHEMISTRY

Crystal cuts on the nanoscale

A simple method has been developed to control the shape of nanoscale cuprous oxide crystals. Some shapes turn out to be much better than others as catalysts for a light-activated reaction.

PEIDONG YANG

The most popular diamond cut is the 'modern round brilliant', in which a gem is hewn to expose a specific set of crystal facets so as to produce exceptional brilliance. The arrangement of the facets is crucial for providing the maximum light return through the top of the diamond. It is becoming increasingly clear that crystal shape at the nanometre scale is similarly important for getting the best performance from solid catalysts. Writing in the *Journal of the American Chemical Society*, Huang *et al.*[1] report a beautiful example of how the specific crystal facets on nanoparticles of a material affect the catalytic properties of the particles in light-activated reactions.

Cuprous oxide (Cu_2O) has commonly been used as a pigment, a fungicide and an antifouling agent for marine paints. More recently, it has been reintroduced as a promising material for the cathode of photoelectrochemical cells, which use sunlight to split water into hydrogen and oxygen[2]. Huang *et al.*[1] have discovered a simple process for controllably synthesizing cuprous oxide nanocrystals as cubes, rhombic dodecahedra (polyhedra with 12 rhombic faces) and a variety of geometries in between (Fig. 1). The rhombic dodecahedra expose only one kind of facet (known in crystallographic jargon as {110} facets), and the authors observed that these nanocrystals are exceptionally good catalysts for the light-induced degradation of the organic compound methyl orange. This reaction serves as a model for reactions involved in clearing organic pollutants from the environment.

One of the tricks often used to control which shapes and facets form during the synthesis of nanocrystals is to preferentially adsorb certain molecular species to specific planes of atoms exposed on crystal surfaces. This strategy generates direction-dependent nanocrystal growth by stabilizing a particular facet — growth is limited on crystal planes where adsorption (and so stabilization) is strong, but is promoted on planes where adsorption is weak. A wide variety of chemical species can facilitate shape control in the growth of metal and oxide nanocrystals, including: surfactants, polymers and biomolecules; small molecules such as those in gases; and even atomic species, such as anions or metal ions.

It has previously been reported[3] that the shape of cuprous oxide nanocrystals can be controlled by varying the ratio of chloride ions to sodium dodecyl sulphate ions in the solutions from which the crystals form; the chloride ions stabilize the {100} planes of the crystals, whereas the dodecyl sulphate ions stabilize the {111} planes. In this way, a range of nanoscale polyhedra has been produced.

To make their cuprous oxide nanocrystals, Huang *et al.*[1] used a different recipe from that previously reported[3], and found that, by simply adjusting the amount of the reducing agent in the reaction mixture, they could control the shapes of the crystals. Their approach allowed them to make an alternative series of polyhedra (Fig. 1) to that produced in the earlier work. In addition, their shape-control method can be used at room temperature, unlike many previously reported strategies, which typically require higher temperatures.

Different nanocrystal shapes naturally display crystallographically distinct facets. In the absence of any major surface reconstruction processes, each facet type contains surface

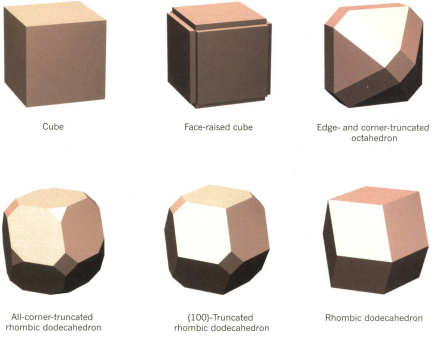

Figure 1 | Nanocrystal shapes. Huang *et al.*[1] report a simple process for controlling the shape of cuprous oxide nanocrystals during synthesis; the shapes made are depicted. The authors observed that the catalytic properties of the nanocrystals in a light-activated reaction — the degradation of methyl orange — largely depend on the kind of facets that the crystals have. Cubic crystals are essentially inactive, octahedra are moderately active, and rhombic dodecahedra are exceptionally active.

atoms that reside in particular environments (arrangements of nearby atoms). This in turn causes the surface atoms in different facets to have distinct catalytic activities. This fundamental insight dates back to the classic discovery that {111} surfaces on single crystals of platinum are typically much more catalytically active than {100} surfaces in reactions that form aromatic compounds.

Indeed, Huang and colleagues' cuprous oxide nanocrystals clearly exhibit very different catalytic properties depending on the facets displayed. The authors found that cubic nanocrystals that are bound exclusively by {100} faces are essentially inactive in the photodegradation reaction of methyl orange, whereas octahedra bound by {111} surfaces are moderately active catalysts. Rhombic dodecahedra bound by {110} surfaces, however, caused much faster photodegradation of methyl orange than the other nanocrystal shapes. The authors speculate that the observed catalytic activities correlate with the surface density of copper sites on the different facets, although they report no direct evidence for this. It is also unclear whether many of the atoms on nanocrystal surfaces undergo rearrangements during the reactions, or how ligand molecules that are bound to the different surfaces — either during crystal formation or in the photodegradation reactions — affect catalytic activity.

The new findings[1] form part of a growing body of literature documenting surface-dependent catalytic activities, perhaps most notably for metals. For example, key studies performed on the surfaces of samples of macroscopic single crystals under ultra-high-vacuum conditions have shown that some reactions are sensitive to surface structure[4]. A quintessential case is the platinum-catalysed reaction of benzene with hydrogen: the {100} platinum surface yields only cyclohexane (a saturated hydrocarbon) as a product, whereas the {111} surface also yields cyclohexene (an unsaturated analogue of cyclohexane)[4].

This dependence of catalytic activity on surface structure extends to metal nanocrystals, particularly in the case of platinum, palladium and rhodium. For instance, in the hydrogenation of benzene, platinum nanocrystals that expose well-defined {100} and {111} surfaces behave[5] in much the same way as larger crystals. In another example, faceted palladium nanocrystals that have high-index surfaces — {730} and {221} surfaces, which contain a high density of atomic steps and ledges — were found[6] to be much more active catalysts in 'Suzuki' carbon–carbon bond-formation reactions than nanoparticles that have typical {100} surfaces. Such high-index faceted nanoparticles are also better catalysts for some electrochemical reactions[7,8]. And returning to cuprous oxide, highly faceted polyhedral microcrystals that display high-index {311} surfaces are especially good catalysts for the oxidation of carbon monoxide[9].

Although it is clear that the reactivity and selectivity of nanoparticle catalysts depend on the shape (and hence the exposed surfaces) of the particles, in many cases it is unclear whether these effects are truly surface-dependent. This is especially true for reactions in solution or in the gas phase, where there is evidence that changes to particle surfaces and shapes may occur during the reactions[10]. Methods for the direct *in situ* surface analysis of molecules adsorbed to nanocrystals in solution, analogous to the techniques commonly used to study larger single crystals, need to be developed to address this issue. Nevertheless, as Huang *et al.*[1] have shown, sculpting the shape of nanocrystals is a promising approach for developing catalysts that produce only one desired reaction product out of many other possible products at high reaction rates — an essential requirement for a wide variety of industrially important reactions. ■

Peidong Yang *is in the Department of Chemistry, University of California, Berkeley, Berkeley, California 94720, USA, and at King Abdulaziz University, Jeddah, Saudi Arabia.*
e-mail: p_yang@berkeley.edu

1. Huang, W.-C., Lyu, L.-M., Yang, Y.-C. & Huang, M. H. *J. Am. Chem. Soc.* **134,** 1261–1267 (2012).
2. Paracchino, A., Laporte, V., Sivula, K., Grätzel, M. & Thimsen, E. *Nature Mater.* **10,** 456–461 (2011).
3. Siegfried, M. J. & Choi, K.-S. *Adv. Mater.* **16,** 1743–1746 (2004).
4. Somorjai, G. A. & Li, Y. *Introduction to Surface Chemistry and Catalysis* 2nd edn, Ch. 9 (Wiley, 1994).
5. Bratlie, K. M., Lee, H., Komvopoulos, K., Yang, P. & Somorjai, G. A. *Nano Lett.* **7,** 3097–3101 (2007).
6. Wang, F. *et al. J. Am. Chem. Soc.* **133,** 1106–1111 (2011).
7. Chen, Q.-S. *et al. J. Am. Chem. Soc.* **133,** 12930–12933 (2011).
8. Habas, S. E., Lee, H., Radmilovic, V., Somorjai, G. A. & Yan, P. *Nature Mater.* **6,** 692–697 (2007).
9. Leng, M. *et al. J. Am. Chem. Soc.* **132,** 17084–17087 (2010).
10. Joo, S. *et al. Nature Mater.* **8,** 126–131 (2009).

PLANT BIOLOGY

Equal-parenting policy

During early embryo development in animals, maternal genes are expressed in preference to those of the zygote — the newly fertilized egg. But in plants it seems that zygote genomes switch on within hours of fertilization. SEE LETTER P.94

CHRISTOPHER J. HALE & STEVEN E. JACOBSEN

Fertilization occurs when two gametes merge to form a zygote. The zygote's genome comprises two sets of chromosomes — one maternal, the other paternal. In animals, the stages of development immediately after fertilization are disproportionally controlled by maternally inherited factors, with the zygotic genome being switched on gradually in waves of activation[1]. Whether plants undergo a similar maternal-to-zygotic transition in genomic activity has been a long-standing question. In contrast to previous work[2], Nodine and Bartel[3] show (page 94 of this issue) that a plant zygote's protein-coding transcriptome — its total complement of protein-coding RNA transcripts — contains relatively equal maternal and paternal contributions. It seems, therefore, that plants and animals have evolved distinct strategies for managing the early steps in the transition from two gametes to an organism with maternal and paternal copies of the genome*.

For the plant species *Arabidopsis thaliana*, a wealth of whole-genome sequence data exists for closely related yet genetically distinct lines known as ecotypes[4]. To directly measure the respective contributions of the maternal and paternal genomes to the zygotic transcriptome, Nodine and Bartel crossed two of these ecotypes and sequenced the RNA content of the resulting zygote. Using the genetic differences between the parents, they then matched these RNAs to either the maternal or the paternal genome.

The authors observed a near-equal abundance of RNA sequences derived from each parental genome in the plant embryos as early as the one- to two-cell stage. Only a small number of genes showed biased expression. They also performed reciprocal crosses — switching which ecotype provided the male and female gamete. It emerged that most of these cases of bias were probably due to genetic or epigenetic differences (chemical modifications that alter gene expression without affecting the DNA sequence) between the two ecotypes used, rather than being a result of which ecotype was used as the male or the female parent. These findings imply that the plant zygotic genome is essentially switched on only hours after fertilization.

Nodine and Bartel's results are in contrast to other reports[2,5] suggesting that the maternal-to-zygotic transition in plants is gradual, as is the case for animals. The most comprehensive of these reports[5], published last year, used a genomics approach similar to that of the current study, and found that more than 80% of the *Arabidopsis* transcriptome in early

*This article and the paper[3] under discussion were published online on 22 January 2012.

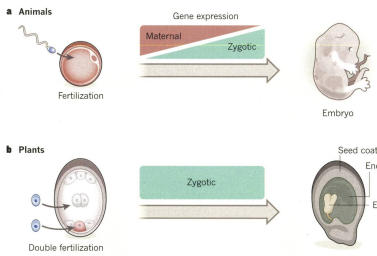

Figure 1 | Maternal-to-zygotic genomic transition in plants and animals. **a**, In animals, a single fertilization event between maternal and paternal gametes forms the zygote (not shown). Initially, the animal embryo is under predominant control of the maternal genome, and the zygotic genome is only gradually activated over the course of embryogenesis. **b**, In plants, a double fertilization process generates the zygote and the endosperm tissue. Both the endosperm and the embryo are encased in maternal tissue that generates the seed coat. Chromosome symbols represent maternal (red) and paternal (blue) genomes. Nodine and Bartel[3] show that, in contrast to the case for animals, the plant zygotic genome is activated almost immediately after fertilization.

embryos is derived from the maternal genome.

What might explain such different results between the two studies? Nodine and Bartel[3] suggest that the most likely answer is that the embryo samples of the earlier study were contaminated by maternal tissue. This is because, in *Arabidopsis* as in other flowering plants, the embryo is surrounded by a seed coat and other maternally derived tissue (Fig. 1), making the isolation of high-purity embryonic tissue difficult — a problem for the extremely sensitive genome-sequencing techniques used in both studies. After observing this maternal-contamination effect in pilot studies, Nodine and Bartel[3] overcame the problem by extensively washing the isolated embryo cells.

One question arising from Nodine and Bartel's study is why activation of the zygotic genome is so different between plants and animals. Because the two kinds of organisms evolved multicellularity independently[6], and have very different life histories, it is perhaps not surprising that the maternal-to-zygotic transition also differs between them. In plants, gametes are generated from cells derived from a pool of undifferentiated cells that are also responsible for generating structures such as leaves[7,8], rather than from a distinct germ-cell lineage as occurs in animals. In addition, fertilization itself is radically different in flowering plants compared with animals, with each seed being the product of two fertilization events (Fig. 1b). In this process, one fertilization event forms the endosperm, a tissue that is functionally similar to the mammalian placenta, and which contains two sets of maternal chromosomes and one set of paternal chromosomes. A second fertilization event results in the formation of the embryo. It is noteworthy that, although Nodine and Bartel show that the embryo experiences equal transcriptome contributions from both parental genomes, gene expression in the embryo-nourishing endosperm shows extensive parental influence[9]; these effects are due to uneven nuclear 'dosage' as well as to epigenetic imprinting effects.

Another question is how the early plant embryo coordinates rapid integration of two genomes and the concomitant activation of a resulting zygotic genome. In animals, a suite of mechanisms acts to clear maternal factors, such as proteins and RNAs, from the developing zygote and to activate the zygotic genome[1,10]. It is unclear whether similar mechanisms operate in plants. Tantalizingly, epigenetic processes such as DNA methylation and demethylation, as well as regulatory small RNA molecules, have recently been implicated[9] in the control of both gamete and endosperm development. Future studies of these pathways may reveal mechanisms for the regulation of gene expression in embryonic plants.

Understanding how a functional plant genome so quickly emerges from two progenitor genomes is vital for understanding plant development, and for informing approaches to plant breeding and plant biotechnology. In many crop species, combining two different parental genomes can generate regular and predictable hybrid vigour, known as heterosis. In some species this vigour is obvious very early in development[11]. Consistent with these observations, Nodine and Bartel's work[3] suggests that

50 Years Ago

In a Cantor Lecture … Dr. Tom A. Margerison described how science could be presented on television not only to the specialist audience but especially to the layman. In spite of the absolute necessity of science and technology, the 10–15 per cent of the population who guide the destiny of Britain, the professional men, the majority of teachers, the industrialists, the politicians, are almost completely ignorant about science. The bridging of this gap in this most influential part of the population is of great urgency. There are many ways in which television can help to close the gap.
From *Nature* 3 February 1962

100 Years Ago

Mr. Harding's letter … reminds me of an experience which … may be of sufficient interest to place upon record in these columns … It must, I think, have been in 1866 or 1867 … that I had occasion to go from the West to the East End of London. Starting upon my journey about 10 p.m., it began to rain soon after I left the house in Bayswater, and I opened an umbrella, which, to my surprise, became stiffer and heavier every moment, and was found on examination to be so thickly glazed over with ice that it was impossible to close it. At the same time the pavements and roadway were also becoming uniformly glazed; pedestrian movement was most difficult, and all horse traffic was suspended. Although an experience of some forty-five years ago, the impression left upon my memory is still vivid — the ludicrous sight of people carrying ponderous and rigidly frozen umbrellas which they could not close, the stream of skaters down Oxford Street and Holborn, and the silence due to the absence of vehicles, all came to mind on reading Mr. Harding's letter.
From *Nature* 1 February 1912

zygotic-genome dynamics in plants, including, perhaps, some aspects of heterosis, are established almost immediately after fertilization. ■

Christopher J. Hale *is in the Department of Molecular, Cell and Developmental Biology, and* **Steven E. Jacobsen** *is at the Howard Hughes Medical Institute, University of California, Los Angeles, Los Angeles, California 90095, USA.*
e-mails: cjhale@ucla.edu; jacobsen@ucla.edu

1. Tadros, W. & Lipshitz, H. D. *Development* **136,** 3033–3042 (2009).
2. Autran, D. *et al. Cell* **145,** 707–719 (2011).
3. Nodine, M. D. & Bartel, D. P. *Nature* **482,** 94–97 (2012).
4. Cao, J. *et al. Nature Genet.* **43,** 956–963 (2011).
5. Vielle-Calzada, J.-P., Baskar, R. & Grossniklaus, U. *Nature* **404,** 91–94 (2000).
6. Grosberg, R. K. & Strathmann, R. R. *Annu. Rev. Ecol. Evol. Syst.* **38,** 621–654 (2007).
7. Sundaresan, V. & Alandete-Saez, M. *Development* **137,** 179–189 (2010).
8. Twell, D. *Sex. Plant Reprod.* **24,** 149–160 (2011).
9. Feng, S., Jacobsen, S. E. & Reik, W. *Science* **330,** 622–627 (2010).
10. Walser, C. B. & Lipshitz, H. D. *Curr. Opin. Genet. Dev.* **21,** 431–443 (2011).
11. Meyer, S., Pospisil, H. & Scholten, S. *Plant Mol. Biol.* **63,** 381–391 (2007).

MOLECULAR MOTORS

A staggering giant

The protein dynein 'walks' along filaments to transport various cargoes within the cell. Two studies reveal that, unlike other motor proteins, dynein's steps are not strictly coordinated.

WILHELM J. WALTER & STEFAN DIEZ

When you are walking down the street your feet probably take alternating steps, with one foot passing the other each time. Alternatively, you might walk without letting your feet pass one other, in a limping motion. However, regardless of the stepping pattern, your walking will be highly coordinated. At the molecular scale, the motor protein dynein also 'walks' along filaments to carry vesicles and organelles to specific locations within a cell. But is coordination between dynein's two 'feet' required for walking? Two papers — one by DeWitt *et al.*[1] in *Science* and another by Qiu *et al.*[2] in *Nature Structural & Molecular Biology* — independently address this question and come to the surprising conclusion that dynein uses both random and coordinated walking.

Cytoplasmic dynein is a giant, multi-subunit protein that uses the chemical energy stored in the molecule ATP to transport cargoes[3]. It moves along microtubules — long polymeric tubes composed of dimers of the protein tubulin, typically arranged to form 13 parallel tracks. Dynein has two 'head' domains linked by their respective 'tails', whereby the heads act as 'feet' for walking along the microtubules. Each head contains four binding pockets for ATP and a microtubule-binding site. Of the four ATP-binding pockets, one catalyses ATP hydrolysis to generate energy for walking; the other three are thought to be important for the regulation of dynein activity[4].

Previous work[5,6] using single dynein motors bound to beads revealed that during processive motility on microtubules — the process by which a motor takes multiple steps without dissociating from the microtubule — dynein moves by 8-nanometre steps. This distance corresponds to the periodicity of the dimeric tubulin subunits along the microtubule tracks. However, little is known about the coordination of the two dynein heads during motion.

To make the dynein heads visible and study the stepping mechanism during processive motion, DeWitt *et al.*[1] and Qiu *et al.*[2] attached fluorescent markers to the dynein heads and used fluorescence microscopy. Moreover, to distinguish between the movement of the two individual heads, both groups used markers that emitted fluorescence of a different colour for each head, a method previously applied[7,8] to another motor protein, myosin V.

To facilitate the two-colour labelling, both groups generated dynein molecules in which the two subunits had been artificially linked to each other. DeWitt *et al.* attached different fluorescent quantum dots (semiconductor nanocrystals) to modified dynein heads that dimerized in the presence of the small molecule rapamycin. By contrast, Qiu *et al.* attached complementary DNA strands and different fluorescent organic molecules (less stable but smaller than quantum dots) to dynein heads, so that the DNA molecules self-associated to link both heads together. To observe the stepping mechanism, both groups[1,2] slowed dynein's movement by using an ATP concentration that was much lower than that normally found in the cell's cytoplasm. From computerized image analysis, they were able to track the positions of individual dynein heads in two dimensions with an accuracy of about 3 nm.

The primary finding of both studies is that dynein has a highly variable stepping pattern (Fig. 1). For most steps, the heads moved alternately, but they passed each other only infrequently. After each step, the head-to-head distance varied widely, from less than 5 nm to 50 nm, which is indicative of uncoordinated stepping. By contrast, other motor proteins such as kinesin-1 show strictly coordinated stepping. In kinesin-1, only the lagging head can bind ATP, because of a mechanism that relies on the strain between the two heads. This mechanical coupling forces the heads to step in a strictly alternating pattern, because the hydrolysis of the ATP molecule causes the lagging head to make the next step[9].

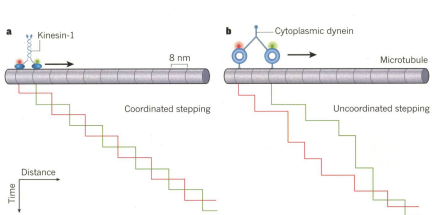

Figure 1 | Stepping patterns in motor proteins. a, Some motor proteins, such as kinesin-1, move in a highly coordinated way along microtubules (polymeric protein tubes; grey). The traces show the stepping of individual motor heads (each labelled with a different fluorescent marker, red or green). **b,** DeWitt *et al.*[1] and Qiu *et al.*[2] show that, by contrast, cytoplasmic dynein moves in a variable stepping pattern. Although the heads often move alternately, they only seldom pass each other, and the spacing between them varies strongly over time.

Interestingly, the current studies[1,2] show that the degree of coordination in dynein stepping depends on the head-to-head distance: the stepping pattern is random when the distance is small, but becomes coordinated when the distance is large. This implies a tension-based coordination mechanism similar to the mechanical coupling seen in kinesin-1, but less pronounced.

To further test for the necessity of coordination to dynein motility, DeWitt *et al.*[1] generated a dynein motor in which one of the two heads could not hydrolyse ATP. This head associated only weakly with the microtubule track, probably because transition to a strong binding state requires ATP hydrolysis. This motor moved reliably along microtubules, however, suggesting that coordination is not required for long-range transport.

The high accuracy with which both groups[1,2] managed to track dynein's motion on the surface of microtubules allowed them to make yet another discovery: the two heads exhibit an inherent left–right asymmetry, with the right head more likely to be in the lead. Thus, dynein can be described as staggering sideways along the microtubule.

In light of the two papers' unexpected findings, several exciting questions and ideas for follow-up experiments arise. First, the observed effect of the suggested tension-based mechanism for head coordination is rather small; however, because both groups used modified dyneins, the effect might be more pronounced in normal dynein. It is known[10] that slight modifications to the tail domains, which help to link dynein's two subunits, affect the protein's stepping pattern. Full coordination might thus rely on full-length tail domains and additional subunits, both of which are present in wild-type dynein but lacking in the artificially linked constructs analysed here.

Second, the regulatory ATP-binding sites should not be neglected. It is possible that the disordered stepping patterns observed by the authors are the result of limited ATP binding to the regulatory ATP-binding sites, because all experiments were performed at low concentrations of ATP.

And, third, the highly variable step sizes of the dynein heads — smaller than 16 nm on average — suggest that the centre of mass of the motor dimers tends to move less than 8 nm per step. But it is not clear how this can be reconciled with the aforementioned results of previous studies[3–6] of similar dynein constructs, which were found to take 8-nm steps.

Further development of optical technologies — towards even faster image-acquisition rates at tracking accuracies similar to the outstanding ones presented by DeWitt *et al.*[1] and Qiu *et al.*[2] — will, step by step, allow for fascinating insight into the functioning of dynein and other molecular motors under physiological conditions. Knowledge about the flexibility in the stepping behaviours of various motors might allow us to explain their astonishing ability to move along crowded microtubules in a dense cytoplasmic environment. ■

Wilhelm J. Walter and **Stefan Diez** *are at the B CUBE — Center for Molecular Bioengineering, Technische Universität Dresden and at the Max Planck Institute of Molecular Cell Biology and Genetics, Dresden, Germany.*
e-mails: walter@bcube-dresden.de; diez@bcube-dresden.de

1. DeWitt, M. A., Chang, A. Y., Combs, P. A. & Yildiz, A. *Science* **335,** 221–225 (2012).
2. Qiu, W. *et al. Nature Struct. Mol. Biol.* http://dx.doi.org/10.1038/nsmb.2205 (2012).
3. Vallee, R. B., Williams, J. C., Varma, D. & Barnhart, L. E. *J. Neurobiol.* **58,** 189–200 (2004).
4. Sakakibara, H. & Oiwa, K. *FEBS J.* **278,** 2964–2979 (2011).
5. Toba, S., Watanabe T. M., Yamaguchi-Okimoto, L., Toyoshima, Y. Y. & Higuchi, H. *Proc. Natl Acad. Sci. USA* **103,** 5741–5745 (2006).
6. Gennerich, A., Carter, A. P., Reck-Peterson, S. L. & Vale, R. D. *Cell* **131,** 952–965 (2007).
7. Warshaw, D. M. *et al. Biophys. J.* **88,** L30–L32 (2005).
8. Churchman, L. S., Ökten, Z., Rock, R. S., Dawson, J. F. & Spudich, J. A. *Proc. Natl Acad. Sci. USA* **102,** 1419–1423 (2005).
9. Rosenfeld, S. S., Fordyce, P. M., Jefferson, G. M., King, P. H. & Block, S. M. *J. Biol. Chem.* **278,** 18550–18556 (2003).
10. Ori-McKenney, K. M., Xu, J., Gross, S. P. & Vallee, R. B. *Nature Cell Biol.* **12,** 1228–1234 (2010).

PRECISION MEASUREMENT

A comb in the extreme ultraviolet

A 'comb' of photons at evenly spaced frequencies in the extreme ultraviolet has been generated. It will allow a more precise search for variation in the fine-structure constant, which sets the strength of the electromagnetic force. SEE LETTER P.68

LINDA YOUNG

That improved measurement precision yields new physics is axiomatic. In the case of optical spectroscopy, the quest for ultimate precision was revolutionized around the turn of the century by the realization of the optical frequency comb[1–3]. This elegant invention, which was honoured by the 2005 Nobel Prize in Physics[4,5], provides a direct link between radio and optical frequencies, allowing one to count cycles of an electromagnetic field at near-petahertz frequencies (1 petahertz is 10^{15} Hz). On page 68 of this issue, Cingöz *et al.*[6] extend the frequency range of combs to the extreme-ultraviolet spectral regime.

An optical frequency comb is produced by a mode-locked ultra-fast laser in which a light pulse of sub-picosecond duration (1 picosecond is 10^{-12} s) circulates inside an optical cavity made up of a set of highly reflective mirrors. The laser emits an infinite train of pulses at a certain repetition rate (f_{rep}) that is determined by the time the pulses take to make a round trip of the cavity's mirrors[7,8]. This train of pulses has two distinguishing properties: the pulses are equally spaced in time, and the phase (where a wave's peaks and troughs lie) of the electromagnetic field in each pulse is precisely shifted from that in the subsequent pulse (the locked-phase relationship). The train produces a comb of sharp spectral lines uniformly spaced in frequency.

The frequencies of the comb teeth are defined by a simple formula: $f_n = nf_{rep} + f_o$, where f_{rep} and f_o are radio frequencies, f_n is optical frequency and n is an integer of the order of 10^6–10^7 (Fig. 1). With one comb tooth, f_o, referenced to an absolute standard such as the frequency of a caesium atomic clock, the absolute frequency of an unknown optical laser may be counted as a beat note relative to another comb tooth with an accuracy at the level of one part in 10^{14}. This greatly exceeds the accuracy achievable using conventional wavelength-based measurements, which are limited by wavefront distortion to an accuracy at the 10^{-10} level.

A prominent early example of the application of the frequency comb was the measurement[3] of a two-photon transition in hydrogen to an accuracy of more than 2×10^{-14}. This measurement, combined with one performed about four years later[9], placed a limit on the variability of the fine-structure constant — a fundamental constant that characterizes the strength of the electromagnetic interaction and whose variation in time informs the standard model of particle physics. Beyond precision spectroscopy, the optical frequency comb has fostered a multitude of applications, including a clock based on optical frequencies, massively parallel multi-wavelength spectroscopy of unknown chemicals, and long-distance transmission of ultra-stable clock signals, which are useful for next-generation telescope arrays or accelerator systems.

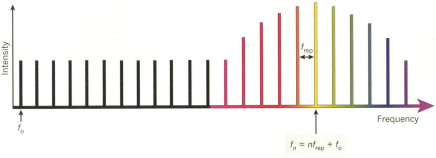

Figure 1 | Frequency comb. The intensity spectrum of a frequency comb consists of an array of sharp lines uniformly spaced in frequency by f_{rep}. The frequencies of the lines, f_n, are determined by a simple relationship, $f_n = nf_{rep} + f_o$, where f_o is an offset frequency and n is an integer. Cingöz *et al.*[6] demonstrate a frequency comb in the extreme-ultraviolet frequency range.

A question that naturally arises is whether frequency-comb technology can be extended to wavelengths shorter than those of the optical spectral range: to the ultraviolet or even the X-ray regime. A route to generating short-wavelength frequency combs that is directly linked to optical frequencies was pioneered by the ultra-fast-laser community, namely by researchers who study high-harmonic generation (HHG). HHG is the process of generating light of frequencies that are multiples (high harmonics) of a fundamental frequency, and is achieved by focusing intense optical pulses into a gaseous target.

In the case of a single atom, HHG involves three steps: ionization of the atom by a laser field; propagation of the resulting electron in the laser field; and recombination of the electron with the parent ion in a process that is accompanied by the emission of high-harmonic light. Although this model captures most of the underlying physics, a complete picture requires an understanding of how waves propagate through partially ionized media[10]. Because the laser intensity required for this extreme nonlinear process to occur is high (more than 10^{13} watts per square centimetre), amplified femtosecond lasers at low repetition rates (10 Hz to 100 kHz) with 10^{-3}-joules per pulse are typically used. The 10^{-8}-joule pulses of a typical 100-MHz optical frequency comb are simply not powerful enough for HHG.

In 2005, researchers reported[11,12] that the requisite intensity for HHG could be obtained by adding pulses from an optical frequency comb using an 'enhancement' or 'power build-up' cavity, in which successive pulses add constructively because the phases of the pulses' electromagnetic waves are locked. In such a cavity, the pulse energy can be multiplied nearly 1,000-fold. In addition, it is essential for the HHG process to retain the locked-phase relationship over many consecutive pulses to preserve the underlying comb structure (about 10^5 teeth spaced by f_{rep} for each harmonic) and effectively make the resulting HHG a shorter-wavelength comb. In these two early experiments[11,12], the frequency comb originating from a mode-locked titanium–sapphire laser (with a power of 1 W, repetition rate of about 100 MHz and pulses of roughly 50 fs) was fed into an enhancement cavity containing a jet of xenon gas located at an intracavity focus to produce HHG, in one case[11] up to the 15th harmonic.

However, simply detecting HHG radiation is not sufficient to verify that comb structure exists. Therefore, both groups[11,12] mixed third-harmonic radiation at a wavelength of 266 nm with an independently derived reference signal to observe beat signals that have a spectral linewidth of a few hertz, much less than the roughly 10^{12} Hz expected from the uncertainty principle for 50-fs pulses. These demonstrations were a solid first step towards realizing extreme-ultraviolet combs. But the extracted power per comb tooth was insufficient for applications such as precision spectroscopy, and comb structure was verified up to only the third harmonic.

In their study, Cingöz *et al.*[6] lift these barriers to a more widespread application of extreme-ultraviolet-frequency combs. In contrast to the early demonstrations, the authors show comb structure out to the 13th harmonic (82 nm), and with enough power (200 μW per harmonic) for applications. They achieved these results by using the highest-power near-infrared frequency comb, which is based on an 80-W, 120-fs ytterbium-fibre laser[13] coupled into an enhancement cavity of novel design. The design strategy was informed by a better understanding of the intracavity HHG process[14]. Nonlinearities in the HHG process at the intracavity focus clamp the peak power of the circulating pulses and lead to instabilities that make the constructive addition of the pulses difficult[15]. Cingöz *et al.* used an enhancement cavity that is more robust but loses more power. In this cavity, pulses are amplified only 200-fold, compared with the original 600-fold used by the same group[12].

Cingöz and colleagues went on to perform single-photon spectroscopy of an argon transition using an individual comb tooth (with a linewidth of 11 MHz) with an unprecedentedly high accuracy for the extreme-ultraviolet spectral region. They repeated this measurement as a function of f_{rep}, unambiguously establishing the comb structure at the 13th harmonic. However, single-photon spectroscopy is limited to probing narrow, well-isolated absorption lines; here it was performed with a single comb tooth containing about 10 pW of power. Notably, spectroscopy of two-photon transitions with a frequency comb can use a much larger fraction of the total comb power because pairs of comb teeth whose frequencies sum to the transition frequency also drive the transition.

The authors' demonstration of an extreme-ultraviolet frequency comb, which allows robust linkage between the radio and extreme-ultraviolet spectral regions, ushers in an era of precision metrology in the extreme ultraviolet. A recognized application of their extreme-ultraviolet comb is the aforementioned search for variability in the fine-structure constant: transitions in highly charged ions that have energy in the extreme ultraviolet range are calculated[16] to have higher sensitivity to variations in the fine-structure constant than do optical transitions. As powerful extreme-ultraviolet frequency combs[6,17] are developed that enable a higher precision than that achieved by the optical frequency comb, it will be exciting to see what other applications might emerge. ■

Linda Young *is in the X-ray Science Division, Argonne National Laboratory, Argonne, Illinois 60439, USA.*
e-mail: young@anl.gov

1. Reichert, J. *et al. Phys. Rev. Lett.* **84,** 3232–3235 (2000).
2. Jones, D. J. *et al. Science* **288,** 635–639 (2000).
3. Diddams, S. A. *et al. Phys. Rev. Lett.* **84,** 5102–5105 (2000).
4. Hall, J. L. *Rev. Mod. Phys.* **78,** 1279–1295 (2006).
5. Hänsch, T. W. *Rev. Mod. Phys.* **78,** 1297–1309 (2006).
6. Cingöz, A. *et al. Nature* **482,** 68–71 (2012).
7. Udem, Th., Holzwarth, R. & Hänsch, T. W. *Nature* **416,** 233–237 (2002).
8. Cundiff, S. T. & Ye, J. *Rev. Mod. Phys.* **75,** 325–342 (2003).
9. Fischer, M. *et al. Phys. Rev. Lett.* **92,** 230802 (2004).
10. Brabec, T. & Krausz, F. *Rev. Mod. Phys.* **72,** 545–591 (2000).
11. Gohle, C. *et al. Nature* **436,** 234–237 (2005).
12. Jones, R. J., Moll, K. D., Thorpe, M. J. & Ye, J. *Phys. Rev. Lett.* **94,** 193201 (2005).
13. Ruehl, A., Marcinkevicius, A., Fermann, M. E. & Hartl, I. *Opt. Lett.* **35,** 3015–3017 (2010).
14. Allison, T. K., Cingöz, A., Yost, D. C. & Ye, J. *Phys. Rev. Lett.* **107,** 183903 (2011).
15. Yost, D. C *et al. Opt. Exp.* **19,** 23483–23493 (2011).
16. Berengut, J. C., Dzuba V. A., Flambaum V. V. & Ong, A. *Phys. Rev. Lett.* **106,** 210802 (2011).
17. Lee, J., Carlson, D. R. & Jones, R. J. *Opt. Exp.* **19,** 23315–23326 (2011).

ARTICLE

doi:10.1038/nature10776

Conditional modulation of spike-timing-dependent plasticity for olfactory learning

Stijn Cassenaer[1,2] & Gilles Laurent[1,3]

Mushroom bodies are a well-known site for associative learning in insects. Yet the precise mechanisms that underlie plasticity there and ensure their specificity remain elusive. In locusts, the synapses between the intrinsic mushroom body neurons and their postsynaptic targets obey a Hebbian spike-timing-dependent plasticity (STDP) rule. Although this property homeostatically regulates the timing of mushroom body output, its potential role in associative learning is unknown. Here we show *in vivo* that pre–post pairing causing STDP can, when followed by the local delivery of a reinforcement-mediating neuromodulator, specify the synapses that will undergo an associative change. At these synapses, and there only, the change is a transformation of the STDP rule itself. These results illustrate the multiple actions of STDP, including a role in associative learning, despite potential temporal dissociation between the pairings that specify synaptic modification and the delivery of reinforcement-mediating neuromodulator signals.

Behavioural and genetic experiments in *Drosophila* and honeybees have revealed that the mushroom body, a brain area containing up to hundreds of thousands of neurons called Kenyon cells, is critical for associative learning of odours[1–11] but not for the expression of innate odour-driven behaviours[5] (Fig. 1a). Recent electrophysiological experiments in locusts and other insects show that the responses of Kenyon cells to odours are highly selective and, thus, rare[12–14]. By contrast, antennal lobe neurons, the source of the olfactory input to Kenyon cells, are few and promiscuous[12]. Odour codes are thus 'compact' in the antennal lobe—that is, the representation of each odour engages many neurons in a small population—but 'sparse' in the mushroom bodies (Fig. 1a). Although sparse codes require larger neuron populations, they are beneficial for memory because they can reduce interference between memory traces[12,15,16]. Kenyon cells project to two regions, called α- and β-lobes, where they synapse onto small populations of 'extrinsic' neurons. In locusts, the synapses between Kenyon cells and β-lobe neurons (bLNs) are modifiable by a Hebbian STDP rule[17–19] (Fig. 1a), but nothing so far implicates STDP in associative learning there; rather, STDP causes the homeostatic regulation of bLN spike timing[17]. Recent experimental results in moths[14] show that Kenyon cell responses to odours recorded during behavioural learning generally occur and end well before reward delivery, indicating that STDP alone cannot support associative conditioning[20,21]. Neuromodulation has been proposed recently as a potential solution[22,23]. We address this issue with *in vivo* electrophysiology in locusts and discover a complex interplay between STDP, reinforcer signals and odour codes in mushroom bodies.

Dense odour representations in β-lobes

We first examine odour representations in the β-lobes. Using intradendritic recordings, we sampled the responses of 55 bLNs to up to 16 odours (Methods and Fig. 1b). Each bLN responded to nearly every odour, with responses that differed in intensity, patterning, delay and duration across neuron–odour pairs. The probability that a given bLN responded to an odour was 0.97. On average, a bLN fired action potentials in approximately half of the local field potential (LFP) oscillation cycles during the odour presentation (0.502 ± 0.219, $n = 126$ neuron–odour pairs, 25 LFP cycles per response): on average, half of the population was active in any given cycle. Hence, these representations resemble those in the antennal lobes[12] (and exceed them in promiscuity) rather than the sparse representations by Kenyon cells, to which bLNs are directly connected.

We tested whether the broad tuning of bLNs might be explained by known features of mushroom body circuits. We implemented a simple model (Methods and ref. 17) constrained by Kenyon cell response statistics and timing[12], by the properties of STDP at Kenyon cell synapses[17] and by Kenyon cell/bLN (KC–bLN) connectivity ratios estimated from experiments[17]. With such a model, we could reproduce the bLN firing phase observed experimentally[17] (Fig. 2a, left) but not the odour-response intensity or probability (Fig. 2a, right, and Supplementary Fig. 1.1a). Rather, activity across the model bLN (mbLN) population saturated rapidly when STDP was turned on. This behaviour is a known property of rate-based Hebbian learning in model networks and can be counteracted by imposing synaptic weight bounds or renormalization rules[24].

Inhibition limits STDP and saturation

In examining our experimental data on bLN responses to odours, we observed that the periodic excitatory input originating from Kenyon cells was often curtailed by phasic inhibitory postsynaptic potentials (Fig. 2b, arrowheads), with onsets at the typical phase of bLN action potentials. We hypothesized that these inhibitory postsynaptic potentials originate from lateral inhibition among bLNs (as put forward in a theoretical exploration[25]). This was supported by extracellular stimulation of Kenyon cells (Supplementary Fig. 2) and confirmed in paired bLN recordings. Beta-lobe neurons inhibit each other (Fig. 2c) with an estimated connection probability of 28% ($n = 32$ connections, 2 reciprocally connected pairs). Although unknown so far, other interneuron populations may also contribute to bLN inhibition.

In each oscillation cycle, lateral inhibition reduces the likelihood of late bLN spikes; thus, it should limit the ability of STDP to potentiate KC–bLN synapses. This in turn should curb bLN population activity (see also ref. 26). As predicted, implementing lateral inhibition

[1]Division of Biology, California Institute of Technology, Pasadena, California 91125, USA. [2]Broad Fellows Program in Brain Circuitry, California Institute of Technology, Pasadena, California 91125, USA. [3]Max Planck Institute for Brain Research, 60528 Frankfurt am Main, Germany.

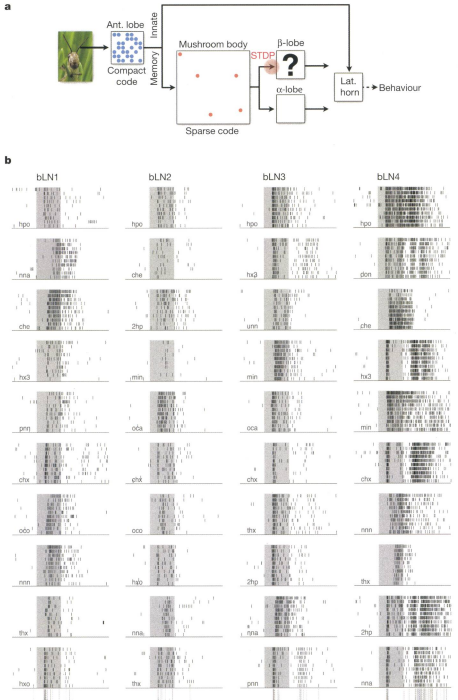

Figure 1 | Beta-lobe neurons are promiscuous. a, Olfactory circuit in which bLNs are embedded. Ant., antennal; lat., lateral. **b**, Rasters constructed from *in vivo* intracellular dendritic recordings, illustrating responses of four bLNs (different animals) to ten odours. Shaded region represents odour delivery (1 s). For each bLN, intracellular traces at bottom correspond to the tenth trial with the last odour. Horizontal scale bars, 500 ms; vertical scale bars, 10 mV; spikes are clipped. Odours: 2-heptanone (2hp), cherry (che), *cis*-3-hexen-1-ol (chx), 3,7-dimethyl-2,6-octadiene-nitrile (don), 1-heptanol (hpo), 1-hexen-3-ol (hx3), 1-hexanol (hxo), mint (min), nonanal (nna), 5-nonanone (nnn), octanal (oca), 1-octanol (oco), 3-pentanone (pnn), *trans*-2-hexen-1-ol (thx), 6-undecanone (unn).

between mbLNs (based on the experimental connectivity estimate and amplitude distribution) reduced population activity to ~50% ($p_{response} = 0.51 \pm 0.14$ (response probability), $n = 30$ mbLNs; compare with $p_{response} = 0.49 \pm 0.18$, $n = 30$ bLNs from experiment; Fig. 2d–f). The mbLN spike phase remained centred on π (LFP trough). In addition, the response profiles of those mbLNs were very similar to those recorded experimentally (compare distributions in Fig. 2e, f and moments in Fig. 2g; see also Supplementary Figs 3–5).

We conclude that bLN activity, although very different from the sparse output of Kenyon cells, can be explained by the combined effects of Hebbian STDP at KC–bLN synapses and lateral inhibition between bLNs. The useful consequences are that bLN spikes are tightly phase-locked to the LFP[17] and that instantaneous bLN population activity lies around the midpoint of its dynamic range. This increases the coding capacity of this small population of output neurons and is relevant for plasticity, as explored below.

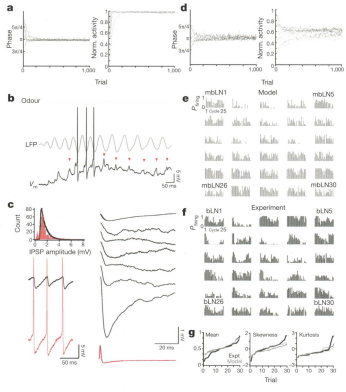

Figure 2 | Saturation of activity caused by STDP can be counteracted by lateral inhibition. **a**, Mean firing phase (left) and normalized population activity (right) in a simulation of a KC–bLN network (30 Izhikevich units[44], one LFP cycle, 1,000 trials). Each point is a ten-trial average; STDP is turned on in trial 11. Each curve is run with n Kenyon cell inputs per mbLN ($20 < n < 80$, 10% connections in common). STDP regulates bLN firing phase (ref. 17) but inexorably drives bLN population to saturation. **b**, *In vivo* intradendritic recording of bLN membrane potential, V_m, together with LFP during odour presentation. Arrowheads indicate onsets of inhibitory postsynaptic potentials, timed on LFP troughs. **c**, Top left: frequency distribution of inhibitory postsynaptic potential amplitudes, measured at baseline, in 30 bLNs; black curve, fit used for model in **d**. IPSP, inhibitory postsynaptic potential. Bottom left: paired bLN recording revealing direct inhibitory connection. Right: bLN spike-triggered averages from seven distinct bLN pairs. **d**, Simulation of a bLN network as in **a**, except with n Kenyon cell inputs per bLN (here $22 < n < 130$, same drive at simulation onset as in **a**). Lateral inhibition among bLNs is as determined experimentally. Mean phase (left) is minimally affected; network activity (right) settles near midrange. **e**, Simulation of a bLN network as in **d**, extended over 25 LFP cycles, with time-varying Kenyon cell input profiles derived from experiments[12,17,45]. Post-stimulus time histograms plotted as firing probability versus cycle rank for each of the 30 mbLNs (ten trials), post STDP. **f**, *In vivo* intradendritic responses of 30 bLNs to *trans*-2-hexen-1-ol represented as in **e** (from 16 different animals). **g**, Comparison of experimental (black) and model (grey) bLN response statistics. Same simulation as in **e** (darkest grey) together with two other simulations of the same network with different Kenyon cell input profiles (lighter shades of grey).

Conditional modulation of STDP rule

Mushroom bodies are critical for associative conditioning in insects[6–11,27], and second-messenger pathways involved in memorization and retrieval have been described in *Drosophila*[1,4–7,28,29]. Yet we know little about the synaptic mechanisms underlying conditioning there[30], and even less about how specificity is achieved or about the roles that STDP might have in it. Associative learning in insects seems to rely on neuromodulators[31–35] (for example octopamine (OCT) and dopamine) to mediate unconditioned signals (appetitive and aversive, respectively, for OCT and dopamine). In locusts and other insects, these neuromodulators are delivered nonspecifically by small numbers of octopaminergic[36] and dopaminergic[37] neurons with projections to the mushroom body lobes (among others), that is, where Kenyon cells contact bLNs.

We assessed the effect of local OCT injection into the β-lobes on plasticity and tuning of those bLNs *in vivo* (Fig. 3). Figure 3d illustrates our experimental schemes, which were designed to probe specificity, that is, the question of how the system determines which synapses should change when the reinforcer is global. During an odour stimulus, two features distinguish odour-evoked Kenyon cell spikes from 'stray' spikes produced randomly by non-responding Kenyon cells (most of the Kenyon cells): odour-evoked spikes are synchronized and cause bLNs to spike by their collective action. Hence, odour-evoked release at Kenyon cell synapses occurs within the time window for STDP. We thus tested the effect of OCT injection on synapses that differed only in their temporal features of pre- and postsynaptic activation. In each experiment, we measured the responses of one bLN to Kenyon cell stimulation at a rate of $0.1\ s^{-1}$ at two locations (a pairing location (P) and a control location (C)) and two different times (C 300 ms before P). We found Kenyon cell stimulation sites that converged onto the same recorded bLN in 13 out of 20 experiments.

In 'test' trials (Fig. 3d, top), the bLN was depolarized by a brief pulse of current to produce one single action potential 5 s after Kenyon cell stimulation at P, hence well outside the window of $\delta t = t_{post} - t_{pre} = \pm 25$ ms required for STDP[17], where t_{post} and t_{pre} are respectively the post- and presynaptic spike times. Pairing consisted of five trials at $0.1\ s^{-1}$, of either of two kinds. In 'STDP' trials, the bLN was fired within ±25 ms of a Kenyon cell stimulus at P (Fig. 3d, middle). In 'STDP + OCT' trials, pairing was as in STDP trials but was followed by one OCT injection (5 pl) 1 s after pairing (Fig. 3d, bottom). Test trials were carried out before STDP trials (Fig. 3a–c, red), after STDP trials (black) and after STDP + OCT trials (blue). All test and pairing trials thus contained the same numbers of pre- and postsynaptic pulses; only their relative timings differed. Examples with three values of δt are shown (Fig. 3a–c). In each, OCT caused a depression. We note that only connections between cells co-activated within the STDP window were depressed (that is, P but not C; see also Supplementary Fig. 6). The depressive action of OCT on synapses undergoing STDP (20 different values of δt; Fig. 3e, f and Supplementary Fig. 7) was greatest for $\delta t > 0$, converting baseline Hebbian STDP into one where only depression occurred.

To rule out the possibility that the action of OCT resulted not from the pairing *per se*, but from the temporal proximity of OCT delivery to the pairing (P), we reversed the order of C and P ($n = 3$; Supplementary Fig. 8). Again, only the P pathway was affected by OCT (effect of OCT on control (mean ± s.e.m.): $-0.9 \pm 0.49\%$, $n = 3$ (P then C); $0.2 \pm 2.28\%$, $n = 10$ (C then P); sets statistically equivalent: $P > 0.66$, t-test). Hence, because the control and paired synapses shared the same postsynaptic partner (C and P differed only in the identity of the presynaptic cells and in the timings of the presynaptic spikes relative to those in their common bLN), and because the two sets of presynaptic cells were stimulated within only 300 ms of one another (C then P or P then C), we conclude that the relative timing of pre- and postsynaptic firing is what contributes to making the synapses susceptible to OCT action. We do not know whether pre–post delays longer than ±25 ms (but shorter than 300 ms) would have equivalent effects. However, almost all odour-evoked Kenyon cell action potentials occur within the range of delays we tested. We conclude that, despite its global release, OCT affects specific synapses—those in which pre- and postsynaptic partners fired within the appropriate delay between one another. This is the case even though OCT was delivered 1 s after the relevant pairing (reproducing a temporal dissociation between conditioned stimulus and unconditioned stimulus[14]).

Conditional changes of STDP are specific

The STDP curves in Fig. 3f were obtained *in vivo* with electrical activation of the pre- and postsynaptic cells. We next tested the effect of OCT on the responses of bLNs to odours. We predicted that if OCT depresses KC–bLN synapses that fire within the STDP time window,

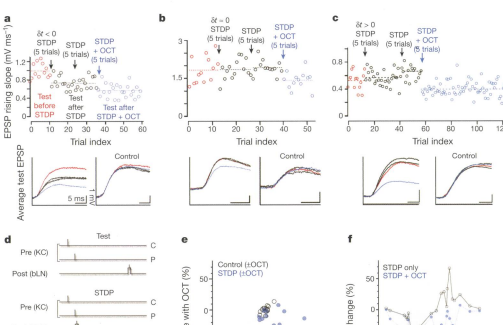

Figure 3 | OCT changes the STDP rule. a, Five trials pairing OCT with depressing STDP ($\delta t < 0$) reduced KC–bLN excitatory postsynaptic potential (EPSP) size (blue) more than did two sets of five-trial STDP with negative δt alone (black). EPSPs evoked by interleaved stimulation with the control electrode (embedded among Kenyon cells in a different location) were unaffected (control, bottom right), despite equal exposure to OCT. **b**, Five trials pairing OCT with $\delta t \approx 0$ STDP reduced KC–bLN EPSP size (blue), whereas STDP alone with this δt value had no effect (black). Control EPSPs were unaffected (bottom right). **c**, Five trials pairing OCT with potentiating STDP ($\delta t > 0$) reduced KC–bLN EPSP size after it was potentiated by two bouts of STDP alone with this δt value. Control EPSPs were unaffected (bottom right). **d**, Stimulation protocols. Test trials were used to evaluate the amplitudes of KC–bLN EPSPs before STDP, after STDP and after STDP + OCT, as shown in **a**–**c**, and to compute (from multiple experiments) values in **e** and **f**. C, control Kenyon cell input; P, paired Kenyon cell input. In test trials, bLNs were depolarized with a 5-ms d.c. pulse (causing a single bLN spike) ~5 s after extracellular stimulation (0.1-ms pulses) of Kenyon cells in two different locations (C and P, 300 ms apart). In STDP trials, bLNs were depolarized as above, causing a single spike in a narrow window around the time of Kenyon cell stimulation (P). Control Kenyon cell stimulation (C) was offset by 300 ms. STDP + OCT trials were the same as STDP trials, only with the addition of localized OCT injection (50-ms pressure-pulse) in the β-lobe, 1 s after P Kenyon cell stimulation. **e**, Summary data from 20 experiments, plotting for each experiment the effect of STDP + OCT versus STDP alone (blue dots) and plotting control data, with and without OCT, for 13 of 20 experiments (black circles). Changes due to STDP + OCT differ significantly from control + OCT ($P < 0.003$, t-test). Changes due to OCT in control not significantly different from zero ($P > 0.84$, t-test; see also Supplementary Fig. 7). **f**, Comparison between change due to STDP + OCT and change due to STDP alone, each plotted as a function of δt. Changes due to STDP + OCT differ significantly from zero (relative to before STDP: $P < 0.0001$; relative to STDP only: $P < 0.0002$, t-test; see also Supplementary Fig. 7).

it should also reduce bLN output. This was tested first with our model, using an STDP rule modified according to Fig. 3f: responses were reduced in 28 of 30 mbLNs (Fig. 4a, b). We then tested the prediction experimentally with 12 bLNs (18 bLN–odour pairs), each recorded intracellularly from a dendrite. In 16 of 18 instances, OCT caused a reduction of bLN output, averaged over the odour response (Fig. 4c, d). LFP power in the mushroom body calyx was unaffected (Fig. 4f), consistent with unchanged input to the mushroom body.

We also evaluated the specificity of changes in bLN–odour responses. A bLN was presented with three odours in blocks of trials in the order indicated (Fig. 4e, left). OCT was injected 800 ms after odour onset, paired each time with only one of the three odours. As in Fig. 4c, d, the responses of the bLN to the three odours (assembled by odour in three graphs; Fig. 4e, right) were reduced after pairing with OCT (compare blue and red post-stimulus time histograms). The reduction of the response to an odour occurred only after pairing of that particular odour with OCT. For example, responses to cherry and *trans*-2-hexen-1-ol were minimally affected by pairing OCT with 2-heptanone; they became significantly reduced only after the appropriate pairing of either cherry or *trans*-2-hexen-1-ol with OCT. Figure 4f compares summary data for odours paired with OCT ($n = 18$ bLN–odour pairs) to controls ($n = 12$ bLN–odour pairs: odour responses after pairing of a different odour with OCT ($n = 7$) and odour responses after pairing of electrical Kenyon cell stimulation with OCT ($n = 5$); $n = 18$ LFP recordings simultaneous with intracellular bLN recordings). These results support the observation that OCT specifically depresses contacts between cells co-activated within the STDP window (Fig. 3); they also indicate that KC–bLN pairing and OCT should co-occur within an interval of at most a few tens of seconds.

Discussion

In the absence of OCT, STDP at KC–bLN synapses adaptively regulates the bLN spike phase[17] and bLN population output, helped by the action of lateral inhibition between bLNs (Fig. 2). In the context of reinforcer delivery, STDP gains a new role: it tags—presumably through biochemical changes dependent on pairing—the synapses between connected Kenyon cells and bLNs that have fired an action potential within the STDP pairing window, itself commensurate with the oscillation period in this system[38]. This renders those synapses susceptible to the action of OCT (which is proposed to mediate positive reinforcement in insect learning[14,34,39]) and reduces the inhibitory output of the mushroom body mediated by bLNs. Hence, the action of OCT can be specific, even though its release is diffuse and often delayed

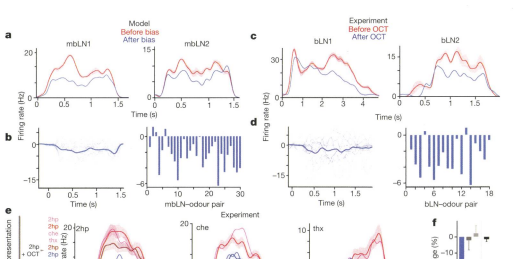

Figure 4 | Odour-specific decrease of mushroom body output by OCT. **a**, Simulation of bLN network as in Fig. 2e. Smoothed post-stimulus time histograms (PSTHs) for two mbLNs (ten trials; shading, s.e.). Red, responses at equilibrium; blue, responses before pairing with STDP + OCT curve shown in Fig. 3f. **b**, Left: difference in PSTHs for all 30 mbLN responses before and after five trials of STDP + OCT ('PSTH after pairing' minus 'PSTH before pairing', thin lines). Responses of individual units at particular times can increase or decrease, but average difference (thick line) is less than zero at all times. Right: time-averaged differences for each of the 30 mbLNs ('PSTH after pairing' minus 'PSTH before pairing'). In some instances, mbLN responses increased (for most units this occurred transiently; for a few mbLNs the entire time-averaged response increased). This is due to reduced lateral inhibition (that is, disinhibition) because mbLN population activity decreased. **c**, *In vivo* intradendritic recordings of bLN odour responses before and after pairing of the odour with localized OCT injection in the β-lobe (50-ms pressure-pulse, 800 ms after odour onset, either five ($n = 5$) or ten pairing trials ($n = 13$)). PSTHs for two bLNs (ten trials; shading, s.e.): red, responses before odour–OCT pairing; blue, responses after ten trials of odour paired with OCT injection. **d**, Same difference of PSTHs as in **b**, for 18 recorded bLN–odour pairs (12 bLNs). As in the model, responses of individual bLNs can increase or decrease transiently, but on average there is a net decrease. **e**, OCT-induced changes are odour specific. Three odours are sequentially paired (during five trials) with OCT to assess carry-over of pairing across odours. Order of stimuli is shown at left. Red colours, responses before pairing with OCT; blue colours, responses after pairing. Odours are presented in ten-trial blocks and PSTHs are shown for each block (shading, s.e.). Changes due to nonspecific pairing are minimal by comparison with those due to odour-specific pairing. **f**, Summary data comparing the effect of odour–OCT pairing (blue: $n = 18$ bLN–odour pairs, 12 bLNs) with those of controls (grey: $n = 12$ bLN–odour pairs, 9 bLNs; black (LFP controls): $n = 18$ recordings simultaneous with intracellular bLN recordings). Dark grey ($n = 7$), effect on bLN response to non-paired odour before and after pairing another odour with OCT. Light grey ($n = 5$), effect on bLN response to non-paired odour before and after pairing electrical activation of Kenyon cells with OCT. Black, effect on LFP power (10–30-Hz band, recorded in mushroom body) before and after pairing odour with OCT. Changes due to pairing odour with OCT differ significantly from zero ($P < 0.0006$, t-test) and from those in the three control conditions ($P < 0.002$–0.022, t-test). Changes in control conditions were not significantly different from zero ($P > 0.72$ (dark grey), 0.64 (light grey) and 0.33 (black)).

relative to the conditioned (odour) stimulus. This provides experimental support for related theoretical propositions[23,40,41]. Our results also solve the temporal dissociation puzzle revealed in experiments[14].

Because the selectivity of synaptic change allowed by STDP relies on the rare co-occurrence of pre- and postsynaptic spikes, it is beneficial that Kenyon cell firing is rare and that odour representations by Kenyon cells are sparse, as observed[12–14]. We propose that olfactory associative memories are stored, at least in part, as sparse sets of synaptic weights between Kenyon cells and mushroom body output neurons. In the absence of reinforcer, STDP and lateral inhibition between bLNs set the (default) instantaneous output of the β-lobe network near the middle of its dynamic range. This serves at least two purposes. First, it maximizes the number of possible distinct combinations of simultaneously active bLNs. Second, it ensures that the output of the network can be increased or decreased, if an associative reinforcer is to co-occur. It is possible that some of the molecular pathways revealed by *Drosophila* neurogenetics[6,9,11] have a role in the phenomenon described here. The functional form of STDP has recently been shown to depend on neuromodulatory context in mammalian brain slices[22,42,43], suggesting that our results may have broad implications for STDP and learning.

METHODS SUMMARY

All results were obtained *in vivo* from locusts housed in a crowded colony. Odours were delivered by injection of a controlled volume of odorized air within a constant stream of desiccated air. The results presented here are derived from intradendritic recordings, made using sharp micropipettes, of 76 neurons in 55 locusts. LFPs were recorded with silicon probes (NeuroNexus) in the mushroom body Kenyon cell soma cluster. Octopamine (100 μM) was injected locally into the mushroom body β-lobe using a picopump (WPI). Electrical stimulation of Kenyon cell somata was done with modified tetrodes (FHC). Stimulation protocols and data analysis were carried out using specialized software (LABVIEW, National Instruments; IGOR, Wavemetrics; and MC_STIMULUS, Multichannel Systems). Simulations of networks of 'Izhikevich units'[44] were done using MATLAB (Mathworks).

Full Methods and any associated references are available in the online version of the paper at www.nature.com/nature.

Received 16 September; accepted 8 December 2011.
Published online 25 January 2012.

1. McGuire, S. E., Le, P. T. & Davis, R. L. The role of *Drosophila* mushroom body signaling in olfactory memory. *Science* **293,** 1330–1333 (2001).
2. Tully, J. B. C. T. in *Drosophila: A Practical Approach* (ed. Roberts, D. B.) 265–317 (Oxford Univ. Press, 1998).
3. de Belle, J. S. & Heisenberg, M. Associative odor learning in *Drosophila* abolished by chemical ablation of mushroom bodies. *Science* **263,** 692–695 (1994).
4. Tully, T. & Quinn, W. G. Classical conditioning and retention in normal and mutant *Drosophila melanogaster*. *J. Comp. Physiol. A* **157,** 263–277 (1985).
5. Heisenberg, M., Borst, A., Wagner, S. & Byers, D. *Drosophila* mushroom body mutants are deficient in olfactory learning. *J. Neurogenet.* **2,** 1–30 (1985).
6. Quinn, W. G., Harris, W. A. & Benzer, S. Conditioned behavior in *Drosophila melanogaster*. *Proc. Natl Acad. Sci. USA* **71,** 708–712 (1974).

7. Keene, A. C. & Waddell, S. *Drosophila* olfactory memory: single genes to complex neural circuits. *Nature Rev. Neurosci.* **8,** 341–354 (2007).
8. Akalal, D. B. *et al.* Roles for *Drosophila* mushroom body neurons in olfactory learning and memory. *Learn. Mem.* **13,** 659–668 (2006).
9. Davis, R. L. Olfactory memory formation in *Drosophila*: from molecular to systems neuroscience. *Annu. Rev. Neurosci.* **28,** 275–302 (2005).
10. Gerber, B., Tanimoto, H. & Heisenberg, M. An engram found? Evaluating the evidence from fruit flies. *Curr. Opin. Neurobiol.* **14,** 737–744 (2004).
11. Heisenberg, M. Mushroom body memoir: from maps to models. *Nature Rev. Neurosci.* **4,** 266–275 (2003).
12. Perez-Orive, J. *et al.* Oscillations and sparsening of odor representations in the mushroom body. *Science* **297,** 359–365 (2002).
13. Turner, G. C., Bazhenov, M. & Laurent, G. Olfactory representations by *Drosophila* mushroom body neurons. *J. Neurophysiol.* **99,** 734–746 (2008).
14. Ito, I., Ong, R. C.-Y., Raman, B. & Stopfer, M. Sparse odor representation and olfactory learning. *Nature Neurosci.* **11,** 1177–1184 (2008).
15. Kanerva, P. *Sparse Distributed Memory* (MIT Press, 1988).
16. Papadopoulou, M., Cassenaer, S., Nowotny, T. & Laurent, G. Normalization for sparse encoding of odors by a wide-field interneuron. *Science* **332,** 721–725 (2011).
17. Cassenaer, S. & Laurent, G. Hebbian STDP in mushroom bodies facilitates the synchronous flow of olfactory information in locusts. *Nature* **448,** 709–713 (2007).
18. Markram, H., Lübke, J., Frotscher, M. & Sakmann, B. Regulation of synaptic efficacy by coincidence of postsynaptic APs and EPSPs. *Science* **275,** 213–215 (1997).
19. Bi, G. Q. & Poo, M. M. Synaptic modifications in cultured hippocampal neurons: dependence on spike timing, synaptic strength, and postsynaptic cell type. *J. Neurosci.* **18,** 10464–10472 (1998).
20. Abbott, L. F. & Nelson, S. B. Synaptic plasticity: taming the beast. *Nature Neurosci.* **3,** 1178–1183 (2000).
21. Meeks, J. P. & Holy, T. E. Pavlov's moth: olfactory learning and spike-timing-dependent plasticity. *Nature Neurosci.* **11,** 1126–1127 (2008).
22. Pawlak, V. Timing is not everything: neuromodulation opens the STDP gate. *Front. Syn. Neurosci.* **2,** 146 (2010).
23. Izhikevich, E. M. Solving the distal reward problem through linkage of STDP and dopamine signaling. *Cereb. Cortex* **17,** 2443–2452 (2007).
24. Gütig, R., Aharonov, R., Rotter, S. & Sompolinsky, H. Learning input correlations through nonlinear temporally asymmetric Hebbian plasticity. *J. Neurosci.* **23,** 3697–3714 (2003).
25. Huerta, R., Nowotny, T., García-Sanchez, M., Abarbanel, H. D. I. & Rabinovich, M. I. Learning classification in the olfactory system of insects. *Neural Comput.* **16,** 1601–1640 (2004).
26. Masquelier, T. & Thorpe, S. J. Unsupervised learning of visual features through spike timing dependent plasticity. *PLoS Comput. Biol.* **3,** e31 (2007).
27. Waddell, S. & Quinn, W. G. Learning how a fruit fly forgets. *Science* **293,** 1271–1272 (2001).
28. Isabel, G., Pascual, A. & Preat, T. Exclusive consolidated memory phases in *Drosophila*. *Science* **304,** 1024–1027 (2004).
29. Gervasi, N., Tchénio, P. & Preat, T. PKA dynamics in a *Drosophila* learning center: coincidence detection by rutabaga adenylyl cyclase and spatial regulation by dunce phosphodiesterase. *Neuron* **65,** 516–529 (2010).
30. Wang, Y., Mamiya, A., Chiang, A. S. & Zhong, Y. Imaging of an early memory trace in the *Drosophila* mushroom body. *J. Neurosci.* **28,** 4368–4376 (2008).
31. Claridge-Chang, A. *et al.* Writing memories with light-addressable reinforcement circuitry. *Cell* **139,** 405–415 (2009).
32. Kim, Y. C., Lee, H. G. & Han, K. A. D1 dopamine receptor dDA1 is required in the mushroom body neurons for aversive and appetitive learning in *Drosophila*. *J. Neurosci.* **27,** 7640–7647 (2007).
33. Riemensperger, T., Voller, T., Stock, P., Buchner, E. & Fiala, A. Punishment prediction by dopaminergic neurons in *Drosophila*. *Curr. Biol.* **15,** 1953–1960 (2005).
34. Schwaerzel, M. *et al.* Dopamine and octopamine differentiate between aversive and appetitive olfactory memories in *Drosophila*. *J. Neurosci.* **23,** 10495–10502 (2003).
35. Mizunami, M. & Matsumoto, Y. Roles of aminergic neurons in formation and recall of associative memory in crickets. *Front. Behav. Neurosci.* **4,** 172 (2010).
36. Braunig, P. Suboesophageal DUM neurons innervate the principal neuropiles of the locust brain. *Phil. Trans. R. Soc. Lond. B* **332,** 221–240 (1991).
37. Wendt, B. & Homberg, U. Immunocytochemistry of dopamine in the brain of the locust *Schistocerca gregaria*. *J. Comp. Neurol.* **321,** 387–403 (1992).
38. Laurent, G. & Naraghi, M. Odorant-induced oscillations in the mushroom bodies of the locust. *J. Neurosci.* **14,** 2993–3004 (1994).
39. Hammer, M. An identified neuron mediates the unconditioned stimulus in associative olfactory learning in honeybees. *Nature* **366,** 59–63 (1993).
40. Gütig, R. & Sompolinsky, H. The tempotron: a neuron that learns spike timing-based decisions. *Nature Neurosci.* **9,** 420–428 (2006).
41. Huerta, R. & Nowotny, T. Fast and robust learning by reinforcement signals: explorations in the insect brain. *Neural Comput.* **21,** 2123–2151 (2009).
42. Seol, G. H. *et al.* Neuromodulators control the polarity of spike-timing- dependent synaptic plasticity. *Neuron* **55,** 919–929 (2007).
43. Shen, W., Flajolet, M., Greengard, P. & Surmeier, D. J. Dichotomous dopaminergic control of striatal synaptic plasticity. *Science* **321,** 848–851 (2008).
44. Izhikevich, E. M. Simple model of spiking neurons. *IEEE Trans. Neural Netw.* **14,** 1569–1572 (2003).
45. Mazor, O. & Laurent, G. Transient dynamics versus fixed points in odor representations by locust antennal lobe projection neurons. *Neuron* **48,** 661–673 (2005).

Supplementary Information is linked to the online version of the paper at www.nature.com/nature.

Acknowledgements This work was funded by the Lawrence Hanson Chair at Caltech, the National Institutes on Deafness and other Communication Disorders, Caltech's Broad Fellows Program, the Office of Naval Research (grants N00014-07-1-0741 and N00014-10-1-0735) and the Max Planck Society. We are grateful to L.-P. Mok for help with locust dissections and to E. Schuman, A. Siapas, E. Lubenov, M. Papadopoulou and members of the Laurent lab for comments on the manuscript.

Author Contributions S.C. and G.L. designed the experiments and simulations, discussed the results and wrote the paper. S.C. carried out the experiments and simulations.

Author Information Reprints and permissions information is available at www.nature.com/reprints. The authors declare no competing financial interests. Readers are welcome to comment on the online version of this article at www.nature.com/nature. Correspondence and requests for materials should be addressed to G.L. (gilles.laurent@brain.mpg.de) or S.C. (stijn@caltech.edu).

ARTICLE

doi:10.1038/nature10802

DNA breaks and chromosome pulverization from errors in mitosis

Karen Crasta[1,2,3], Neil J. Ganem[1,2,3], Regina Dagher[1,2,3], Alexandra B. Lantermann[1], Elena V. Ivanova[4], Yunfeng Pan[5], Luigi Nezi[1], Alexei Protopopov[4], Dipanjan Chowdhury[5] & David Pellman[1,2,3]

The involvement of whole-chromosome aneuploidy in tumorigenesis is the subject of debate, in large part because of the lack of insight into underlying mechanisms. Here we identify a mechanism by which errors in mitotic chromosome segregation generate DNA breaks via the formation of structures called micronuclei. Whole-chromosome-containing micronuclei form when mitotic errors produce lagging chromosomes. We tracked the fate of newly generated micronuclei and found that they undergo defective and asynchronous DNA replication, resulting in DNA damage and often extensive fragmentation of the chromosome in the micronucleus. Micronuclei can persist in cells over several generations but the chromosome in the micronucleus can also be distributed to daughter nuclei. Thus, chromosome segregation errors potentially lead to mutations and chromosome rearrangements that can integrate into the genome. Pulverization of chromosomes in micronuclei may also be one explanation for 'chromothripsis' in cancer and developmental disorders, where isolated chromosomes or chromosome arms undergo massive local DNA breakage and rearrangement.

Whole-chromosome aneuploidy is a major feature of cancer genomes, yet its role in tumour development remains controversial[1,2]. This contrasts with chromosome breaks and rearrangements, which are known to produce cancer-causing mutations. Recent genetic evidence demonstrates that increased rates of whole-chromosome mis-segregation can accelerate oncogenesis[3–5]; however, the only established mechanism by which whole-chromosome segregation errors promote tumorigenesis is by facilitating the loss of heterozygosity for tumour suppressors[7]. Intriguingly, two animal models where whole-chromosome segregation errors result in robust tumour development also display extensive structural alterations in chromosomes[6,8]. This raises the question of whether errors in mitosis can predispose to DNA damage. We considered the possibility that segregation of chromosomes into micronuclei might produce DNA damage. Whole-chromosome-containing micronuclei form from anaphase lagging chromosomes[9–13]; micronuclei can also be generated from acentric fragments of chromosomes[11]. Micronuclei have many features of primary nuclei, but much controversy surrounds their actual composition and functional properties. Studies differ on whether micronuclei are transcriptionally active, replicate DNA, mount a normal DNA damage response, or assemble normal nuclear envelopes; moreover, the ultimate fate of chromosomes trapped within micronuclei remains unclear[11,14,15].

DNA damage in micronuclei

To determine if newly formed whole-chromosome micronuclei develop DNA damage, we generated micronuclei in synchronized cells and tracked them through the cell cycle. As a first synchronization approach, micronuclei were generated in non-transformed RPE-1 and transformed U2OS cells by release from nocodazole-induced microtubule depolymerization. When mitotic cells are released from nocodazole, spindles reassemble abnormally, producing merotelic kinetochore attachments (one kinetochore attached to two opposite spindle poles), lagging chromosomes, and ~10% of cells with micronuclei[16]. Because prolonged mitotic arrest causes DNA damage[17–19], RPE-1 cells were arrested for a short (6 h) interval with nocodazole. After release from the 6 h nocodazole block, neither the primary nuclei nor the newly formed kinetochore-positive micronuclei showed significant DNA damage during the subsequent G1 phase as measured by damage-dependent phosphorylation of the histone variant H2AX[20] (γ-H2AX foci formation; Fig. 1a–c and Supplementary Fig. 2a–f), TdT-mediated dUTP nick end labelling (TUNEL) to detect DNA breaks[21] (Fig. 1d and Supplementary Fig. 2e, f), and visualization of DNA breaks with the comet assay[22] (Supplementary Fig. 3d, e).

Because aneuploidy can produce a p53-dependent G1 cell-cycle arrest[23,24], p53 was silenced by RNA interference (RNAi) to allow us to monitor the fate of micronucleated RPE-1 cells at later stages of the cell cycle. As expected, after S-phase entry, low-level DNA damage was detected in both the micronuclei and the primary nucleus[25]; however, in G2 phase cells, most micronuclei showed DNA damage whereas almost none was detected in the primary nucleus (Fig. 1a–d). Similar results were observed in U2OS cells (Supplementary Fig. 3) and in cells where merotelic kinetochore–microtubule attachments were generated by knockdown of the kinetochore-associated microtubule depolymerase MCAK[26] or the kinetochore protein NUF2 (ref. 27) (Supplementary Fig. 4a–c). MCAK knockdown does not delay cells in mitosis, demonstrating that the acquisition of DNA damage in micronuclei is independent of mitotic arrest[17–19]. This damage did not represent activation of apoptosis because it was not accompanied by caspase-3 activation, and it was not suppressed by a pan-caspase inhibitor (Supplementary Fig. 5).

As a completely independent method for generating micronuclei, we used a human cell line (HT1080) carrying a human artificial chromosome (HAC) with a kinetochore that could be conditionally inactivated[28]. In this system, kinetochore assembly on the HAC is blocked by washout of doxycycline from the medium; consequently, the HAC is unable to attach to the mitotic spindle and is left behind at anaphase,

[1]Department of Pediatric Oncology, Dana-Farber Cancer Institute, 450 Brookline Avenue, Boston, Massachusetts 02115, USA. [2]Department of Cell Biology, Harvard Medical School, 240 Longwood Avenue, Boston, Massachusetts 02115, USA. [3]Howard Hughes Medical Institute, 450 Brookline Avenue, Boston, Massachusetts 02115, USA. [4]Beller Institute for Applied Cancer Science, Dana-Farber Cancer Institute, 4 Blackfan Street, Boston, Massachusetts 02115, USA. [5]Department of Radiation Oncology, Dana-Farber Cancer Institute, 450 Brookline Avenue, Boston, Massachusetts 02115, USA.

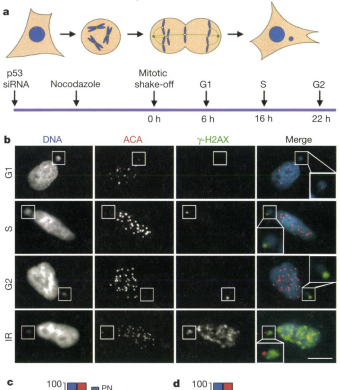

Figure 1 | Micronuclei from lagging chromosomes develop DNA breaks. **a**, Schematic of the experiment. **b**, Representative images of micronucleated G1 (6 h), S (16 h), G2 (22 h) and irradiated RPE-1 cells (IR) labelled for DNA (blue), centromeres (ACA, red) and γ-H2AX (green). Insets show enlarged images of micronuclei. Scale bars, 10 μm. **c**, **d**, Percentage of primary nuclei (PN, blue bars) and centric micronuclei (MN, red bars) with γ-H2AX foci (**c**) and TUNEL labelling (**d**) (3 experiments, $n = 100$). Errors bars indicate s.e.m.

ultimately reforming as a micronucleus (Fig. 2a). Results obtained with the HAC-containing micronuclei (Fig. 2b–d) were in agreement with the results obtained by the other synchronization methods described above. Taken together, micronuclei do not exhibit significant DNA damage during G1, but a large fraction of micronuclei acquire DNA damage during S phase that persists into G2.

Defective DNA replication in micronuclei

To determine directly whether acquisition of DNA damage in micronuclei requires DNA replication, synchronized micronucleated cells were released into medium containing thymidine to block DNA replication. Blocking DNA replication with thymidine abolished the acquisition of DNA damage (Fig. 3a–c), demonstrating that the breaks in micronuclei occur in a replication-dependent manner.

We next tested whether the acquisition of DNA damage in micronuclei is mediated by aberrant DNA replication. This possibility was suggested because micronuclei in G2 cells that had γ-H2AX foci were almost always additionally labelled for phosphorylated RPA2 (Ser 33)[29], a marker of DNA replication stress (Supplementary Fig. 4d). Moreover, the characteristic 5-bromodeoxyuridine (BrdU) labelling patterns of early, mid and late S-phase cells[30] suggested that DNA replication in micronuclei is inefficient and asynchronous with the primary nucleus (Fig. 3d). By measuring the fluorescence intensity of BrdU relative to DNA area from single focal plane confocal images, DNA replication in micronuclei was detected at a markedly reduced level throughout S phase when compared to the primary nuclei (Fig. 3e). Notably, pulse-labelling with BrdU demonstrated asynchronous DNA replication of the micronuclei relative to the primary nucleus, with ~30% of micronuclei replicating DNA in G2 cells (22 h; Fig. 3d).

The compromised DNA replication observed in newly formed micronuclei led us to test whether complexes necessary to license DNA replication origins are recruited to chromosomes in micronuclei. The first step in assembling replication origins is the loading of the origin recognition complex (ORC) after chromosome decondensation during telophase[31]. Quantitative fluorescence imaging suggested that ORC recruitment is equally efficient in the micronuclei as in the primary nucleus (Supplementary Fig. 6a). By contrast, newly generated micronuclei showed significant reduction in the recruitment of replicative DNA helicase components MCM2 and MCM3 (refs 32, 33) as well as the replication initiation factor CDT1 (ref. 31) (Fig. 4a, b and Supplementary Fig. 6b, c). We observed an increased recruitment of MCM subunits into micronuclei as cells progressed through the cell cycle, but the levels of MCM subunits never exceeded 20% of that observed in the primary nucleus (Fig. 4b).

To examine whether the DNA damage response in micronuclei was also abnormal, cells were treated with replication inhibitor (aphidicolin) or exposed to 2 Gy irradiation to induce damage and then labelled to detect components of the DNA damage response. After aphidicolin treatment, micronuclei showed clear signal for γ-H2AX and its kinase ATR (ataxia telangectasia mutated-related), but downstream constituents of the DNA damage response such as 53BP1 were not efficiently recruited, as previously reported[34] (Supplementary Fig. 7). A similar defect in the recruitment of DNA-damage-response factors into micronuclei was also observed after irradiation (Supplementary Fig. 8a). This recruitment defect had clear consequences for DNA damage repair: whereas γ-H2AX foci were resolved in primary nuclei by 6 h after 2 Gy irradiation, γ-H2AX foci persisted in micronuclei for >24 h (Supplementary Fig. 8b). The failure of micronuclei to recruit MCM subunits and components of the DNA repair machinery may be due, at least in part, to a defect in nucleocytoplasmic transport. Newly formed micronuclei have a marked reduction in the density of nuclear pores[11,14,15] (Supplementary Fig. 9) and exhibit strongly reduced nuclear import (Fig. 4c, d and Supplementary Fig. 10).

Micronuclei and chromosome pulverization

Next we tested the prediction that abnormal DNA replication in micronuclei could generate chromosome breaks. Chromosome spreads were prepared from non-transformed cells in the first cell cycle after release from nocodazole or from DMSO-treated controls (Fig. 5a–f and Supplementary Fig. 11a). Notably, 7.6% of chromosome spreads prepared from micronucleated cells released from nocodazole block ($n = 722$) exhibited chromosomes with a 'pulverized' appearance, characterized by fragments of 4′,6-diamidino-2-phenylindole (DAPI)-stained material that were often clustered into a discrete location on the spread[35] (Fig. 5a, d (yellow arrows), i and Supplementary Fig. 11b). By contrast, pulverization was exceedingly rare (0.14%) in controls. Multicolour fluorescence chromosome painting (SKY) confirmed that 34 of 47 spreads with pulverized chromosomes were composed of fragments from a single chromosome and another eight were from two chromosomes (Fig. 5a–i and Supplementary Fig. 11). Despite this marked disruption to chromosomal structure, only one cell harboured non-reciprocal chromosome translocations 24 h after nocodazole release ($n = 101$), whereas no translocations were observed in control cells (data not shown). At 72 h after nocodazole release ($n = 100$), we still did not detect chromosome translocations, but we did detect truncated or derivative single chromosomes in three cells. Although our experiments show that whole-chromosome mis-segregation does not produce frequent non-reciprocal translocations, we do not exclude the possibility that the DNA damage acquired in micronuclei could result in translocations, albeit at a frequency lower than ~1/100 per generation.

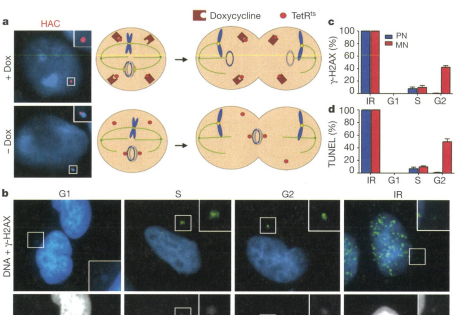

Figure 2 | DNA breaks in a HAC targeted to a micronucleus. **a**, Right: schematic; left: fluorescence *in situ* hybridization images of HAC (red) in a primary nucleus (+Dox) or micronucleus (−Dox). **b**, Images of micronucleated cells as in Fig. 1b (enlarged and brightened in insets). Scale bars, 10 μm. **c**, **d**, Percentage of primary nuclei (blue bars) and centric micronuclei (red bars) with γ-H2AX foci (**c**) and TUNEL labelling (**d**) (3 experiments, $n = 100$). Errors bars indicate s.e.m.

Chromosome pulverization has been observed in cell-fusion experiments where chromosomes from an S-phase cell are pulverized because of exposure to signals from mitotic cytoplasm[36]. It has also been observed when aberrant late-replicating chromosome translocations are generated[37]. The mechanism of pulverization involves compaction of partially replicated chromosomes induced by mitotic cyclin-dependent kinase activity, termed premature chromosome compaction[35,38,39]. By labelling micronucleated and control cells for 2 h with BrdU immediately before chromosome condensation and mitotic arrest, we found that 25 of 30 pulverized chromosomes were undergoing DNA replication (Fig. 5h). The fact that only micronuclei incorporate BrdU in G2 cells (Figs 3d and 5g) demonstrates that the pulverized chromosomes are derived from micronuclei.

The fate of chromosomes in micronuclei

We next addressed the potential for chromosome aberrations acquired in micronuclei to be reincorporated into the genome. We used long-term live-cell imaging to determine the fate of spontaneously arising or experimentally induced micronuclei in a variety of cell lines (Supplementary Table 1). Imaging analysis revealed that the vast majority of micronuclei (525 of 541; 97%) are stably maintained during interphase. Although micronuclei may be extruded in some cells[11], extrusion was not detected in our imaging experiments. Furthermore, micronuclei were not visibly degraded[11], did not co-localize with lysosomes (Supplementary Fig. 12), and did not appear to fuse with the primary nucleus. By contrast, our experiments indicated that after nuclear envelope breakdown some micronuclei might join the other mitotic chromosomes and be distributed to daughter nuclei. Of the 331 micronucleated cells that were tracked as they underwent cell division, 16% (53 of 331) gave rise to daughter cells

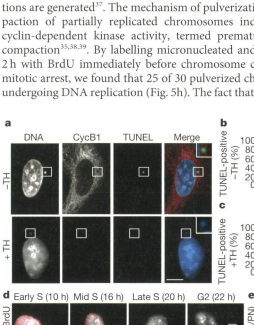

Figure 3 | DNA damage in micronuclei results from aberrant DNA replication. **a**–**c**, DNA replication requirement for acquisition of DNA damage in micronuclei. **a**, RPE-1 cells were synchronized as in Fig. 1a and released into media with (+TH) or without (−TH) 2 mM thymidine. Cells were co-labelled for TUNEL (green) and cyclin B1 (red). Shown are images from the 22 h sample. Scale bar, 10 μm. **b**, **c**, Percentage of TUNEL-positive primary nuclei (blue bars) and micronuclei (red bars) with (**c**) or without (**b**) thymidine treatment; (3 experiments, $n = 100$). Errors bars indicate s.e.m. **d**, Inefficient and asynchronous DNA replication in micronuclei. RPE-1 cells as in Fig. 1a were pulse-labelled with BrdU and labelled: DNA (white) and BrdU (red). **e**, The ratio of BrdU incorporation in micronuclei relative to primary nuclei after a 30-min pulse label. Normalized fluorescence intensity (FI) measurements are as shown in the box and whisker plots (2 experiments, $n = 50$). Boxes represent upper and lower quartiles, lines within boxes represent median, and the error bars comprise the whiskers which extend to the maximum and minimum value data sets.

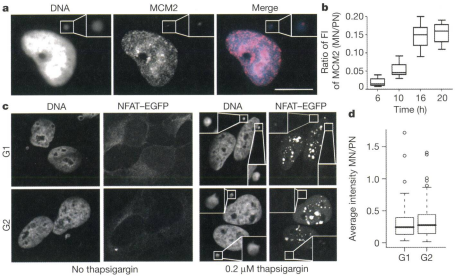

Figure 4 | Defective MCM2-7 complex recruitment, DNA damage response and nucleocytoplasmic transport in micronuclei. **a**, Impaired MCM2 recruitment into micronuclei. G1 RPE-1 cells were synchronized as in Fig. 1a and stained for chromatin-bound MCM2 and DNA. Scale bar, 10 μm. **b**, Relative MCM2 fluorescence intensity (FI) as in Fig. 3e. Approximate cell cycle stage of time points: 6 h, G1; 10 h, early S phase; 16 h, mid S phase; 20 h, late S phase; (2 experiments, $n = 50$). **c**, **d**, Micronuclei are partially defective for nuclear import of NFATc1–EGFP. **c**, Representative images of micronucleated U2OS cells stably expressing NFATc1–EGFP in G1 and G2 with or without treatment with 0.2 μM thapsigargin for 10 min. **d**, Ratio of NFATc1–EGFP fluorescence intensity between micronuclei and primary nuclei; (3 experiments, $n = 30$). For **b** and **d**, error bars comprise the whiskers which extend to the maximum and minimum value data sets.

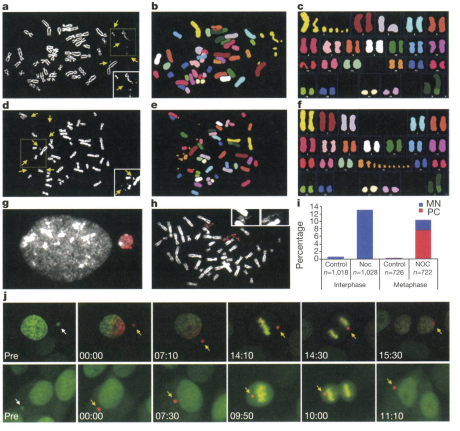

Figure 5 | The fate of chromosomes in micronuclei. Micronuclei were induced in RPE-1 cells as described in Fig. 1a (after p53 knockdown) and chromosome spreads were prepared 24 h after nocodazole release. **a**–**c**, Pulverization of chromosome 1 demonstrated by DAPI staining (chromosome fragments, brightened in inset, yellow arrows) (**a**), SKY probes (pseudo-coloured) (**b**), and aligned SKY karyotype (**c**). **d**–**f**, Pulverization of chromosome 16, viewed as in **a**–**c**. **g**, A BrdU-positive micronuclei-containing G2 RPE-1 cell. 2 h BrdU pulse label. DNA, white; BrdU, red. **h**, Selective BrdU labelling of a pulverized chromosome. **i**, The percentage of cells with intact micronuclei (blue bars) or pulverized chromosomes (PC, red bars) from control or nocodazole-released (NOC) RPE-1 cells. Interphase is 18-h sample and metaphase is 24 h. **j**, Images from live-cell experiment showing a pre-converted green fluorescent micronucleus (white arrows) photo-converted to a red-fluorescent micronucleus (yellow arrows) imaged through mitosis. After anaphase, the micronucleus either reincorporated with the primary nucleus or failed to reincorporate and reformed as a micronucleus. Top row: reincorporation of micronuclei into primary nucleus; bottom row: no reincorporation. Time is shown as h:min.

that lacked micronuclei (Supplementary Table 1 and Supplementary Movies 1 and 2).

To test directly whether micronuclei reincorporate during mitosis, we generated a U2OS cell line stably expressing H2B fused to the photoconvertible fluorescent protein Kaede[40], which converts from green to red fluorescence emission after ultraviolet illumination. This enabled us to photoactivate selectively and subsequently track a single chromosome encapsulated in a micronucleus throughout mitosis (Fig. 5j and Supplementary Movies 3 and 4). This experiment demonstrated that chromosomes within micronuclei reincorporate into daughter nuclei at a significant frequency (11 of 29; 38%). The remaining micronuclei persisted in cells well into the second generation.

Discussion

Together, our findings indicate a novel mechanism by which whole-chromosome segregation errors can cause chromosome breaks and potentially cancer-causing mutations. Mitotic errors can lead to lagging chromosomes which in turn can be partitioned into micronuclei[13]. This can produce DNA damage in two ways. First, DNA damage can result as a direct consequence of aberrant DNA replication, potentially due to a reduced density of replication origins. Second, chromosome pulverization due to premature chromosome compaction can occur if a micronucleated cell enters mitosis with micronuclei still undergoing DNA replication. This may not be the only mechanism by which whole-chromosome mis-segregation can cause DNA damage, as it was recently proposed that lagging chromosomes can be damaged by the cytokinetic furrow[41]. In contrast to previous studies that have suggested that most micronuclei are inactive, discarded or degraded[11], we find that micronuclei persist over several generations but that the chromosomes within the micronuclei can be segregated at a significant frequency into daughter cell nuclei. Thus, DNA rearrangements and mutations acquired in micronuclei could be incorporated into the genome of a developing cancer cell.

Our experiments suggest a mechanism that could explain the recently discovered phenomenon of chromothripsis[42,43]. Chromothripsis was discovered by cancer genome sequencing and DNA copy number analysis[42]. It is defined by small-scale DNA copy number changes and extensive intrachromosomal rearrangements that are restricted to a single chromosome or chromosome arm. Two non-exclusive models have been proposed for chromothripsis are: (1) fragmentation of a chromosome followed by stitching together of the resulting fragments by non-homologous end joining[42]; and (2) aberrant DNA replication resulting in fork stalling and template switching or microhomology-mediated break-induced replication[43,44]. Partitioning of a chromosome into a spatially isolated micronucleus can explain why a single chromosome would be subject to aberrant DNA replication and can explain how extensive DNA damage can be restricted to a single chromosome. Because micronuclei may persist as discrete entities over several generations, damage to the chromosome need not occur all at once[42,43], but could accrue from multiple failed attempts at DNA replication. Chromothripsis restricted to a chromosome arm could be generated from acentric chromosome fragments, as chromosome pulverization was previously correlated with the presence of micronuclei in cancer cell lines after DNA damage[35,45]. Although chromothripsis seems to be relatively rare, DNA damage in micronuclei could be more common. We propose that chromothripsis may be an extreme outcome of a mutagenesis mechanism that could be widespread in human cancer.

METHODS SUMMARY

All cell lines were maintained at 37 °C with 5% CO_2 atmosphere. To generate micronuclei, cells were treated with nocodazole (100 ng ml^{-1}) for 6 h followed by mitotic shake-off and nocodazole washout. Alternatively, micronuclei were generated by depletion of MCAK or NUF2 by short interfering RNA (siRNA). Micronuclei were also generated in HT1080 cells by inactivation of the kinetochore of the human artificial chromosome by washout of doxycycline. Detailed descriptions of immunofluorescence, RNAi, BrdU labelling, comet assays, inactivation of the human artificial chromosomes (HAC), flow cytometry, quantitative analysis of nuclear import, chromosome spreads, spectral karyotyping, antibodies used, photoconversion of H2B-Kaede and long-term live-cell imaging experiments can be found in Methods.

Full Methods and any associated references are available in the online version of the paper at www.nature.com/nature.

Received 28 August; accepted 20 December 2011.
Published online 18 January 2012.

1. Gordon, D. J., Resio, B. & Pellman, D. Causes and consequences of aneuploidy in cancer. *Nature Rev. Genet.* http://dx.doi.org/10.1038/nrg3123 (in the press).
2. Weaver, B. A. & Cleveland, D. W. Aneuploidy: instigator and inhibitor of tumorigenesis. *Cancer Res.* **67,** 10103–10105 (2007).
3. Schvartzman, J. M., Sotillo, R. & Benezra, R. Mitotic chromosomal instability and cancer: mouse modelling of the human disease. *Nature Rev. Cancer* **10,** 102–115 (2010).
4. Ricke, R. M., van Ree, J. H. & van Deursen, J. M. Whole chromosome instability and cancer: a complex relationship. *Trends Genet.* **24,** 457–466 (2008).
5. Weaver, B. A., Silk, A. D., Montagna, C., Verdier-Pinard, P. & Cleveland, D. W. Aneuploidy acts both oncogenically and as a tumor suppressor. *Cancer Cell* **11,** 25–36 (2007).
6. Sotillo, R. *et al.* Mad2 overexpression promotes aneuploidy and tumorigenesis in mice. *Cancer Cell* **11,** 9–23 (2007).
7. Baker, D. J., Jin, F., Jeganathan, K. B. & van Deursen, J. M. Whole chromosome instability caused by Bub1 insufficiency drives tumorigenesis through tumor suppressor gene loss of heterozygosity. *Cancer Cell* **16,** 475–486 (2009).
8. Fujiwara, T. *et al.* Cytokinesis failure generating tetraploids promotes tumorigenesis in p53-null cells. *Nature* **437,** 1043–1047 (2005).
9. Cimini, D. Merotelic kinetochore orientation, aneuploidy, and cancer. *Biochim. Biophys. Acta* **1786,** 32–40 (2008).
10. Ganem, N. J., Godinho, S. A. & Pellman, D. A mechanism linking extra centrosomes to chromosomal instability. *Nature* **460,** 278–282 (2009).
11. Terradas, M., Martin, M., Tusell, L. & Genesca, A. Genetic activities in micronuclei: is the DNA entrapped in micronuclei lost for the cell? *Mutat. Res.* **705,** 60–67 (2010).
12. Gisselsson, D. *et al.* Abnormal nuclear shape in solid tumors reflects mitotic instability. *Am. J. Pathol.* **158,** 199–206 (2001).
13. Thompson, S. L. & Compton, D. A. Chromosome missegregation in human cells arises through specific types of kinetochore-microtubule attachment errors. *Proc. Natl Acad. Sci. USA* **108,** 17974–17978 (2011).
14. Hoffelder, D. R. *et al.* Resolution of anaphase bridges in cancer cells. *Chromosoma* **112,** 389–397 (2004).
15. Géraud, G. *et al.* Three-dimensional organization of micronuclei induced by colcimine in PtK1 cells. *Exp. Cell Res.* **181,** 27–39 (1989).
16. Cimini, D. *et al.* Merotelic kinetochore orientation is a major mechanism of aneuploidy in mitotic mammalian tissue cells. *J. Cell Biol.* **153,** 517–528 (2001).
17. Dalton, W. B., Nandan, M. O., Moore, R. T. & Yang, V. W. Human cancer cells commonly acquire DNA damage during mitotic arrest. *Cancer Res.* **67,** 11487–11492 (2007).
18. Quignon, F. *et al.* Sustained mitotic block elicits DNA breaks: one-step alteration of ploidy and chromosome integrity in mammalian cells. *Oncogene* **26,** 165–172 (2007).
19. Orth, J. D., Loewer, A., Lahav, G. & Mitchison, T. J. Prolonged mitotic arrest induces partial activation of apoptosis, DNA damage and p53 activation. *Mol. Biol. Cell* http://dx.doi.org/10.1091/mbc.E11-09-0781 (2011).
20. Rogakou, E. P., Pilch, D. R., Orr, A. H., Ivanova, V. S. & Bonner, W. M. DNA double-stranded breaks induce histone H2AX phosphorylation on serine 139. *J. Biol. Chem.* **273,** 5858–5868 (1998).
21. Gavrieli, Y., Sherman, Y. & Ben-Sasson, S. A. Identification of programmed cell death *in situ* via specific labeling of nuclear DNA fragmentation. *J. Cell Biol.* **119,** 493–501 (1992).
22. Singh, N. P., McCoy, M. T., Tice, R. R. & Schneider, E. L. A simple technique for quantitation of low levels of DNA damage in individual cells. *Exp. Cell Res.* **175,** 184–191 (1988).
23. Thompson, S. L. & Compton, D. A. Proliferation of aneuploid human cells is limited by a p53-dependent mechanism. *J. Cell Biol.* **188,** 369–381 (2010).
24. Li, M. *et al.* The ATM-p53 pathway suppresses aneuploidy-induced tumorigenesis. *Proc. Natl Acad. Sci. USA* **107,** 14188–14193 (2010).
25. Branzei, D. & Foiani, M. Maintaining genome stability at the replication fork. *Nature Rev. Mol. Cell Biol.* **11,** 208–219 (2010).
26. Kline-Smith, S. L., Khodjakov, A., Hergert, P. & Walczak, C. E. Depletion of centromeric MCAK leads to chromosome congression and segregation defects due to improper kinetochore attachments. *Mol. Biol. Cell* **15,** 1146–1159 (2004).
27. DeLuca, J. G., Moree, B., Hickey, J. M., Kilmartin, J. V. & Salmon, E. D. hNuf2 inhibition blocks stable kinetochore-microtubule attachment and induces mitotic cell death in HeLa cells. *J. Cell Biol.* **159,** 549–555 (2002).
28. Nakano, M. *et al.* Inactivation of a human kinetochore by specific targeting of chromatin modifiers. *Dev. Cell* **14,** 507–522 (2008).
29. Binz, S. K., Sheehan, A. M. & Wold, M. S. Replication protein A phosphorylation and the cellular response to DNA damage. *DNA Repair* **3,** 1015–1024 (2004).
30. O'Keefe, R. T., Henderson, S. C. & Spector, D. L. Dynamic organization of DNA replication in mammalian cell nuclei: spatially and temporally defined replication of chromosome-specific alpha-satellite DNA sequences. *J. Cell Biol.* **116,** 1095–1110 (1992).
31. DePamphilis, M. L. & Bell, S. D. *Genome Duplication* (Garland Science, 2011).

32. Dimitrova, D. S., Prokhorova, T. A., Blow, J. J., Todorov, I. T. & Gilbert, D. M. Mammalian nuclei become licensed for DNA replication during late telophase. *J. Cell Sci.* **115,** 51–59 (2002).
33. Mendez, J. & Stillman, B. Chromatin association of human origin recognition complex, cdc6, and minichromosome maintenance proteins during the cell cycle: assembly of prereplication complexes in late mitosis. *Mol. Cell. Biol.* **20,** 8602–8612 (2000).
34. Terradas, M., Martin, M., Tusell, L. & Genesca, A. DNA lesions sequestered in micronuclei induce a local defective-damage response. *DNA Repair* **8,** 1225–1234 (2009).
35. Obe, G., Beek, B. & Vaidya, V. G. The human leukocyte test system. III. Premature chromosome condensation from chemically and x-ray induced micronuclei. *Mutat. Res.* **27,** 89–101 (1975).
36. Johnson, R. T. & Rao, P. N. Mammalian cell fusion: induction of premature chromosome condensation in interphase nuclei. *Nature* **226,** 717–722 (1970).
37. Smith, L., Plug, A. & Thayer, M. Delayed replication timing leads to delayed mitotic chromosome condensation and chromosomal instability of chromosome translocations. *Proc. Natl Acad. Sci. USA* **98,** 13300–13305 (2001).
38. Nichols, W. W., Levan, A., Aula, P. & Norrby, E. Chromosome damage associated with the measles virus *in vitro*. *Hereditas* **54,** 101–118 (1965).
39. Kato, H. & Sandberg, A. A. Chromosome pulverization in human binucleate cells following colcemid treatment. *J. Cell Biol.* **34,** 35–45 (1967).
40. Ando, R., Hama, H., Yamamoto-Hino, M., Mizuno, H. & Miyawaki, A. An optical marker based on the UV-induced green-to-red photoconversion of a fluorescent protein. *Proc. Natl Acad. Sci. USA* **99,** 12651–12656 (2002).
41. Janssen, A., van der Burg, M., Szuhai, K., Kops, G. J. & Medema, R. H. Chromosome segregation errors as a cause of DNA damage and structural chromosome aberrations. *Science* **333,** 1895–1898 (2011).
42. Stephens, P. J. *et al.* Massive genomic rearrangement acquired in a single catastrophic event during cancer development. *Cell* **144,** 27–40 (2011).
43. Liu, P. *et al.* Chromosome catastrophes involve replication mechanisms generating complex genomic rearrangements. *Cell* **146,** 889–903 (2011).
44. Hastings, P. J., Lupski, J. R., Rosenberg, S. M. & Ira, G. Mechanisms of change in gene copy number. *Nature Rev. Genet.* **10,** 551–564 (2009).
45. Sen, S., Hittelman, W. N., Teeter, L. D. & Kuo, M. T. Model for the formation of double minutes from prematurely condensed chromosomes of replicating micronuclei in drug-treated Chinese hamster ovary cells undergoing DNA amplification. *Cancer Res.* **49,** 6731–6737 (1989).

Supplementary Information is linked to the online version of the paper at www.nature.com/nature.

Acknowledgements We thank A. D'Andrea, M. E. McLaughlin, T. A. Rapoport, J. Walters and Pellman laboratory members for discussions and/or comments on the manuscript; L. Cameron for advice and help on microscopy; H. Li for irradiation of cells; M. Nitta and M. Hennessy for preliminary experiments; and V. Larionov, B. Stillman, J. Ellenberg, I. Mattaj, A. Miyawaki and T. Kuroda for reagents. D.P. was supported by the Howard Hughes Medical Institute and the NIH (GM083299); K.C. was a fellow of A*STAR Singapore; N.J.G. was a fellow of the Leukemia and Lymphoma Society; Y.P. and D.C. were funded by the NIH (1R01CA142698-01).

Author Contributions D.P. conceived the project; K.C., N.J.G., R.D., A.B.L., D.C. and D.P. designed the experiments; D.P., K.C. and N.J.G. wrote the manuscript with edits from all authors; K.C. contributed Figs. 1–3, 4a, b and Supplementary Figs 2–8 with help from R.D. N.J.G. contributed Fig. 5j, Supplementary Fig. 12, Supplementary Table 1 and Supplementary Movies. R.D., E.V.I. and A.P. contributed Fig. 5a–i and Supplementary Figs 1 and 11; A.B.L. contributed Fig. 4c, d and Supplementary Figs 9 and 10; Y.P. and D.C. contributed Supplementary Fig. 3d; L.N. contributed Fig. 2a.

Author Information Reprints and permissions information is available at www.nature.com/reprints. The authors declare no competing financial interests. Readers are welcome to comment on the online version of this article at www.nature.com/nature. Correspondence and requests for materials should be addressed to david_pellman@dfci.harvard.edu.

LETTER

doi:10.1038/nature10746

Creation and diagnosis of a solid-density plasma with an X-ray free-electron laser

S. M. Vinko[1], O. Ciricosta[1], B. I. Cho[2], K. Engelhorn[2], H.-K. Chung[3], C. R. D. Brown[4], T. Burian[5], J. Chalupský[5], R. W. Falcone[2,6], C. Graves[7], V. Hájková[5], A. Higginbotham[1], L. Juha[5], J. Krzywinski[7], H. J. Lee[7], M. Messerschmidt[7], C. D. Murphy[1], Y. Ping[8], A. Scherz[7], W. Schlotter[7], S. Toleikis[9], J. J. Turner[7], L. Vysin[5], T. Wang[7], B. Wu[7], U. Zastrau[10], D. Zhu[7], R. W. Lee[2], P. A. Heimann[7], B. Nagler[7] & J. S. Wark[1]

Matter with a high energy density ($>10^5$ joules per cm^3) is prevalent throughout the Universe, being present in all types of stars[1] and towards the centre of the giant planets[2,3]; it is also relevant for inertial confinement fusion[4]. Its thermodynamic and transport properties are challenging to measure, requiring the creation of sufficiently long-lived samples at homogeneous temperatures and densities[5,6]. With the advent of the Linac Coherent Light Source (LCLS) X-ray laser[7], high-intensity radiation ($>10^{17}$ watts per cm^2, previously the domain of optical lasers) can be produced at X-ray wavelengths. The interaction of single atoms with such intense X-rays has recently been investigated[8]. An understanding of the contrasting case of intense X-ray interaction with dense systems is important from a fundamental viewpoint and for applications. Here we report the experimental creation of a solid-density plasma at temperatures in excess of 10^6 kelvin on inertial-confinement timescales using an X-ray free-electron laser. We discuss the pertinent physics of the intense X-ray–matter interactions, and illustrate the importance of electron–ion collisions. Detailed simulations of the interaction process conducted with a radiative-collisional code show good qualitative agreement with the experimental results. We obtain insights into the evolution of the charge state distribution of the system, the electron density and temperature, and the timescales of collisional processes. Our results should inform future high-intensity X-ray experiments involving dense samples, such as X-ray diffractive imaging of biological systems, material science investigations, and the study of matter in extreme conditions.

The experiment was performed at the LCLS soft X-ray materials science instrument (SXR), where a 1.0-μm-thick aluminium (Al) foil was irradiated with 80-fs X-ray pulses at photon energies in the range 1,560–1,830 eV (at and above the Al K edge). The LCLS pulse contained $\sim 10^{12}$ photons with an energy bandwidth of $\sim 0.4\%$. The X-ray pulse was focused by means of bendable Kirkpatrick-Baez mirrors, and the focal spot was characterized *ex situ* by analysing imprints in lead tungstate (ref. 9), indicating a spot size of 9.1 ± 0.8 μm^2, that is, a peak intensity of 1.1×10^{17} W cm^{-2}. Aluminium was studied because it is a prototypical free-electron metal, presenting all the intricacies of a high-electron-density system, yet possessing a relatively simple atomic structure. Our main target diagnostic is X-ray emission spectroscopy, sensitive to recombination from the L to the K shell, that is, to Al Kα emission, in the spectral range 1,460–1,680 eV.

The absorption process in the Al foil is dominated by K-shell photo-absorption, ejecting a core electron into the continuum, because the cross-section for L-shell and valance-band photoionization is over a factor 10 smaller. After photoionization, the filling of the K-shell hole proceeds mainly by KLL Auger decay, producing an ion with two holes in the L shell. Radiative emission accounts for the remaining 3.8% of the total recombination from the L shell[10]. In Fig. 1 we plot the spectrally resolved X-ray emission over a range of excitation photon energies between 1,560 and 1,830 eV. The spectra show the main Kα peak around 1,487 eV, followed by a series of peaks corresponding to emission from higher charge states due to a growing number of L-shell holes.

The observation of Kα emission from highly charged ions in a dense system is not of itself novel, being routinely observed when charged-particle beams (such as ions or optical-laser-generated energetic electrons) interact with solid targets[11–17]. However, our results differ from these experiments in two important ways. First, in our experiment the K-shell holes are created exclusively by intense, quasi-monochromatic X-ray photons rather than by collisions with broadband energetic particles. The main absorption process (creating K-shell holes) will therefore only take place in a particular ion if the photon energy lies above that ion's K edge, or, given that the X-rays are so intense, if a K electron is resonantly pumped to a vacant L-shell state. It follows that the X-ray free-electron laser (FEL) acts not only as a pump—exciting electrons and heating the system—but also as a selective probe, in that

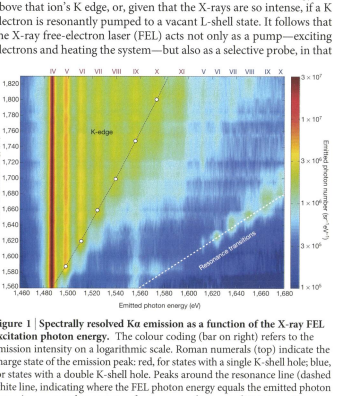

Figure 1 | Spectrally resolved Kα emission as a function of the X-ray FEL excitation photon energy. The colour coding (bar on right) refers to the emission intensity on a logarithmic scale. Roman numerals (top) indicate the charge state of the emission peak: red, for states with a single K-shell hole; blue, for states with a double K-shell hole. Peaks around the resonance line (dashed white line, indicating where the FEL photon energy equals the emitted photon energy) correspond to emission from resonantly-pumped K–L transitions. Open circles, K edges for the various charge states calculated in the SCFLY code, which includes the ionization potential depression in the dense plasma according to a modified version of the Stewart-Pyatt model[21,22].

[1]Department of Physics, Clarendon Laboratory, University of Oxford, Parks Road, Oxford OX1 3PU, UK. [2]Lawrence Berkeley National Laboratory, 1 Cyclotron Road, California 94720, USA. [3]Atomic and Molecular Data Unit, Nuclear Data Section, IAEA, PO Box 100, A-1400, Vienna, Austria. [4]Plasma Physics Department, AWE Aldermaston, Reading RG7 4PR, UK. [5]Institute of Physics ASCR, Na Slovance 2, 18221 Prague 8, Czech Republic. [6]Department of Physics, University of California, Berkeley, California 94720, USA. [7]SLAC National Accelerator Laboratory, 2575 Sand Hill Road, Menlo Park, California 94025, USA. [8]Lawrence Livermore National Laboratory, 7000 East Avenue, Livermore, California 94550, USA. [9]Deutsches-Elektronensynchrotron DESY, Notkestrasse 85, 22603 Hamburg, Germany. [10]OQ, Friedrich-Schiller-Universität Jena, Max-Wien-Platz 1, 07743 Jena, Germany.

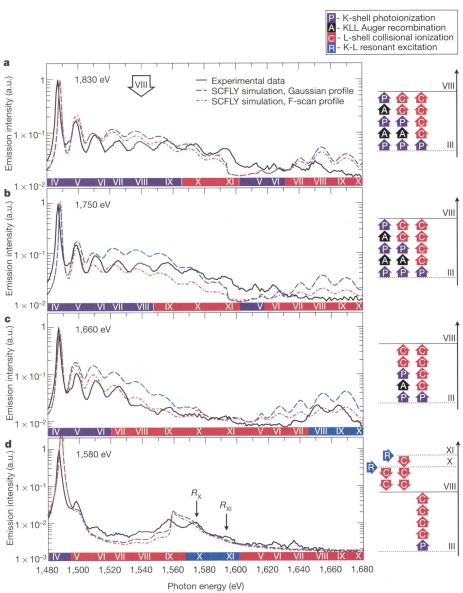

Figure 2 | Experimental and theoretical spectra, and charge-state emission pathways. Left, calculated emission spectra (dashed lines) according to the SCFLY code for four X-ray energies (**a**, 1,830 eV; **b**, 1,750 eV; **c**, 1,660 eV; **d**, 1,580 eV), compared with the experimental results presented in Fig. 1 (solid lines). The two simulation curves correspond to different X-ray intensity distributions on target: a Gaussian profile and the measured F-scan profile. Also shown (right) are the various pathways leading to emission from an ion with five L-shell holes in the final state (VIII), observed as the fifth emission peak: these pathways depend strongly on the wavelength of the X-ray excitation. R_K and R_{XI} correspond to emission from resonant transitions between K- and L-shell states in an ion containing seven or eight L-shell holes, respectively (states X and XI). Colour bars below each plot on left indicate the dominant mechanism contributing to the emission intensity for the various charge states (Roman numerals). a.u., arbitrary units.

the K-shell holes and subsequent Kα emission only occur from a select range of ion charge states, depending on the FEL photon energy. As shown in Fig. 1, the range of ions from which we see K-shell emission is indeed strongly dependent on the energy of the incident photon: at photon energies just above the neutral K edge only a limited number of ionization stages is observed, whereas at the highest photon energy of 1,830 eV we observe all possible ionization stages corresponding to the filling of a single K-shell hole. In addition, at specific photon pump energies, we observe emission from resonantly pumped single- and double-hole K-shell states, marked as resonance transitions in Fig. 1. We label all emission peaks according to their K- and L-shell charge state (the three M-shell electrons are free-electron-like in ground-state Al): that is, the main Kα peak corresponds to charge state IV and the higher energy peaks correspond to states in the range V–XI. The second important difference to note is that in our experiment the population of L-shell states, and the charge state distribution (CSD), is seen to be determined predominantly by electron–ion collisional processes within the heated dense system, rather than directly by the X-ray pulse. Therefore, provided the photon energy is sufficiently high to satisfy the probe condition described above for all charge states, the Kα emission spectrum contains information on the CSD of the hot system, on the electron temperature and on electron–ion collision rates (best observed in the case of resonances where not one but several emission peaks are observed at a single pump energy).

This pivotal role of collisions in determining the observed spectra and the CSD is evinced by two main features in the data. The first is the relatively uniform intensity of the Kα emission as a function of charge state. For isolated atoms, successive sequential photoionization of the K-shell occurs, with the dominant ionization pathway being a P-A-P-A… process (where P indicates photoionization, and A Auger decay)[8]. As each P-A sequence results in two electrons being ejected from the L shell, the populations of ions with an even number of ejected electrons dominate over those with an odd number ejected. In contrast, for the solid-density system, the dynamics are distinctly different, and we observe no odd–even asymmetry in the Kα emission. This is due to the high electron–ion collision rates, which compete with both the P and A processes. Our simulations (below) show that the collisional and Auger rates are comparable at the peak of the pulse at the highest intensities. The second piece of evidence for the important role of collisions is the observation of emission corresponding to resonantly pumped single and double-core-hole states in ion stages for which direct photo-ionization of a K-shell electron is energetically forbidden. As the number of electrons in the L shell decreases, the reduced screening results in tighter binding of the K electrons, increasing the K-edge energy as a function of ion stage (see Fig. 1). Thus, for a particular photon energy, the ejection of a K electron is only possible up to a certain ion stage, explaining the observed fundamental trend where Kα emission is seen from higher charge states as the photon energy is

increased. Nevertheless, this principle can be violated, as the density is so high that additional collisional ionization occurs, promoting further L electrons to the continuum (in addition to those ionized by Auger recombination). Such collisional ionization takes place for ions with two K electrons present and, importantly, is also sufficiently rapid that it can produce further L-shell vacancies in ions already containing a K-shell hole (that is, after photoabsorption, yet before Auger or radiative decay). In the former case, ions with K-edge energies higher than the incident photon energy can be created, but further photo-excitation of K-shell electrons to the continuum for these ions is no longer possible, as the K edge exceeds the photon energy. In the latter case, two interesting effects arise.

First, some Kα emission is still seen from ion stages which have K-edge energies higher than the photon energy, via a process whereby photo-excitation of the K shell occurs at a lower ion stage, collisions ionize further L-shell electrons in the presence of the K-shell hole, then radiative decay occurs producing Kα emission. This effect can be seen in Fig. 1 by comparing the spectrum for a given LCLS photon energy with the calculated energy of the K edge for a particular ion stage. Although accurate independent measurements of the K-edge positions in these hot-dense conditions are not available (we note that our results provide some information in this regard, albeit blurred by strong collisional effects), forcing us to rely on computational modelling, we note that in order to explain the spectra in terms of a K-edge shift alone in the absence of collisional ionization, the calculated shifts would need to be incorrect by several hundred electron volts for the highest charge states. Such a large discrepancy is implausible, but more importantly, would also lead to severely inconsistent simulation results for the emission spectrum. We further note that this observation also cannot be explained by multi-photon ionization, which scales with the square of wavelength, and is negligible even at these intensities in the X-ray regime.

Second, resonant photo-pumping of K-shell electrons to the L shell (rather than to the continuum) is energetically permitted for ions with both a single and a double K-shell hole in the final state. Radiative decay of these states produces the resonance emission highlighted in Fig. 1. Such emission appears prominently for states with two holes in the K-shell (marked as V–X for X-ray excitation in the range 1,600–1,680 eV), as well as from highly ionized states with a single K-shell hole (emission from peaks X and XI at excitation energies around 1,580 eV). In particular, we note that several peaks are observed on resonance rather than just one, indicating that the collisional rates are similar to, or larger than, Auger recombination rates.

To further interpret our results, we have performed time-dependent population kinetics calculations, using the SCFLY code[18]. These simulations provide atomic level populations, CSDs, emission spectra, total absorbed energies and electron temperatures. The calculations are based on a rate-equation model that includes sequential single-photon absorption, spontaneous and stimulated emission, collisional excitation, ionization and their inverses, as well as the effects of opacity via an escape-factor formalism. We plot the calculated spectra for four X-ray excitation energies compared with our experimental measurements in Fig. 2. The interaction processes leading to the observed emission from a specific charge state (VIII) are shown alongside for the four X-ray photon energies, illustrating the different pathways resulting from a combination of direct K-shell photoionization, electron collisional ionization and resonant K–L transitions. We note that the emission intensity from the various charge states is not trivially related to the population of those charge states.

The simulated spectra successfully reproduce the experimental trends in a qualitative manner, however, quantitative differences can still be observed for several charge state emission intensities. This is in part due to uncertainties in the experimental intensity distribution on target, which is challenging to accurately account for (illustrated by the two simulation curves in Fig. 2, corresponding to different spatial profiles), in part to the simplifications made necessary for an efficient atomic-kinetics code, but mostly to uncertainties regarding fundamental physical parameters in warm and hot dense systems, such as the rates for inner-shell transitions, collisional ionization, Auger recombination in highly ionized hollow atoms, and the ionization potential depression. This last point regarding physical parameters is particularly acute in the case of emission from double-core-hole states, where the agreement between experiment and simulation is poorest. Nonetheless, given the qualitative agreement with the spectra and the straightforward energy absorption mechanism, the combined effect of these uncertainties on the basic thermodynamic quantities is not expected to be significant. The calculated electron temperature, free-electron density and CSD are shown in Fig. 3. Temperatures in excess of 100 eV are found, which do not depend strongly on the excitation wavelength. Further, higher X-ray photon energies invariably yield higher temperatures by the end of the pulse, despite having an initially lower absorption cross-section. This can be explained by thermal collisions governing the CSD: as the temperature rises, low charge states are depleted and higher-energy X-rays, which couple more efficiently to higher charge state transitions, deposit more energy in the system. To quantitatively evaluate this collisional effect, we illustrate in Fig. 4 the photoionization, Auger recombination and collisional ionization rates as a function of time for transitions populating and de-populating the single-core-hole charge state VII. We observe that by the peak of the pulse, at temperatures above 100 eV, electron–ion collisional

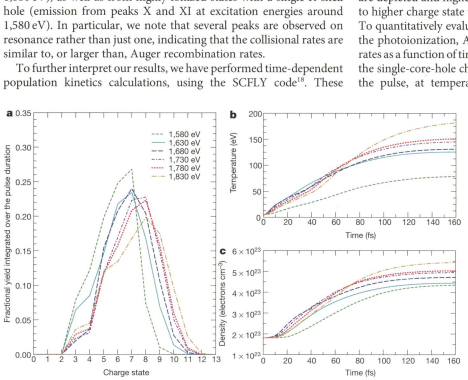

Figure 3 | Temperature, density and charge state distribution at peak intensity. **a**, Calculated charge state distribution, integrated over the duration of a temporally Gaussian pulse. The calculations correspond to the centre of the X-ray spot, at the highest spatial intensities. **b**, **c**, The temperature (**b**) and density (**c**) of the electronic system over a range of excitation energies. The peak of the X-ray pulse is centred at 80 fs, with a FWHM of 80 fs.

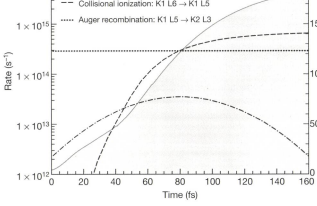

Figure 4 | Rates for atomic and collisional processes. Comparison between K-shell photoionization, collisional ionization and Auger recombination rates (broken curves, left-hand vertical axis) involved in populating and depopulating charge state VII at an X-ray photon energy of 1,830 eV. This state is one of the most populated for conditions leading to a peak temperature of ~100 eV. The calculation is conducted with a Gaussian beam (80 fs FWHM) centred at 80 fs. The electron temperature is given by the solid curve with grey shading under (right-hand vertical axis). By the peak of the pulse at 80 fs, the collisional ionization rate exceeds all others, dominating the population dynamics.

processes dominate the evolution of the CSD, and the dynamics of the system is determined by its temperature rather than by the intense X-ray excitation field. This result is fully consistent with our experimental results shown in Fig. 1.

Finally, in the context of creating well-defined states of matter in extreme conditions, we note that the duration of the pulse, heating of the electrons, photoionization and Auger decay are all rapid processes compared with atomic motion and hydrodynamic expansion of the target. For example, an aluminium ion at 150 eV travels only 5 nm in 100 fs, and thus a crude estimate of the hydrodynamic expansion time would be 20 ps for a 1 μm target. Given that electron–ion relaxation times are expected to be less than 10 ps (ref. 19), these results bode well for the creation of uniform-density hot and warm dense matter.

METHODS SUMMARY

A schematic illustration of the experimental set-up is given in Supplementary Fig. 1. The spectroscopy was conducted by means of a flat ammonium dihydrogen phosphate crystal (ADP) in the ⟨101⟩ orientation with a spectral resolution of 0.9–1.3 eV across the photon energy range of interest. All spectroscopic data were collected in single-shot acquisition mode, with a fresh region of the target exposed for every shot. Figure 1 was obtained by binning a total of around 550 single-shot spectra according to the measured X-ray photon energy in 5-eV bins.

Simulations of the experimental emission were conducted using an adapted version of the collisional-radiative code SCFLY[16], which is based on the widely available FLYCHK simulation suite[20]. SCFLY solves the rate equations for non-LTE (local thermal equilibrium) plasmas using a super-configuration description of the atomic structure of the system and provides a spectral module, which uses the computed level populations to calculate the X-ray emission spectra. Several important improvements have been included to make SCFLY applicable to X-ray FEL-driven systems: an increased number of super-configurations, the inclusion of hollow atoms and a self-consistent, absorption-driven temperature calculation. Each calculation provides an emission spectrum for a single X-ray intensity. To account for the experimental intensity distribution on target, 26 simulations covering the full range of probed intensities were computed for each X-ray excitation energy. The final spectra are obtained by averaging these over the three-dimensional interaction region, weighted according to the intensity distribution profile measured by the imprints technique in lead tungstate ($PbWO_4$). This intensity distribution, named the F-scan profile, which is obtained following the method described in ref. 9, is compared to the Gaussian intensity distribution consistent with the measured spot size (full-width at half-maximum, FWHM) in Fig. 2.

Full Methods and any associated references are available in the online version of the paper at www.nature.com/nature.

Received 27 August; accepted 29 November 2011.
Published online 25 January 2012.

1. Taylor, R. J. *The Stars: Their Structure and Evolution* 2nd edn (Cambridge Univ. Press, 1994).
2. Chabrier, G. Plasma physics and planetary astrophysics. *Plasma Phys. Contr. Fusion* **51,** 124014 (2009).
3. Helled, R., Anderson, J. D., Podolak, M. & Schubert, G. Interior models of Uranus and Neptune. *Astrophys. J.* **726,** 15 (2011).
4. Lindl, J. Development of the indirect-drive approach to inertial confinement fusion and the target physics basis for ignition and gain. *Phys. Plasmas* **2,** 3933–4024 (1995).
5. Remington, B. A., Drake, R. P. & Ryutov, D. D. Experimental astrophysics with high power lasers and Z pinches. *Rev. Mod. Phys.* **78,** 755–807 (2006).
6. Nagler, B. *et al.* Turning solid aluminium transparent by intense soft X-ray photoionization. *Nature Phys.* **5,** 693–696 (2009).
7. Linac Coherent Light Source. https://lcls.slac.stanford.edu (2011).
8. Young, L. *et al.* Femtosecond electronic response of atoms to ultra-intense X-rays. *Nature* **466,** 56–61 (2010).
9. Chalupský, J. *et al.* Spot size characterization of focused non-Gaussian X-ray laser beams. *Opt. Express* **18,** 27836–27845 (2010).
10. Bambynek, W. *et al.* X-Ray fluorescence yields, Auger, and Coster-Kronig transition probabilities. *Rev. Mod. Phys.* **44,** 716–813 (1972).
11. Saemann, A. *et al.* Isochoric heating of solid aluminium by ultrashort laser pulses focused on a tamped target. *Phys. Rev. Lett.* **82,** 4843–4846 (1999).
12. Rossall, A. K. *et al.* X-ray back-lighter characterization for iron opacity measurements using laser-produced aluminium K-alpha emission. *J. Phys. At. Mol. Opt. Phys.* **43,** 155403 (2010).
13. Bailey, J. *et al.* Observation of Kα X-ray satellites from a target heated by an intense ion beam. *Laser Part. Beams* **8,** 555–562 (1990).
14. Burnett, N. H., Enright, G. D., Avery, A., Loen, A. & Kieffer, J. C. Time-resolved Kα spectra in high-intensity laser-target interaction. *Phys. Rev. A* **29,** 2294–2297 (1984).
15. Back, C. A. *et al.* Study of Kα absorption structures in a subcritical-density laser-produced plasma. *Phys. Rev. A* **46,** 3405–3412 (1992).
16. Rousse, A. *et al.* Efficient Kα x-ray source from femtosecond laser-produced plasmas. *Phys. Rev. E* **50,** 2200–2207 (1994).
17. Gauthier, J.-C. *et al.* Theoretical and experimental studies of laser-produced plasmas driven by high-intensity femtosecond laser pulses. *Phys. Plasmas* **4,** 1811–1817 (1997).
18. Chung, H.-K., Chen, M. H. & Lee, R. W. Extension of atomic configuration sets of the non-LTE model in the application to the Kα diagnostics of hot dense matter. *High Energy Density Phys.* **3,** 57–64 (2007).
19. Siwick, B. J., Dwyer, J. R., Jordan, R. E. & Miller, R. J. D. An atomic-level view of melting using femtosecond electron diffraction. *Science* **302,** 1382–1385 (2003).
20. Chung, H.-K., Chen, M. H., Morgan, W. L., Ralchenko, Y. & Lee, R. W. FLYCHK: Generalized population kinetics and spectral model for rapid spectroscopic analysis for all elements. *High Energy Density Phys.* **1,** 3–12 (2005).
21. Stewart, J. C. & Pyatt, K. D. Jr. Lowering of ionization potentials in plasmas. *Astrophys. J.* **144,** 1203–1211 (1966).
22. Chung, H.-K., Lee, R. W., Chen, M. H. & Ralchenko, Y. *The How To for FLYCHK* (NIST, 2008).

Supplementary Information is linked to the online version of the paper at www.nature.com/nature.

Acknowledgements Portions of this research were carried out on the SXR instrument at the LCLS, a division of SLAC National Accelerator Laboratory and an Office of Science user facility operated by Stanford University for the US Department of Energy. The SXR instrument and the Resonant Coherent Imaging (RCI) endstation are funded by a consortium whose membership includes the LCLS, Stanford University through the Stanford Institute for Materials Energy Sciences (SIMES), Lawrence Berkeley National Laboratory (LBNL), University of Hamburg through the BMBF priority programme FSP 301, and the Center for Free Electron Laser Science (CFEL). S.M.V., O.C. and J.S.W. thank the UK EPSRC for funding (EP/F020449/1 and EP/H035877/1). B.I.C., K.E., R.W.F. and P.A.H. acknowledge US DOE Basic Energy Science contract DE-AC03-76SF00098 and SSAA programme contract DE-FG52-06NA26212. T.B., J.C., L.J. and L.V. appreciate funding by grants LC510, LC528, LA08024, ME10046, P108/11/1312, P205/11/0571, IAAX01100903 and KAN300100702. U.Z. thanks the German Ministry for Education and Research (BMBF) for funding (FSP 301. C.D.M. was supported by UK EPSRC (EP/G007187/1). We also thank G. Gregori (Oxford University) for discussions.

Author Contributions S.M.V., B.I.C., K.E., C.R.D.B., A.H., H.J.L., C.D.M., Y.P., S.T., U.Z., P.A.H., B.N. and J.S.W. performed the experiment and acquired the data. B.I.C., K.E., R.W.F. and P.A.H. analysed the data. S.M.V., O.C., H.-K.C., R.W.L. and J.S.W. performed the theoretical work. S.M.V., R.W.L. and J.S.W. wrote the paper. M.M., W.S. and J.J.T. operated the SXR beamline and the LCLS diagnostics. C.G., A.S., T.W., B.W. and D.Z. operated the RCI endstation. T.B., J.C., V.H., L.J., J.K. and L.V. performed the spot-size characterisation and analysis. All authors contributed to the work presented here and to the final paper.

Author Information Reprints and permissions information is available at www.nature.com/reprints. The authors declare no competing financial interests. Readers are welcome to comment on the online version of this article at www.nature.com/nature. Correspondence and requests for materials should be addressed to S.M.V. (sam.vinko@physics.ox.ac.uk).

LETTER

doi:10.1038/nature10787

Quantum-coherent coupling of a mechanical oscillator to an optical cavity mode

E. Verhagen[1]*, S. Deléglise[1]*, S. Weis[1,2]*, A. Schliesser[1,2]* & T. J. Kippenberg[1,2]

Optical laser fields have been widely used to achieve quantum control over the motional and internal degrees of freedom of atoms and ions[1,2], molecules and atomic gases. A route to controlling the quantum states of macroscopic mechanical oscillators in a similar fashion is to exploit the parametric coupling between optical and mechanical degrees of freedom through radiation pressure in suitably engineered optical cavities[3–6]. If the optomechanical coupling is 'quantum coherent'—that is, if the coherent coupling rate exceeds both the optical and the mechanical decoherence rate—quantum states are transferred from the optical field to the mechanical oscillator and vice versa. This transfer allows control of the mechanical oscillator state using the wide range of available quantum optical techniques. So far, however, quantum-coherent coupling of micromechanical oscillators has only been achieved using microwave fields at millikelvin temperatures[7,8]. Optical experiments have not attained this regime owing to the large mechanical decoherence rates[9] and the difficulty of overcoming optical dissipation[10]. Here we achieve quantum-coherent coupling between optical photons and a micromechanical oscillator. Simultaneously, coupling to the cold photon bath cools the mechanical oscillator to an average occupancy of 1.7 ± 0.1 motional quanta. Excitation with weak classical light pulses reveals the exchange of energy between the optical light field and the micromechanical oscillator in the time domain at the level of less than one quantum on average. This optomechanical system establishes an efficient quantum interface between mechanical oscillators and optical photons, which can provide decoherence-free transport of quantum states through optical fibres. Our results offer a route towards the use of mechanical oscillators as quantum transducers or in microwave-to-optical quantum links[11–15].

Mechanical oscillators are at the heart of many precision experiments and can exhibit exceptionally low dissipation. The possibility of controlling the quantum states of engineered micro- or nano-mechanical oscillators has been a subject of long-standing interest[3,16]. Recent experiments have successfully prepared such devices in their quantum ground state, either using standard cryogenic techniques[7] or via dynamical back-action cooling[8,10]. Full control over the quantum state of a mechanical oscillator can be achieved by coupling it to an auxiliary system—whose quantum state can be controlled and measured—under the condition that the coherent coupling rate exceeds the decoherence rate of each of the subsystems. Such quantum-coherent coupling and control at the single-phonon level has been recently demonstrated in the microwave domain by achieving strong coupling of a gigahertz piezoelectrical dilatation oscillator to a (frequency-degenerate) superconducting qubit[7]. Moreover, an electromechanical system has reached the quantum-coherent regime using parametric coupling of a megahertz micromechanical oscillator to a gigahertz microwave resonator[8,17]. Achieving quantum-coherent coupling in the optical domain would provide an interface between mechanical quantum states and optical fields, whose low thermal occupancy at room temperature allows decoherence-free propagation of quantum states out of a cryogenic environment and which can be coupled to a variety of quantum systems. Additionally, optical techniques benefit from the wide availability of quantum-limited detection techniques. In fact, simultaneous achievement of quantum-coherent coupling in the optical and microwave domain provides the possibility of realizing optical-to-microwave conversion of quantum states[15].

Parametric optomechanical coupling occurs in an optical microcavity that simultaneously exhibits a mechanical resonator mode, whose displacement alters the optical resonance frequency. The coupling can be described by the interaction Hamiltonian $H = \hbar g_0 \hat{a}^\dagger \hat{a} \left(\hat{b}^\dagger + \hat{b}\right)$, where $\hat{a}$ ($\hat{a}^\dagger$) and $\hat{b}$ ($\hat{b}^\dagger$) are the photon and phonon annihilation (creation) operators, respectively, $\hbar$ is the reduced Planck constant and g_0 is the vacuum optomechanical coupling rate. In the resolved sideband regime (where the mechanical resonance frequency Ω_m exceeds the cavity energy decay rate κ), with an intense laser tuned close to the lower optomechanical sideband, one obtains in the rotating wave approximation the effective Hamiltonian

$$H = \hbar g \left(\hat{a}\hat{b}^\dagger + \hat{a}^\dagger \hat{b}\right) \tag{1}$$

for the operators $\hat{a}$ and $\hat{b}$ now displaced by their steady state values. We have introduced here the field-enhanced coupling rate[18–20] $g = \sqrt{\bar{n}_c} g_0$, where $\bar{n}_c$ denotes the average number of photons in the cavity. In the absence of decoherence, the unitary evolution given by equation (1) corresponds to swapping of the (displaced) optical and mechanical quantum states with a period of $2\pi/\Omega_c$, where $\Omega_c = 2g$ is the coherent coupling rate, that is, the rate at which the two systems exchange energy. This state swapping is at the heart of most quantum control protocols[11–14,21,22]. In practice, however, this unitary evolution is compromised by the coupling of both degrees of freedom to their respective environments. Hence, it is important for Ω_c to exceed both the optical decoherence rate κ and the relevant mechanical decoherence rate γ. If the mechanical linewidth is limited by dissipation (as is the case in our system[23]), the mechanical decoherence is caused by energy relaxation to the hot environment. Thus, both decoherence rates are defined here as the inverse of the time needed for a single excitation to be lost into the environment. Importantly, the mechanical mode is coupled to an environment that generally has a large thermal occupancy $\bar{n}_m \approx k_B T/\hbar\Omega_m$ (where k_B is Boltzmann's constant and T is temperature) owing to the relatively small mechanical frequency. Therefore, the mechanical decoherence rate $\gamma = \Gamma_m(\bar{n}_m + 1) \approx k_B T/\hbar Q_m$ (where $Q_m = \Omega_m/\Gamma_m$; refs 1, 14) is much larger than the dissipation rate Γ_m. This means that the strong coupling regime $\Omega_c > (\kappa, \Gamma_m)$ (ref. 9) does not suffice to enable quantum control, in contrast to the situation in atomic cavity quantum electrodynamics[2] or in resonant coupling to superconducting qubits of sufficiently high frequency[7]. Instead, for parametrically coupled systems the more stringent condition $\Omega_c > (\kappa, \gamma)$ signals the relevant regime, which we call quantum-coherent coupling.

Here we realize quantum-coherent coupling of an optical cavity field to a micromechanical oscillator. In this regime, the system is

[1]Ecole Polytechnique Fédérale de Lausanne (EPFL), 1015 Lausanne, Switzerland. [2]Max-Planck-Institut für Quantenoptik, Hans-Kopfermann-Strasse 1, 85748 Garching, Germany.
*These authors contributed equally to this work.

appropriately described as an optomechanical polariton whose decoherence time exceeds the period of the Rabi oscillations between light and mechanics. Although the ground state has recently been reported with optical cooling[10], in that work Ω_c was much smaller than κ. In contrast, the present system achieves a coupling rate exceeding both the optical and mechanical decoherence rates, thereby satisfying the necessary conditions for full control of the quantum state of a mechanical oscillator with optical fields[9,12–14,21,22]. The experimental setting is a micro-optomechanical system in the form of a spoke-anchored toroidal optical microcavity[24]. Such devices exhibit whispering gallery mode resonances of high quality factor (with a typical cavity decay rate $\kappa/2\pi < 10$ MHz) coupled to mechanical radial breathing modes via radiation pressure[25]. The vacuum optomechanical coupling rate $g_0 = (\omega_c/R)x_{ZPM}$ can be increased by reducing the radius R of the cavity (here ω_c is the optical cavity resonance frequency and x_{ZPM} is the zero point motion). However, the larger per photon force $\hbar\omega_c/R$ is then usually partially compensated by the increase in the mechanical resonance frequency Ω_m—and correspondingly smaller zero point motion, given by $x_{ZPM} = \sqrt{\hbar/(2m_{eff}\Omega_m)}$ (where m_{eff} is the effective oscillator mass). Moreover, small structures also generally feature larger dissipation through clamping losses. To compensate these opposing effects, we use an optimized spoke-anchor design (see Fig. 1 and Supplementary Information) that maintains low clamping losses and a moderate mechanical resonance frequency while reducing the dimensions of the structure. Devices fabricated in this manner (with $R = 15$ μm) exhibited coupling rates as high as $g_0 = 2\pi \times 3.4$ kHz for a resonance frequency of 78 MHz and a critically coupled sideband factor $\Omega_m/\kappa = 11$.

To reduce the mechanical decoherence rate $\gamma \approx \Gamma_m \bar{n}_m$, the microcavity is embedded in a ^{3}He cryostat (minimum temperature $T_{min} = 650$ mK)[26]. A continuous-wave Ti:sapphire laser beam, whose phase and amplitude quadrature noises are quantum-limited for the Fourier frequencies of interest, is coupled to the microcavity using a tapered optical fibre. The weak mechanical displacement fluctuations are recorded by measuring the phase fluctuations imprinted on the field emerging from the cryostat using balanced homodyne detection. Whereas the coherent coupling rate Ω_c can be determined unambiguously by probing the coherent response of the system[27], the mechanical decoherence rate is affected in a non-trivial way by the light-absorption-dependent sample temperature and the mechanical mode's coupling to its environment, which is dominated by two-level fluctuators at cryogenic temperatures[23,26]. In order to systematically assess the aforementioned effects on the decoherence rate, the coupling laser's frequency $\omega_l = \omega_c + \Delta$ (where Δ denotes the laser detuning) is varied in the vicinity of the lower mechanical sideband, while keeping the launched power constant. This allows the displaced cavity mode $\hat{a}$ (of frequency $|\Delta|$) to be brought in and out of resonance with the mechanical mode $\hat{b}$ (of frequency Ω_m). For each detuning point, we acquire the coherent response of the system to an optical excitation of swept frequency $\omega_l + \Omega_{mod}$ in a first step (Ω_{mod} is the frequency difference from the coupling laser). These spectra (Fig. 2a) allow us to determine all parameters of the model characterizing the optomechanical interaction (Supplementary Information). For large detunings $|\Delta| > \Omega_m$, they essentially feature a Lorentzian response of width κ and centre frequency $|\Delta|$. The sharp dip at $\Omega_{mod} \approx \Omega_m$ originates from optomechanically induced transparency[27] (OMIT), and for $\Omega_m = -\Delta$, its width is approximately Ω_c^2/κ. The coupling rate, as derived from a fit of the coherent response for a laser power of 0.56 mW, is $\Omega_c = 2\pi \times (3.7 \pm 0.05)$ MHz (corresponding to an intracavity photon number of $\bar{n}_c = 3 \times 10^5$).

Additionally, for each value of the detuning, the noise spectrum of the homodyne signal is recorded in the absence of any external excitation (Fig. 2b). The observed peak represents the phase fluctuations imprinted on the transmitted light by the mechanical mode's thermal motion. The constant noise background on these spectra is the shot-noise level for the (constant) laser power used throughout the laser sweep (see Supplementary Information for details). Importantly, the amplitude of the peak is determined by the coupling to and the temperature of the environment, and therefore allows us to extract the mechanical decoherence rate. All parameters now having been measured, it is moreover possible to retrieve the mechanical displacement spectrum (Fig. 2c inset). As can be seen, for detunings close to the sideband, when the (displaced) optical and mechanical modes are degenerate, the fluctuations are strongly reduced. This effect of optomechanical resolved sideband cooling[28] can be understood in a simple picture: in the regime $\Omega_c \ll \kappa$, the optical decay is faster than the swapping between the vacuum in the displaced optical field and the thermal state in the mechanical oscillator. In this case, the mechanical oscillator is coupled to an effective optical bath at near-zero thermal occupancy $\bar{n}_{min}$ with the rate $\Gamma_{cool} = \Omega_c^2/\kappa$. Ideally, $\bar{n}_{min} = \kappa^2/16\Omega_m^2 \ll 1$ is governed by non-resonant Stokes terms $\hat{a}^\dagger\hat{b}^\dagger + \hat{a}\hat{b}$ neglected in the Hamiltonian (equation (1))[18,19].

Evaluating the mechanical decoherence rate for $\Delta = -\Omega_m$ at a cryostat set point of 0.65 K, we find $\gamma = 2\pi \times (2.2 \pm 0.2)$ MHz—significantly smaller than Ω_c. Simultaneously, the average occupancy of the mechanical mode is reduced to $\bar{n} = 1.7 \pm 0.1$ (corresponding to $37 \pm 4\%$ ground state occupation), which is limited by the onset of normal mode splitting. Indeed, as Ω_c approaches κ, the thermal fluctuations are only partially dissipated into the optical bath, and are partially written back onto the mechanics after one Rabi cycle.

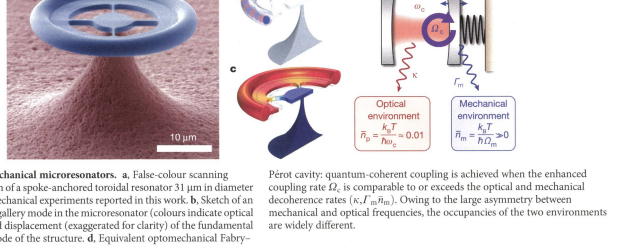

Figure 1 | Optomechanical microresonators. a, False-colour scanning electron micrograph of a spoke-anchored toroidal resonator 31 μm in diameter used for the optomechanical experiments reported in this work. **b**, Sketch of an optical whispering gallery mode in the microresonator (colours indicate optical phase). **c**, Simulated displacement (exaggerated for clarity) of the fundamental radial breathing mode of the structure. **d**, Equivalent optomechanical Fabry–Pérot cavity: quantum-coherent coupling is achieved when the enhanced coupling rate Ω_c is comparable to or exceeds the optical and mechanical decoherence rates ($\kappa, \Gamma_m\bar{n}_m$). Owing to the large asymmetry between mechanical and optical frequencies, the occupancies of the two environments are widely different.

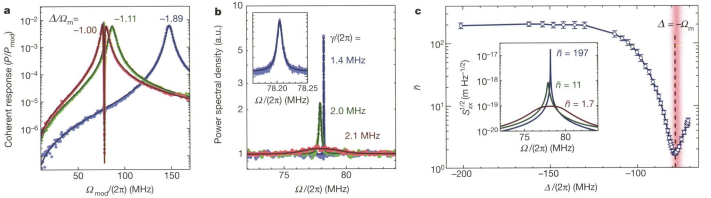

Figure 2 | Optomechanical interaction in the weak coupling regime ($\Omega_c \lesssim \kappa/2$). **a**, The coherent response of the system is obtained by sweeping a weak probe beam (at frequency $\omega_l + \Omega_{mod}$) over the cavity resonance and recording the homodyne signal P (normalized to the power P_{mod} used to create the probe beam). The fitted detuning (Δ/Ω_m) is indicated for each of the traces. The fit provides accurate estimation of the coupling rate Ω_c via the OMIT window (Supplementary Information). **b**, The measured Brownian noise spectrum in the absence of a coherent probe for each of the detunings in **a**. The spectra are corrected for the detector response and a small contribution of Guided Acoustic Wave Brillouin scattering (GAWBS) in the fibres (see Supplementary Information). The inset shows a close-up of the spectrum obtained for $\Delta/\Omega_m = -1.89$. The indicated decoherence rates γ are deduced from the amplitude of each noise spectrum (curves show the result of the model with fitted γ). **c**, Retrieved occupancy as a function of detuning. The minimum occupancy is 1.7 ± 0.1, meaning that the oscillator has a $37 \pm 4\%$ probability of occupying its ground state. The inset shows the inferred mechanical displacement spectral density S_{xx} for detunings used in **a** and **b** calculated using the extracted parameters. Error bars, estimated s.d. (see Supplementary Information).

We subsequently increase the strength of the coupling field to reach $\Omega_c \approx \kappa$. The signature of normal mode splitting[9,17,19,20] can be seen from both the coherent response and the fluctuation spectra (Fig. 3). Both detuning series exhibit a clear anti-crossing, the splitting frequency Ω_c being 5.7 MHz. Note that, in contrast to microwave experiments[8], no squashing is observed in the normal mode splitting data. The decoherence rate (Fig. 3d) is slightly raised compared to Fig. 2 owing to laser heating and a higher buffer gas temperature of 0.8 K, amounting to $\gamma = 2\pi \times (5.6 \pm 0.9)$ MHz at the lower mechanical sideband. We hence demonstrate $\Omega_c/\gamma = 1.0$, which constitutes an improvement of four orders of magnitude over the only previous work demonstrating strong coupling in the optical domain[9], and brings the system into the regime of quantum-coherent coupling. Even though all observed signatures are consistent with classical behaviour, entering this regime opens the door to preparation and control of non-classical states of mechanical motion with light.

As a proof of principle and as a first classical illustration of the potential of time-domain experiments, we demonstrate the dynamical exchange of a pulsed coherent excitation between the optical and mechanical degrees of freedom. By measuring the homodyne signal upon launching a weak pulse resonant with the cavity in the presence of the detuned coupling field (Fig. 4a), it is possible to directly observe the coherent exchange of energy. In the regime of weak coupling, the optical pulse excites the mechanical mode to a finite oscillation amplitude,

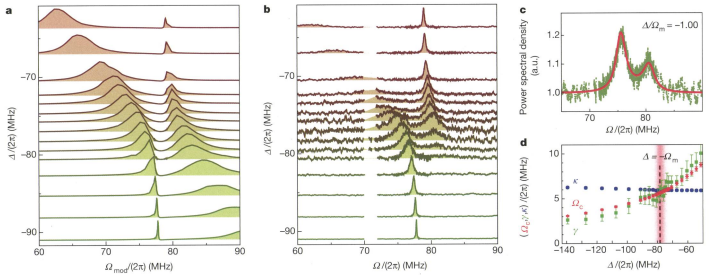

Figure 3 | Quantum-coherent coupling. a, **b**, The coherent optical response (**a**) and the incoherent mechanical noise spectrum (**b**) for various detunings of the coupling laser (with constant power $P = 1.4$ mW). All curves are normalized, and vertically displaced by the detuning. Evident in both panels is the avoided crossing which originates from optomechanical normal mode splitting. A second much more weakly coupled mechanical mode at 71 MHz is omitted and the curves are shaded for clarity. **c**, Homodyne noise spectrum obtained for $\Delta = -\Omega_m$. The red line is a fit of the model. Only the decoherence rate (determining the amplitude) is fitted, while the shape is fixed through the parameters determined from the coherent response. **d**, Comparison of the mechanical (green) and optical (blue) decoherence rates with the coherent coupling rate (red) as a function of detuning. The increase of γ close to resonance reflects heating of the cavity owing to the larger amount of absorbed light. On the lower mechanical sideband, where the interaction is resonant, the decoherence rates are comparable to the coupling rate, achieving quantum-coherent coupling. Error bars, estimated s.d. (see Supplementary Information).

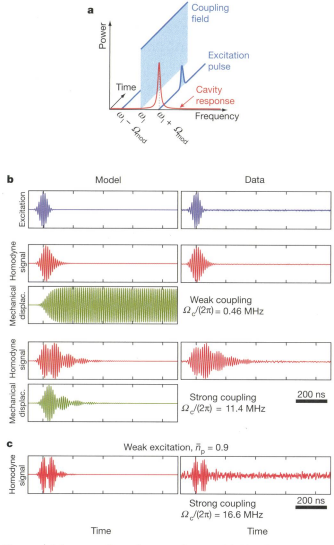

Figure 4 | Coherent exchange between the optical field and the micromechanical oscillator. This exchange is probed in the time domain as measured ('Data') and as calculated numerically ('Model'). A modulation pulse (blue traces) applied to the phase modulator creates an excitation pulse probing the dynamics of the optomechanical system in the presence of the coupling field. The response of the system is encoded into the homodyne output signal (red traces). Using the full model of the system, the mechanical displacement can be simulated in addition (green traces). **a**, Schematic of the excitation scheme, with the cavity frequency response sketched as the red curve. **b**, In the regime of weak coupling (upper panels), the optical output pulse exhibits only a weak signature of the mechanical ringdown excited by the short burst of radiation pressure. In the case of strong coupling (lower panels) the modulated envelopes of the time-domain response indicate several cycles of oscillation between coherent optical and mechanical excitations of the system. **c**, Results for weak excitation (average photon number $\bar{n}_p = 0.9$) and strong coupling.

which decays slowly at the optically damped mechanical dissipation rate. This in turn only imprints a weak signature on the homodyne signal (Fig. 4b). Increasing the laser power, we reach $\Omega_c/2\pi = 11.4\,\mathrm{MHz} > \kappa/2\pi = 7.1\,\mathrm{MHz}$, and the envelope of the homodyne signal—corresponding to the amplitude of the measured sideband field—undergoes several cycles of energy exchange with the mechanical oscillator, before it decays with a modified rate of $(\kappa + \Gamma_m)/2 \approx \kappa/2$, corresponding to the decay rate of the excited optomechanical polariton. Using our model (which has been matched to separately taken coherent response measurements), we can derive not only the homodyne signature—which reproduces our data very well—but also the expected mechanical oscillations resulting from this pulsed excitation. These reveal how the excitation cycles continuously between the optical and mechanical modes. Reducing the excitation further, so that one pulse contains less than one photon on average, a clear signature of several swapping cycles can still be observed (Fig. 4c). Although the average evolution observed here follows classical dynamics and is not affected by decoherence, replacing the weak coherent state in this experiment by a single photon[13,22] is expected to result in Rabi-like oscillation of the Fock state from optics to mechanics as the system resides in the quantum-coherent regime (which we have proved above on the basis of measurements of classical signatures). A repeated quadrature measurement yielding a bimodal distribution would then provide an unambiguous signature of the quantum nature of the state after the full swap[29].

Obtaining quantum-coherent coupling $\Omega_c \gtrsim (\gamma, \kappa)$ has several interesting consequences. It allows the mapping of elemental quantum states of the optical field onto the mechanical mode via the use of a time-dependent coupling field. For example, preparation of the mode in the ground state or the Fock state $|1\rangle$ can be efficiently achieved in this regime using a π-pulse which swaps the thermal state of the oscillator and the quantum state of the displaced optical field. Note that the manipulation of large quantum states becomes increasingly challenging because the lifetime of the number state $|n\rangle$ scales with $1/n$. In this context, it will be beneficial to reduce spurious laser heating and employ materials with low intrinsic loss, as well as to increase the optomechanical coupling rate by further miniaturization. The regime of quantum-coherent coupling demonstrated here has been proposed as a general quantum link between electromagnetic fields of vastly different frequencies—for example, different wavelengths in the optical spectrum or microwave and optical photons[12,15]. Electrical actuation of whispering gallery mode resonators has recently been demonstrated at an elementary level[30]. In this context, the efficient coupling of the demonstrated system to a low-loss single mode optical fibre is beneficial. Moreover, quantum-coherent coupling enables the use of the mechanical oscillator as a transducer to link otherwise incompatible elements in hybrid quantum systems, such as solid-state spin, charge, or superconducting qubits and propagating optical fields[14].

The reported experiments—which achieve quantum-coherent coupling between a micromechanical oscillator and an optical mode—represent an important step into the experimental investigation and optical quantum control of the most tangible harmonic oscillator: a mechanical vibration.

METHODS SUMMARY

The quoted value of g_0 is determined independently at room temperature via a calibrated phase modulation technique. The microcavity is evanescently coupled to a tapered optical fibre in a ^{3}He cryostat using piezoelectric positioning stages. For low optical power, the ^{3}He buffer gas enables thermalization of the resonator over the entire cryogenic temperature range in spite of its weak thermal anchoring to the substrate. A balanced homodyne detection scheme is employed, and a continuous wave Ti:sapphire laser is used to derive both the coupling field and the homodyne local oscillator. Care is taken to avoid excess noise in the coupling beam, as this would cause an effective increase of $\bar{n}_{\mathrm{noise}}$ and preclude any quantum state manipulation. In practice it has proven crucial to eliminate phase noise originating from guided acoustic wave Brillouin scattering in the optical fibres by engineering their acoustic modes using HF etching (Supplementary Information). For the time-domain experiments, the coupling laser's phase is modulated at the mechanical resonance frequency, with a Gaussian envelope of 54 ns duration, creating a pair of sidebands—one of which is resonant with the optical cavity—that contain on average ten quanta per pulse (Supplementary Information). Although the detection used is far from optimized for time-domain experiments, a signal-to-noise ratio of 40 is achieved in Fig. 4b by averaging 250,000 traces within two minutes.

Received 5 September; accepted 9 December 2011.

1. Wineland, D. J. *et al.* Experimental issues in coherent quantum-state manipulation of trapped atomic ions. *J. Res. Natl Inst. Stand. Technol.* **103,** 259–328 (1998).
2. Kimble, H. J. Strong interactions of single atoms and photons in cavity QED. *Phys. Scripta* **T76,** 127–137 (1998).

3. Braginsky, V. B. *Measurement of Weak Forces in Physics Experiments* (Univ. Chicago Press, 1977).
4. Kippenberg, T. J. & Vahala, K. J. Cavity optomechanics: back-action at the mesoscale. *Science* **321,** 1172–1176 (2008).
5. Favero, I. & Karrai, K. Optomechanics of deformable optical cavities. *Nature Photon.* **3,** 201–205 (2009).
6. Clerk, A. A., Devoret, M. H., Girvin, S. M., Marquardt, F. & Schoelkopf, R. J. Introduction to quantum noise, measurement, and amplification. *Rev. Mod. Phys.* **82,** 1155–1208 (2010).
7. O'Connell, A. D. *et al.* Quantum ground state and single-phonon control of a mechanical resonator. *Nature* **464,** 697–703 (2010).
8. Teufel, J. D. *et al.* Sideband cooling of micromechanical motion to the quantum ground state. *Nature* **475,** 359–363 (2011).
9. Gröblacher, S., Hammerer, K., Vanner, M. R. & Aspelmeyer, M. Observation of strong coupling between a micromechanical resonator and an optical cavity field. *Nature* **460,** 724–727 (2009).
10. Chan, J. *et al.* Laser cooling of a nanomechanical oscillator into its quantum ground state. *Nature* **478,** 89–92 (2011).
11. Zhang, J., Peng, K. & Braunstein, S. L. Quantum-state transfer from light to macroscopic oscillators. *Phys. Rev. A* **68,** 013808 (2003).
12. Tian, L. & Wang, H. Optical wavelength conversion of quantum states with optomechanics. *Phys. Rev. A* **82,** 053806 (2010).
13. Akram, U., Kiesel, N., Aspelmeyer, M. & Milburn, G. J. Single-photon optomechanics in the strong coupling regime. *N. J. Phys.* **12,** 083030 (2010).
14. Stannigel, K., Rabl, P., Sorensen, A. S., Zoller, P. & Lukin, M. D. Optomechanical transducers for long-distance quantum communication. *Phys. Rev. Lett.* **105,** 220501 (2010).
15. Regal, C. A. & Lehnert, K. W. From cavity electromechanics to cavity optomechanics. *J. Phys. Conf. Ser.* **264,** 012025 (2011).
16. Schwab, K. C. & Roukes, M. L. Putting mechanics into quantum mechanics. *Phys. Today* **58,** 36–42 (2005).
17. Teufel, J. D. *et al.* Circuit cavity electromechanics in the strong coupling regime. *Nature* **471,** 204–208 (2011).
18. Wilson-Rae, I., Nooshi, N., Zwerger, W. & Kippenberg, T. J. Theory of ground state cooling of a mechanical oscillator using dynamical backaction. *Phys. Rev. Lett.* **99,** 093901 (2007).
19. Marquardt, F., Chen, J. P., Clerk, A. A. & Girvin, S. M. Quantum theory of cavity-assisted sideband cooling of mechanical motion. *Phys. Rev. Lett.* **99,** 093902 (2007).
20. Dobrindt, J. M., Wilson-Rae, I. & Kippenberg, T. J. Parametric normal-mode splitting in cavity optomechanics. *Phys. Rev. Lett.* **101,** 263602 (2008).
21. Khalili, F. *et al.* Preparing a mechanical oscillator in non-Gaussian quantum states. *Phys. Rev. Lett.* **105,** 070403 (2010).
22. Romero-Isart, O. *et al.* Optically levitating dielectrics in the quantum regime: theory and protocols. *Phys. Rev. A* **83,** 013803 (2011).
23. Arcizet, O., Rivière, R., Schliesser, A., Anetsberger, G. & Kippenberg, T. J. Cryogenic properties of optomechanical silica microcavities. *Phys. Rev. A* **80,** 021803(R) (2009).
24. Anetsberger, G., Rivière, R., Schliesser, A., Arcizet, O. & Kippenberg, T. J. Ultralow-dissipation optomechanical resonators on a chip. *Nature Photon.* **2,** 627–633 (2008).
25. Kippenberg, T. J., Rokhsari, H., Carmon, T., Scherer, A. & Vahala, K. J. Analysis of radiation-pressure induced mechanical oscillation of an optical microcavity. *Phys. Rev. Lett.* **95,** 033901 (2005).
26. Rivière, R. *et al.* Optomechanical sideband cooling of a micromechanical oscillator close to the quantum ground state. *Phys. Rev. A* **83,** 063835 (2011).
27. Weis, S. *et al.* Optomechanically induced transparency. *Science* **330,** 1520–1523 (2010).
28. Schliesser, A., Rivière, R., Anetsberger, G., Arcizet, O. & Kippenberg, T. Resolved-sideband cooling of a micromechanical oscillator. *Nature Phys.* **4,** 415–419 (2008).
29. Lvovsky, A. I. *et al.* Quantum state reconstruction of the single-photon Fock state. *Phys. Rev. Lett.* **87,** 050402 (2001).
30. Lee, K. H., McRae, T. G., Harris, G. I., Knittel, J. & Bowen, W. P. Cooling and control of a cavity optoelectromechanical system. *Phys. Rev. Lett.* **104,** 123604 (2010).

Supplementary Information is linked to the online version of the paper at www.nature.com/nature.

Acknowledgements We acknowledge R. Rivière for early contributions to this project and E. Gavartin and I. Vázquez García for assistance in the early microfabrication phase. This work was supported by an ERC Starting Grant (SiMP), the DARPA/MTO ORCHID program through a grant from the AFOSR, the NCCR Quantum Science and Technology and the Swiss National Science Foundation. E.V. acknowledges a Rubicon Grant from the Netherlands Organization for Scientific Research (NWO), co-financed by a Marie Curie Cofund Action. S.D. is supported by a Marie Curie Individual Fellowship.

Author Contributions The cryogenic cooling, measurement, and sample design and fabrication was carried out jointly by S.D., E.V and S.W. The theoretical model for data analysis was developed by A.S. All authors discussed the experimental data and jointly wrote the manuscript. T.J.K. supervised the work.

Author Information Reprints and permissions information is available at www.nature.com/reprints. The authors declare no competing financial interests. Readers are welcome to comment on the online version of this article at www.nature.com/nature. Correspondence and requests for materials should be addressed to T.J.K. (tobias.kippenberg@epfl.ch).

LETTER

doi:10.1038/nature10711

Direct frequency comb spectroscopy in the extreme ultraviolet

Arman Cingöz[1]*, Dylan C. Yost[1]*, Thomas K. Allison[1], Axel Ruehl[2]†, Martin E. Fermann[2], Ingmar Hartl[2] & Jun Ye[1]

The development of the optical frequency comb (a spectrum consisting of a series of evenly spaced lines) has revolutionized metrology and precision spectroscopy owing to its ability to provide a precise and direct link between microwave and optical frequencies[1,2]. A further advance in frequency comb technology is the generation of frequency combs in the extreme-ultraviolet spectral range by means of high-harmonic generation in a femtosecond enhancement cavity[3,4]. Until now, combs produced by this method have lacked sufficient power for applications, a drawback that has also hampered efforts to observe phase coherence of the high-repetition-rate pulse train produced by high-harmonic generation, which is an extremely nonlinear process. Here we report the generation of extreme-ultraviolet frequency combs, reaching wavelengths of 40 nanometres, by coupling a high-power near-infrared frequency comb[5] to a robust femtosecond enhancement cavity. These combs are powerful enough for us to observe single-photon spectroscopy signals for both an argon transition at 82 nanometres and a neon transition at 63 nanometres, thus confirming the combs' coherence in the extreme ultraviolet. The absolute frequency of the argon transition has been determined by direct frequency comb spectroscopy. The resolved ten-megahertz linewidth of the transition, which is limited by the temperature of the argon atoms, is unprecedented in this spectral region and places a stringent upper limit on the linewidth of individual comb teeth. Owing to the lack of continuous-wave lasers, extreme-ultraviolet frequency combs are at present the only promising route to extending ultrahigh-precision spectroscopy to the spectral region below 100 nanometres. At such wavelengths there is a wide range of applications, including the spectroscopy of electronic transitions in molecules[6], experimental tests of bound-state and many-body quantum electrodynamics in singly ionized helium and neutral helium[7–9], the development of next-generation 'nuclear' clocks[10–12] and searches for variation of fundamental constants[13] using the enhanced sensitivity of highly charged ions[14].

Techniques developed to control a train of ultrashort pulses in the frequency domain have led to rapid advancements not only in ultrahigh-precision metrology[1] but also in the generation of attosecond pulses for time-resolved studies[15]. This close relationship between time and frequency techniques continues with the development of the extreme-ultraviolet (XUV) frequency combs, in which high-harmonic generation (HHG), a standard technique in attosecond physics, is used to produce phase-coherent XUV radiation. In conventional HHG, a single infrared pulse generates a burst of attosecond pulses separated by half cycles of the driving laser field, resulting in an odd-harmonic spectrum (Fig. 1). By contrast, in intracavity HHG, a phase-coherent infrared pulse train is used to produce a train of such bursts that repeat at the repetition frequency of the fundamental comb. This new temporal structure is responsible for the much finer frequency comb at each harmonic order. We anticipate that the XUV frequency comb will allow high-precision characterization of the HHG process and provide further insights into attosecond physics.

The existence of the XUV comb structure is critically dependent on the phase coherence of the HHG process. The temporal coherence of HHG in an isolated pulse has been studied extensively[16,17], but the

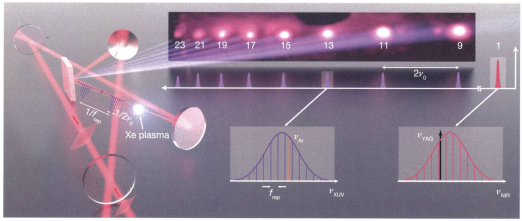

Figure 1 | Intracavity high-harmonic generation. An infrared frequency comb is passively amplified in a power build-up cavity with a mirror/diffraction grating hybrid output coupler for the XUV range[20]. Xenon gas is introduced at the tight focus of the cavity. The resultant HHG spectrum (top inset) from a single infrared pulse consists of odd harmonics of the infrared carrier frequency, ν_0. By using an infinite train of pulses, we create a new comb structure in every harmonic at the repetition frequency (f_{rep}) of the pulse train (lower insets). This comb structure is stabilized using a continuous-wave laser (frequency, ν_{VAG}) and slowly scanned over an argon transition (frequency, ν_{AT}) at 82 nm. ν_{XUV} and ν_{NIR} respectively represent frequencies in the XUV and near-infrared spectral regions.

[1]JILA, National Institute of Standards and Technology and University of Colorado, Department of Physics, University of Colorado, Boulder, Colorado 80309-0440, USA. [2]IMRA America Inc., 1044 Woodridge Avenue, Ann Arbor, Michigan 48105, USA. †Present address: Institute for Lasers, Life and Biophotonics, Vrije Universiteit Amsterdam, De Boelelaan 1081, 1081HV Amsterdam, The Netherlands.
*These authors contributed equally to this work.

requirements are more stringent for XUV comb generation, where the phase coherence must be maintained over many consecutive pulses. This issue has been a topic of investigation since the first demonstrations of intracavity HHG[3,4], in which only the phase coherence of the third harmonic was verified. In subsequent work, pulse-to-pulse temporal coherence of the seventh harmonic at 152 nm, below the ionization threshold, was demonstrated interferometrically[18]. The pulse-to-pulse phase coherence of above-threshold harmonics in the XUV range was first demonstrated in ref. 8. This coherence was critical for two-pulse Ramsey spectroscopy of helium at 51 nm with a systematic uncertainty of 6 MHz (ref. 8) in a widely tunable system[19]. We note that this approach differs fundamentally from the work presented here. The two-pulse Ramsey sequence is a phase measurement and, as a result, is susceptible to systematic phase errors between the two pulses. These errors lead to apparent frequency shifts. Thus, all sources of phase error must be considered and characterized before an absolute frequency measurement can be made. By contrast, a frequency comb consisting of an infinite pulse train is an optical frequency synthesizer with equally spaced frequency comb teeth, defined by only two numbers: the repetition frequency (f_{rep}) of the pulse train and the carrier envelope offset frequency (f_{ceo}). Thus, the phase instabilities can lead to broadening of the comb teeth, but the absolute frequencies of the XUV comb remain simply and robustly determined. It is precisely this characteristic that led to the recent frequency comb revolution in metrology even though multipulse Ramsey spectroscopy in the visible and infrared spectral regions has existed since the late 1970s[20]. In this Letter, we demonstrate the extension of frequency comb spectroscopy to the XUV spectral region, which will lead to many applications in short-wavelength metrology.

In intracavity HHG, a high-average-power infrared frequency comb[5] is coupled to a dispersion-controlled optical cavity (Fig. 1), which allows for passive coherent pulse build-up at the full repetition rate of 154 MHz (Supplementary Information). The high repetition rate of intracavity HHG should in principle provide increased average flux relative to conventional single-pass HHG systems, which typically use lasers with repetition frequencies and average powers that are smaller by orders of magnitude. However, until now the presence of the optical cavity has presented challenges to matching the average flux of these systems, owing to optical damage problems associated with the large average intracavity power and to the nonlinear-response of the HHG medium. At the high intensities and gas densities required to optimize the XUV flux, the plasma density at the intracavity focus reaches levels that can lead to various nonlinearities such as optical bistability, self-phase modulation and pulse distortion. Recently, these effects have been studied in detail with both simulations and experiments[21,22]. These effects, amplified by the narrow cavity linewidth, clamp the achievable intracavity peak power and lead to instabilities in the lock between the comb and the cavity, limiting the attainable XUV flux and coherence time. Thus, a robust means of mitigating these effects is to decrease the finesse. However, this requires that a more powerful laser be used to excite the enhancement cavity to keep the intracavity pulse energy high. This obstacle has been overcome by recent advances in high-repetition-rate, high-average-power chirped-pulse amplified Yb:fibre lasers[5,23–25].

Our ability to reach high intracavity pulse energies while minimizing the deleterious effects of a large plasma density has resulted in the generation of unprecedented power in high harmonics spectrally separated for spectroscopy. We measure the power in the fifteenth harmonic to be 21 μW with xenon as the target gas (Fig. 2), which corresponds to more than 200 μW per harmonic produced in the cavity. This is an increase of more than an order of magnitude over previous intracavity HHG results[26,27]. Similar outcoupled power (not spectrally separated) was recently reported[28]. We have also observed shorter-wavelength radiation by using krypton as the target gas for HHG. Owing to the higher ionization potential of krypton, we were able to detect the twenty-fifth and twenty-seventh harmonic orders

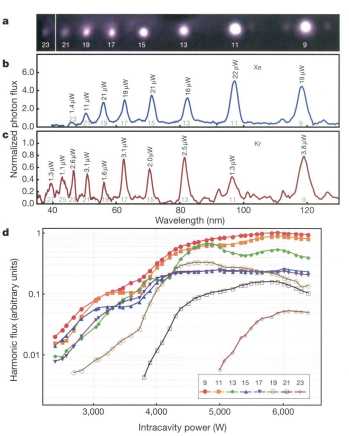

Figure 2 | Power scaling results. a, Characteristic image of the harmonics in xenon dispersed on a plate coated with fluorescent material. The threshold of the image was adjusted for the twenty-third harmonic to make it more visible. **b**, **c**, Vertically integrated intensity from a charge-coupled-device (CCD) image for xenon (**b**) and krypton (**c**) target gas, and corresponding integrated harmonic powers (Methods Summary). The observed widths of the harmonic orders are given by the instrument wavelength resolution. The photon flux has been normalized by the spectral bandwidth. **d**, Harmonic powers generated in xenon as functions of infrared intracavity power, showing saturation at powers greater than 5.5 kW. The oscillations visible for some harmonics are due to quantum path interference[18].

with 8 kW of intracavity power (peak intensity of 9×10^{13} W cm^{-2}) (Fig. 2c), extending intracavity HHG to photon energies above 30 eV. As shown in Fig. 2d, there are only modest improvements in power for most harmonics as the intracavity infrared power is increased above 5.5 kW. As the plasma density increases, depletion of the on-axis neutral atomic density and a decrease in phase matching cause the XUV power clamp. These results show that future gains in harmonic power in a similar system will most probably be achieved by increasing the focal area at the interaction region.

To demonstrate the comb structure of XUV radiation, we have spectrally resolved the $3s^23p^6\ J = 0 \rightarrow 3s^23p^55d\ J = 1$ electric dipole (E1) transition in argon with an upper-state energy of 121,932.8 cm^{-1} (corresponding to a wavelength of ~82 nm) and the $2s^22p^6\ J = 0 \rightarrow 2s^22p^54s\ J = 1$ E1 transition in neon with an upper-state energy of 159,534.6 cm^{-1} (~63 nm) by means of resonance fluorescence spectroscopy. These transitions lie within the thirteenth and seventeenth harmonic bandwidths of our source, respectively. To reduce the Doppler width of the transition below the repetition frequency of the comb, we use pulsed supersonic atomic beams propagating orthogonally to the XUV beam. The average harmonic power available for spectroscopy is ~1 μW owing to a single reflection from a mirror to steer the XUV beam into the interaction region and several pinholes to isolate the central part of the beam that contains the phase-coherent short trajectories[18]. Moreover, owing to the electric dipole nature of these transitions, only a single comb tooth with ~10^{-5} of the total power,

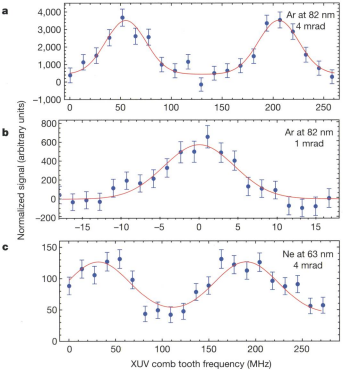

Figure 3 | Atomic fluorescence signal. **a**, **b**, Photomultiplier signals as functions of an XUV comb tooth frequency for argon beam collimation angles of ~4 mrad (**a**) and ~1 mrad (**b**). The signal is normalized to the incident XUV power and the scattered photon background is subtracted (Methods Summary). Error bars (1 s.d.) are determined from the shot noise of counted fluorescence photons. The red curves are least-squares fits to a Gaussian model. **c**, Signal for the neon transition with a collimation angle of ~4 mrad. The contrast and signal-to-noise ratio are lower owing to the increased Doppler width and the smaller absorption cross-section, respectively.

10 pW, contributes to the signal. Nevertheless, we have achieved a ratio of signal to scattered photon background in the range of 0.5–1 using a photomultiplier tube to detect directly the XUV spontaneous emission to the ground state.

The fundamental infrared comb is controlled by phase-locking a comb tooth to a continuous-wave neodymium-doped yttrium aluminium garnet (Nd:YAG) laser by feedback onto the laser cavity length[2]. The Nd:YAG laser frequency (ν_{YAG}) is referenced to a molecular iodine transition and serves as an absolute optical frequency marker with an uncertainty of 5 kHz (ref. 29). The comb offset frequency, f_{ceo}, has a free-running linewidth of 15 kHz (ref. 5) and is adjusted to optimize intracavity power, but is otherwise unlocked. Its value is deduced from the knowledge of ν_{YAG} and f_{rep}, which we measure against the hydrogen maser at the US National Institute of Standards and Technology (Supplementary Information). Figure 3 shows the fluorescence signal as the phase-locked-loop offset frequency, δ, is slowly changed and XUV comb teeth are scanned across the atomic resonance for two different collimation angles of the atomic beam. With the scattered photon background subtracted, the signal contrast is 100%, confirming the sharp comb structure. Least-squares fits for the argon data reveal respective Gaussian full-widths at half-maximum of 47 ± 5 and 11 ± 1 MHz for the two angles. These results are consistent with what would be expected from the geometric collimation. Thus, the observed linewidth places only an upper bound on the comb teeth linewidth, and this bound is less than 10 MHz. The statistical uncertainty in the determination of the line centre for the narrower line shape is 500 kHz, demonstrating an unprecedented fractional frequency precision of better than 2×10^{-10} in the XUV range.

To determine the absolute frequency of the argon transition, it is necessary to determine the comb tooth number in addition to f_{rep} and f_{ceo}. This requires making several measurements at different values of f_{rep} and keeping track of the change in the comb tooth number (Supplementary Information). Figure 4 shows the results of ten measurements at different values of f_{rep} chosen to provide absolute comb mode determination. The data analysis is carried out by noting that the fixed point of the infrared comb (comb tooth phase locked to the Nd:YAG laser) is multiplied by the HHG process to create corresponding fixed points for every harmonic comb. These fixed points are offset from $q\nu_{YAG}$ by $\Delta = q\delta$(modulo f_{rep}), where q is the harmonic order. Thus, the argon transition frequency is

$$\nu_{Ar} = nf_{rep} + 13f_{ceo} = mf_{rep} + 13\nu_{YAG} + \Delta$$

where n is the absolute comb tooth number and m is the difference in comb tooth number between the thirteenth harmonic fixed point and the actual comb tooth probing the argon transition. This point of view not only makes the analysis independent of drifts in f_{ceo}, but also highlights the direct frequency link between the infrared and the higher-harmonic combs.

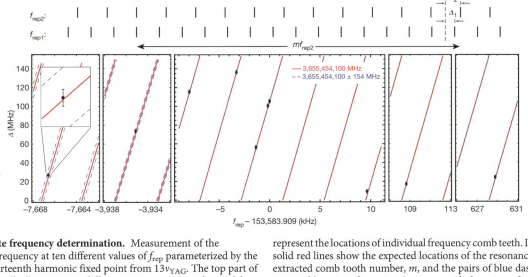

Figure 4 | Absolute frequency determination. Measurement of the resonance centre frequency at ten different values of f_{rep} parameterized by the offset, Δ, of the thirteenth harmonic fixed point from $13\nu_{YAG}$. The top part of the figure schematically illustrates two different measurements at f_{rep1} and f_{rep2}, with corresponding respective offsets of Δ_1 and Δ_2. The short black lines represent the locations of individual frequency comb teeth. In the main plot, the solid red lines show the expected locations of the resonance centres for the extracted comb tooth number, m, and the pairs of blue dashed lines show the expected locations for $m \pm 1$. Inset, magnified version of a measurement, demonstrating that the comb tooth number is unambiguously determined.

Once m is determined, we correct the final value for residual Doppler shifts arising from imperfect orthogonal alignment of the laser and the atomic beam. This is done by comparing the measured transition frequency of a pure argon beam (velocity of 520 ± 20 m s^{-1}) with that of a helium–argon mixture (5:1 ratio of partial pressures; velocity of 740 ± 60 m s^{-1}) and translating the collimation slit until the two measured frequencies match, ensuring orthogonality between the laser and the atomic beams. Owing to the small fractional change in the velocity of the two beams, the uncertainty in the procedure is ~3 MHz. All other systematic shifts such as recoil, density and Stark shifts, as well as the contribution due to the uncertainty in ν_{YAG}, are estimated to be smaller than 1 MHz. We have also binned our data for different laser operation conditions and find no systematic shifts at the 2-MHz level for a 30% change in xenon backing pressure or a 20% change in the intracavity power for HHG, again highlighting the robustness of the XUV comb for frequency measurements. The final absolute frequency for this transition is $3{,}655{,}454{,}073 \pm 3$ MHz, which agrees well with previous measurements that have an uncertainty of 2.3 GHz (ref. 30).

Now that the XUV frequency comb has been developed into a robust tool, it is imperative to determine its ultimate coherence. The current upper bound on the thirteenth harmonic comb linewidth is less than 10 MHz, limited by the atomic thermal motion. We plan to implement a heterodyne beat measurement between two intracavity HHG sources to overcome this limitation, improving the phase noise characterization by orders of magnitude. With these developments, ultrahigh-precision spectroscopy in the XUV range is firmly within our grasp, enabling a wide range of applications.

METHODS SUMMARY

The Ybfibre comb delivers 120-fs pulses at a 154-MHz repetition frequency with a maximum average power of 80 W (ref. 5). For the studies presented here, we run the laser at ~30 W. Target gas is injected at the intracavity focus using a glass nozzle with a 100-μm aperture and a backing pressure of ~2 atm. The XUV light is coupled out of the cavity using an intracavity diffraction grating with 10% efficiency[28].

The power of the thirteenth harmonic is measured with an XUV photodiode. The power in the other harmonics is determined using a plate coated with sodium salicylate, which fluoresces at 420 nm when excited by XUV radiation, with uniform quantum efficiency between 40 and 100 nm (ref. 18). The fluorescence is imaged using a CCD camera and calibrated using the thirteenth harmonic, which can be measured with either the photodiode or the CCD. The estimated calibration uncertainty is 20–30%.

The supersonic argon source consists of a pulsed valve nozzle (0.5-mm diameter), a 0.5-mm-diameter skimmer and a secondary slit located 33 cm from the skimmer. Both the slit width and slit position can be adjusted to study the Doppler width and shifts. The valve generates 500-μs-long pulses at a repetition rate of 20 Hz with a backing pressure of 0.5 atm.

The fluorescence is detected with a photomultiplier tube and pulse counter. The counter has two gates: one coincident with the argon pulse arrival time, to measure the signal; and another located between argon pulses, to measure the background. Most of the laser light passes through the interaction region unimpeded and is detected with a second XUV photodiode, which provides the normalization signal. Individual frequency scans take ~150 s. Results presented in Fig. 3 are averages of 3–10 scans with an acquisition time of 8–25 min.

Received 9 September; accepted 3 November 2011.

1. Udem, T., Holzwarth, R. & Hänsch, T. W. Optical frequency metrology. *Nature* **416,** 233–237 (2002).
2. Cundiff, S. T. & Ye, J. Femtosecond optical frequency combs. *Rev. Mod. Phys.* **75,** 325–342 (2003).
3. Jones, R. J., Moll, K. D., Thorpe, M. J. & Ye, J. Phase-coherent frequency combs in the vacuum ultraviolet via high-harmonic generation inside a femtosecond enhancement cavity. *Phys. Rev. Lett.* **94,** 193201 (2005).
4. Gohle, C. *et al.* A frequency comb in the extreme ultraviolet. *Nature* **436,** 234–237 (2005).
5. Ruehl, A., Marcinkevicius, A., Fermann, M. E. & Hartl, I. 80 W, 120 fs Yb-fiber frequency comb. *Opt. Lett.* **35,** 3015–3017 (2010).
6. Merkt, F. & Softley, T. P. Final-state interactions in the zero-kinetic-energy-photoelectron spectrum of H_2. *J. Chem. Phys.* **96,** 4149–4156 (1992).
7. Herrmann, M. *et al.* Feasibility of coherent XUV spectroscopy on the 1S–2S transition in singly ionized helium. *Phys. Rev. A* **79,** 052505 (2009).
8. Kandula, D. Z., Gohle, C., Pinkert, T. J., Ubachs, W. & Eikema, K. S. E. Extreme ultraviolet frequency comb metrology. *Phys. Rev. Lett.* **105,** 063001 (2010).
9. Eyler, E. E. *et al.* Prospects for precision measurements of atomic helium using direct frequency comb spectroscopy. *Eur. Phys. J. D* **48,** 43–55 (2008).
10. Peik, E. & Tamm, C. Nuclear laser spectroscopy of the 3.5 eV transition in Th-229. *Europhys. Lett.* **61,** 181–186 (2003).
11. Rellergert, W. G. *et al.* Constraining the evolution of the fundamental constants with a solid-state optical frequency reference based on the ^{229}Th nucleus. *Phys. Rev. Lett.* **104,** 200802 (2010).
12. Campbell, C. J., Radnaev, A. G. & Kuzmich, A. Wigner crystals of ^{229}Th for optical excitation of the nuclear isomer. *Phys. Rev. Lett.* **106,** 223001 (2011).
13. Murphy, M. T., Webb, J. K. & Flambaum, V. V. Further evidence for a variable fine-structure constant from Keck/HIRES QSO absorption spectra. *Mon. Not. R. Astron. Soc.* **345,** 609–638 (2003).
14. Berengut, J. C., Dzuba, V. A., Flambaum, V. V. & Ong, A. Electron-hole transitions in multiply charged ions for precision laser spectroscopy and searching for variations in alpha. *Phys. Rev. Lett.* **106,** 210802 (2011).
15. Krausz, F. & Ivanov, M. Attosecond physics. *Rev. Mod. Phys.* **81,** 163–234 (2009).
16. Bellini, M. *et al.* Temporal coherence of ultrashort high-order harmonic pulses. *Phys. Rev. Lett.* **81,** 297–300 (1998).
17. Mairesse, Y. *et al.* Attosecond synchronization of high-harmonic soft X-rays. *Science* **302,** 1540–1543 (2003).
18. Yost, D. C. *et al.* Vacuum-ultraviolet frequency combs from below-threshold harmonics. *Nature Phys.* **5,** 815–820 (2009).
19. Pinkert, T. J. *et al.* Widely tunable extreme UV frequency comb generation. *Opt. Lett.* **36,** 2026–2028 (2011).
20. Eckstein, J. N., Ferguson, A. I. & Hänsch, T. W. High-resolution two-photon spectroscopy with picosecond light pulses. *Phys. Rev. Lett.* **40,** 847–850 (1978).
21. Allison, T. K., Cingöz, A., Yost, D. C. & Ye, J. Extreme nonlinear optics in a femtosecond enhancement cavity. *Phys. Rev. Lett* **107,** 183903 (2011).
22. Carlson, D. R., Lee, J., Mongelli, J., Wright, E. M. & Jones, R. J. Intracavity ionization and pulse formation in femtosecond enhancement cavities. *Opt. Lett.* **36,** 2991–2993 (2011).
23. Hartl, I. *et al.* Cavity-enhanced similariton Yb-fiber laser frequency comb: 3×10^{14} W/cm^2 peak intensity at 136 MHz. *Opt. Lett.* **32,** 2870–2872 (2007).
24. Schibli, T. R. *et al.* Optical frequency comb with submillihertz linewidth and more than 10 W average power. *Nature Photon.* **2,** 355–359 (2008).
25. Eidam, T. *et al.* Femtosecond fiber CPA system emitting 830 W average output power. *Opt. Lett.* **35,** 94–96 (2010).
26. Yost, D. C., Schibli, T. R. & Ye, J. Efficient output coupling of intracavity high-harmonic generation. *Opt. Lett.* **33,** 1099–1101 (2008).
27. Ozawa, A. *et al.* High harmonic frequency combs for high resolution spectroscopy. *Phys. Rev. Lett.* **100,** 253901 (2008).
28. Lee, J., Carlson, D. & Jones, R. J. Optimizing intracavity high harmonic generation for XUV fs frequency combs. *Opt. Express* **19,** 23315–23326 (2011).
29. Ye, J., Ma, L.-S. & Hall, J. L. Molecular iodine clock. *Phys. Rev. Lett.* **87,** 270801 (2001).
30. Minnhagen, L. Spectrum and the energy levels of neutral argon, Ar I. *J. Opt. Soc. Am.* **63,** 1185–1198 (1973).

Supplementary Information is linked to the online version of the paper at www.nature.com/nature.

Acknowledgements We thank J. L. Hall for the use of an iodine-stabilized laser, M. D. Swallows for the assistance with the hydrogen maser frequency transfer, and S. T. Cundiff and A. Foltynowicz for reading a draft of the manuscript. This research is funded by the DARPA, AFOSR, NIST and NSF. A.C. and T.K.A. are National Research Council postdoctoral fellows. A.R. acknowledges funding from the Alexander von Humboldt Foundation (Germany).

Author Contributions A.C., D.C.Y., T.K.A. and J.Y. conceived of, designed and carried out the XUV power and spectroscopy measurements. A.R., M.E.F. and I.H. designed and built the Yb:fibre laser. All authors discussed the results and worked on the manuscript.

Author Information Reprints and permissions information is available at www.nature.com/reprints. The authors declare no competing financial interests. Readers are welcome to comment on the online version of this article at www.nature.com/nature. Correspondence and requests for materials should be addressed to A.C. (acingoz@jila.colorado.edu) or J.Y. (junye@jila.colorado.edu).

LETTER

doi:10.1038/nature10739

Nonlinear material behaviour of spider silk yields robust webs

Steven W. Cranford[1,2], Anna Tarakanova[1,2,3], Nicola M. Pugno[4] & Markus J. Buehler[1,2,5]

Natural materials are renowned for exquisite designs that optimize function, as illustrated by the elasticity of blood vessels, the toughness of bone and the protection offered by nacre[1–5]. Particularly intriguing are spider silks, with studies having explored properties ranging from their protein sequence[6] to the geometry of a web[7]. This material system[8], highly adapted to meet a spider's many needs, has superior mechanical properties[9–15]. In spite of much research into the molecular design underpinning the outstanding performance of silk fibres[1,6,10,13,16,17], and into the mechanical characteristics of web-like structures[18–21], it remains unknown how the mechanical characteristics of spider silk contribute to the integrity and performance of a spider web. Here we report web deformation experiments and simulations that identify the nonlinear response of silk threads to stress—involving softening at a yield point and substantial stiffening at large strain until failure—as being crucial to localize load-induced deformation and resulting in mechanically robust spider webs. Control simulations confirmed that a nonlinear stress response results in superior resistance to structural defects in the web compared to linear elastic or elastic–plastic (softening) material behaviour. We also show that under distributed loads, such as those exerted by wind, the stiff behaviour of silk under small deformation, before the yield point, is essential in maintaining the web's structural integrity. The superior performance of silk in webs is therefore not due merely to its exceptional ultimate strength and strain, but arises from the nonlinear response of silk threads to strain and their geometrical arrangement in a web.

Although spider silk is used by spiders for many purposes, from wrapping prey to lining retreats[22,23], here we focus on silk's structural role in aerial webs and on how silk's material properties relate to web function. The mechanical behaviour of silk, like that of other biological materials, is determined by the nature of its constituent molecules and their hierarchical assembly into fibres[13,16,17,24–26] (Supplementary Fig. 1). Spider webs themselves are characterized by a highly organized geometry that optimizes their function[7,9,18–20]. To explore the contribution of the material characteristics to web function, we developed a web model with spiral and radial threads based on the geometry commonly found in orb webs[1]. The silk material behaviour was parameterized from atomistic simulations of dragline silk from the species *Nephila clavipes* (model A)[16,17] (Fig. 1a, b) and validated against experiments[10] (Methods Summary). Properties of silk can vary across evolutionary lineages by over 100% (refs 9, 27 and 28; Supplementary Information section 1), so we avoided species-specific silk properties and instead used a representative model to reflect the characteristic nonlinear stress–strain (σ–ε) behaviour of silk found in a web. The mechanical performance of individual silk threads has been previously investigated[10,12,13], and is in agreement with our model in terms of tensile deformation behaviour.

It is rare to see a perfectly intact web—debris, attack or unstable anchorage lead to loss of threads (see inset to Fig. 1c)—but the structure usually remains functional for a spider's use. We assessed a web's ability to tolerate defects by removing web sections (silk threads) and applying a local load (Fig. 1c). Removal of up to 10% of threads, at different locations relative to the load, had little impact on the web's response; in fact, the ultimate load capacity increased by 3–10% with the introduction of defects (Fig. 1c). We observed in all cases that failure is limited to the thread to which the force is applied. Loading of a spiral thread resulted in relatively isolated web distortion (Fig. 1e), whereas loading of a radial thread (Fig. 1f) resulted in larger deformation (about 20% more deflection and about 190% increase in energy dissipation; Fig. 1d). But in both cases, failure was localized (Fig. 1e, f). A comparative study of loading radial versus spiral threads demonstrated that the web's structural performance is dominated by the properties of the stiffer and stronger radial dragline silk (with the force required to break radial threads within the web approximately 150% higher), suggesting that the spiral threads play non-structural roles (such as capturing prey).

In situ experiments on a garden spider (*Araneus diadematus*) web (Fig. 1e, f) were in qualitative agreement with the simulations: they confirmed the prediction that failure is localized when loading either a spiral or a radial thread. Complementing these findings, we used our atomistic silk model[16,17] to connect the stress states in the web (Fig. 2a, top row) with molecular deformation mechanisms in the threads (Fig. 1a). Under loading and immediately before failure, most radial threads in the structure exhibited deformation states equivalent to the yield regime (regime II in Fig. 1a), where the presence of polymer-like semi-amorphous regions permits entropic unfolding of the silk nanocomposite under relatively low stress[16,17,29]. Once unfolding is complete, the system stiffens as stress is transferred to relatively rigid β-sheet nanocrystals[17] (regimes III–IV in Fig. 1a); it finally fails, at the thread where force is applied, because the applied stress is sufficient to rupture the nanocrystals.

Simulation and experiment both indicated that localized failure is a universal characteristic of spider webs. It is unresolved whether this behaviour is unique to silk-like materials or a result of the web's architecture (that is, a property of the construction material or of the structural design). We therefore systematically compared the response of webs constructed from three different types of fibres with distinct mechanical behaviour (Fig. 2a, left panels): in addition to fibres with the atomistically derived stress–strain behaviour of dragline silk (model A), we used idealized engineered fibres that exhibited either linear elastic behaviour (model A′) or elastic–perfectly plastic behaviour that involves severe softening (plastic yield) (model A″). In all cases, we loaded one of the radial threads and assumed that the failure stress (about 1,400 MPa) and strain (about 67%) of silk threads are constant, so that any changes in deformation behaviour (Fig. 2a, right

[1]Laboratory for Atomistic and Molecular Mechanics (LAMM), Department of Civil and Environmental Engineering, Massachusetts Institute of Technology, 77 Massachusetts Avenue, Cambridge, Massachusetts 02139, USA. [2]Center for Materials Science and Engineering, Massachusetts Institute of Technology, 77 Massachusetts Avenue, Cambridge, Massachusetts 02139, USA. [3]Department of Applied and Engineering Physics, Cornell University, Ithaca, New York 14853, USA. [4]Laboratory of Bio-Inspired Nanomechanics "Giuseppe Maria Pugno", Department of Structural Engineering and Geotechnics, Politecnico di Torino, Corso Duca degli Abruzzi 24, 10129 Torino, Italy. [5]Center for Computational Engineering, Massachusetts Institute of Technology, 77 Massachusetts Avenue, Cambridge, Massachusetts 02139, USA.

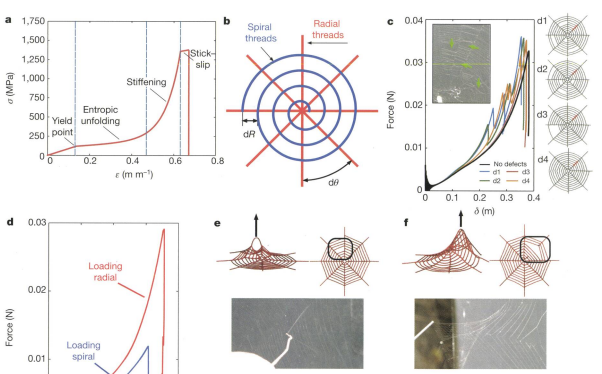

Figure 1 | Material behaviour of dragline spider silk, web model, and behaviour of webs under load. **a**, Derived stress–strain (σ–ε) behaviour of dragline silk, parameterized from atomistic simulations and validated against experiments[16,17]. There are four distinct regimes characteristic of silk[16,17]. I, stiff initial response governed by homogeneous stretching; II, entropic unfolding of semi-amorphous protein domains; III, stiffening regime as molecules align and load is transferred to the β-sheet crystals; and IV, stick–slip deformation of β-sheet crystals[16] until failure. **b**, Schematic of web model, approximated by a continuous spiral (defined by dR) supported by eight regular radial silk threads (defined by $d\theta$), typical of orb webs[7]. **c**, Force–displacement curves for loading a defective web (results for model A; loaded region shown in red). Case studies include missing spiral segments (d1 to d3) and a missing radial thread (d4). The inset to **c** shows the *in situ* orb web as discovered, containing many defects (marked by green arrows). **d**, Force–displacement behaviour of web, comparing the loading of a single radial thread and a single spiral thread (model A). **e**, Loading of a spiral thread results in small web deformation. **f**, Loading applied at radial threads results in an increase in web deformation. In both cases (**e** and **f**) failure is isolated to the pulled thread in simulation and experiment, restricting damage to a small section of the web (indicated by white rectangles).

panels) and web damage (Fig. 2a, middle panels) would be a direct result of differences in the stress–strain behaviour of the fibres. In the case of a web comprised of natural dragline silk (top panels of Fig. 2a), all radial threads contributed partially to the resistance to loading, but the fact that the material suddenly softened at the yield point, which immediately reduced the initial modulus (about 1,000 MPa) by around 80%, ensured that only the loaded radial thread entered regime III and began to stiffen before it finally failed. With linear elastic material behaviour (middle panels of Fig. 2a), the loaded radial thread was still subjected to the bulk of the load; but adjacent radial threads bore a higher fraction of the ultimate load, which resulted in a greater delocalization of damage upon failure. With elastic–perfectly plastic behaviour (bottom panels of Fig. 2a), the softening of radial threads enhanced the load distribution even more throughout the web and thereby greatly increased the damage zone once failure occurred. The increased contribution of the auxiliary radial threads to load resistance as we moved from the natural to linear elastic to elastic–perfectly plastic behaviour resulted in 34% higher maximum strength, but 30% less displacement at failure (Fig. 2b).

The above simulations using atomistically derived silk properties (model A) assume that the spiral threads and radial threads are made of dragline silk and behave identically, except for differences arising from their different thread diameters. But in real spider webs, spiral threads are composed of more compliant and extensible viscid silk (for example, a failure strain of around 270% for the species *Araneus diadematus*[1]). To explore the effect of different silks making up the spiral and radial threads, we introduced empirically parameterized viscid spiral threads[1] (model B) and found that the results were only marginally affected (Fig. 2b). We also used a model in which we parameterized both spiral and radial threads according to empirical data[1] (model C), subjected this model to the same loading conditions and systematically compared its performance against that of models with linear elastic (model C′) and elastic–perfectly plastic behaviours (model C″). We found similar web responses and although the web made from natural silk is weaker, it still localizes damage near the loaded region (Supplementary Information section 5).

To explore global loading responses, we subjected the web models to a homogeneously distributed wind load with effective wind speeds up to 70 m s^{-1} (a threshold at which all models fail). The system-level deflection curves (Fig. 2c) reflect the mechanical behaviour of the radial threads, which ultimately transferred load to the web's anchoring points. Although the spiral threads underwent increased deflection and captured more of the wind load owing to their larger exposed length, they were effectively pinned to the much stiffer dragline radial threads that limit web deflection (Fig. 2c, Supplementary Information section 8). For wind speeds less than 10 m s^{-1} there was little difference between the models (Fig. 2c, Supplementary Information section 8) and deflections are <12% of the total span of the web. We attributed

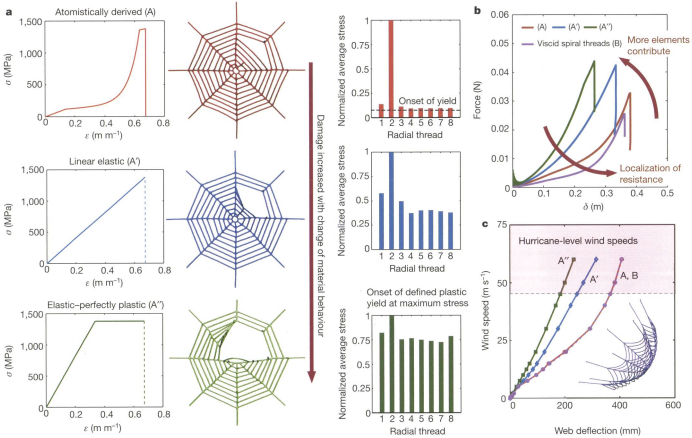

Figure 2 | Web response for varied silk behaviour under targeted (local) and distributed (global) loading. a, Comparison of failure for derived dragline silk, linear elastic and elastic–perfectly plastic behaviours (left, models A, A′ and A″). Comparison of failure (centre) confirms localized stresses and minimized damage for the natural nonlinear stiffening silk behaviour. The average stress of each radial thread (bar plots, right) reflects the nonlinear deformation states in the silk. When load is applied locally to a radial thread, other radial threads not subject to applied force reach a stress corresponding to the onset of yielding (that is, regime II in Fig. 1a). The elastic–perfectly plastic behaviour leads to an almost homogeneous distribution of stress. **b**, Force–displacement curves for varying material behaviours (models A, A′ and A″ and model B). **c**, Web behaviour under distributed (global) wind loading. The plot shows a comparison of the wind-deflection behaviour (models A, A′, A″ and B). The initial high stiffness of natural dragline silk enhances the structural integrity of the web under such loading. Failure of all webs occurs at wind speeds in excess of 60 m s^{-1}.

this relatively uniform structural rigidity of the web to the initial stiffness of the dragline silk before yield (Fig. 1a). Under higher wind loads, the softening behaviour of dragline silk at moderate deformation resulted in significant web deflection that was greater than the deflections seen with linear elastic and elastic–perfectly plastic material behaviour (Fig. 2c). We found that yield in the threads occurred at wind speeds exceeding around 5 m s^{-1}, defining a reasonable wind speed regime in which webs are operational.

Although all web models performed similarly under moderate global (wind) loading (Fig. 2c), the linear elastic and elastic–perfectly plastic models responded to targeted force application with a more catastrophic, brittle-like failure that resulted in significantly increased damage. Defining web damage as percentage of failed (broken) threads, we found that the damage of 2.5% for the natural silk behaviour increases sixfold to 15% for the elastic–perfectly plastic model (Fig. 2a, centre panel). Web performance under local loading was generalized by invoking quantized fracture mechanics[30], a theory that describes the failure mechanisms of discrete structures (such as a spider web) and adapted here to incorporate the material behaviours (Supplementary Information section 10). A generalized stress–strain behaviour, where $\sigma \propto \varepsilon^{\kappa}$ (κ is a parameter that defines the nonlinear nature of the stress–strain relationship) treated with quantized fracture mechanics revealed that the size of the damaged zone in the proximity to a defect increases for materials that feature a softening behaviour (elastic–perfectly plastic behaviour), whereas a stiffening material (natural silk) results in a decrease of the damage zone (Fig. 3). This is captured by a scaling law $\Omega(\alpha) = 1 - S^{2\alpha}$, defining the structural robustness Ω as the undamaged fraction of the web after failure. Here $\alpha = \kappa/(\kappa + 1)$ reflects the stress–strain response (linear elastic case when $\alpha = 1/2$; stiffening when α tends to 1 and softening when α tends to 0), and S is a system-dependent constant (independent of stress–strain relation). Our simulation results agreed with the predictions of quantized fracture mechanics (Supplementary Table 5) and confirmed that the relative size of the damage zone is a function of the material stress–strain relation and enhanced by the discreteness of the web (Supplementary Information section 10). This phenomenon is exemplified in spider webs (Figs 1 and 2), where the nonlinear stiffening behaviour (as α tends to 1) is essential for localizing damage and ensuring that a loaded thread becomes a sacrificial element while the majority of the web remains intact. Given the presumed metabolic effort required by the spider for rebuilding an entire web, localized failure is preferential as it does not compromise the structural integrity of the web (see Fig. 1c) and hence allows it to continue to function for prey capture in spite of the damage.

The remarkable strength, toughness and extensibility of individual spider silk threads are thus not the dominating properties that underpin the excellent structural performance of a spider web. Rather, it is the distinct nonlinear softening and subsequent stiffening of dragline silk that is essential to function, as it results in localization of damage to sacrificial threads in a web subjected to targeted (local) loading while minimizing web deformations under moderate wind (global) loading. Each regime of the nonlinear material behaviour of silk (Fig. 1a) thus

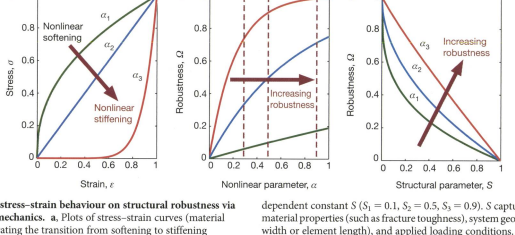

Figure 3 | Effects of stress–strain behaviour on structural robustness via quantized fracture mechanics. **a**, Plots of stress–strain curves (material behaviour) demonstrating the transition from softening to stiffening behaviours by the nonlinear parameter α ($\alpha_1 = 0.3$, $\alpha_2 = 0.5$, $\alpha_3 = 0.9$). **b**, Structural robustness Ω, defined as the undamaged fraction of the structure, versus α (dashed lines indicating α_1, α_2, α_3), given for three values of the system-dependent constant S ($S_1 = 0.1$, $S_2 = 0.5$, $S_3 = 0.9$). S captures a range of material properties (such as fracture toughness), system geometry (that is, crack width or element length), and applied loading conditions. **c**, Ω versus S. Universally, the robustness increases with an increase in α ($\alpha_1 < \alpha_2 < \alpha_3$), implying that larger nonlinear stiffening results in larger structural robustness, and hence less damage.

plays a key part in defining the overall system response in a variety of environmental settings. Other natural silk threads used to form solid materials such as cocoons, rather than aerial webs, typically display different mechanical responses[11]. Indeed, cocoon silk conforms closely to elastic–perfectly plastic behaviour, which is not suitable for web construction. The softening behaviour typically seen in such silks, combined with a solid material structure rather than a discrete mesh, results in a greater spreading of damage that effectively enhances the system's fracture toughness. This is clearly an advantage for the protective role of cocoons, and is reminiscent of other biomaterials where mechanical robustness has been attributed to the formation of large plastic regions[2,5]. The opposite is true for webs, where robustness arises from extreme localization of failure at sacrificial elements, with this behaviour enhanced by the stiffening of threads (Figs 1a and 2a).

The enhanced mechanical performance of the web relies on the integration of material and structure, which ultimately derives from the particular molecular structure of silk that features a composite of semi-amorphous protein and β-sheet nanocrystals. We suggest that web design principles might be considered in engineering, where current practice uses sacrificial elements solely to dissipate energy (for example, impact loading, seismic response). In spider webs, discrete sacrificial elements are instead a means to avoid potentially dangerous system-level loading and mitigate structural damage so that despite the small decrease in spider-web load capacity (Fig. 2b), the robustness of the structure overall is greatly enhanced (Fig. 3). This allows a spider to repair rather than rebuild completely, should failure occur. Such an engineering design could ignore the requirements for the magnitude of a potential load and allow local failure to occur, a design stipulation that requires the consideration of both material behaviour and structural architecture.

METHODS SUMMARY

The web consists of an arithmetic spiral[7] supported by radial threads at regular intervals, constructed from two primary elements, radial threads and spiral threads[7] (Fig. 1b), and is modelled using molecular dynamics procedures. We implement five material behaviours: (1) atomistically derived dragline silk behaviour (parameterized from molecular simulations of dragline silk[16,17]) (Fig. 1a); (2) empirically parameterized dragline silk (from experimental data[3]); (3) empirically parameterized viscid silk (from experimental data[3]); (4) ideal linear elastic behaviour; (5) ideal elastic–perfectly plastic behaviour, incorporated in three arrangements in models A, B and C. We consider two types of application of loading, targeted (local) and global (wind) loading. To characterize the mechanical response of the web under targeted loading, a spring-load is imposed to a small section of the web and increased until failure is incurred (defined by the failure of loaded threads). Wind loading is applied via a constant drag force applied to all web threads. *In situ* experiments through simple mechanical assays are applied to an orb web of the common European garden spider. We identify a web in its natural environment and deform radial and spiral threads using a mechanical applicator (a metal wire to load threads). During deformation we control the displacement and monitor images using a digital camera. For theoretical analysis we use quantized fracture mechanics[30], a theory that describes the failure of discrete structures such as a spider web and adapted here to incorporate the nonlinear stress–strain behaviour of silk. For a detailed description of the models see Methods and Supplementary Information.

Full Methods and any associated references are available in the online version of the paper at www.nature.com/nature.

Received 22 November 2010; accepted 25 November 2011.

1. Gosline, J. M., Guerette, P. A., Ortlepp, C. S. & Savage, K. N. The mechanical design of spider silks: from fibroin sequence to mechanical function. *J. Exp. Biol.* **202,** 3295–3303 (1999).
2. Gao, H., Ji, B., Jäger, I. L., Arzt, E. & Fratzl, P. Materials become insensitive to flaws at nanoscale: lessons from nature. *Proc. Natl Acad. Sci. USA* **100,** 5597–5600 (2003).
3. Aizenberg, J. *et al.* Skeleton of *Euplectella* sp.: structural hierarchy from the nanoscale to the macroscale. *Science* **309,** 275–278 (2005).
4. Vollrath, F. Spider webs and silks. *Sci. Am.* **266,** 70–76 (1992).
5. Kamat, S., Su, X., Ballarini, R. & Heuer, A. H. Structural basis for the fracture toughness of the shell of the conch *Strombus gigas*. *Nature* **405,** 1036–1040 (2000).
6. Lefèvre, T., Rousseau, M. E. & Pézolet, M. Protein secondary structure and orientation in silk as revealed by Raman spectromicroscopy. *Biophys. J.* **92,** 2885–2895 (2007).
7. Vollrath, F. & Mohren, W. Spiral geometry in the garden spider's orb web. *Naturwissenschaften* **72,** 666–667 (1985).
8. Vollrath, F. Silk evolution untangled. *Nature* **466,** 319 (2010).
9. Agnarsson, I., Kuntner, M. & Blackledge, T. A. Bioprospecting finds the toughest biological material: extraordinary silk from a giant riverine orb spider. *PLoS ONE* **5,** e11234 (2010).
10. Du, N. *et al.* Design of superior spider silk: from nanostructure to mechanical properties. *Biophys. J.* **91,** 4528–4535 (2006).
11. Shao, Z. Z. & Vollrath, F. Materials: surprising strength of silkworm silk. *Nature* **418,** 741 (2002).
12. Omenetto, F. G. & Kaplan, D. L. New opportunities for an ancient material. *Science* **329,** 528–531 (2010).
13. Ko, K. K. *et al.* Engineering properties of spider silk. *Adv. Fibers Plastics Laminates Composites* **702,** 17–23 (2002).
14. Rammensee, S., Slotta, U., Scheibel, T. & Bausch, A. R. Assembly mechanism of recombinant spider silk proteins. *Proc. Natl Acad. Sci. USA* **105,** 6590–6595 (2008).
15. Vollrath, F., Holtet, T., Thogersen, H. C. & Frische, S. Structural organization of spider silk. *Proc. R. Soc. Lond. B* **263,** 147–151 (1996).
16. Keten, S., Xu, Z. P., Ihle, B. & Buehler, M. J. Nanoconfinement controls stiffness, strength and mechanical toughness of beta-sheet crystals in silk. *Nature Mater.* **9,** 359–367 (2010).
17. Keten, S. & Buehler, M. J. Nanostructure and molecular mechanics of spider dragline silk protein assemblies. *J. R. Soc. Interf.* **7,** 1709–1721 (2010).
18. Aoyanagi, Y. & Okumura, K. Simple model for the mechanics of spider webs. *Phys. Rev. Lett.* **104,** 038102 (2010).
19. Ko, F. K. & Jovicic, J. Modeling of mechanical properties and structural design of spider web. *Biomacromolecules* **5,** 780–785 (2004).

20. Alam, M. S., Wahab, M. A. & Jenkins, C. H. Mechanics in naturally compliant structures. *Mech. Mater.* **39,** 145–160 (2007).
21. Alam, M. S. & Jenkins, C. H. Damage tolerance in naturally compliant structures. *Int. J. Damage Mech.* **14,** 365–384 (2005).
22. Foelix, R. F. *Biology of Spiders* 2nd edn (Oxford University Press/Georg Thieme, 1996).
23. Vollrath, F. Biology of spider silk. *Int. J. Biol. Macromol.* **24,** 81–88 (1999).
24. Termonia, Y. Molecular modeling of spider silk elasticity. *Macromolecules* **27,** 7378–7381 (1994).
25. Vepari, C. & Kaplan, D. L. Silk as a biomaterial. *Prog. Polym. Sci.* **32,** 991–1007 (2007).
26. Swanson, B. O., Blackledge, T. A. & Hayash, C. Y. Spider capture silk: performance implications of variation in an exceptional biomaterial. *J. Exp. Zool. A* **307A,** 654–666 (2007).
27. Swanson, B. O., Anderson, S. P., DiGiovine, C., Ross, R. N. & Dorsey, J. P. The evolution of complex biomaterial performance: the case of spider silk. *Integr. Comp. Biol.* **49,** 21–31 (2009).
28. Vollrath, F. & Selden, P. The role of behavior in the evolution of spiders, silks, and webs. *Annu. Rev. Ecol. Evol. Syst.* **38,** 819–846 (2007).
29. Keten, S. & Buehler, M. J. Atomistic model of the spider silk nanostructure. *Appl. Phys. Lett.* **96,** 153701 (2010).
30. Pugno, N. M. & Ruoff, R. S. Quantized fracture mechanics. *Phil. Mag.* **84,** 2829–2845 (2004).

Supplementary Information is linked to the online version of the paper at www.nature.com/nature.

Acknowledgements This work was supported primarily by the Office of Naval Research (N000141010562) with additional support from the National Science Foundation (MRSEC DMR-0819762, the NSF-REU programme, as well as CMMI-0642545) and the Army Research Office (W911NF-09-1-0541 and W911NF-10-1-0127). Support from the MIT-Italy programme (MITOR) and a Robert A. Brown Presidential Fellowship is gratefully acknowledged. N.M.P. is supported by the METREGEN grant (2009-2012) "Metrology on a cellular and macromolecular scale for regenerative medicine". An Ideas Starting Grant 2011 BIHSNAM on "Bio-inspired hierarchical super nanomaterials" was awarded to N.M.P. from the European Research Council, under the European Union's Seventh Framework Programme (FP7/2007-2013)/ERC grant (agreement number 279985). All simulations have been carried out at MIT's Laboratory for Atomistic and Molecular Mechanics (LAMM). We acknowledge assistance from S. and E. Buehler in taking photographs of the spider web.

Author Contributions S.W.C. and M.J.B. designed the research and analysed the results. S.W.C. and A.T. developed the material models, performed the simulations, and conducted the simulation data analysis. M.J.B. performed the *in situ* experiments and analysed the results. N.M.P. contributed the theoretical analysis and predictions and analysed the results. S.W.C., M.J.B., A.T. and N.M.P. wrote the paper.

Author Information Reprints and permissions information is available at www.nature.com/reprints. The authors declare no competing financial interests. Readers are welcome to comment on the online version of this article at www.nature.com/nature. Correspondence and requests for materials should be addressed to M.J.B. (mbuehler@mit.edu).

LETTER

doi:10.1038/nature10706

Decadal to monthly timescales of magma transfer and reservoir growth at a caldera volcano

T. H. Druitt[1,2,3], F. Costa[4], E. Deloule[5], M. Dungan[6] & B. Scaillet[7]

Caldera-forming volcanic eruptions are low-frequency, high-impact events capable of discharging tens to thousands of cubic kilometres of magma explosively on timescales of hours to days, with devastating effects on local and global scales[1]. Because no such eruption has been monitored during its long build-up phase, the precursor phenomena are not well understood. Geophysical signals obtained during recent episodes of unrest at calderas such as Yellowstone, USA, and Campi Flegrei, Italy, are difficult to interpret, and the conditions necessary for large eruptions are poorly constrained[2,3]. Here we present a study of pre-eruptive magmatic processes and their timescales using chemically zoned crystals from the 'Minoan' caldera-forming eruption of Santorini volcano, Greece[4], which occurred in the late 1600s BC. The results provide insights into how rapidly large silicic systems may pass from a quiescent state to one on the edge of eruption[5,6]. Despite the large volume of erupted magma[4] (40–60 cubic kilometres), and the 18,000-year gestation period between the Minoan eruption and the previous major eruption, most crystals in the Minoan magma record processes that occurred less than about 100 years before the eruption. Recharge of the magma reservoir by large volumes of silicic magma (and some mafic magma) occurred during the century before eruption, and mixing between different silicic magma batches was still taking place during the final months. Final assembly of large silicic magma reservoirs may occur on timescales that are geologically very short by comparison with the preceding repose period, with major growth phases immediately before eruption. These observations have implications for the monitoring of long-dormant, but potentially active, caldera systems.

Crystals in volcanic rocks provide records of magma reservoir processes and timescales before eruptions[7]. A crystal growing from a magmatic melt incorporates trace elements in quantities governed by thermodynamic and kinetic laws[8,9]. If the crystal is subsequently mixed into another melt, trace elements that diffuse sufficiently fast will begin to re-equilibrate with the new host melt, generating intracrystalline diffusion gradients that can be used to obtain time information[10–12] (Supplementary Fig. 1).

A novel technique for extracting multiple timescales from single crystals has been applied to plagioclase crystals in rhyodacitic (71–72 wt% SiO_2) pumices from the Minoan eruption. The pumices from all four phases of the eruption (phase 1, Plinian; phases 2 and 3, phreatomagmatic; phase 4, ignimbrite[13]) contain ~10 vol% crystals set in rhyolitic[14] (73–74 wt% SiO_2) glass. Plagioclase is the dominant crystalline phase, the others being orthopyroxene, clinopyroxene, magnetite, ilmenite and apatite. It occurs as zoned crystals, whose compositional variations are dominated by charge-coupled solid solution between the endmembers, anorthite ($An, CaAl_2Si_2O_8$) and albite ($NaAlSi_3O_8$).

Two types of plagioclase have been recognized from examination of about 300 crystals (Fig. 1 and Supplementary Figs 2 and 3). A dominant type (type 1) has euhedral to partly resorbed cores of $An_{58–43}$ (58–43 mol% An) overgrown by variably developed, euhedral rims of $An_{43–36}$ containing multiple dissolution surfaces (Fig. 1a–d). The cores and rims form compositionally distinct populations (Fig. 1g). In some crystals, the cores also contain euhedral to anhedral inner cores of $An_{88–58}$ ('calcic inner cores'; Fig. 1 a, c). A spectrum of type-1 crystals is observed, from those with thick rims (up to 100 μm) to those with thin rims to those in which the rim is absent (Fig. 1f). In rimmed type-1 crystals, the plagioclase in contact with the host glass is $An_{\sim 40}$, whereas in rimless ones it is $An_{\sim 50}$ (that is, the core composition). Rimmed type-1 crystals occur in pumices from all four eruptive phases, but rimless ones have only been observed in pumices from phase 4. Type-2 crystals are very rare; they are reversely zoned, with cores of

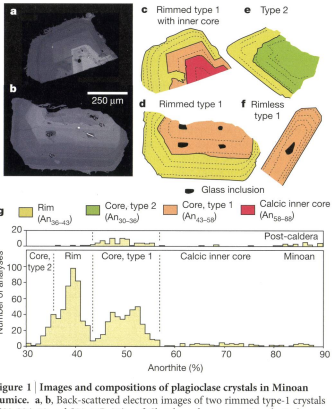

Figure 1 | Images and compositions of plagioclase crystals in Minoan pumice. a, **b**, Back-scattered electron images of two rimmed type-1 crystals (S82-30A 12 and S82-34B A2). **c**–**f**, Sketches of representative plagioclase crystals of the different types: S82-30A 12 (**c**); S82-34B A2 (**d**); S82-20D 76 (**e**); S82-20D C1 (**f**). More crystals are shown in Supplementary Fig. 2. **g**, Histogram of Minoan plagioclase compositions (bottom), based on 922 analyses, showing the different compositional groups. A histogram of plagioclase compositions from the post-caldera lavas[16,17] (top) is shown for comparison.

[1]Clermont Université, Université Blaise Pascal, Laboratoire Magmas et Volcans, BP 10448, F-63000 Clermont-Ferrand, France. [2]CNRS, UMR 6524, LMV, F-63038 Clermont-Ferrand, France. [3]IRD, R 163, LMV, F-63038 Clermont-Ferrand, France. [4]Earth Observatory of Singapore, Nanyang Technological University, Singapore 639798. [5]CRPG-CNRS, BP20, 54501 Vandoeuvre les Nancy, France. [6]Département de Minéralogie, Université de Genève, Rue des Maraîchers, 13 CH-1205 Genève, Switzerland. [7]ISTO–UMR 6113 CNRS/Université d'Orléans/Université Francois Rabelais de Tours, 1A rue de la Ferollerie, 45071 Orleans, France.

An_{36-30} mantled by rims identical to those of type 1 (Fig. 1e). The broad range of plagioclase compositions in Minoan pumices shows that the rhyodacite was the product of open-system magmatic processes involving multiple, compositionally diverse magmas.

We analysed trace elements in four rimmed type-1 crystals, one rimless type-1 crystal, some interstitial glasses and some inclusions of glass contained within the crystals (Fig. 2 and Supplementary Tables 1 and 2). Magnesium (Mg), strontium (Sr) and titanium (Ti) are particularly useful elements for characterizing coexisting melt compositions and mixing timescales because they partition differently between melt and plagioclase[8] and diffuse at different rates. Mg diffuses faster than Sr (ref. 7); Ti probably diffuses slowly owing to its high charge. We used published An-dependent partition coefficients[8] to invert melt trace-element contents to those of equivalent plagioclase (Fig. 2), and vice versa (Fig. 3). Rimmed type-1 crystals have core-to-rim gradients in all three elements (Fig. 2). Rim compositions record equilibrium with interstitial glass, but concentrations of Mg, Sr and Ti in the cores and calcic inner cores are significantly higher than those calculated to be in equilibrium with the glass (Fig. 2, green lines). The rimless type-1 crystal has concentrations of Mg and Sr throughout that are too high to have been in equilibrium with the glass. None of these crystals resided in the host melt long enough for any of these elements to reach total equilibrium with the host melt.

This observation is reinforced by a comparison of calculated Mg, Ti and Sr concentrations of melts in equilibrium with the different plagioclase zones (referred to as Mg_{melt}, Ti_{melt} and Sr_{melt}, respectively), with those of Santorini lavas, pumices and glasses. The latter represent an approximate liquid line of descent of the magmatic system (Fig. 3a, b). The calculated concentrations of Sr_{melt} and Ti_{melt} span the entire range of erupted compositions, whereas those of Mg_{melt} fall below the liquid line of descent, especially in the calcic inner cores. These crystals have retained near-primary values of Sr and Ti, but Mg seems to have been partly re-equilibrated by diffusion.

We used the Sr contents of the crystals to calculate the compositions of melts from which the different zones crystallized (Fig. 3). The rims of the type-1 and type-2 crystals formed from melts with 60–90 p.p.m. Sr (71–74 wt% SiO_2), which encompasses the range of whole-rock to glass compositions of the host rhyodacite. The cores of the type-1 crystals formed from melts with 110–170 p.p.m. Sr (dacite with 63–69 wt% SiO_2), and the cores of the type-2 crystals formed from melts with 40–60 p.p.m. Sr (rhyolite with 74–76 wt% SiO_2). We interpret these observations as recording the mixing of a dacite (carrying plagioclase of the type-1 core composition) with a rhyolite (carrying plagioclase of the type-2 core composition) to generate a hybrid rhyodacite (followed by growth of the rim) that was erupted as the Minoan pumice. The rimless type-1 crystals were derived directly from the dacite, and had not resided in the hybrid rhyodacite long enough to grow rims. The calcic inner cores formed from basaltic andesite melts, with >200 p.p.m. Sr and <57 wt% SiO_2, that were mixed into the dacite at an earlier stage. The possibility that the crystal cores and inner cores are derived from older plutonic mush is not favoured on the balance of evidence (Supplementary Discussion).

The times elapsed between the different mixing events and eruption have been calculated by modelling the partial relaxation of Mg concentrations in different parts of the crystals[1,2] (Fig. 2 and Table 1). We first modelled the entire crystal ('one-step model'), which assumes that diffusion started only after the entire crystal had grown. Model results for the elapsed time ranged from 1 to 60 yr, but good fits could not be obtained. We therefore approximated the more realistic situation of simultaneous crystal growth and diffusion by modelling the crystals incrementally zone by zone ('two-step model'). In this manner, we obtained better overall fits to the data (Fig. 2), from which we infer that (1) a first magma mixing episode recorded by incorporation of the calcic inner cores of the type-1 crystals into the dacite occurred no more than ~100 yr before eruption; (2) a second mixing episode, or series of episodes, involving the dacite and the rhyolite occurred less than ~10 yr before eruption; and (3) the rimless type-1 crystals cannot have resided in the Minoan magma more than a few months without some diffusive loss of Mg from the rim. We have no constraints on the ages of the cores of the rare type-2 crystals. These estimates are accurate to better than one order of magnitude (Methods). The Mg-derived times were tested against the diffusive equilibration of Sr using the comprehensive diffusion data for this element (Fig. 2). Taking the measured profiles of Sr as being close to initial values, diffusion times an order of magnitude longer than those obtained from Mg would significantly blur the observed tight correlation between Sr and An contents (Fig. 3c), and are ruled out.

Our reconstruction of events, which is justified more fully in Supplementary Discussion, is as follows. During the century before eruption, dacitic magma containing crystals of calcic plagioclase began to ascend from a deep storage zone beneath Santorini, possibly pushed by injections of mafic magma (Supplementary Fig. 4). Once at shallow

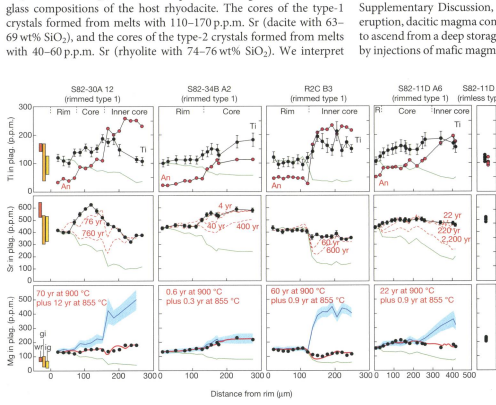

Figure 2 | Concentration–distance profiles of An (red dots) and of Sr, Ti and Mg (black dots) in Minoan plagioclase crystals. Equilibrium profiles for Sr, Ti and Mg (green lines) were calculated using published partition functions[8] at 855 °C. Calculated plagioclase compositions in equilibrium with interstitial glasses (ig), glass inclusions (gi) and whole-rock (wr) pumice compositions[13] are also shown. The blue lines in the Mg plots are the initial Mg profiles (with 1σ range). The red solid lines in the Mg plots are the best-fit two-step Mg diffusion models (time shown in years). The red dotted lines in the Sr plots are diffusion models (one-step models; 900 °C; time shown in years) in which we assume that the measured profile is close to the initial condition, as suggested by Fig. 3a. Error bars, 1σ.

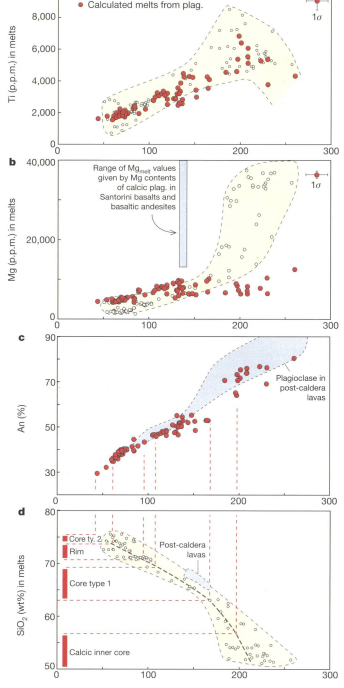

Figure 3 | Melt compositions calculated by inversion of plagioclase trace-element compositions. a, **b**, Ti, Mg and Sr melt contents calculated using the plagioclase–liquid partition functions of ref. 8. Temperature was obtained from $T = 855\ ^{\circ}C + 200\ ^{\circ}C \times (\%An - \%An_{40})/(\%An_{80} - \%An_{40})$, which assumes that An_{40} plagioclase crystallized at 855 °C and that An_{80} crystallized at 1,055 °C, the temperature of Santorini basaltic andesite. The values are compared with the compositional fields of Santorini cycle-2 lavas[17], Minoan pumices and Minoan glasses. The range of Mg_{melt} values calculated in the same way from the Mg contents of calcic ($An_{>80}$) plagioclase in Santorini basalts and basaltic andesites are much higher (14,000–47,000 p.p.m.) than those in the calcic inner cores of Minoan crystals, showing that the latter have lost Mg by diffusion. **c**, **d**, Use of calculated melt Sr contents from plagioclase allows estimation of the SiO_2 contents of the melts from which each plagioclase compositional group crystallized. The compositional field of plagioclases in the post-caldera lavas is taken from ref. 32.

levels, the dacite intersected one or more extant bodies of rhyolite situated at a depth of a few kilometres[14]. The cores of the type-1 crystals grew during the ascent of the dacite and/or its ponding at the base of the reservoir. Then, starting about a decade before eruption, the dacite mixed with the rhyolite to form rim overgrowths on the type-1 crystals. Mixing caused resorption of most crystals initially present in the rhyolite, and formed the hybrid rhyodacite that was subsequently erupted. Successive waves of recharge and heating of the reservoir are recorded as multiple dissolution surfaces within crystal rims. Dacite was still being mixed into the shallow reservoir less than a few months before eruption, supplying the rimless type-1 crystals. Efficient mixing of the two silicic magmas on these timescales is compatible with fluid dynamics principles (Supplementary Discussion). Andesite and basaltic andesite were also injected at a late stage, accounting for small quantities of quenched enclaves discharged during the first eruptive phase[13]. The plagioclase crystals in the rhyodacite have lower Sr isotopic ratios than their host glass[15], so the resident rhyolite may have been more radiogenic than the dacite owing to crustal contamination. The dacite may have been an advance batch of the magmas that have erupted over the last 2,000 yr to form the post-caldera Kameni Islands[13]. This interpretation is based on similarities in An and Sr contents between the cores of type-1 plagioclases and those of plagioclases in the post-caldera lavas[16,17] (Figs 1g and 3c).

Calculations based on chemical mass balance and magma crystallinity show that the dacitic component accounted for at least 15% of the erupted magma (Supplementary Discussion). Assembly of the Minoan reservoir during the 18,000 yr since the previous major eruption of Santorini terminated in a growth spurt involving injection of at least several cubic kilometres of dacitic magma, and an unknown volume of more-mafic magma, in about a century. This implies a transient recharge flux ($>0.05\ km^3\ yr^{-1}$) much higher than the long-term magma production rate at the volcano[13] ($\sim 0.001\ km^3\ yr^{-1}$). Rapid and sustained supply of compositionally diverse magmas eventually led to overturn and homogenization of the different magma batches, and eruption followed about a decade later.

Accommodation of such a large recharge volume purely by roof uplift could have caused great inflation of the volcano during the century preceding eruption. A maximum estimate of this is given by the elevation of a rigid, piston-like roof block with the same area as the caldera (several tens of metres of uplift at a mean rate of $\sim 1\ m\ yr^{-1}$; broader doming of the volcano[18], or consideration of rock and magma compressibilities, would give lower values). Although this is possible, such high uplift values have not been observed, or inferred, before past caldera-forming eruptions such as that of Mt Pinatubo in 1991. However, exhumed granitoid plutons reveal that injection of silicic magma at depths of >3 km is often accommodated by lowering of the intrusion floor due to down-sagging of underlying crystal-rich magmatic mushes and crustal layers[5,19–21]. Extraction of magma from deep storage regions can result in compaction of the crustal column beneath the volcano. Had foundering beneath the Minoan reservoir taken place rapidly enough, precursory uplift might have been greatly reduced. Subsidence rates of several decimetres per year beneath growing magma reservoirs are compatible with theoretical models[5,20].

Our study shows that the reactivation, growth and final assembly of large silicic magma bodies before eruption can take place on decadal to monthly timescales that are very short by comparison with the lengths of the preceding repose periods. It is consistent with evidence for voluminous, late-stage recharge on similar timescales before caldera eruptions elsewhere[11,22–24]. High rates of magma supply sustained over many decades may be necessary to 'prime' such bodies for eruption, by generating overpressures high enough to propagate dykes of viscous magma to the surface and initiate discharge[25,26]. Long-term monitoring of large, dormant caldera systems[27–29], even in remote areas of the world, is essential if late-stage growth spurts of shallow magma reservoirs are to be detected well in advance of caldera-forming eruptions.

Table 1 | Mixing-to-eruption times obtained by diffusion modelling of Mg in Minoan plagioclase

Pumice sample	Eruption phase	Crystal (type)	Time (yr), one-step model	Time (yr), two-step model				
			900 °C	CIC-dm 900 °C	CIC-C-R-rm 855 °C	CIC-R-rm 855 °C	C-rm 855 °C	C-R-rm 855 °C
S82-30A	1	12 (rimmed 1)	47^{+38}_{-20}	70^{+56}_{-30}	12^{+10}_{-5}	—	—	—
S82-34B	2	A2 (rimmed 1)	$0.8^{+0.6}_{-0.3}$	—	—	—	$0.6^{+0.5}_{-0.3}$	$0.3^{+0.3}_{-0.1}$
R2C	3	B3 (rimmed 1)	60^{+48}_{-26}	60^{+48}_{-26}	—	$<0.9^{+0.8}_{-0.4}$	—	—
S82-11D	4	A6 (rimmed 1)	24^{+20}_{-10}	22^{+17}_{-9}	$0.9^{+0.8}_{-0.4}$	—	—	—
S82-11D	4	A5 (rimless 1)	—	—	—	—	$<0.3^{+0.3}_{-0.1}$	—

The calculations were done at the temperatures shown, which correspond to those of dacitic and rhyodacitic melts. The quoted errors correspond to a temperature uncertainty of ±25 °C in the calculated time. CIC, calcic inner core; C, core; R, rim; dm, dacitic melt; rm, rhyodacitic melt. The different crystals are shown in Supplementary Fig. 2.

METHODS SUMMARY

The zoning textures of about 300 crystals from eight pumices (from all four eruptive phases) were studied using a combination of back-scattered electron microscopy and Normarski differential interference contrast microscopy. Major-element compositions of minerals and glasses were analysed by electron microprobe, and trace elements by secondary ion mass spectrometry. The pre-eruptive temperature of the Minoan rhyodacite (853 ± 12 °C) was calculated using analyses of touching magnetite–ilmenite pairs in pumices from all eruptive phases. Trace-element diffusion modelling was carried out in one dimension using a forward modelling approach in which the diffusion equation[12] was solved numerically by a finite-difference scheme, and visual best fits were made between modelled and observed concentration profiles. The An-dependent diffusion coefficient for Mg was taken from ref. 12, which is based on the experimental data of ref. 30, and that for Sr was taken from ref. 31. Initial profiles for Mg were calculated using the Sr–An correlation of Fig. 3c and the Mg–Sr liquid line of descent (Fig. 3b). The boundary conditions were determined by the measured concentrations at the crystal rims or at other major boundary zones. The calculated times are probably overestimates because some of the cores have re-equilibrated significantly and, hence, the effect of diffusion in multiple dimensions could have been significant[7]. However, the main errors associated with the calculations arise from uncertainties in temperature and diffusion coefficients. The modelling was carried out at either 855 or 900 °C, depending on the melt involved (Table 1), but we considered a nominal uncertainty of ±25 °C, which when propagated into the time estimates leads to relative errors of 45–75% (Table 1). Effects of uncertainties in the diffusion parameters for Mg are discussed in Methods.

Full Methods and any associated references are available in the online version of the paper at www.nature.com/nature.

Received 26 May; accepted 4 November 2011.

1. Miller, C. F. & Wark, D. A. Supervolcanoes and their explosive supererruptions. *Elements* **4,** 11–15 (2008).
2. Newhall, C. G. & Dzurizin, D. *Historical Unrest at Large Calderas of the World* Vols 1 and 2 (Bull. US Geol. Surv. 1855, USGS, 1988).
3. Gottsmann, J. & Marti, J. (eds) *Caldera Volcanism: Analysis, Modelling and Response* (Dev. Volcanol. 10, Elsevier, 2008).
4. Sigurdsson, H. & Carey, S. and 12 others. Marine investigations of Greece's Santorini volcanic field. *Trans. Am. Geophys. Union* **87,** 337–342 (2006).
5. Bachmann, O. & Bergantz, G. W. On the origin of crystal-poor rhyolites: extracted from batholithic crystal mushes. *J. Petrol.* **45,** 1565–1582 (2004).
6. Burgisser, A. & Bergantz, G. W. A rapid mechanism to remobilize and homogenize highly crystalline magma bodies. *Nature* **471,** 212–215 (2011).
7. Costa, F., Dohmen, R. & Chakraborty, S. Timescales of magmatic processes from modeling the zoning patterns of crystals. *Rev. Mineral. Geochem.* **69,** 545–594 (2008).
8. Bindeman, I. N., Davis, A. M. & Drake, M. J. Ion microprobe study of plagioclase-basalt partition experiments at natural concentration levels of trace elements. *Geochim. Cosmochim. Acta* **62,** 1175–1193 (1998).
9. Blundy, J. & Wood, B. Crystal-chemical control on the partitioning of Sr and Ba between plagioclase feldspar, silicate melts, and hydrothermal solutions. *Geochim. Cosmochim. Acta* **55,** 193–209 (1991).
10. Zellmer, G. F., Blake, S., Vance, D., Hawkesworth, C. & Turner, S. Plagioclase residence times at two island arc volcanoes (Kameni Islands, Santorini, and Soufriere, St Vincent) determined by Sr diffusion systematics. *Contrib. Mineral. Petrol.* **136,** 345–357 (1999).
11. Morgan, D. J. *et al.* Magma chamber recharge at Vesuvius in the century prior to the eruption of A.D. 79. *Geology* **34,** 845–848 (2006).
12. Costa, F., Chakraborty, S. & Dohmen, R. Diffusion coupling between trace and major elements and a model for calculation of magma residence time using plagioclase. *Geochim. Cosmochim. Acta* **67,** 2189–2200 (2003).
13. Druitt, T. H. *et al. Santorini Volcano* (J. Geol. Soc. Lond. Mem. 19, Geological Society, 1999).
14. Cottrell, E., Gardner, J. E. & Rutherford, M. J. Petrologic and experimental evidence for the movement and heating of the pre-eruptive Minoan rhyodacite (Santorini, Greece). *Contrib. Mineral. Petrol.* **135,** 315–331 (1999).
15. Martin, V., Davidson, J., Morgan, D. & Jerram, D. Using the Sr isotope compositions of feldspars and glass to distinguish magma system components and dynamics. *Geology* **38,** 539–542 (2010).
16. Francalanci, L. *et al.* in *The European Laboratory Volcanoes* 175–186 (Official Publ. Eur. Comm., 1998).
17. Huijsmans, J. *Calc-Alkaline Lavas from the Volcanic Complex of Santorini, Aegean Sea, Greece* (Geologica Ultraiectina 41, Inst. Aardwetenschappen Rijksuniversiteit Utrecht, 1985).
18. Aizawa, K., Acocella, V. & Yoshida, T. How the development of magma chambers affects collapse calderas: insights from an overview. *Spec. Publ. Geol. Soc. (Lond.)* **269,** 65–81 (2006).
19. Wiebe, R. A. & Collins, W. J. Depositional features and stratigraphic sections in granitic plutons: implications for the emplacement and crystallization of granitic magma. *J. Struct. Geol.* **20,** 1273–1289 (1998).
20. Cruden, A. R. On the emplacement of tabular granites. *J. Geol. Soc. Lond.* **155,** 853–862 (1998).
21. Grocott, J. Arévalo, C. Welkner, D. & Cruden, A. Fault-assisted vertical pluton growth: Coastal Cordillera, north Chilean Andes. *J. Geol. Soc. Lond.* **166,** 295–301 (2009).
22. Wark, D. A., Hildreth, W., Spear, F. S., Cherniak, D. J. & Watson, E. B. Pre-eruption recharge of the Bishop magma system. *Geology* **35,** 235–238 (2007).
23. Saunders, K. E., Morgan, D. J., Baker, J. A. & Wysoczanski, R. J. The magmatic evolution of the Whakamaru supererruption, New Zealand, constrained by a microanalytical study of plagioclase and quartz. *J. Petrol.* **51,** 2465–2488 (2010).
24. de Silva, S., Salas, G. & Schubring, S. Triggering explosive eruptions: the case for silicic magma recharge at Huaynaputina, southern Peru. *Geology* **36,** 387–390 (2008).
25. McLeod, P. & Tait, S. R. The growth of dykes from magma chambers. *J. Volcanol. Geotherm. Res.* **92,** 231–245 (1999).
26. Jellinek, A. M. & DePaulo, D. J. A model for the origin of large silicic magma chambers: precursors of caldera-forming eruptions. *Bull. Volcanol.* **65,** 363–381 (2003).
27. Gottsmann, J. & Battaglia, M. Deciphering causes of unrest at explosive collapse calderas: Recent advances and future challenges of joint time-lapse gravimetric and ground deformation studies. *Dev. Volcanol.* **10,** 417–446 (2008).
28. Hill, D. P. Unrest in Long Valley caldera, California, 1978–2004. *Spec. Publ. Geol. Soc. (Lond.)* **269,** 1–24 (2006).
29. Dzurisin, D., Yamashita, K. M. & Kleinman, J. W. Mechanisms of crustal uplift and subsidence at the Yellowstone caldera, Wyoming. *Bull. Volcanol.* **56,** 261–270 (1994).
30. LaTourrette, T. & Wasserburg, G. J. Mg diffusion in anorthite: implications for the formation of early solar system planetismals. *Earth Planet. Sci. Lett.* **158,** 91–108 (1998).
31. Giletti, B. J. & Casserly, J. E. D. Strontium diffusion kinetics in plagioclase feldspars. *Geochim. Cosmochim. Acta* **58,** 3785–3793 (1994).
32. Santo, A. P. Magmatic evolution processes as recorded in plagioclase phenocrysts of Nea Kameni rocks (Santorini Volcano, Greece). *Dev. Volcanol.* **7,** 139–160 (2005).

Supplementary Information is linked to the online version of the paper at www.nature.com/nature.

Acknowledgements This study was funded partly by the French Agence National de Recherche (ANR STOMIXAN, contract no. ANR-08CEA080, to B.S.). We are grateful to R. Armstrong, P. Crançon and R. Girardin for their contributions during the early stages of this study, and to J. Blundy and M. Reid for reviews. This is Laboratory of Excellence ClerVolc contribution no. 1.

Author Contributions T.H.D. defined the project strategy, analysed the data and wrote the first draft of the manuscript, which was then revised by all the authors. E.D., M.D. and T.H.D. made the trace-element analyses, F.C. did the diffusion modelling and B.S. performed the fluid dynamic calculations.

Author Information Reprints and permissions information is available at www.nature.com/reprints. The authors declare no competing financial interests. Readers are welcome to comment on the online version of this article at www.nature.com/nature. Correspondence and requests for materials should be addressed to T.H.D. (t.druitt@opgc.univ-bpclermont.fr).

LETTER

doi:10.1038/nature10757

Serial translocation by means of circular intermediates underlies colour sidedness in cattle

Keith Durkin[1], Wouter Coppieters[1], Cord Drögemüller[2], Naima Aharizi[1], Nadine Cambisano[1], Tom Druet[1], Corinne Fasquelle[1], Aynalem Haile[3], Petr Horin[4], Lusheng Huang[5], Yohichiro Kamatani[6], Latifa Karim[1], Mark Lathrop[6], Simon Moser[7], Kor Oldenbroek[8], Stefan Rieder[7], Arnaud Sartelet[1], Johann Sölkner[9], Hans Stålhammar[10], Diana Zelenika[6], Zhiyan Zhang[1], Tosso Leeb[2], Michel Georges[1] & Carole Charlier[1]

Colour sidedness is a dominantly inherited phenotype of cattle characterized by the polarization of pigmented sectors on the flanks, snout and ear tips[1]. It is also referred to as 'lineback' or 'witrik' (which means white back), as colour-sided animals typically display a white band along their spine. Colour sidedness is documented at least since the Middle Ages and is presently segregating in several cattle breeds around the globe, including in Belgian blue and brown Swiss[1,2]. Here we report that colour sidedness is determined by a first allele on chromosome 29 (Cs_{29}), which results from the translocation of a 492-kilobase chromosome 6 segment encompassing *KIT* to chromosome 29, and a second allele on chromosome 6 (Cs_6), derived from the first by repatriation of fused 575-kilobase chromosome 6 and 29 sequences to the *KIT* locus. We provide evidence that both translocation events involved circular intermediates. This is the first example, to our knowledge, of a phenotype determined by homologous yet non-syntenic alleles that result from a novel copy-number-variant-generating mechanism.

To gain insights into the molecular basis of colour sidedness (Fig. 1), we genotyped 21 colour-sided and 30 control Belgian blue animals with a custom-made 50K single nucleotide polymorphism (SNP) array[3]. As a result of segregation at the *roan* locus, Belgian blue animals are either black spotted ($r^{Bl}r^{Bl}$), blue spotted ($r^{Bl}r^{Wh}$) or white ($r^{Wh}r^{Wh}$)[4]. As white is epistatic to colour sidedness, we selected non-white control animals. We assumed autosomal dominant inheritance (*Cs* allele) and genetic homogeneity in Belgian blue, and thus scanned the genome of colour-sided animals for a shared haplotype (present in at least one copy) using the ASSDOM software (see Methods). This analysis yielded a single genome-wide significant signal ($P < 0.03$), mapping the *Cs* locus to bovine chromosome 29 (BTA29) (Fig. 2a and Supplementary Fig. 1). A sire transmitting the colour-sided phenotype to all its pigmented offspring was homozygous for the corresponding haplotype as expected. The shared haplotype spanned 1.9 Mb, and encompassed *LUZP2*—not known to be involved in pigmentation—as the only gene. Sequencing the *LUZP2* open reading frame (ORF) from colour-sided and control animals did not reveal any protein-sequence-altering variant (data not shown).

In an independent effort, we scanned the genome for copy number variants (CNVs) using a database of 50K SNP genotypes from >4,500 animals of different breeds and the PennCNV software[5]. Intriguingly, this analysis revealed a private duplication encompassing 26 SNPs on chromosome 6 (BTA6), shared by the 21 colour-sided Belgian blue animals (Fig. 2b). We confirmed and refined the boundaries of this ~480 kb duplication by comparative genome hybridization (CGH) of genomic DNA of a *Cs*/*Cs* and +/+ Belgian blue animal on a genome-wide Nimblegen tiling array (Fig. 2c). The corresponding CNV encompassed the *KIT* gene, known to be essential for melanocyte migration and survival[6], and to be associated with coat colour variation[7,8].

To reconcile these apparently discrepant results, we performed fluorescence *in situ* hybridization (FISH) with bacterial artificial chromosome (BAC) clones mapping respectively to the BTA29 association interval (labelled with a red fluorophore), and to the BTA6 CNV interval (labelled with a green fluorophore) on lymphocytes of a *Cs*/+ and a +/+ animal. Overlapping red and green signals on one of the BTA29 homologues of the colour-sided animal demonstrated that the

Figure 1 | Colour-sided Belgian blue and brown Swiss animals. a, All represented Belgian blue animals are heterozygous *Cs*/+. In addition to the effect of the *Cs* locus, which causes polarization of pigmented sectors to the flanks, ears and snout, Belgian blue animals exhibit considerable polygenic variation in the degree of white spotting. The colour-sided phenotype of the two nearly completely white animals (extensive degree of white spotting) is apparent from the pigmentation of ear tips and snout. **b**, **c**, In brown Swiss, which are generally devoid of white spotting, homozygous *Cs*/*Cs* (**b**) and heterozygous *Cs*/+ (**c**) animals differ by the extent of pigmentation, explaining why colour sidedness is also referred to as semi-dominant.

[1]Unit of Animal Genomics, GIGA-R & Faculty of Veterinary Medicine, University of Liège (B34), 1 Avenue de l'Hôpital, 4000-Liège (Sart Tilman), Belgium. [2]Institute of Genetics, University of Bern, Bremgartenstrasse 109a, Postfach 8466, 3001 Bern, Switzerland. [3]International Center for Agricultural Research in the Dry Areas (ICARDA), PO Box 5466, Aleppo, Syria. [4]Institute of Genetics, University of Veterinary and Pharmaceutical Sciences Brno, 612 42 Brno, Czech Republic. [5]Key Laboratory for Animal Biotechnology of Jiangxi Province and the Ministry of Agriculture of China, NanChang, Jiangxi Province, 330045, China. [6]Fondation Jean Dausset – Centre d'Etude du Polymorphisme Humain, 27 Rue Juliette Dodu, Paris 75012, France and CEA-IC Centre National de Génotypage, 2 Rue Gaston Crémieux, CP 5721, 91057 Evry Cedex, France. [7]Swiss College of Agriculture, Bern University of Applied Sciences, 3052 Zollikofen, Switzerland. [8]Centre for Genetic Resources the Netherlands (CGN), 6701 BH Wageningen, The Netherlands. [9]Division of Livestock Sciences, University of Natural Resources and Applied Life Sciences, A-1180 Vienna, Austria. [10]Viking Genetics, Örnsro, Box 64, S-532 21 Skara, Sweden.

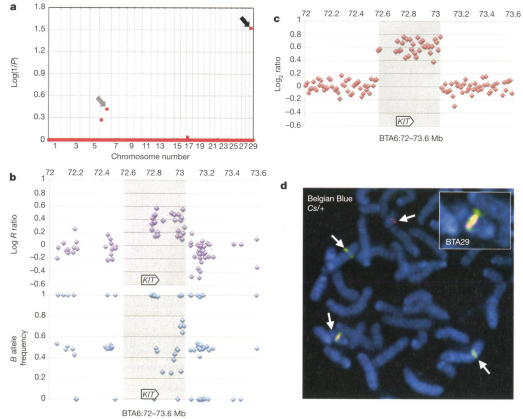

Figure 2 | Identification and mapping of the colour-sided locus in the Belgian blue. **a**, Genome-wide association mapping using ASSDOM (see Methods), revealing a genome-wide significant association ($P < 0.03$) on BTA29 (black arrow) and suggestive association on BTA6 (grey arrow). Vertical lines separate chromosomes. **b**, Detection of a duplication on the BTA6 segment shared by 21 colour-sided Belgian blue animals using 50K SNP array data[3] and PennCNV[3]. **c**, Confirmation and boundary definition using CGH on a Nimblegen bovine tiling array. Shaded areas in **b** and **c** mark the boundaries of the CNV as defined by CGH. **d**, Demonstration by FISH of the translocation of a *KIT*-encompassing BTA6 segment onto BTA29 in a heterozygous *Cs*/+ Belgian blue animal. Magnification, ×100.

CNV signal resulted from the translocation of the ~480 kb BTA6 segment to BTA29 (Fig. 2d). Retrospective examination of the SNP genotypes indicated that on average 3.17 of the 26 SNPs mapping to the ~480 kb duplication could not be called in colour-sided animals, yet the remaining genotypes were sufficient to yield a suggestive association signal (genome-wide $P = 0.37$), reflecting the sharing of the extra *KIT* haplotype by colour-sided animals (Fig. 2a).

To define the translocation breakpoints, we generated mate-pair libraries from self-ligated ~5 kb DNA fragments of a homozygous *Cs*/*Cs* Belgian blue animal, and generated ~10 Gb of sequence on an Illumina GAIIx instrument. We expected two clusters of aberrant mate pairs spanning the left and the right breakpoint resulting from the insertion of an intact BTA6 fragment in a BTA29 segment. We refer to the intact BTA6 fragment as **A**–**B**–**C**–**D**–**E**, the BTA29 segment in which it inserts as α–β, and the resulting left and right breakpoints as α–**A** and **E**–β, respectively. However, we observed three aberrant mate-pair clusters corresponding respectively to α–**D**, **E**–**A** and **C**–β fusions (Supplementary Fig. 2). The corresponding topology is most parsimoniously explained by assuming that: (1) the translocated BTA6 fragment circularized (generating fusion **E**–**A**); (2) reopened in the **C**–**D** interval; and (3) integrated in the α–β BTA29 interval (generating fusions α–**D** and **C**–β; Fig. 3).

Using the genomic coordinates of the clustered mate pairs, we designed primer sets to amplify the three corresponding fusion points. Productive amplification was only achieved using genomic DNA from colour-sided Belgian blue animals, as expected (Supplementary Fig. 3A). We sequenced the corresponding PCR products to define the breakpoints at single-nucleotide resolution. The **E**–**A** fusion was characterized by 2 bp micro-homology typical of non-homologous end joining (NHEJ) (Supplementary Fig. 4A), whereas the α–**D** and **C**–β fusions exhibited micro-duplications and micro-deletions reminiscent of replication-dependent microhomology-mediated break-induced replication (MMBIR) (Supplementary Fig. 4B)[9]. All breakpoints mapped to interspersed non-homologous repeat elements (data not shown).

The dominance of the *Cs* allele is expected to reflect a gain of function resulting from dysregulated expression of the translocated *KIT* gene. To verify the transcriptional competence of the translocated

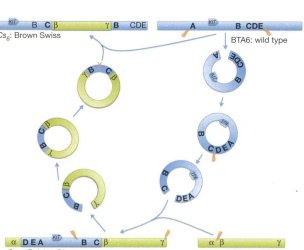

Figure 3 | Model for the generation of the colour-sided Cs_{29} and Cs_6 alleles by serial translocation via circular shuttling intermediates.

KIT copy, we performed polymerase chain reaction with reverse transcription (RT–PCR) experiments using amplicons spanning two SNPs: the ss469414206 G-to-A transition in intron 1, and the ss469414207 C-to-T transition in intron 7. We extracted total RNA from pigmented and unpigmented skin sectors of a *Cs*/+ colour-sided Belgian blue animal with the GG genotype on BTA6 and the A genotype on BTA29 ($(GG)_6/A_{29}$) for ss469414206 and the $(CC)_6/T_{29}$ genotype for ss469414207. The resulting pre-mRNA-dependent RT–PCR products were directly sequenced and the ratio of T/C and A/G species was estimated using Peakpicker[10]. T/A transcripts accounted for ~33% of the *KIT* output in both pigmented and unpigmented sectors, demonstrating the transcriptional potential of the translocated gene copy. Long-range RT–PCR analysis of the near complete *KIT* mRNA with primers located respectively in exon 1 and the 3′ untranslated region (UTR) followed by amplicon sequencing did not show evidence for alternate transcripts in colour-sided animals (Supplementary Fig. 5).

Linkage analysis performed in a brown Swiss pedigree segregating for colour sidedness with microsatellite markers targeting candidate genes (*KIT*, *KITL*, *MITF*, *EDNRB*, *ADAMTS20*), yielded a log of odds (lod) score of 6.9 maximizing in the immediate vicinity of the *KIT* locus (Supplementary Table 1). We genotyped four colour-sided (three *Cs*/*Cs* and one *Cs*/+), and five control brown Swiss animals using a 50K SNP array[3]. Colour-sided *Cs*/*Cs* brown Swiss animals indeed shared a 2.0 Mb autozygous haplotype encompassing the *KIT* locus. At first glance, these findings suggested a distinct determinism of colour sidedness in Belgian blue and brown Swiss.

We analysed the corresponding SNP genotypes with PennCNV and performed CGH using genomic DNA from brown Swiss *Cs*/*Cs* versus +/+ animals. This revealed the duplication of a ~120-kb BTA6 segment nested in the Belgian blue duplication, but excluding the *KIT* gene. Intriguingly, it also revealed the duplication of a ~418-kb BTA29 segment immediately flanking the Belgian blue insertion site and encompassing the last four of twelve *LUZP2* exons (β–γ; Fig. 4a, b). Moreover, fusion point **C**–β (but not α–**C** and **D**–A), specifying the Belgian blue *Cs* allele, could be amplified by PCR from genomic DNA of all examined brown Swiss colour-sided but not control animals (Supplementary Fig. 3). These findings established a clear link between the Belgian blue and brown Swiss *Cs* alleles.

We performed FISH analysis on lymphocytes of a *Cs*/+ brown Swiss animal using BTA6 and BTA29 BAC clones. Remarkably, we observed overlapping red and green signals on one of the BTA6 homologues, hence revealing the translocation of a BTA29 fragment on BTA6 (Fig. 4c). We generated mate-pair libraries from self-ligated ~5-kb and ~2-kb DNA fragments of a brown Swiss *Cs*/*Cs* animal and generated ~15 Gb of sequence on an Illumina GAIIx instrument (Supplementary Fig. 2). Analysis of the resulting sequence traces revealed two aberrant mate-pair clusters. The first corresponds to the Belgian blue **C**–β fusion point, previously detected by PCR. The second corresponds to a novel **B**–γ fusion point (Supplementary Fig. 2). The most parsimonious explanation accounting for all the data is that the brown Swiss *Cs* allele derives from the Belgian blue *Cs* allele by (1) excision of the **B**-**C**-β-γ fragment from the Belgian blue *Cs* allele on BTA29, (2) circularization, and (3) re-integration in the wild-type *KIT* locus by homologous recombination. This would result in a novel *Cs* allele mapping to the *KIT* locus and characterized by tandem duplicates of the B–C segment flanking the translocated β–γ BTA29 fragment (A-B-**C**-β-γ-**B**–C-D-E; Fig. 3).

Our model predicts that the **C** and **B** BTA6 segments immediately flanking β–γ carry the same haplotype as the *Cs*-allele of Belgian blue. To test this, we developed long-range PCR assays that would specifically

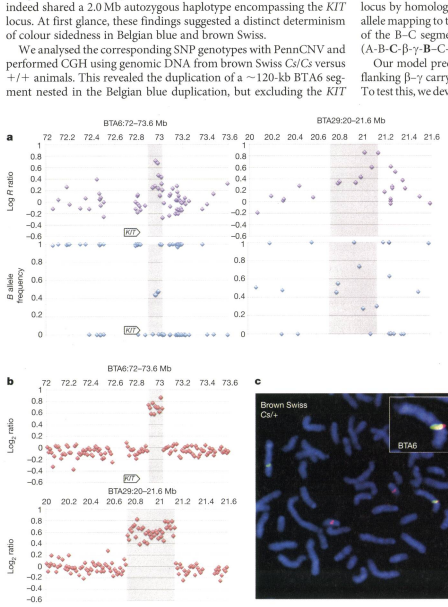

Figure 4 | Identification and mapping of the colour-sided locus in brown Swiss animals. **a**, PennCNV evidence for BTA6 and BTA29 duplications in brown Swiss colour-sided animals. The slightly different distribution of BTA6 SNPs when compared to Fig. 2 is due to the use of a different version of the 50K SNP array[3]. **b**, Confirmation and boundary definition of the *Cs*-associated BTA6 and BTA29 duplication in brown Swiss animals using CGH on Nimblegen bovine tiling arrays. The shaded areas in **a** and **b** mark the boundaries of the CNV, as defined by CGH. **c**, Demonstration by FISH of the translocation of a BTA29 segment onto BTA6 in a heterozygous *Cs*/+ brown Swiss animal.

amplify B, **C**, **B** and C segments from genomic DNA of a *Cs*/*Cs* brown Swiss animal, and—by sequencing the corresponding amplicons—determined the genotype of B and **B** and C and **C** for four SNP positions heterozygous in the high-throughput sequence reads of the brown Swiss *Cs*/*Cs* animal. We then determined the genotype of the Belgian blue *Cs* allele for the corresponding variants and showed that it matched the **C** and **B** segments of the brown Swiss *Cs* allele, in agreement with our model of homologous-recombination-dependent resolution of the circular intermediate (Fig. 3 and Supplementary Fig. 6).

Using the mate-pair genomic coordinates, we designed primer pairs to amplify the γ–**B** fusion point. As expected, productive amplification was only achieved using genomic DNA from colour-sided brown Swiss animals (Supplementary Fig. 3). We sequenced the corresponding PCR products to define the breakpoints at single-nucleotide resolution. The γ–**B** fusion presented hallmarks typical of microhomology mediated break induced replication (MMBIR) (Supplementary Fig. 4).

We obtained genomic DNA from colour-sided animals from seven additional cattle breeds and domestic yaks (Supplementary Fig. 7), which we tested by PCR for the presence of the two Belgian-blue-specific fusion points (**E**–**A**, α–**D**), the brown-Swiss-specific fusion point (γ–**B**), and the Belgian blue/brown Swiss shared fusion point (**C**–β). Colour-sided Dutch witrik and Ethiopian fogera animals were shown to carry the Belgian blue *Cs* allele (Cs_{29}), Austrian pustertaler sprinzen, Czech red-spotted cattle and French vosgienne the brown Swiss *Cs* allele (Cs_6), and Irish moiled, Swedish mountain and domestic yak carried both the Cs_{29} and Cs_6 alleles (Supplementary Fig. 3). We assume that Cs_{29} and Cs_6 alleles were introgressed in yak after domestication via well-documented hybridization of *Bos taurus* and *Bos grunniens*. These findings indicate that the Cs_{29} and Cs_6 alleles account for most if not all colour sidedness in cattle.

Analysis of colour sidedness has revealed a novel CNV-generating translocation mechanism involving circular intermediates. Whether this is a bovine idiosyncrasy or a more common mechanism remains to be determined. That some CNVs reflect translocation events is well established. As an example, 75 probable dispersed duplications in the human genome have been reported[11], as well as at least four interchromosomal duplications[12,13]. We ourselves performed genome-wide association mapping between the SNP and CNV genotype in human and cattle, and observed 21 and 4 putative '*trans*-associations' (that is, non-syntenic CNV-defining SNPs and associated SNPs), respectively (Supplementary Material). Some of these dispersed duplications might involve circular intermediates. In support of the occurrence of other instances involving circular intermediates are recent observations of repeated translocation of five clustered ORFs in wine and bioethanol strains of *Saccharomyces cerevisiae*, apparently via resolution of circular intermediates[14]. The same mechanism may contribute to somatic mutations in tumours. Indeed, episomes with the *NUP214*–*ABL1* fusion gene (observed in ~6% of T-cell acute lymphoblastic leukaemia) have been proposed to result from circularization and excision of a chromosome 9 segment bounded by the *NUP214* and *ABL1* genes, and to reintegrate ectopically by the same resolving mechanism proposed for colour sidedness in at least some patients[15]. The repatriation of exogenous sequences (including exons) back to the original chromosomal location via circular 'shuttling' intermediates suggests that this mechanism might underlie a specific mode of exon shuffling.

METHODS SUMMARY

A custom 50K SNP array[5] was used to genotype 21 colour-sided and 30 control Belgian blue animals. The genome of colour-sided animals was scanned for a shared haplotype using the ASSDOM software. In the brown Swiss, microsatellites adjacent to five candidate genes were genotyped in three half-sibling families and two point linkage calculated using the Merlin software[16]. CNVs were identified in the 50K SNP array data using the PennCNV software[5]. Array CGH was carried out on a custom 2.1 M oligonucleotide array (Roche-Nimblegen) with a non-colour-sided Belgian blue used as the reference in each hybridization. Metaphase spreads were generated from short-term lymphocyte cultures. BACs from the duplicated regions on BTA6 and BTA29 were identified using end sequences from the bovine RPCI42 BAC library. BACs were labelled with the appropriate fluorochrome by nick translation (Abbott Molecular), hybridized to the metaphase spreads and examined by fluorescent microscopy. Mate-pair libraries were generated using the Illumina mate-pair library kit v.2 for a *Cs*/*Cs* Belgian blue and a *Cs*/*Cs* brown Swiss animal. A paired-end library was also generated for a *Cs*/+ Belgian blue using the Illumina paired-end kit. Sequencing was carried out on an Illumina GAIIx instrument. PCR products spanning regions of interest were purified using QIAquick PCR purification kit (Qiagen), sequenced using Big Dye terminator cycle-sequencing kit v.3.1 (Applied Biosystems) and run on an ABI PRISM 3730 DNA analyser (Applied Biosystems). RNA was extracted form skin using the RNeasy fibrous tissue mini kit (Qiagen) and cDNA was synthesized using SuperScript II first-strand Synthesis SuperMix (Invitrogen). Long-range PCR was carried out using the Expand Long Template PCR System (Roche).

Full Methods and any associated references are available in the online version of the paper at www.nature.com/nature.

Received 4 September; accepted 5 December 2011.

1. Olson, T. *The Genetics of Cattle* (CAB International, 1999).
2. Porter, V. & Mason, I. L. *Mason's World Dictionary of Livestock Breeds, Types, and Varieties* (CAB International, 2002).
3. Charlier, C. *et al.* Highly effective SNP-based association mapping and management of recessive defects in livestock. *Nature Genet.* **40,** 449–454 (2008).
4. Charlier, C. *et al.* Microsatellite mapping of the bovine *roan* locus: a major determinant of white heifer disease. *Mamm. Genome* **7,** 138–142 (1996).
5. Wang, K. *et al.* PennCNV: an integrated hidden Markov model designed for high-resolution copy number variation detection in whole-genome SNP genotyping data. *Genome Res.* **17,** 1665–1674 (2007).
6. Yoshida, H. *et al.* Melanocyte migration and survival controlled by *SCF/c-kit* expression. *J. Investig. Dermatol. Symp. Proc.* **6,** 1–5 (2001).
7. Brooks, S. A. *et al.* A chromosome inversion near the *KIT* gene and the Tobiano spotting pattern in horses. *Cytogenet. Genome Res.* **119,** 225–230 (2007).
8. Marklund, S. *et al.* Molecular basis for the dominant white phenotype in the domestic pig. *Genome Res.* **8,** 826–833 (1998).
9. Hastings, P. J., Lupski, J. R., Rosenberg, S. M. & Ira, G. Mechanisms of change in gene copy number. *Nature Rev. Genet.* **10,** 551–564 (2009).
10. Ge, B. *et al.* Survey of allelic expression using EST mining. *Genome Res.* **15,** 1584–1591 (2005).
11. Conrad, D. F. *et al.* Origins and functional impact of copy number variation in the human genome. *Nature* **464,** 704–712 (2010).
12. Liu, G. E. *et al.* Analysis of copy number variations among diverse cattle breeds. *Genome Res.* **20,** 693–703 (2010).
13. Liu, G. E. *et al.* Analysis of recent segmental duplications in the bovine genome. *BMC Genomics* **10,** 571 (2009).
14. Borneman, A. R. *et al.* Whole-genome comparison reveals novel genetic elements that characterize the genome of industrial strains of *Saccharomyces cerevisiae*. *PLoS Genet.* **7,** e1001287 (2011).
15. Graux, C. *et al.* Heterogeneous patterns of amplification of the *NUP214-ABL1* fusion gene in T-cell acute lymphoblastic. *Leukemia* **23,** 125–133 (2009).
16. Abecasis, G. *et al.* Merlin-rapid analysis of dense genetic maps using sparse gene flow trees. *Nature Genet.* **30,** 97–101 (2002).

Supplementary Information is linked to the online version of the paper at www.nature.com/nature.

Acknowledgements This work was funded by the Walloon Direction General Operationnelle Agriculture, Resources Naturelles et Environnement (grants D31-1206 and D31-1214) and the Swiss National Science Foundation (grant 31003A_133034 to T.L.). We are grateful for the support of the GIGA-R Genomics platform, to P. Melvin, to G. Mekuriaw and staff of the Andassa livestock research center, Viking Genetics, Swissgenetics and the Schweizer Braunviehzuchtverband for their assistance in sample collection, to J. Vermeesch and B. Nowakowska for their assistance with array CGH.

Author Contributions K.D. performed the PennCNV, CGH, FISH, next-generation sequencing, breakpoint, DNA sequence variant and expression analyses. W.C. performed the bioinformatic analyses of the high-throughput sequencing reads. A.H., P.H., L.H., K.O., A.S., J.S. and H.S. provided samples from colour-sided animals. C.D., S.M. and S.R. performed linkage analyses in brown Swiss animals. T.L. supervised the work in Switzerland. C.C., M.G., T.D. and Z.Z. performed the association analyses. N.A. and N.C. performed SNP genotyping. C.F. and L.K. performed amplicon sequencing. Y.K., M.L. and D.Z. provided human CNV genotype data. K.D., M.G. and C.C. analysed data and wrote the manuscript.

Author Information Reprints and permissions information is available at www.nature.com/reprints. The authors declare no competing financial interests. Readers are welcome to comment on the online version of this article at www.nature.com/nature. Correspondence and requests for materials should be addressed to M.G. (michel.georges@ulg.ac.be).

LETTER

doi:10.1038/nature10754

Neuron-type-specific signals for reward and punishment in the ventral tegmental area

Jeremiah Y. Cohen[1]*, Sebastian Haesler[1]*, Linh Vong[2], Bradford B. Lowell[2] & Naoshige Uchida[1]

Dopamine has a central role in motivation and reward. Dopaminergic neurons in the ventral tegmental area (VTA) signal the discrepancy between expected and actual rewards (that is, reward prediction error)[1–3], but how they compute such signals is unknown. We recorded the activity of VTA neurons while mice associated different odour cues with appetitive and aversive outcomes. We found three types of neuron based on responses to odours and outcomes: approximately half of the neurons (type I, 52%) showed phasic excitation after reward-predicting odours and rewards in a manner consistent with reward prediction error coding; the other half of neurons showed persistent activity during the delay between odour and outcome that was modulated positively (type II, 31%) or negatively (type III, 18%) by the value of outcomes. Whereas the activity of type I neurons was sensitive to actual outcomes (that is, when the reward was delivered as expected compared to when it was unexpectedly omitted), the activity of type II and type III neurons was determined predominantly by reward-predicting odours. We 'tagged' dopaminergic and GABAergic neurons with the light-sensitive protein channelrhodopsin-2 and identified them based on their responses to optical stimulation while recording. All identified dopaminergic neurons were of type I and all GABAergic neurons were of type II. These results show that VTA GABAergic neurons signal expected reward, a key variable for dopaminergic neurons to calculate reward prediction error.

Dopaminergic neurons fire phasically (100–500 ms) after unpredicted rewards or cues that predict reward[1–3]. Their response to reward is reduced when a reward is fully predicted. Furthermore, their activity is suppressed when a predicted reward is omitted. From these observations, previous studies hypothesized that dopaminergic neurons signal discrepancies between expected and actual rewards (that is, they compute reward prediction error (RPE)), but how dopaminergic neurons compute RPE is unknown.

Dopaminergic neurons make up about 55–65% of VTA neurons; the rest are mostly GABAergic inhibitory neurons[4–6]. Many addictive drugs inhibit VTA GABAergic neurons, which increases dopamine release (called disinhibition), a potential mechanism for reinforcing the effects of these drugs[7–12]. Despite the known role of VTA GABAergic neurons inhibiting dopaminergic neurons *in vitro*[13], little is known about their role in normal reward processing. One obstacle has been the difficulty of identifying different neuron types with extracellular recording techniques. Conventionally, spike waveforms and other firing properties have been used to identify presumed dopaminergic and GABAergic neurons[1,2,14,15], but this approach has been questioned recently[5,16]. We thus aimed to observe how dopaminergic and GABAergic neurons process information about rewards and punishments.

We classically conditioned mice with different odour cues that predicted appetitive or aversive outcomes. The possible outcomes were big reward, small reward, nothing, or punishment (a puff of air delivered to the animal's face). Each behavioural trial began with a conditioned stimulus (CS; an odour, 1 s), followed by a 1-s delay and an unconditioned stimulus (US; the outcome). Within the first two behavioural sessions, mice began licking towards the water-delivery tube in the delay before rewards arrived, indicating that they quickly learned the CS–US associations (Fig. 1). The lick rate was significantly higher preceding big rewards than small ones (paired t-tests between lick rates for big versus small rewards for each session, $P < 0.05$ for each mouse).

We recorded the activity of VTA neurons while mice performed the conditioning task. All 95 neurons showed task-related responses (analysis of variance (ANOVA), all $P < 0.001$), thus all recorded neurons were used in the following analyses. Observing the temporal profiles of responses in trials with rewards, we found neurons that showed firing patterns that resemble those of dopaminergic neurons found in non-human primates[1,2,15]. These neurons were excited phasically by reward-predicting stimuli or reward (Fig. 2a, top). We also found many neurons with firing patterns distinct from typical dopaminergic neurons. These neurons showed persistent excitation during the delay before rewards, in response to reward-predicting odours (Fig. 2a, middle). Other neurons showed persistent inhibition to reward-predicting odours (Fig. 2a, bottom). To characterize the responses of the population, we measured the temporal response profile of each neuron during big-reward trials by quantifying firing rate changes from baseline in 100-ms bins using a receiver operating characteristic (ROC) analysis (Fig. 2b and Supplementary Fig. 1). We calculated the area under the ROC curve (auROC) at each time bin. Values greater than 0.5 indicate increases in firing rate relative to baseline, whereas values less than 0.5 indicate decreases.

To classify these response profiles, we used principal component analysis (PCA) followed by unsupervised, hierarchical clustering. This yielded three clusters of neurons that were separated according to (1) the magnitude of activity during the delay between CS and US, and (2) the magnitude of responses to the CS or US (Fig. 2c). Forty-nine neurons (52%) were classified as type I, which showed phasic responses. Twenty-nine neurons (31%) were classified as type II, which showed sustained excitation to reward-predicting odours, whereas 17 neurons (18%) were classified as type III, which showed sustained inhibition (Fig. 2d).

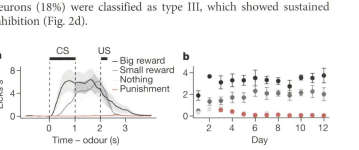

Figure 1 | Odour-outcome association task in mice. a, Licking behaviour from a representative experimental session. Black bars indicate CS and US delivery. Shaded regions around lick traces denote standard error of the mean (s.e.m.). **b**, Mean ± s.e.m. licks during the delay between CS and US as a function of days of the experiment across animals.

[1]Department of Molecular and Cellular Biology, Center for Brain Science, Harvard University, Cambridge, Massachusetts 02138, USA. [2]Division of Endocrinology, Department of Medicine, Beth Israel Deaconess Medical Center, Harvard Medical School, Boston, Massachusetts 02215, USA.
*These authors contributed equally to this work.

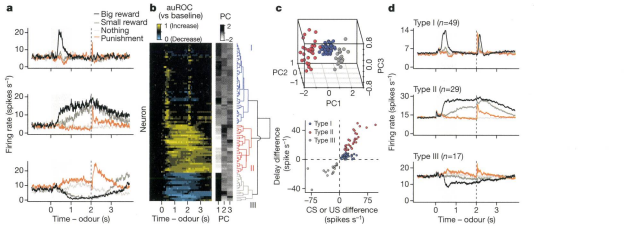

Figure 2 | VTA neurons show three distinct response types. **a**, Responses of example neurons. **b**, Responses of all neurons. Yellow, increase from baseline; cyan, decrease from baseline. Each row represents one neuron. The similarity order of the three main clusters is arranged to match the order presented in **a**. **c**, Top: the first three principal components of the auROC curves. Points are coloured based on hierarchical clustering from the dendrogram. Bottom: classification of neurons based on response differences between big-reward and no-reward trials during the delay versus during the CS or US. **d**, Average firing rates from type I–III neurons.

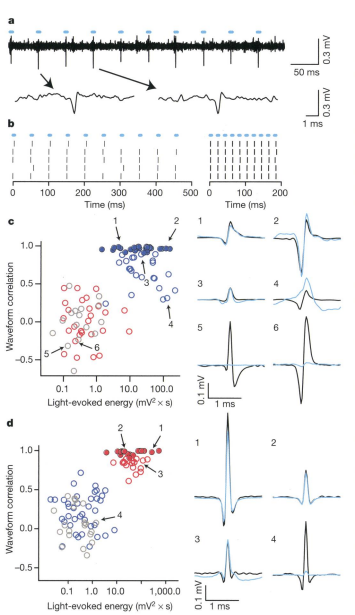

To identify dopaminergic neurons, we expressed channelrhodopsin-2 (ChR2), a light-gated cation channel[17,18], in dopaminergic neurons (see Methods). We confined expression to dopaminergic neurons by injecting adeno-associated virus containing FLEX-ChR2 (AAV-FLEX-ChR2)[19] into transgenic mice expressing Cre recombinase under the control of the promoter of the dopamine transporter (*DAT*; also called *Slc6a3*) gene (Supplementary Figs 2 and 3). For each neuron, we measured the response to light pulses and the shape of spontaneous spikes. We observed many neurons that fired after light pulses (Fig. 3a, b). We calculated the correlation between the spontaneous spike waveform and light-evoked voltage response and plotted it against the energy of light-evoked responses for each recording (Fig. 3c). This yielded two distinct clusters: one that showed significant responses to light pulses and one that did not. To identify dopaminergic neurons stringently, we applied the criterion that the light-evoked waveform must look almost identical to the spontaneous waveform (correlation coefficient >0.9). Twenty-six neurons met this criterion (filled blue points in Fig. 3c). Consistent with direct light activation rather than indirect, synaptic activation, all 26 neurons showed light-evoked spikes within a few milliseconds of light onset with small jitter, and followed high-frequency light stimulation of 50 Hz (Supplementary Fig. 4). These properties strongly indicate that these 26 neurons expressed ChR2. We therefore designate these 26 neurons as identified dopaminergic neurons. All identified dopaminergic neurons were of type I. Conversely, none of type II or III neurons was activated by light (red and grey points in Fig. 3c).

Next, we asked whether GABAergic neurons could be mapped to type II or III neurons. We recorded from 92 VTA neurons in mice expressing Cre recombinase under the control of the endogenous vesicular γ-aminobutyric acid (GABA) transporter (*Vgat*; also called *Slc32a1*) gene. These mice showed similar licking behaviour to *DAT*-Cre mice (Supplementary Fig. 5). We applied the PCA parameters

Figure 3 | Identifying dopaminergic and GABAergic neurons. **a**, Voltage trace from 10 pulses of 20 Hz light stimulation (cyan bars). Two light-triggered spikes are shown below. **b**, Response from this neuron to 20 Hz (left) and 50 Hz (right) stimulation. Ticks represent spikes. **c**, Quantification of light-evoked responses and mapping of response types in *DAT*-Cre mice. Blue, type I; red, type II; grey, type III neurons. Identified dopaminergic neurons are indicated by filled circles. Abscissa: energy (integral of the squared voltage values, $\int v^2 dt$) of the light-evoked response from each neuron. Ordinate: cross-correlation between the mean spontaneous spike and the light-evoked response. Example neurons are shown to the right (black, spontaneous spikes; cyan, light-evoked voltages). **d**, Light-evoked responses in *Vgat*-Cre mice. Conventions are the same as in **c**.

from the 95 neurons from *DAT*-Cre mice to the 92 neurons from *Vgat*-Cre mice. This yielded 38 type I neurons, 34 type II neurons and 20 type III neurons. Using the same criteria for GABAergic neurons as we used for dopaminergic neurons, we identified 17 GABAergic neurons (Fig. 3d and Supplementary Fig. 4). All 34 type II neurons fell in the upper cluster in Fig. 3d. We also found type I neurons that were inhibited by optical stimulation, consistent with local GABAergic stimulation (Supplementary Fig. 6).

Our data set of identified dopaminergic neurons allows us to characterize their diversity. We observed that some were excited by reward, some were excited by a reward-predicting CS, and some were excited by both (Fig. 4a–c). Although previous studies in non-human primates found similar variability[20,21] (Supplementary Fig. 7), this result may suggest that some dopaminergic neurons do not strictly follow canonical RPE coding. However, the US responses may be due to the delay between CS and US, known to increase the US response due to temporal uncertainty[20]. In addition, this diversity was correlated with the effect of training that occurred over several days across the population of dopaminergic neurons, even after animals had reached asymptotic behavioural performance (Fig. 1b). Soon after reaching a behavioural performance criterion, many dopaminergic neurons showed stronger responses to US over CS but the preference gradually shifted to CS over several days (Fig. 4d; Pearson correlation, $r = 0.42$, $P < 0.05$). This is consistent with a previous study in non-human primates that showed US responses gradually disappear over >1 month of training[21]. Thus, identified dopaminergic neurons appear to respond to CS and US similarly to those reported in non-human primate studies.

Another important response property that supports RPE coding in dopaminergic neurons is their decrease in firing rate when an expected reward is omitted[1,3]. We thus omitted reward unexpectedly on 10% of big-reward trials in some sessions. Fifteen of seventeen dopaminergic neurons showed a decrease in firing rate upon reward omission relative to reward delivery (Fig. 4f, g). The two dopaminergic neurons that were not modulated by reward omission were excited by big-reward CS, but fired close to 0 spikes s^{-1} otherwise; the low firing rate at the time of reward left little room to 'dip' further. We obtained similar results when we compared the firing rate upon reward omission to the baseline firing rate (9 of 17 neurons $P < 0.05$, t-test; mean auROC = 0.407, $t_{16} = 2.56$, $P < 0.05$; Supplementary Fig. 8a, b). Thus, most dopaminergic neurons coded RPE when expected reward was omitted.

GABAergic neurons showed persistent activity during the delay period, which parametrically encoded the value of upcoming outcomes (paired t-tests between no-, small- and big-reward trials, all $P < 0.001$ for 16 of 17 identified GABAergic neurons, Supplementary Fig. 7a; regression slopes, Supplementary Fig. 10i). This suggests that these neurons encode expectation about rewards. If this is the case, one prediction is that the activity of these neurons is not modulated by delivery or omission of reward. Indeed, GABAergic (and unidentified type II) and type III neurons were not significantly modulated by the presence or absence of reward itself (Fig. 4f, g and Supplementary Fig. 8), in contrast to identified dopaminergic neurons. None of the identified GABAergic neurons, and only 2 of 17 unidentified type II neurons, showed significant decreases in firing rate relative to when reward was delivered. None of the 11 type III neurons showed significant modulation by reward omission. Thus, the activity of type II and III neurons was modulated predominantly by reward-predicting cues but not actual reward.

Recent studies have revealed a diversity of responses of dopaminergic neurons to aversive stimuli: some are excited, others inhibited[15]. To test whether this diversity exists in dopaminergic and GABAergic VTA neurons, we delivered air puffs in some sessions. Identified dopaminergic neurons showed some diversity: although most significant responses were inhibitory, some were excitatory (Fig. 4h, i and Supplementary Fig. 9). In contrast, most type II and III neurons (and 13 of 14 identified GABAergic neurons) were excited by air puffs.

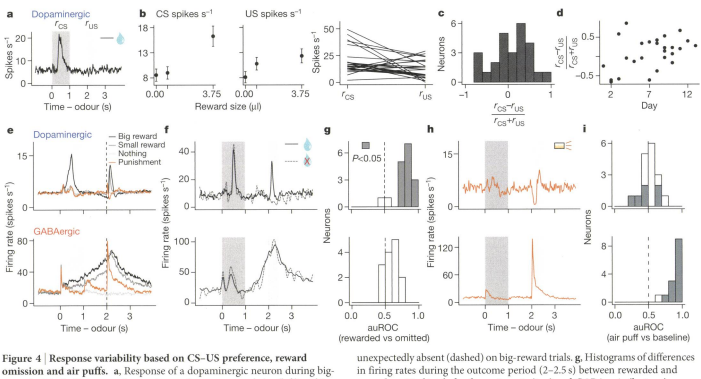

Figure 4 | Response variability based on CS–US preference, reward omission and air puffs. a, Response of a dopaminergic neuron during big-reward trials. **b**, Firing rate (mean ± s.e.m.) versus reward size (left) and in response to big-reward-predicting CS and big-reward US for each dopaminergic neuron (right). **c**, Histogram of CS–US index for dopaminergic neurons. **d**, CS–US index versus day after the behaviour was learned. **e**, Average responses of dopaminergic and GABAergic neurons. **f**, Responses of a dopaminergic and GABAergic neuron for reward present (solid) and unexpectedly absent (dashed) on big-reward trials. **g**, Histograms of differences in firing rates during the outcome period (2–2.5 s) between rewarded and reward-omitted trials for dopaminergic (top) and GABAergic (bottom) neurons. Values are represented using auROC (<0.5, rewarded < omitted; 0.5, no difference; >0.5, rewarded > omitted). Significant values are filled (t-test, $P < 0.05$). **h**, Responses of a dopaminergic and GABAergic neuron during punishment trials. **i**, Histograms of auROC values during the air puff (2–2.5 s) relative to baseline (<0.5, decrease; >0.5, increase from baseline).

Detecting the discrepancy between expected and actual outcomes has a critical role in optimal learning[1,22,23]. Although phasic firing of VTA dopaminergic neurons may act as such an error signal, how this is computed remains largely unknown. Models have postulated the existence of value-dependent, inhibitory input to dopaminergic neurons that persists during the delay between a CS and US (Supplementary Fig. 11a)[1,23]. Our data indicate that VTA GABAergic neurons provide such an inhibitory input that counteracts excitatory drive from primary reward when the reward is expected. In addition, these neurons were excited by aversive stimuli, potentially contributing to suppression of firing in some dopaminergic neurons in response to aversive events (Fig. 4). Previous work showed that VTA GABAergic neurons receive inputs from prefrontal cortex and subcortical areas that could provide reward-related signals[24–29]. Phasic excitation of VTA GABAergic neurons could be driven by inputs from lateral habenula neurons that are phasically excited by aversive stimuli[29]. These habenular neurons do not show sustained activity between CS and US, so it is unlikely that they provide reward expectation signals to VTA GABAergic neurons. Instead, these signals may come from the pedunculopontine nucleus[25] or orbitofrontal cortex[27] (Supplementary Fig. 11b). VTA GABAergic neurons form synapses preferentially onto dendrites of dopaminergic neurons[28], whereas other inhibitory inputs form synapses onto their somata[29]. Dendritic inhibition is thought to be weaker than somatic 'shunting' inhibition[28] but appears well suited for deriving graded outputs by 'arithmetically' combining excitatory and inhibitory inputs.

A major effect of drugs of addiction is inhibition of VTA GABAergic neurons[7,8]. If VTA GABAergic neurons are involved in computation of RPE, inhibition of GABAergic neurons by addictive drugs could lead to sustained RPE even after the learned effects of drug intake are well established, thereby resulting in sustained reinforcement of drug taking[30]. Understanding local circuits in VTA in the context of learning theory may thus provide crucial insights into normal as well as abnormal functions of reward circuits.

METHODS SUMMARY

All surgical and experimental procedures were in accordance with the National Institutes of Health Guide for the Care and Use of Laboratory Animals and approved by the Harvard Institutional Animal Care and Use Committee. We injected male *DAT*-Cre and *Vgat*-Cre mice with adeno-associated virus carrying FLEX-ChR2 into the VTA and implanted a head plate and a microdrive containing six tetrodes and an optical fibre. While mice performed a classical conditioning task, we recorded spiking activity from VTA neurons. We delivered pulses of light to activate ChR2 and classified neurons as dopaminergic, GABAergic or unidentified. After experiments, we performed immunohistochemistry to localize recording sites amid dopaminergic neurons.

Full Methods and any associated references are available in the online version of the paper at www.nature.com/nature.

Received 9 May; accepted 2 December 2011.
Published online 18 January 2012.

1. Schultz, W., Dayan, P. & Montague, P. R. A neural substrate of prediction and reward. *Science* **275,** 1593–1599 (1997).
2. Bayer, H. M. & Glimcher, P. W. Midbrain dopamine neurons encode a quantitative reward prediction error signal. *Neuron* **47,** 129–141 (2005).
3. Schultz, W. Behavioral theories and the neurophysiology of reward. *Annu. Rev. Psychol.* **57,** 87–115 (2006).
4. Swanson, L. W. The projections of the ventral tegmental area and adjacent regions: a combined fluorescent retrograde tracer and immunofluorescence study in the rat. *Brain Res. Bull.* **9,** 321–353 (1982).
5. Margolis, E. B., Lock, H., Hjelmstad, G. O. & Fields, H. L. The ventral tegmental area revisited: is there an electrophysiological marker for dopaminergic neurons? *J. Physiol.* **577,** 907–924 (2006).
6. Nair-Roberts, R. G. *et al.* Stereological estimates of dopaminergic, GABAergic and glutamatergic neurons in the ventral tegmental area, substantia nigra and retrorubral field in the rat. *Neuroscience* **152,** 1024–1031 (2008).
7. Hyman, S. E., Malenka, R. C. & Nestler, E. J. Neural mechanisms of addiction: the role of reward-related learning and memory. *Annu. Rev. Neurosci.* **29,** 565–598 (2006).
8. Lüscher, C. & Malenka, R. C. Drug-evoked synaptic plasticity in addiction: from molecular changes to circuit remodeling. *Neuron* **69,** 650–663 (2011).
9. Johnson, S. W. & North, R. A. Opioids excite dopamine neurons by hyperpolarization of local interneurons. *J. Neurosci.* **12,** 483–488 (1992).
10. Mansvelder, H. D., Keath, J. R. & McGehee, D. S. Synaptic mechanisms underlie nicotine-induced excitability of brain reward areas. *Neuron* **33,** 905–919 (2002).
11. Szabo, B., Siemes, S. & Wallmichrath, I. Inhibition of GABAergic neurotransmission in the ventral tegmental area by cannabinoids. *Eur. J. Neurosci.* **15,** 2057–2061 (2002).
12. Tan, K. R. *et al.* Neural bases for addictive properties of benzodiazepines. *Nature* **463,** 769–774 (2010).
13. Dobi, A., Margolis, E. B., Wang, H.-L., Harvey, B. K. & Morales, M. Glutamatergic and nonglutamatergic neurons of the ventral tegmental area establish local synaptic contacts with dopaminergic and nondopaminergic neurons. *J. Neurosci.* **30,** 218–229 (2010).
14. Steffensen, S. C., Svingos, A. L., Pickel, V. M. & Henriksen, S. J. Electrophysiological characterization of GABAergic neurons in the ventral tegmental area. *J. Neurosci.* **18,** 8003–8015 (1998).
15. Matsumoto, M. & Hikosaka, O. Two types of dopamine neuron distinctly convey positive and negative motivational signals. *Nature* **459,** 837–841 (2009).
16. Lammel, S. *et al.* Unique properties of mesoprefrontal neurons within a dual mesocorticolimbic dopamine system. *Neuron* **57,** 760–773 (2008).
17. Nagel, G. *et al.* Channelrhodopsin-2, a directly light-gated cation-selective membrane channel. *Proc. Natl Acad. Sci. USA* **100,** 13940–13945 (2003).
18. Boyden, E. S., Zhang, F., Bamberg, E., Nagel, G. & Deisseroth, K. Millisecond-timescale, genetically targeted optical control of neural activity. *Nature Neurosci.* **8,** 1263–1268 (2005).
19. Atasoy, D., Aponte, Y., Su, H. H. & Sternson, S. M. A FLEX switch targets Channelrhodopsin-2 to multiple cell types for imaging and long-range circuit mapping. *J. Neurosci.* **28,** 7025–7030 (2008).
20. Fiorillo, C. D., Newsome, W. T. & Schultz, W. The temporal precision of reward prediction in dopamine neurons. *Nature Neurosci.* **11,** 966–973 (2008).
21. Takikawa, Y., Kawagoe, R. & Hikosaka, O. A possible role of midbrain dopamine neurons in short- and long-term adaptation of saccades to position-reward mapping. *J. Neurophysiol.* **92,** 2520–2529 (2004).
22. Rescorla, R. A. & Wagner, A. R. in *Classical Conditioning II: Current Research and Theory* (eds Black, A. H. & Wagner, A. R.) 64–99 (New York, 1972).
23. Houk, J. C., Adams, J. L. & Barto, A. G. in *Models of Information Processing in the Basal Ganglia* (eds Houk, J. C., Davis, J. L. & Beiser, D. G.) 249–270 (MIT Press, 1995).
24. Carr, D. B. & Sesack, S. R. Projections from the rat prefrontal cortex to the ventral tegmental area: target specificity in the synaptic associations with mesoaccumbens and mesocortical neurons. *J. Neurosci.* **20,** 3864–3873 (2000).
25. Okada, K., Toyama, K., Inoue, Y., Isa, T. & Kobayashi, Y. Different pedunculopontine tegmental neurons signal predicted and actual task rewards. *J. Neurosci.* **29,** 4858–4870 (2009).
26. Matsumoto, M. & Hikosaka, O. Lateral habenula as a source of negative reward signals in dopamine neurons. *Nature* **447,** 1111–1115 (2007).
27. Takahashi, Y. K. *et al.* Expectancy-related changes in firing of dopamine neurons depend on orbitofrontal cortex. *Nature Neurosci.* **14,** 1590–1597 (2011).
28. Omelchenko, N. & Sesack, S. R. Ultrastructural analysis of local collaterals of rat ventral tegmental area neurons: GABA phenotype and synapses onto dopamine and GABA cells. *Synapse* **63,** 895–906 (2009).
29. Jhou, T. C., Fields, H. L., Baxter, M. G., Saper, C. B. & Holland, P. C. The rostromedial tegmental nucleus (RMTg), a GABAergic afferent to midbrain dopamine neurons, encodes aversive stimuli and inhibits motor responses. *Neuron* **61,** 786–800 (2009).
30. Redish, A. D. Addiction as a computational process gone awry. *Science* **306,** 1944–1947 (2004).

Supplementary Information is linked to the online version of the paper at www.nature.com/nature.

Acknowledgements We thank M. Meister, V. N. Murthy, J. D. Schall and R. P. Heitz for comments, C. Dulac for sharing resources, C. I. Moore, J. Ritt and J. Siegle for advice about microdrives, K. Deisseroth for the AAV-FLEX-ChR2 construct, and E. Soucy and J. Greenwood for technical support. This work was supported by a Howard Hughes Medical Institute Fellowship from the Helen Hay Whitney Foundation (J.Y.C.); the Human Frontiers Science Program (S.H.); a Howard Hughes Medical Institute Collaborative Innovation Award, a Smith Family New Investigator Award, the Alfred Sloan Foundation, the Milton Fund (N.U.); F32 DK078478, P30 DK046200 (L.V.); and R01 DK075632, R01 DK089044, P30 DK046200, P30 DK057521 (B.B.L.).

Author Contributions J.Y.C. and S.H. collected and analysed data. J.Y.C., S.H. and N.U. designed experiments and wrote the paper. L.V. and B.B.L. generated *Vgat*-Cre mice.

Author Information Reprints and permissions information is available at www.nature.com/reprints. The authors declare no competing financial interests. Readers are welcome to comment on the online version of this article at www.nature.com/nature. Correspondence and requests for materials should be addressed to N.U. (uchida@mcb.harvard.edu).

LETTER

doi:10.1038/nature10766

Vaccine protection against acquisition of neutralization-resistant SIV challenges in rhesus monkeys

Dan H. Barouch[1,2], Jinyan Liu[1], Hualin Li[1], Lori F. Maxfield[1], Peter Abbink[1], Diana M. Lynch[1], M. Justin Iampietro[1], Adam SanMiguel[1], Michael S. Seaman[1], Guido Ferrari[3], Donald N. Forthal[4], Ilnour Ourmanov[5], Vanessa M. Hirsch[5], Angela Carville[6], Keith G. Mansfield[6], Donald Stablein[7], Maria G. Pau[8], Hanneke Schuitemaker[8], Jerald C. Sadoff[8], Erik A. Billings[9], Mangala Rao[9], Merlin L. Robb[9], Jerome H. Kim[9], Mary A. Marovich[9], Jaap Goudsmit[8]* & Nelson L. Michael[9]*

Preclinical studies of human immunodeficiency virus type 1 (HIV-1) vaccine candidates have typically shown post-infection virological control, but protection against acquisition of infection has previously only been reported against neutralization-sensitive virus challenges[1–3]. Here we demonstrate vaccine protection against acquisition of fully heterologous, neutralization-resistant simian immunodeficiency virus (SIV) challenges in rhesus monkeys. Adenovirus/poxvirus and adenovirus/adenovirus-vector-based vaccines expressing SIV_{SME543} Gag, Pol and Env antigens resulted in an 80% or greater reduction in the per-exposure probability of infection[4,5] against repetitive, intrarectal SIV_{MAC251} challenges in rhesus monkeys. Protection against acquisition of infection showed distinct immunological correlates compared with post-infection virological control and required the inclusion of Env in the vaccine regimen. These data demonstrate the proof-of-concept that optimized HIV-1 vaccine candidates can block acquisition of stringent, heterologous, neutralization-resistant virus challenges in rhesus monkeys.

Despite the recent demonstration of partial HIV-1 vaccine efficacy in humans[6], the immune responses required to protect against acquisition of infection have remained unclear. Preclinical studies of HIV-1 vaccine candidates have begun to elucidate immunological correlates of protection against neutralization-sensitive viruses[1–3], but no study has to date reported vaccine protection against acquisition of heterologous, neutralization-resistant virus challenges[1,7,8]. Mucosal SIV_{MAC251} infection of rhesus monkeys represents a stringent preclinical model of a highly pathogenic, neutralization-resistant virus swarm[1,9,10], and repetitive mucosal challenges more closely mimic sexual HIV-1 transmission in humans than do single high-dose challenges[10]. We therefore performed two studies to evaluate the protective efficacy of optimized adenovirus/poxvirus and adenovirus/adenovirus vector-based vaccines against repetitive, heterologous, intrarectal SIV_{MAC251} challenges in rhesus monkeys.

In the first study, 40 Indian-origin rhesus monkeys (*Macaca mulatta*) that did not express the class I alleles *Mamu-A*01*, *Mamu-B*08*, and *Mamu-B*17* associated with spontaneous virological control[11–13] were immunized by the intramuscular route with the following vaccine regimens expressing SIV_{SME543} Gag-Pol and Env immunogens ($N = 8$ per group): (1) DNA prime, modified vaccinia Ankara (MVA) boost; (2) MVA prime, MVA boost; (3) adenovirus serotype 26 (Ad26) prime, MVA boost; (4) MVA prime, Ad26 boost; and (5) sham controls. Groups were balanced for susceptible and resistant *TRIM5α* alleles[1,14]. Monkeys were primed once at week 0 with 2×10^{10} viral particles of Ad26 vectors or 10^8 plaque-forming units (p.f.u.) of MVA vectors, or three times at weeks 0, 4, and 8 with 5 mg of DNA vaccines. Animals were then boosted once at week 24 with 2×10^{10} viral particles of Ad26 vectors or 10^8 p.f.u. of MVA vectors.

The vaccine regimens elicited distinct profiles of cellular and humoral immune responses, as measured by IFN-γ ELISPOT assays (Fig. 1a and Supplementary Fig. 1), multiparameter intracellular cytokine staining (ICS) assays[8,15–17] (Fig. 1b and Supplementary Fig. 2), cellular immune breadth (Supplementary Fig. 3), SIV_{MAC251} Env-specific binding antibody ELISAs (Fig. 1c), tier 1 neutralizing antibody (NAb) assays against tissue culture laboratory adapted (TCLA) tier 1 SIV_{SME660} (CP3C-P-A8) and SIV_{MAC251} (TCLA) pseudoviruses (Fig. 1d), and antibody-dependent cellular cytotoxicity (ADCC) and antibody-dependent cell-mediated virus inhibition (ADCVI) assays (Supplementary Fig. 4). Tier 2 NAb responses against neutralization-resistant SIV_{SME660} (CR54-PK-2A5) and SIV_{MAC251} (SIV_{MAC251}-30) pseudoviruses, however, were below the 50% neutralization cutoff for positivity, although positive trends were observed in all vaccinated groups (Supplementary Fig. 4).

To evaluate the protective efficacy of these vaccine regimens, all monkeys were challenged repetitively beginning at week 52 (six months following the boost immunization) with six intrarectal inoculations of the heterologous virus SIV_{MAC251} using a 1:1,000 dilution (930 half-maximal tissue-culture infectious dose ($TCID_{50}$)) of our challenge stock[9]. After the first challenge, 75% of sham control monkeys became infected, compared with only 12–25% of the animals that received the heterologous vector regimens DNA/MVA, Ad26/MVA, and MVA/Ad26 (Fig. 1e). The percentage of uninfected animals declined proportionately with each challenge, and the majority of vaccinees and all controls were infected by the end of the challenge protocol. Monkeys that received the Ad26/MVA and MVA/Ad26 vaccines required three challenges to infect 50% of animals in each group, whereas only one challenge was required to infect 50% of animals in the control group ($P = 0.004$ and $P = 0.006$, respectively, Wald tests, proportional hazard model). The heterologous vector regimens also showed decreased hazard ratios of 0.17 (95% confidence interval (CI) 0.05–0.57) to 0.20 (CI 0.06–0.63) compared with the controls, corresponding to an 80–83% reduction in the per-exposure probability of infection (Fig. 1f; vaccine efficacy VE = 1 – hazard ratio), as previously described[4,5]. These data demonstrate vaccine protection against acquisition of infection following repetitive, heterologous, intrarectal SIV_{MAC251} challenges.

Control monkeys showed peak viral loads on day 14 following infection and then relatively stable mean set point viral loads of 5.85 log SIV RNA copies per millilitre (Supplementary Fig. 5). The Ad26/MVA and the MVA/Ad26 vaccines resulted, respectively, in at least 2.32 and 1.08 log reductions of mean set point viral loads compared with sham controls for over 250 days ($P = 0.0037$ for each vaccine versus sham, Wilcoxon rank-sum tests) (Fig. 1g and Supplementary Fig. 5). Moreover, half the animals in the Ad26/MVA

[1]Division of Vaccine Research, Beth Israel Deaconess Medical Center, Harvard Medical School, Boston, Massachusetts 02215, USA. [2]Ragon Institute of MGH, MIT, and Harvard, Boston, Massachusetts 02114, USA. [3]Duke University Medical Center, Durham, North Carolina 27710, USA. [4]University of California Irvine School of Medicine, Irvine, Californian 92697, USA. [5]National Institute of Allergy and Infectious Diseases, Bethesda, Massachusetts 20892, USA. [6]New England Primate Research Center, Southborough, Massachusetts 01772, USA. [7]EMMES Corporation, Rockville, Maryland 20850, USA. [8]Crucell Holland BV, 2301 CA, Leiden, The Netherlands. [9]US Military HIV Research Program, Walter Reed Army Institute of Research, Silver Spring, Maryland 20910, USA.
*These authors contributed equally to this work.

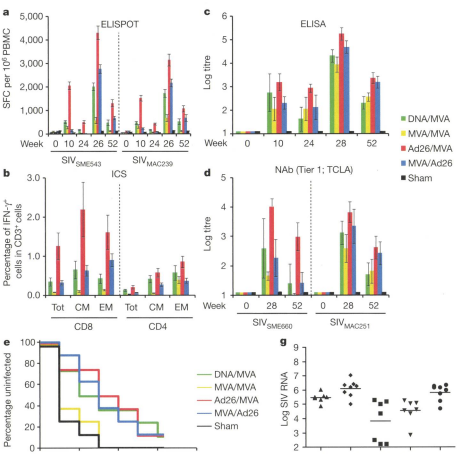

f

	No. of challenges for 50% infection	*P*-value vs sham*	Hazard ratio (95% CI)	Per-exposure vaccine efficacy	Per-exposure risk of infection
DNA/MVA	2	0.006	0.19 (0.06–0.61)	81%	0.27
MVA/MVA	1	0.56	0.73 (0.25–2.13)	27%	0.62
Ad26/MVA	3	0.004	0.17 (0.05–0.57)	83%	0.25
MVA/Ad26	3	0.006	0.20 (0.06–0.63)	80%	0.27
Sham	1	NA	1.0	NA	0.73

*Wald test, proportional hazard model

Figure 1 | Immunogenicity and protective efficacy of the adenovirus/poxvirus vaccines. **a**, Cellular immune responses to SIV_{SME543} and SIV_{MAC239} Gag, Pol and Env as determined by IFN-γ ELISPOT assays at weeks 0, 10, 24, 26, and 52. PBMC, peripheral blood mononuclear cells; SFC, spot-forming cells. **b**, $CD8^+$ and $CD4^+$ total, central/transitional memory (CM; $CD28^+CD95^+$), and effector memory (EM; $CD28^-CD95^+$) responses to Gag, Pol and Env as determined by multiparameter IFN-γ ICS assays at week 26. **c**, SIV_{MAC251} Env ELISAs at weeks 0, 10, 24, 28, and 52. **d**, SIV_{SME660} and SIV_{MAC251} tier 1 pseudovirus NAb assays at weeks 0, 28, and 52. Error bars represent s.e.m. **e**, Number of challenges required for acquisition of infection in each vaccine group. **f**, Statistical analyses include the number of challenges required for 50% infection, hazard ratios with 95% confidence intervals (CI), per-exposure vaccine efficacy and per-exposure risks of infection in each group. *P*-values reflect Wald tests using a proportional hazard model. **g**, Log SIV RNA copies per ml are depicted for each vaccine group at viral set point (day 84). $^{**}P = 0.0037$, Wilcoxon rank-sum tests. The horizontal lines represent mean set point log viral loads. Ad, adenovirus; D, DNA; M, MVA.

group either demonstrated rapid and durable virological control to undetectable levels (Fig. 1g; $N = 3$) or remained uninfected (Fig. 1e; $N = 1$). The Ad26/MVA and MVA/Ad26 vaccines also afforded a survival advantage as compared with the controls ($P = 0.025$, log-rank test) (Supplementary Fig. 6).

We next evaluated the immunological correlates of protection against acquisition of infection, defined as the number of challenges required to establish infection, and virological control, defined as set point viral loads. Our pre-specified primary immunological correlates analysis (Supplementary Table 1) demonstrated that protection against acquisition of infection was best correlated with Env-specific binding ELISA antibody responses (Fig. 2a; $P < 0.0001$, Spearman rank-correlation test) and tier 1 NAb titres (Fig. 2b; $P = 0.0034$) immediately before challenge. Protection against acquisition of infection also correlated with V2-specific antibodies that presumably represented a subset of total Env-specific binding antibodies (Fig. 2e, f; $P < 0.0001$). Virological control was correlated with Gag ELISPOT breadth (Fig. 2c; $P = 0.0002$) and magnitude (Fig. 2d; $P = 0.0058$) immediately before challenge, consistent with our previous observations[18].

In our exploratory immunological correlates analysis, we evaluated 35 humoral and cellular immune parameters at both peak and memory time points before challenge as possible immunological correlates of acquisition and virological control following challenge. No additional immune parameters were significantly correlated with protection

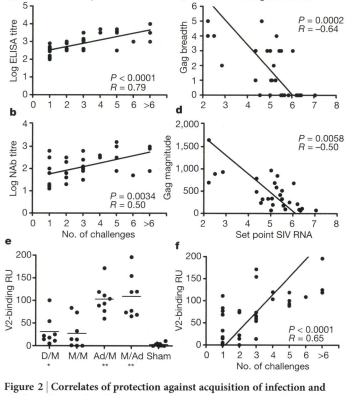

Figure 2 | Correlates of protection against acquisition of infection and virological control with the adenovirus/poxvirus vaccines. **a**, **b**, Correlation of log ELISA titres immediately before challenge (**a**) and log tier 1 NAb titres immediately before challenge (**b**) with the number of challenges required to establish infection. **c**, **d**, Correlation of Gag ELISPOT breadth before challenge (**c**) and Gag ELISPOT magnitude before challenge (**d**) with set point viral loads following challenge. Correlates analyses included the 32 vaccinated monkeys (**a**, **b**) or the 29 vaccinated animals that became infected (**c**, **d**) and did not include the sham controls. *P*-values reflect Spearman rank-correlation tests. **e**, V2-specific binding antibodies assessed by surface plasmon resonance response units (RU) for each vaccine group at week 30. $^{*}P = 0.002$, $^{**}P = 0.0007$, Wilcoxon rank-sum tests. The horizontal lines represent mean responses. **f**, Correlation of V2-specific antibody responses with the number of challenges required to establish infection.

against acquisition of infection in this analysis after multiple comparison adjustments (Supplementary Table 2). Gag-, Pol- and Env-specific effector memory $CD8^+$ T-lymphocyte responses exhibited trends towards protection against acquisition, but did not achieve statistical significance according to our pre-specified criteria. In contrast, multiple humoral and cellular immune responses were significantly correlated with virological control (Supplementary Table 3), including Env ELISA, NAb and ADCC responses as well as Gag ELISPOT magnitude and breadth, Pol ELISPOT magnitude and Env $CD4^+$ effector memory responses. These data support a model in which protection against acquisition of infection is correlated with vaccine-elicited Env antibody responses, whereas virological control is correlated with both T-lymphocyte and antibody responses. These distinct immunological correlates probably reflect fundamentally different biologic requirements for blocking establishment of infection at the mucosal site of inoculation compared with controlling viral replication after infection has become disseminated[19]. However, the actual mechanisms of protection remain to be determined.

We next evaluated directly the hypothesis that Env was critical for blocking acquisition of infection in this system. In the second study, 40 rhesus monkeys that did not express the class I alleles *Mamu-A*01*, *Mamu-B*08* and *Mamu-B*17* were immunized by the intramuscular route with Ad35 prime[20], Ad26 boost[21] vaccine regimens expressing (1) SIV_{SME543} Gag-Pol ($N = 16$), (2) SIV_{SME543} Gag-Pol and Env ($N = 16$) and (3) sham controls ($N = 8$). Groups were balanced for susceptible and resistant *TRIM5α* alleles[1,14]. Monkeys were primed once at week 0 with 2×10^{10} viral particles of Ad35 vectors and boosted once at week 24 with 2×10^{10} viral particles of Ad26 vectors. Cellular immune responses were assessed by IFN-γ ELISPOT assays (Fig. 3a and Supplementary Fig. 7) and multiparameter ICS assays in both the periphery (Fig. 3b and Supplementary Fig. 8) and in colorectal mucosa (Supplementary Fig. 9). Env-specific humoral immune responses were assessed by ELISAs in both the periphery (Fig. 3c) and in colorectal mucosa (Supplementary Fig. 10), tier 1 NAb assays (Fig. 3d) and ADCC assays (Supplementary Fig. 11). Only marginal tier 2 NAb responses were observed (Supplementary Fig. 11).

We assessed protective efficacy of these vaccine regimens against repetitive, heterologous, intrarectal SIV_{MAC251} challenges as described in the first study. After the first challenge, 50% of sham control monkeys became infected, compared with only 12% of the animals that received the Gag-Pol-Env vaccine (Fig. 3e). The monkeys that received the Gag-Pol-Env vaccine required four challenges to infect 50% of animals in each group, whereas only one challenge was required to infect 50% of animals in the control group (Fig. 3f; $P = 0.002$, Wald test, proportional hazard model). Moreover, the Gag-Pol-Env vaccine resulted in a decreased hazard ratio of 0.20 (CI 0.07–0.55), corresponding to an 80% reduction in the per-exposure probability of infection. In contrast, the Gag-Pol vaccine afforded only a marginal protective effect, demonstrating the critical role of Env in blocking acquisition of infection in this model. The Gag-Pol and Gag-Pol-Env vaccines resulted in, respectively, at least 1.59 log and 2.18 log reductions of set point viral loads compared with controls (Fig. 3g and Supplementary Fig. 12; $P = 0.0006$ and 0.0002, respectively, Wilcoxon rank-sum tests). Immunological correlates of protection against acquisition of infection were consistent with the first study, and both peripheral (Fig. 4a–c) and rectal (Fig. 4d) Env-specific IgG correlated with reduced acquisition risk.

Taken together, these data demonstrate that optimized adenovirus/poxvirus and adenovirus/adenovirus vector-based vaccines afforded significant protection against acquisition of infection following highly pathogenic, heterologous, neutralization-resistant SIV_{MAC251} challenges in rhesus monkeys (Figs 1e, 3e and Supplementary Fig. 13). Although several studies have previously shown partial protection against acquisition of neutralization-sensitive virus challenges[1–3], no HIV-1 vaccine candidate has to date blocked acquisition of heterologous, difficult-to-neutralize virus challenges, including Ad5 (ref. 7), DNA/Ad5 (ref. 1) and cytomegalovirus[8] vaccines. In particular, a recent study demonstrated that a DNA/Ad5 vaccine afforded partial protection against acquisition of SIV_{SME660}, which is a neutralization-sensitive tier 1A virus in TZM-bl neutralization assays, but the same vaccine afforded no efficacy against neutralization-resistant SIV_{MAC251} (ref. 1), highlighting important differences in the stringencies between these two SIV challenge models as well as potentially important phenotypic differences between adenovirus serotypes[17]. However, we note that the acquisition effect in the present study was relative rather than absolute, and that the majority of vaccinees became infected by the end of the challenge protocol.

Our studies also demonstrate that inclusion of Env in the vaccine was required for the acquisition effect (Fig. 3e), despite an 18% difference in the Env amino acid sequences between the vaccine strain and challenge virus. Moreover, our immunological correlates analyses (Figs 2, 4 and Supplementary Tables 1–3) suggest that Env-specific antibodies are critical for blocking acquisition of infection, whereas multiple cellular and humoral immune responses correlate with virological control, although the actual mechanisms of protection remain to be determined. In addition, the RV144 immunological correlates analyses raised the hypothesis that vaccine-elicited V1/V2-specific antibodies may reduce HIV-1 acquisition risk in humans[22]. Our data (Figs 2f, 4c) are consistent with this hypothesis, although it remains unclear whether V2-specific antibodies actually protect or simply represent a marker for other Env-specific antibodies or other protective factors.

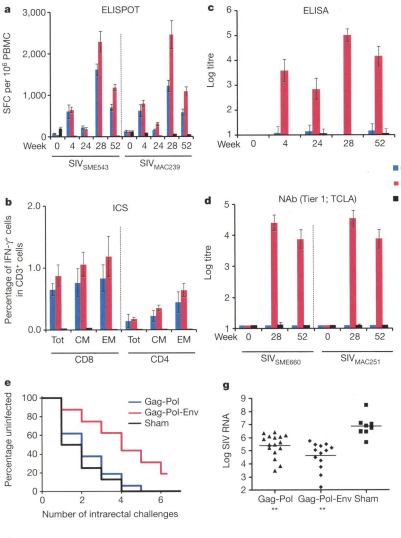

f

	No. of challenges for 50% infection	*P*-value vs sham*	Hazard ratio (95%CI)	Per-exposure vaccine efficacy	Per-exposure risk of infection
Gag-Pol	2	0.46	0.71 (0.29–1.74)	29%	0.44
Gag-Pol-Env	4	0.002	0.20 (0.07–0.55)	80%	0.20
Sham	1	N/A	1.0	N/A	0.53

* Wald test, proportional hazard model

Figure 3 | Immunogenicity and protective efficacy of the adenovirus/adenovirus vaccines. a, Cellular immune responses to SIV_{SME543} and SIV_{MAC239} Gag, Pol and Env as determined by IFN-γ ELISPOT assays at weeks 0, 4, 24, 28 and 52. **b**, $CD8^+$ and $CD4^+$ total, central/transitional memory (CM; $CD28^+CD95^+$), and effector memory (EM; $CD28^-CD95^+$) responses to Gag, Pol and Env as determined by multiparameter IFN-γ ICS assays at week 28. **c**, SIV_{MAC251} Env ELISAs at weeks 0, 4, 24, 28 and 52. **d**, SIV_{SME660} and SIV_{MAC251} tier 1 pseudovirus NAb assays at weeks 0, 28 and 52. Error bars represent s.e.m. **e**, Number of challenges required for acquisition of infection in each vaccine group. **f**, Statistical analyses include the number of challenges required for 50% infection, hazard ratios with 95% confidence intervals (CI), per-exposure vaccine efficacy, and per-exposure risks of infection in each group. *P*-values reflect Wald tests using a proportional hazard model. **g**, Log SIV RNA copies per ml are depicted for each vaccine group at viral set point (day 84). $^{**}P < 0.001$, Wilcoxon rank-sum tests. The horizontal lines reflect mean set point log viral loads.

Considerable efforts are currently underway to identify and to reverse engineer potent, broadly reactive monoclonal antibodies[23,24]. Although the induction of such NAb responses by a vaccine would presumably be highly desirable, no Env immunogens have to date been developed that can elicit these responses. Our findings suggest that a substantial degree of protection can be achieved against stringent virus challenges even in the absence of high titres of tier 2 NAbs, perhaps reflecting the importance of antibody effector functions that may not be fully measured by traditional virus neutralization assays. Of note, the partial protection in the present study was observed with vectored Env and without a purified Env protein subunit boost. The degree to which an Env protein boost may further improve the protective efficacy afforded by these vaccine regimens remains to be determined.

In summary, our data demonstrate the proof-of-concept that vaccination can protect against acquisition of stringent, heterologous, neutralization-resistant SIV_{MAC251} challenges in rhesus monkeys. These findings, together with the observations of a critical requirement for Env and the distinct immunological correlates of protection against acquisition of infection and virological control, pave novel paths forward for HIV-1 vaccine development.

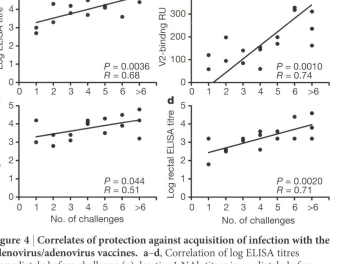

Figure 4 | Correlates of protection against acquisition of infection with the adenovirus/adenovirus vaccines. a–d, Correlation of log ELISA titres immediately before challenge (**a**), log tier 1 NAb titres immediately before challenge (**b**), V2-specific antibody responses (**c**) and rectal IgG antibody responses (**d**) with the number of challenges required to establish infection. Correlates analyses included the 16 Gag-Pol-Env-vaccinated monkeys and did not include the Gag-Pol-vaccinated monkeys or the sham controls. *P*-values reflect Spearman rank-correlation tests.

METHODS SUMMARY

For each study, 40 Indian-origin rhesus monkeys (*Macaca mulatta*) were vaccinated with DNA, MVA^{25}, Ad26 (ref. 21) or Ad35 (ref. 20) expressing SIV_{SME543} Gag-Pol and/or Env antigens or received a sham vaccine. Cellular immune responses were measured by IFN-γ $ELISPOT^{26}$, multiparameter intracellular cytokine staining $(ICS)^{8,15-17}$ and epitope mapping[26] assays. Humoral immune responses were measured by Env $ELISA^{27}$, TZM-bl pseudovirus neutralizing antibody $(NAb)^{28}$, antibody-dependent cellular cytotoxicity $(ADCC)^{29}$ and antibody-dependent cell-mediated virus inhibition $(ADCVI)^{30}$ assays. Six months after the boost immunization, all monkeys received six challenges by the intrarectal route with the fully heterologous, neutralization-resistant virus SIV_{MAC251} using a 1:1,000 dilution (930 $TCID_{50}$) of our challenge stock[9]. Protective efficacy was determined by resistance to acquisition of infection, defined as the number of challenges required to establish infection, and virological control, defined as set point viral loads. Immunological correlates of protection against acquisition of infection and virological control were evaluated by pre-specified primary and exploratory analyses.

Full Methods and any associated references are available in the online version of the paper at www.nature.com/nature.

Received 29 September; accepted 7 December 2011.
Published online 4 January; corrected 1 February 2012 (see full-text HTML version for details).

1. Letvin, N. L. *et al.* Immune and genetic correlates of vaccine protection against mucosal infection by SIV in monkeys. *Sci. Transl. Med.* **3,** 81ra36 (2011).
2. Lai, L. *et al.* Prevention of infection by a granulocyte-macrophage colony-stimulating factor co-expressing DNA/modified vaccinia Ankara simian immunodeficiency virus vaccine. *J. Infect. Dis.* **204,** 164–173 (2011).
3. Barnett, S. W. *et al.* Antibody-mediated protection against mucosal simian-human immunodeficiency virus challenge of macaques immunized with alphavirus replicon particles and boosted with trimeric envelope glycoprotein in MF59 adjuvant. *J. Virol.* **84,** 5975–5985 (2010).
4. Hudgens, M. G. *et al.* Power to detect the effects of HIV vaccination in repeated low-dose challenge experiments. *J. Infect. Dis.* **200,** 609–613 (2009).
5. Hudgens, M. G. & Gilbert, P. B. Assessing vaccine effects in repeated low-dose challenge experiments. *Biometrics* **65,** 1223–1232 (2009).
6. Rerks-Ngarm, S. *et al.* Vaccination with ALVAC and AIDSVAX to prevent HIV-1 infection in Thailand. *N. Engl. J. Med.* **361,** 2209–2220 (2009).
7. Wilson, N. A. *et al.* Vaccine-induced cellular immune responses reduce plasma viral concentrations after repeated low-dose challenge with pathogenic simian immunodeficiency virus SIVmac239. *J. Virol.* **80,** 5875–5885 (2006).
8. Hansen, S. G. *et al.* Profound early control of highly pathogenic SIV by an effector memory T-cell vaccine. *Nature* **473,** 523–527 (2011).
9. Liu, J. *et al.* Low-dose mucosal simian immunodeficiency virus infection restricts early replication kinetics and transmitted virus variants in rhesus monkeys. *J. Virol.* **84,** 10406–10412 (2010).
10. Keele, B. F. *et al.* Low-dose rectal inoculation of rhesus macaques by SIVsmE660 or SIVmac251 recapitulates human mucosal infection by HIV-1. *J. Exp. Med.* **206,** 1117–1134 (2009).
11. Yant, L. J. *et al.* The high-frequency major histocompatibility complex class I allele *Mamu-B*17* is associated with control of simian immunodeficiency virus SIVmac239 replication. *J. Virol.* **80,** 5074–5077 (2006).
12. Mothé, B. R. *et al.* Expression of the major histocompatibility complex class I molecule Mamu-A*01 is associated with control of simian immunodeficiency virus SIV_{mac}239 replication. *J. Virol.* **77,** 2736–2740 (2003).
13. Loffredo, J. T. *et al.* *Mamu-B*08*-positive macaques control simian immunodeficiency virus replication. *J. Virol.* **81,** 8827–8832 (2007).
14. Lim, S. Y. *et al.* TRIM5α modulates immunodeficiency virus control in rhesus monkeys. *PLoS Pathog.* **6,** e1000738 (2010).
15. Okoye, A. *et al.* Progressive $CD4^+$ central memory T cell decline results in $CD4^+$ effector memory insufficiency and overt disease in chronic SIV infection. *J. Exp. Med.* **204,** 2171–2185 (2007).
16. Pitcher, C. J. *et al.* Development and homeostasis of T cell memory in rhesus macaque. *J. Immunol.* **168,** 29–43 (2002).
17. Liu, J. *et al.* Magnitude and phenotype of cellular immune responses elicited by recombinant adenovirus vectors and heterologous prime-boost regimens in rhesus monkeys. *J. Virol.* **82,** 4844–4852 (2008).
18. Liu, J. *et al.* Immune control of an SIV challenge by a T-cell-based vaccine in rhesus monkeys. *Nature* **457,** 87–91 (2009).
19. Haase, A. T. Targeting early infection to prevent HIV-1 mucosal transmission. *Nature* **464,** 217–223 (2010).
20. Vogels, R. *et al.* Replication-deficient human adenovirus type 35 vectors for gene transfer and vaccination: efficient human cell infection and bypass of preexisting adenovirus immunity. *J. Virol.* **77,** 8263–8271 (2003).
21. Abbink, P. *et al.* Comparative seroprevalence and immunogenicity of six rare serotype recombinant adenovirus vaccine vectors from subgroups B and D. *J. Virol.* **81,** 4654–4663 (2007).
22. Haynes, B. Case control study of the RV144 trial for immune correlates: the analysis and way forward. *AIDS Vaccine Conference 2011* (Bangkok, Thailand, 2011).
23. Walker, L. M. *et al.* Broad and potent neutralizing antibodies from an African donor reveal a new HIV-1 vaccine target. *Science* **326,** 285–289 (2009).
24. Wu, X. *et al.* Rational design of envelope identifies broadly neutralizing human monoclonal antibodies to HIV-1. *Science* **329,** 856–861 (2010).
25. Ourmanov, I. *et al.* Comparative efficacy of recombinant modified vaccinia virus Ankara expressing simian immunodeficiency virus (SIV) Gag-Pol and/or Env in macaques challenged with pathogenic SIV. *J. Virol.* **74,** 2740–2751 (2000).
26. Barouch, D. H. *et al.* Mosaic HIV-1 vaccines expand the breadth and depth of cellular immune responses in rhesus monkeys. *Nature Med.* **16,** 319–323 (2010).
27. Nkolola, J. P. *et al.* Breadth of neutralizing antibodies elicited by stable, homogeneous clade A and clade C HIV-1 gp140 envelope trimers in guinea pigs. *J. Virol.* **84,** 3270–3279 (2010).
28. Montefiori, D. C. Evaluating neutralizing antibodies against HIV, SIV and SHIV in luciferase reporter gene assays. *Curr. Protoc. Immunol.* **12,** Unit 12.11 (2004).
29. Ferrari, G. *et al.* An HIV-1 gp120 envelope human monoclonal antibody that recognizes a C1 conformational epitope mediates potent antibody-dependent cellular cytotoxicity (ADCC) activity and defines a common ADCC epitope in human HIV-1 serum. *J. Virol.* **85,** 7029–7036 (2011).
30. Forthal, D. N., Landucci, G. & Daar, E. S. Antibody from patients with acute human immunodeficiency virus (HIV) infection inhibits primary strains of HIV type 1 in the presence of natural-killer effector cells. *J. Virol.* **75,** 6953–6961 (2001).

Supplementary Information is linked to the online version of the paper at www.nature.com/nature.

Acknowledgements We thank M. Pensiero, A. Fauci, E. Borducchi, S. Clark, R. Hamel, S. King, P. Kozlowski, A. La Porte, G. Landucci, A. Oza, J. Perry, L. Peter, A. Riggs, G. Shaw, N. Simmons, K. Smith, K. Stanley, F. Stephens, Y.-H. Sun, G. Weverling and E. Zablowsky for advice, assistance and reagents. We thank L. Picker, G. Silvestri and B. Walker for critically reviewing this manuscript. The SIV_{MAC239} peptide pools were obtained from the NIH AIDS Research and Reference Reagent Program. We acknowledge support from the US Military Research and Material Command and the US Military HIV Research Program (W81XWH-07-2-0067); the Ragon Institute of MGH, MIT and Harvard; the National Institutes of Health (AI066924, AI078526, AI084794, AI095985, AI060354, AI002642, RR000168); and the Bill and Melinda Gates Foundation. The opinions in this manuscript are those of the authors and do not reflect the views of the US Department of Defense.

Author Contributions D.H.B., M.G.P., H.S., J.C.S., J.G., M.L.R., J.H.K., M.A.M. and N.L.M. designed the study and analysed data. J.L., H.L., D.M.L., M.J.I. and A.S. performed the cellular immunogenicity assays. H.L., M.J.I., M.S.S., G.F., D.N.F., E.A.B. and M.R. performed the humoral immunogenicity assays. L.F.M., P.A., I.O. and V.M.H. prepared the vaccine constructs. A.C. and K.G.M. led the clinical care of the rhesus monkeys. D.S. led the statistical analyses. D.H.B. led the study and wrote the paper with all co-authors.

Author Information Reprints and permissions information is available at www.nature.com/reprints. The authors declare no competing financial interests. Readers are welcome to comment on the online version of this article at www.nature.com/nature. Correspondence and requests for materials should be addressed to D.H.B. (dbarouch@bidmc.harvard.edu).

LETTER

doi:10.1038/nature10756

Maternal and paternal genomes contribute equally to the transcriptome of early plant embryos

Michael D. Nodine[1,2] & David P. Bartel[1,2]

In animals, maternal gene products deposited into eggs regulate embryonic development before activation of the zygotic genome[1]. In plants, an analogous period of prolonged maternal control over embryogenesis is thought to occur based on some gene-expression studies[2–6]. However, other gene-expression studies and genetic analyses show that some transcripts must derive from the early zygotic genome[7–14], implying that the prevailing model does not fully explain the nature of zygotic genome activation in plants. To determine the maternal, paternal and zygotic contributions to the early embryonic transcriptome, we sequenced the transcripts of hybrid embryos from crosses between two polymorphic inbred lines of *Arabidopsis thaliana* and used single-nucleotide polymorphisms diagnostic of each parental line to quantify parental contributions. Although some transcripts seemed to be either inherited from primarily one parent or transcribed from imprinted loci, the vast majority of transcripts were produced in near-equal amounts from both maternal and paternal alleles, even during the initial stages of embryogenesis. Results of reporter experiments and analyses of transcripts from genes that are not expressed in sperm and egg indicate early and widespread zygotic transcription. Thus, in contrast to early animal embryogenesis, early plant embryogenesis is mostly under zygotic control.

The prevailing model for the maternal-to-zygotic transition in plants proposes that most early embryonic messenger RNAs are maternally derived transcripts, resulting either from maternal inheritance or from higher transcriptional activity of maternally derived genes until the globular stages (in which the embryo proper has between ~32 to >100 cells)[2,6,15]. Because fundamental patterning events, including apical–basal and radial axis formation[16,17], occur during the preglobular stages, this model implies that key cell-specification decisions are mostly under maternal control. However, this model is difficult to reconcile with other studies that report equivalent maternal and paternal expression of interrogated genes in preglobular stages[8,9,11] and zygotic-recessive behaviour of mutants with preglobular developmental phenotypes[12–14].

To determine the origins of embryonic transcripts globally, we crossed polymorphic Col-0 and Cvi-0 *Arabidopsis thaliana* accessions and performed RNA-seq on poly(A)$^+$ RNA isolated from hybrid embryos with either one-to-two, eight, or ~32 cells in the embryo proper (hereafter referred to as 1-cell/2-cell, 8-cell and ~32-cell embryos). To control for inherent expression differences between Col-0 and Cvi-0 loci, the same procedure was performed using embryos derived from reciprocal crosses. Illumina sequencing of the six samples yielded 73,955,956 reads that both perfectly and uniquely matched the transcribed regions of 23,874 genes (Supplementary Table 1). Overall, transcript levels from the same stage but different reciprocal crosses were highly correlated ($r \geq 0.96$; Supplementary Fig. 1). This reproducibility and sequencing depth indicated that our results would be informative for inferring the maternal, paternal and zygotic contributions to the early embryonic transcriptome.

The prevailing model for the maternal-to-zygotic transition predicted that at the early embryonic stages transcripts would derive primarily from maternal alleles, and then at the globular stage they would derive more evenly from both alleles because at this stage the zygotic genome would be active. In contrast to this expectation, we found equal amounts of paternally and maternally derived reads at all three stages, including the 1-cell/2-cell and 8-cell embryos (Fig. 1a). When examining transcripts with at least five reads overlapping single-nucleotide polymorphisms (SNPs) in each cross, most were expressed equally from the maternal and paternal alleles, even at the earliest stage (Fig. 1b and Supplementary Data 1; note that in the Col-0 × Cvi-0

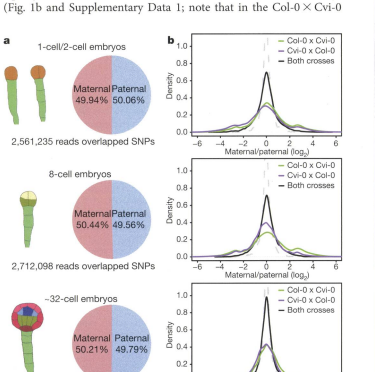

Figure 1 | Maternal and paternal genomes contribute equally to the early embryonic transcriptome. a, Proportion of RNA-seq reads overlapping maternal and paternal SNPs within transcribed regions of annotated genes. Drawings illustrate stages of isolated embryos, coloured to represent the diversity of cell lineages in each stage. Pie charts show proportions of reads overlapping maternal and paternal SNPs. **b**, Distributions of maternal-to-paternal ratios ($\log_2$) in 1-cell/2-cell (top), 8-cell (middle) and ~32-cell (bottom) embryos. Maternal-to-paternal ratios were calculated for transcripts that had ≥5 SNP-overlapping reads from the Col-0 × Cvi-0 cross (green; $n > 7{,}388$ for each stage) or the Cvi-0 × Col-0 cross (purple; $n > 8{,}071$ for each stage), and transcripts that had ≥5 SNP-overlapping reads from both reciprocal crosses (black; $n > 6{,}892$ for each stage). Binomial modelling determined the distributions expected for transcripts examined in both reciprocal crosses if there had been no parent-of-origin effects and no noise apart from stochastic counting variability (grey dashed lines).

[1]Whitehead Institute for Biomedical Research, 9 Cambridge Center, Cambridge, Massachusetts 02142, USA. [2]Howard Hughes Medical Institute and Department of Biology, Massachusetts Institute of Technology, Cambridge, Massachusetts 02139, USA.

cross, the maternal parent is Col-0, as the convention is to write the maternal parent first). In each cross, small but discernable subpopulations of transcripts were derived predominantly from either maternal or paternal alleles. However, in the respective reciprocal cross those same transcripts tended to derive from the opposite parent, which showed that rather than arising from parent-of-origin effects, these subpopulations arose mostly from genotypic effects, that is, from preferential expression from either the Col-0 or Cvi-0 alleles. Thus, when considering results of both crosses together, no overall maternal (or paternal) bias was observed, and at each stage the distribution of maternal-to-paternal ratios resembled that predicted for equal contribution from both alleles, with most of the variability explained by stochastic counting statistics, as modelled by the binomial distribution (Fig. 1b). The remainder of the variability was attributed to both additional noise (both experimental and biological) and a small subset of transcripts with parent-of-origin effects, for which the number that were maternally enriched approximately equalled the number that were paternally enriched.

Because most transcripts were derived from the maternal and paternal genomes in near-equal amounts, we hypothesized that either equal amounts of each transcript were inherited upon fertilization or the zygotic genome was activated much earlier than previously proposed. Supporting the latter possibility, the fold-change distributions centred at 0.0 ($\log_2$), showing no hint of the maternal bias that would be expected if the egg, with its larger cytoplasm, contributed more RNA than the sperm (Fig. 1b). In addition, 543 transcripts had at least four-fold higher reads per million (genome- and cDNA-matching reads) values at the 8-cell stage than at the 1-cell/2-cell stages, which suggested active transcription of the corresponding genes between the 1-cell/2-cell and 8-cell stages (as the alternative model of differential mRNA stability would require a large decrease in total mRNA between these two stages; Supplementary Data 1). Furthermore, 1,138 transcripts that were previously called undetectable in both egg and sperm microarray data sets[18,19] were among the top 50% most abundant transcripts in our 1-cell/2-cell data sets (Supplementary Data 1). These results, taken together with the observation that transcripts for RNA polymerase II subunits were among the most abundant in the early embryo (Supplementary Table 2), suggested that during the initial stages of embryogenesis many transcripts are transcribed from both maternal and paternal alleles, and that this transcription, combined with turnover of inherited transcripts, quickly overwrites most parent-of-origin biases present when the egg and sperm first fuse.

To test directly whether maternally and paternally inherited genes are transcribed in very early embryos, we used the LhG4/pOp transactivation system[20]. In this system, one parent contained a transgene encoding the LhG4 transcription factor under the control of either the *RPS5A* or the *UBI3* promoter (chosen because they generate products that can be found in the early embryo[9,21]), whereas the other parent harboured a nuclear-localized green fluorescent protein (GFP) reporter transgene under the control of the artificial pOp promoter to which LhG4 binds and transcriptionally activates (*pOp::GFP*). Because one gamete contributed the reporter gene and the other gamete contributed its activator, any reporter expression dependent on the activator could not occur until after the zygotic genome was transcriptionally active. No GFP signal was observed in embryos carrying the *pOp::GFP* reporter gene but no activator, which confirmed the absence of leaky expression in either the gametes or embryo (Fig. 2). GFP signal was detected in zygotes within 4–8 h after fertilization from crosses that brought the reporter together with its activator, regardless of whether the reporter was inherited through the egg or sperm (Fig. 2). The GFP signal in the early zygote was not as strong as that in the endosperm, which might indicate a slight delay in activation of the genome of the very early zygote or might result from more robust transcription in the endosperm. Nonetheless, when considered together our results demonstrate that both maternally and paternally inherited chromosomes are transcriptionally active at least in 1-cell embryos and most likely before.

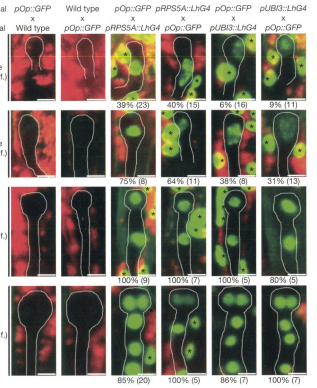

Figure 2 | Maternally and paternally inherited transgenes are transcribed in the initial stages of embryogenesis. Confocal scanning laser microscopy images show early embryos from the indicated crosses, which were between plants with a transgenic reporter (*pOp::GFP*) and either plants without an activator (wild type) or plants with a transgenic activator driven from either the *RPS5A* or the *UBI3* promoter (*pRPS5A::LhG4* or *pUBI3::LhG4*, respectively). Embryonic stages and the approximate number of hours after fertilization (h.a.f.) are shown to the left. GFP signal is indicated by green nuclei; background autofluorescence is shown in red. Embryos are outlined in white for clarity. Asterisks indicate endosperm nuclei. Of the seeds with GFP signal in endosperm (*n* in parentheses), the percentage that also had GFP signal in embryos is indicated below each image. In endosperm, expression from maternal alleles is expected to be twofold higher than that from paternal alleles, but this difference is not observed in these images because the GFP signal in the endosperm was beyond its dynamic range. Scale bars represent 10 μm.

Having established that most early embryonic transcripts derived equally from the maternal and paternal genomes, we turned our attention to the few that might be preferentially inherited or preferentially expressed from the maternal or paternal alleles. For most early embryonic transcripts the genotype of the allele had a larger affect on transcript levels than did parent of origin (Figs 1b and 3a). Indeed, hundreds of transcripts were preferentially expressed from either the Col-0 or Cvi-0 allele irrespective of their parent of origin (Supplementary Data 2), presumably as direct consequences of either DNA-sequence or epigenetic differences between the Col-0 and Cvi-0 alleles. This prevalence of genotypic/epigenotypic effects over parent-of-origin effects led to significant negative correlations between the maternal-to-paternal ratios at each stage (Fig. 3a, Pearson's $r < -0.43$, $P < 10^{-15}$). Nonetheless, at each stage a small subset of transcripts passed our cutoffs for classification as maternally or paternally enriched, that is, fourfold maternally or paternally enriched in each cross, and not exceeding the false discovery rate (FDR) threshold of 0.05 (Pearson's χ^2 tests, Benjamini and Hochberg FDR). With these cutoffs, 77 and 45 transcripts were designated maternally and paternally enriched, respectively, in at least one stage (Fig. 3a and Supplementary Data 3). For five transcripts, an independent assay involving diagnostic cleavage of an amplified polymorphic sequence was performed, and for all five, the parent-of-origin effects were confirmed (Supplementary Fig. 2).

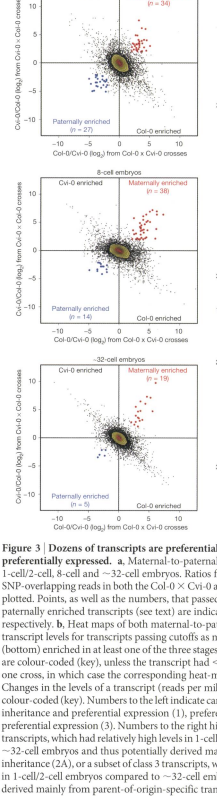

Figure 3 | Dozens of transcripts are preferentially inherited or preferentially expressed. a, Maternal-to-paternal ratios for transcripts in 1-cell/2-cell, 8-cell and ~32-cell embryos. Ratios for transcripts that had ≥8 SNP-overlapping reads in both the Col-0 × Cvi-0 and Cvi-0 × Col-0 crosses are plotted. Points, as well as the numbers, that passed cutoffs for maternally or paternally enriched transcripts (see text) are indicated in red and blue, respectively. **b**, Heat maps of both maternal-to-paternal ratios and changes in transcript levels for transcripts passing cutoffs as maternally (top) or paternally (bottom) enriched in at least one of the three stages. Maternal-to-paternal ratios are colour-coded (key), unless the transcript had <8 SNP-overlapping reads in one cross, in which case the corresponding heat-map value is not coloured. Changes in the levels of a transcript (reads per million) relative to its mean are colour-coded (key). Numbers to the left indicate candidates for both preferential inheritance and preferential expression (1), preferential inheritance (2) or preferential expression (3). Numbers to the right highlight a subset of the class 2 transcripts, which had relatively high levels in 1-cell/2-cell embryos compared to ~32-cell embryos and thus potentially derived mainly from preferential inheritance (2A), or a subset of class 3 transcripts, which had relatively low levels in 1-cell/2-cell embryos compared to ~32-cell embryos and thus potentially derived mainly from parent-of-origin-specific transcription (3A).

Although the maternal enrichment of some transcripts might be due to their transport from maternal sporophytic tissues, such a mechanism cannot explain paternal enrichment. Some transcripts had strong parent-of-origin effects in 1-cell/2-cell embryos, suggesting that they were preferentially inherited from one parent (Fig. 3b). Confirmation that these biases are indeed due to inheritance would substantially add to the single previously documented example of an inherited transcript in plants[22]. Other transcripts had stronger parent-of-origin effects at later stages, suggesting that they were preferentially expressed from either the maternally or the paternally inherited allele (Fig. 3b). This potential parent-of-origin-specific expression implied a form of imprinting in the *Arabidopsis* embryo. Genome-wide approaches similar to ours but looking much later after fertilization greatly expanded the list of genes with parent-of-origin-specific expression in the endosperm but did not identify such genes in embryos[23,24]. Thus, the imprinting-like phenomenon that we observed in early embryos is short lived, which suggests that it differs from the more persistent imprinting previously characterized in either endosperm or mammals[25]. For example, it might involve alternative chromatin states inherited from the egg and sperm, which after several cell divisions equilibrate between the two alleles. Such a mechanism would not necessarily require DNA methylation, although we note that in the only previous report of imprinting in plant embryos (at the *MEE1* locus of maize), methylation marks are lost from maternal alleles at the initial stages of embryogenesis, but then re-established to match the paternal alleles at later stages[26].

Our results showing that during the initial stages of *Arabidopsis* embryogenesis both the maternal and paternal genomes are active and make essentially equivalent contributions to the embryonic transcriptome are in marked contrast to a recent report that ~88% of the 2-cell/4-cell embryonic transcriptome is derived from the maternal genome[2]. That study, published while our manuscript was in preparation, used SNPs in the transcriptomes of hybrid embryos derived from a cross between the Ler-1 (maternal parent) and Col-0 (paternal parent) accessions to estimate maternal and paternal genomic contributions. Because results from the reciprocal cross were not reported, the previous study could not distinguish parent-of-origin effects from genotypic effects. However, because an analysis unable to account for genotypic effects would be expected to misidentify transcripts as paternally derived as frequently as it misidentifies them as maternally derived, we considered other possibilities for the discrepancy between their results and ours. Our pilot studies had shown that early embryos must be extensively washed to prevent seed-coat RNA contamination, and indeed we found evidence that the embryo RNA samples of ref. 2 contained large amounts of seed-coat mRNA (Supplementary Fig. 3). Because the seed coat is a maternal tissue, this contamination explained why they observed such a large bias in maternal RNAs.

Genes zygotically required for the initial zygotic division have been identified in *Arabidopsis*[9,12,13]. Moreover, paternal gene expression has been detected for 24 endogenous genes and a transgene in maize zygotes[8,27], and *de novo* transcription has been demonstrated recently in tobacco zygotes[28]. Rather than interpreting these findings as exceptions to the model or as differences between species, our transcriptome-wide analyses and reporter data strongly support the proposal of an alternative model for the maternal-to-zygotic (or, to put it more precisely, the maternal/paternal-to-zygotic) transition in plants. In this model, the zygotic genome is activated within the first few hours after fertilization, and equal transcription of both maternal and paternal alleles generates most of the early embryonic transcriptome at the 1-cell stage or before. Our model implies that although the maternal and paternal gene products are inherited in the zygote upon fertilization and contribute to its development[22], the zygotic gene products are the ones that primarily control the initial cell-specification events of embryogenesis.

METHODS SUMMARY

Col-0 and Cvi-0 seed stocks were obtained from the *Arabidopsis* Biological Resource Center. Flowers were emasculated 1 day before crossing, and pools of 20 1-cell/2-cell, 8-cell and ~32-cell embryos were hand-dissected approximately 40, 64 and 78 h after pollination, respectively. RNA isolation, linear amplification of poly(A) RNA and strand-specific RNA-seq were as described[21], except that embryos were extensively washed before RNA isolation. After removing adaptor sequences, reads were mapped to both the *A. thaliana* genome and transcript models (Col-0 genome reference, TAIR10) with the Bowtie short-read aligner[29].

Reads were also mapped to a 'pseudo' Cvi-0 genome and Cvi-0 transcript models, in which SNPs in the Col-0 genome and transcript models were replaced with Cvi-0 variants (ftp://ftp.arabidopsis.org/home/tair/Sequences/Polymorphism_datasets/Ecker_Cvi_snps.txt) generated by the 1001 Genomes Project. Reads that both perfectly and uniquely matched either the genomes or transcript models were retained, and those overlapping transcribed regions of annotated genes were evaluated for overlap with SNPs. Those diagnostic of one genome or the other were tallied after normalizing for differences in sequencing yield between samples. Talies for multiple SNPs within the same gene were combined before calculating maternal-to-paternal ratios for each transcript.

Full Methods and any associated references are available in the online version of the paper at www.nature.com/nature.

Received 5 September; accepted 1 December 2011.
Published online 22 January 2012.

1. Tadros, W. & Lipshitz, H. D. The maternal-to-zygotic transition: a play in two acts. *Development* **136,** 3033–3042 (2009).
2. Autran, D. *et al.* Maternal epigenetic pathways control parental contributions to *Arabidopsis* early embryogenesis. *Cell* **145,** 707–719 (2011).
3. Vielle-Calzada, J. P., Baskar, R. & Grossniklaus, U. Delayed activation of the paternal genome during seed development. *Nature* **404,** 91–94 (2000).
4. Baroux, C., Blanvillain, R. & Gallois, P. Paternally inherited transgenes are down-regulated but retain low activity during early embryogenesis in *Arabidopsis*. *FEBS Lett.* **509,** 11–16 (2001).
5. Grimanelli, D., Perotti, E., Ramirez, J. & Leblanc, O. Timing of the maternal-to-zygotic transition during early seed development in maize. *Plant Cell* **17,** 1061–1072 (2005).
6. Baroux, C., Autran, D., Gillmor, C. S., Grimanelli, D. & Grossniklaus, U. The maternal to zygotic transition in animals and plants. *Cold Spring Harb. Symp. Quant. Biol.* **73,** 89–100 (2008).
7. Springer, P. S., Holding, D. R., Groover, A., Yordan, C. & Martienssen, R. A. The essential Mcm7 protein PROLIFERA is localized to the nucleus of dividing cells during the G_1 phase and is required maternally for early *Arabidopsis* development. *Development* **127,** 1815–1822 (2000).
8. Meyer, S. & Scholten, S. Equivalent parental contribution to early plant zygotic development. *Curr. Biol.* **17,** 1686–1691 (2007).
9. Weijers, D., Geldner, N., Offringa, R. & Jurgens, G. Seed development: Early paternal gene activity in *Arabidopsis*. *Nature* **414,** 709–710 (2001).
10. Sprunck, S., Baumann, U., Edwards, K., Langridge, P. & Dresselhaus, T. The transcript composition of egg cells changes significantly following fertilization in wheat (*Triticum aestivum* L.). *Plant J.* **41,** 660–672 (2005).
11. Ingouff, M. *et al.* Zygotic resetting of the HISTONE 3 variant repertoire participates in epigenetic reprogramming in *Arabidopsis*. *Curr. Biol.* **20,** 2137–2143 (2010).
12. Xu, J. *et al.* EMBRYONIC FACTOR 1 encodes an AMP deaminase and is essential for the zygote to embryo transition in *Arabidopsis*. *Plant J.* **42,** 743–758 (2005).
13. Ronceret, A. *et al.* The first zygotic division in *Arabidopsis* requires *de novo* transcription of thymidylate kinase. *Plant J.* **53,** 776–789 (2008).
14. Muralla, R., Lloyd, J. & Meinke, D. Molecular foundations of reproductive lethality in *Arabidopsis thaliana*. *PLoS ONE* **6,** e28398 (2011).
15. Pillot, M. *et al.* Embryo and endosperm inherit distinct chromatin and transcriptional states from the female gametes in *Arabidopsis*. *Plant Cell* **22,** 307–320 (2010).
16. Mayer, U., Torres Ruiz, R. A., Berleth, T., Misera, S. & Jurgens, G. Mutations affecting body organization in the *Arabidopsis* embryo. *Nature* **353,** 402–407 (1991).
17. Laux, T., Wurschum, T. & Breuninger, H. Genetic regulation of embryonic pattern formation. *Plant Cell* **16** (Suppl. 1), S190–S202 (2004).
18. Wuest, S. E. *et al. Arabidopsis* female gametophyte gene expression map reveals similarities between plant and animal gametes. *Curr. Biol.* **20,** 506–512 (2010).
19. Borges, F. *et al.* Comparative transcriptomics of *Arabidopsis* sperm cells. *Plant Physiol.* **148,** 1168–1181 (2008).
20. Moore, I., Galweiler, L., Grosskopf, D., Schell, J. & Palme, K. A transcription activation system for regulated gene expression in transgenic plants. *Proc. Natl Acad. Sci. USA* **95,** 376–381 (1998).
21. Nodine, M. D. & Bartel, D. P. MicroRNAs prevent precocious gene expression and enable pattern formation during plant embryogenesis. *Genes Dev.* **24,** 2678–2692 (2010).
22. Bayer, M. *et al.* Paternal control of embryonic patterning in *Arabidopsis thaliana*. *Science* **323,** 1485–1488 (2009).
23. Gehring, M., Missirian, V. & Henikoff, S. Genomic analysis of parent-of-origin allelic expression in *Arabidopsis thaliana* seeds. *PLoS ONE* **6,** e23687 (2011).
24. Hsieh, T. F. *et al.* Regulation of imprinted gene expression in *Arabidopsis* endosperm. *Proc. Natl Acad. Sci. USA* **108,** 1755–1762 (2011).
25. Feil, R. & Berger, F. Convergent evolution of genomic imprinting in plants and mammals. *Trends Genet.* **23,** 192–199 (2007).
26. Jahnke, S. & Scholten, S. Epigenetic resetting of a gene imprinted in plant embryos. *Curr. Biol.* **19,** 1677–1681 (2009).
27. Scholten, S., Lorz, H. & Kranz, E. Paternal mRNA and protein synthesis coincides with male chromatin decondensation in maize zygotes. *Plant J.* **32,** 221–231 (2002).
28. Zhao, J. *et al.* Dynamic changes of transcript profiles after fertilization are associated with *de novo* transcription and maternal elimination in tobacco zygote, and mark the onset of the maternal-to-zygotic transition. *Plant J.* **65,** 131–145 (2011).
29. Langmead, B., Trapnell, C., Pop, M. & Salzberg, S. L. Ultrafast and memory-efficient alignment of short DNA sequences to the human genome. *Genome Biol.* **10,** R25 (2009).

Supplementary Information is linked to the online version of the paper at www.nature.com/nature.

Acknowledgements We thank J. Ecker and the 1001 Genomes Project for generating the list of Cvi-0 SNPs; the J. Harada and R. Goldberg laboratories for making the *Arabidopsis* seed development LCM microarray data sets publicly available; I. Moore for the transactivation vectors; J. Long for the *UBI3* promoter fragment; the Whitehead Genome Technology Core for sequencing; and D. Meinke for providing a curated list of preglobular zygotic-recessive mutants before publication. This work used the W. M. Keck Biological Imaging Facility at the Whitehead Institute and was supported by NIH grant GM067031 (D.P.B.) and NIH Postdoctoral Fellowship GM084656 (M.D.N). D.P.B. is an Investigator of the Howard Hughes Medical Institute.

Author Contributions M.D.N. designed and performed the experiments. M.D.N. and D.P.B. interpreted the results and wrote the manuscript.

Author Information Raw and processed RNA-seq data sets have been deposited into NCBI GEO (http://www.ncbi.nlm.nih.gov/geo/) under accession number GSE33713. Reprints and permissions information is available at www.nature.com/reprints. The authors declare no competing financial interests. Readers are welcome to comment on the online version of this article at www.nature.com/nature. Correspondence and requests for materials should be addressed to D.P.B. (dbartel@wi.mit.edu).

LETTER

doi:10.1038/nature10814

Mutations in kelch-like 3 and cullin 3 cause hypertension and electrolyte abnormalities

Lynn M. Boyden[1], Murim Choi[1]*, Keith A. Choate[2]*, Carol J. Nelson-Williams[1], Anita Farhi[1], Hakan R. Toka[3], Irina R. Tikhonova[4], Robert Bjornson[4], Shrikant M. Mane[4], Giacomo Colussi[5], Marcel Lebel[6], Richard D. Gordon[7], Ben A. Semmekrot[8], Alain Poujol[9], Matti J. Välimäki[10], Maria E. De Ferrari[5], Sami A. Sanjad[11], Michael Gutkin[12], Fiona E. Karet[13], Joseph R. Tucci[14], Jim R. Stockigt[15], Kim M. Keppler-Noreuil[16], Craig C. Porter[17], Sudhir K. Anand[18], Margo L. Whiteford[19], Ira D. Davis[20], Stephanie B. Dewar[21], Alberto Bettinelli[22], Jeffrey J. Fadrowski[23], Craig W. Belsha[24], Tracy E. Hunley[25], Raoul D. Nelson[26], Howard Trachtman[27], Trevor R. P. Cole[28], Maury Pinsk[29], Detlef Bockenhauer[30], Mohan Shenoy[31], Priya Vaidyanathan[32], John W. Foreman[33], Majid Rasoulpour[34], Farook Thameem[35], Hania Z. Al-Shahrouri[35], Jai Radhakrishnan[36], Ali G. Gharavi[36], Beatrice Goilav[37] & Richard P. Lifton[1]

Hypertension affects one billion people and is a principal reversible risk factor for cardiovascular disease. Pseudohypoaldosteronism type II (PHAII), a rare Mendelian syndrome featuring hypertension, hyperkalaemia and metabolic acidosis, has revealed previously unrecognized physiology orchestrating the balance between renal salt reabsorption and K^+ and H^+ excretion[1]. Here we used exome sequencing to identify mutations in kelch-like 3 (*KLHL3*) or cullin 3 (*CUL3*) in PHAII patients from 41 unrelated families. *KLHL3* mutations are either recessive or dominant, whereas *CUL3* mutations are dominant and predominantly *de novo*. CUL3 and BTB-domain-containing kelch proteins such as KLHL3 are components of cullin–RING E3 ligase complexes that ubiquitinate substrates bound to kelch propeller domains[2–8]. Dominant *KLHL3* mutations are clustered in short segments within the kelch propeller and BTB domains implicated in substrate[9] and cullin[5] binding, respectively. Diverse *CUL3* mutations all result in skipping of exon 9, producing an in-frame deletion. Because dominant *KLHL3* and *CUL3* mutations both phenocopy recessive loss-of-function *KLHL3* mutations, they may abrogate ubiquitination of KLHL3 substrates. Disease features are reversed by thiazide diuretics, which inhibit the Na–Cl cotransporter in the distal nephron of the kidney; KLHL3 and CUL3 are expressed in this location, suggesting a mechanistic link between *KLHL3* and *CUL3* mutations, increased Na–Cl reabsorption, and disease pathogenesis. These findings demonstrate the utility of exome sequencing in disease gene identification despite the combined complexities of locus heterogeneity, mixed models of transmission and frequent *de novo* mutation, and establish a fundamental role for KLHL3 and CUL3 in blood pressure, K^+ and pH homeostasis.

A small number of genes causing Mendelian forms of hypertension have been identified, establishing the role of increased renal salt reabsorption in its pathogenesis[10–12]. The study of PHAII has identified a physiological mechanism that orchestrates activities of diverse electrolyte flux pathways, allowing maximal salt reabsorption in response to aldosterone when angiotensin II (AII) is elevated, as in settings of reduced intravascular volume (hypovolaemia), versus maximal potassium secretion in settings of hyperkalaemia, in which aldosterone is elevated without changes in AII[1]. The role of WNK kinases in this process was revealed by discovery of their mutation in a small fraction of PHAII kindreds[11]. Dominant gain-of-function mutations in *WNK4* or *WNK1* lead to constitutively increased salt reabsorption in the distal nephron regardless of volume status, resulting in hypertension, and inhibition of K^+ secretion despite marked hyperkalaemia[1,11,13–17].

We studied a cohort of 52 PHAII kindreds, including 126 affected subjects with renal hyperkalaemia and otherwise normal renal function; hypertension and acidosis were present in 71% and 82%, respectively. There was wide variation in disease severity and age of clinical presentation (Supplementary Figs 1 and 2). Mutations in *WNK1* or *WNK4* were present in only seven of these kindreds (13%). Those without *WNK* mutations had only 2.0 ± 1.4 affected members, complicating mapping efforts.

Exome sequencing of eleven unrelated PHAII index cases without *WNK* mutations was performed. Index cases and affected relatives (five trios and one quartet) were also subjected to genome-wide SNP genotyping. Tabulation of high quality novel protein-altering variants revealed 124 genes with three or more variants, 50 with four or more, and 23 with five. Concurrent analysis of linkage among the multiplex families was used to prioritize loci harbouring variants that co-segregated with

[1]Department of Genetics and Howard Hughes Medical Institute, Yale University School of Medicine, New Haven, Connecticut 06510, USA. [2]Department of Dermatology, Yale University School of Medicine, New Haven, Connecticut 06510, USA. [3]Renal Division, Brigham and Women's Hospital, Boston, Massachusetts 02115, USA. [4]Yale Center for Genome Analysis, Yale University, New Haven, Connecticut 06510, USA. [5]Nephrology Unit, Niguarda Ca' Granda Hospital, Milan 20162, Italy. [6]Department of Medicine, Laval University, Québec G1K 7P4, Canada. [7]Endocrine Hypertension Research Centre, University of Queensland School of Medicine, Brisbane QLD 4006, Australia. [8]Department of Pediatrics, Canisius Wilhelmina Hospital, Nijmegen 6500 GS, Netherlands. [9]Department of Pediatrics, Pays d'Aix Hospital, Aix-en-Provence 13616, France. [10]Division of Endocrinology, Department of Medicine, Helsinki University Central Hospital, Helsinki 00290, Finland. [11]Department of Pediatrics and Adolescent Medicine, American University Medical Center, Beirut 1107 2020, Lebanon. [12]Hypertension Research Center, University of Medicine and Dentistry of New Jersey, Newark, New Jersey 07103, USA. [13]Department of Medical Genetics, University of Cambridge, Cambridge CB2 1TN, United Kingdom. [14]Division of Endocrinology, Roger Williams Medical Center, Providence, Rhode Island 02908, USA. [15]Department of Endocrinology and Diabetes, Ewen Downie Metabolic Unit, Alfred Hospital, Melbourne VIC 3004, Australia. [16]Division of Medical Genetics, Department of Pediatrics, University of Iowa Children's Hospital, Iowa City, Iowa 52242, USA. [17]Division of Nephrology, Department of Pediatrics, Medical College of Wisconsin, Milwaukee, Wisconsin 53226, USA. [18]Department of Pediatrics, David Geffen School of Medicine at UCLA, Los Angeles, California 12138, USA. [19]Duncan Guthrie Institute of Medical Genetics, Royal Hospital for Sick Children, Glasgow G3 8SJ, United Kingdom. [20]Baxter Healthcare Corporation, McGaw Park, Illinois 60085, USA. [21]Department of Pediatrics, University of Pittsburgh School of Medicine, Pittsburgh, Pennsylvania 15261, USA. [22]Division of Pediatrics, Mandic Hospital, Merate 23807, Italy. [23]Department of Pediatrics, Johns Hopkins School of Medicine, Baltimore, Maryland 21287, USA. [24]Division of Nephrology, Department of Pediatrics, Saint Louis University Health Sciences Center, St Louis, Missouri 63110, USA. [25]Division of Nephrology, Department of Pediatrics, Vanderbilt University Medical Center, Nashville, Tennessee 37232, USA. [26]Division of Nephrology, Department of Pediatrics, University of Utah, Salt Lake City, Utah 84132, USA. [27]Division of Nephrology, Cohen Children's Medical Center of New York, New Hyde Park, New York 11040, USA. [28]West Midlands Regional Genetics Service, Birmingham Women's Hospital, Birmingham B15 2TG, United Kingdom. [29]Division of Nephrology, Department of Pediatrics, University of Alberta, Edmonton T6G 2M7, Canada. [30]Renal Unit, University College London Institute of Child Health, London WC1N 1EH, United Kingdom. [31]Department of Nephrology, Royal Manchester Children's Hospital, Manchester M27 4HA, United Kingdom. [32]Department of Endocrinology, Children's National Medical Center, Washington, District of Columbia 20010, USA. [33]Department of Pediatrics, Duke University Medical Center, Durham, North Carolina 27710, USA. [34]Division of Nephrology, Connecticut Children's Medical Center, Hartford, Connecticut 06106, USA. [35]Division of Nephrology, Department of Medicine, University of Texas Health Science Center, San Antonio, Texas 78229, USA. [36]Department of Medicine, Columbia University College of Physicians and Surgeons, New York, New York 10032, USA. [37]Division of Nephrology, Children's Hospital at Montefiore, Bronx, New York 10467, USA.
*These authors contributed equally to this work.

disease; this identified 28 genes with novel protein-altering variants that co-segregated with disease in two or more multiplex families. This revealed *KLHL3* as a strong candidate, with novel *KLHL3* mutations comprising five alleles in three kindreds, all of which co-segregated with the trait. These include one kindred in which affected members are homozygous for a nonsense mutation (W470X), one in which affected members are compound heterozygotes for two missense mutations (F322C and S410L), and one segregating a heterozygous missense mutation (R528H). As a confirmation of significance, Fisher's exact test was used to compare the prevalence of novel protein-altering variants in all genes in PHAII cases versus 699 control exomes. A single gene, *KLHL3*, showed a burden of mutation that surpassed genome-wide significance ($P = 1.1 \times 10^{-8}$; Supplementary Tables 1–3).

KLHL3 was sequenced in all PHAII index cases, identifying novel mutations in 24 (Fig. 1a, b and Supplementary Figs 3 and 4). Nearly all are at positions conserved among orthologues (Supplementary Fig. 5). Sixteen kindreds have heterozygous mutations that co-segregate with the trait under a dominant model (log of odds (lod) score 6.9, <-2 under other models). In contrast, eight index cases inherited mutations in both *KLHL3* alleles. In these kindreds, affected members are confined to siblings of index cases who inherited the same two mutations, whereas unaffected relatives inherited zero or one mutation (lod score 4.3 for a recessive model, <-2 for other models). Recessive transmission has not been previously described for PHAII. Consistent with two modes of transmission, subjects with dominant *KLHL3* mutations had significantly higher serum K^+ levels (6.2 ± 0.6 mM)

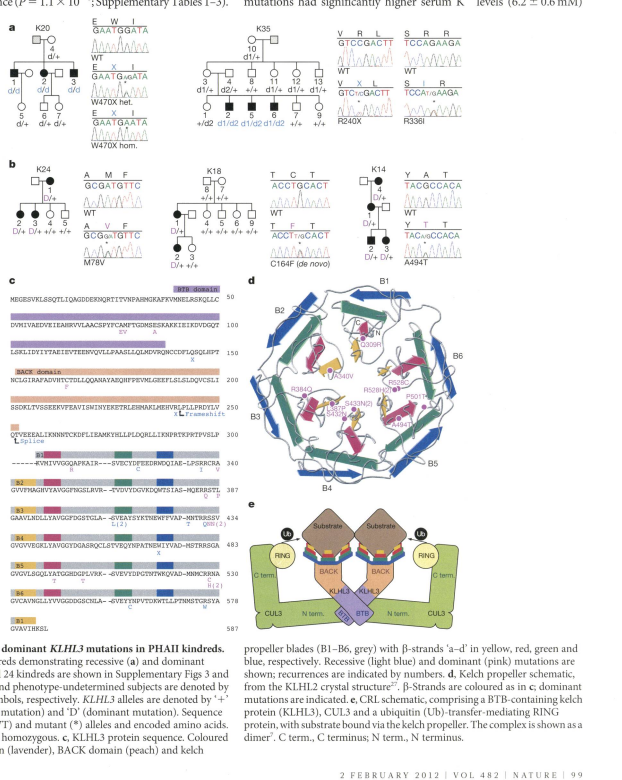

Figure 1 | Recessive and dominant *KLHL3* mutations in PHAII kindreds. **a**, **b**, Representative kindreds demonstrating recessive (**a**) and dominant (**b**) *KLHL3* mutations (all 24 kindreds are shown in Supplementary Figs 3 and 4). Affected, unaffected and phenotype-undetermined subjects are denoted by black, white and grey symbols, respectively. *KLHL3* alleles are denoted by '+' (wild type), 'd' (recessive mutation) and 'D' (dominant mutation). Sequence traces show wild-type (WT) and mutant (*) alleles and encoded amino acids. het., heterozygous; hom., homozygous. **c**, KLHL3 protein sequence. Coloured bars indicate BTB domain (lavender), BACK domain (peach) and kelch propeller blades (B1–B6, grey) with β-strands 'a–d' in yellow, red, green and blue, respectively. Recessive (light blue) and dominant (pink) mutations are shown; recurrences are indicated by numbers. **d**, Kelch propeller schematic, from the KLHL2 crystal structure[27]. β-Strands are coloured as in **c**; dominant mutations are indicated. **e**, CRL schematic, comprising a BTB-containing kelch protein (KLHL3), CUL3 and a ubiquitin (Ub)-transfer-mediating RING protein, with substrate bound via the kelch propeller. The complex is shown as a dimer[7]. C term., C terminus; N term., N terminus.

than heterozygotes for recessive mutations (4.8 ± 0.6 mM) ($P < 10^{-4}$, Student's *t*-test; normal range 3.5–5.0 mM). These findings establish that PHAII can be caused by either recessive or dominant *KLHL3* mutations. Importantly, we infer that mutations in dominant kindreds are probably dominant-negative, because they phenocopy the features of recessive disease.

KLHL3 contains an amino-terminal BTB domain, a BACK domain, and carboxy-terminal kelch-like repeats that form a six-bladed β-propeller structure[2,4,5] (Fig. 1c–e). There are over 50 BTB-containing kelch (BTB-kelch) genes in humans[4]; their propeller domains bind substrate proteins, promoting substrate ubiquitination via interaction of the BTB domain with CUL3, a component of a cullin–RING E3 ubiquitin ligase (CRL)[3,5,6]. Ubiquitination serves diverse functions, including targeting proteins for proteasomal degradation as well as non-degradative roles such as modulation of protein activity, interaction and localization[7,8].

Whereas recessive *KLHL3* mutations are distributed throughout the encoded protein, dominant *KLHL3* mutations show marked clustering (Fig. 1c). Nine of sixteen dominant mutations alter one of the last four amino acids of the six 'd–a' loops that connect the outermost ('d') β-strand of one kelch propeller blade to the innermost ('a') β-strand of the next blade. Two others are in 'b–c' loops. These dominant PHAII mutations lie near the hub of the propeller (Fig. 1d) at or near sites implicated in substrate binding in paralogues[9] (Supplementary Fig. 5). Three other dominant mutations cluster within the BTB domain, at or near sites implicated in cullin binding in paralogues[5]. We infer that dominant mutations in KLHL3 probably impair binding either to specific substrates or to CUL3.

After accounting for *KLHL3*, *WNK1* and *WNK4* mutations, 21 PHAII kindreds without mutations remained. We considered the presumed functional partner of *KLHL3*, *CUL3* (Fig. 1e), as a potential candidate. Among PHAII exomes, novel heterozygous *CUL3* variants were suggested in two. Sequencing *CUL3* in all index cases identified 17 with novel heterozygous mutations, all in cases without *KLHL3*, *WNK1* or *WNK4* mutations (Fig. 2a and Supplementary Fig. 6). Eight of these mutations were documented to be *de novo*, providing overwhelming evidence that these mutations are disease-causing. *CUL3* mutations all cluster in sites implicated in splicing of exon 9, including the intron 8 splice acceptor ($n = 4$), the intron 9 splice donor ($n = 5$), the putative intron 8 splice branch site ($n = 5$), and a putative splice enhancer in exon 9 ($n = 3$, within a TTGGA(T/A)) splice enhancer consensus sequence[18]) (Fig. 2b).

To test the impact of these mutations on splicing, *CUL3* genomic DNA spanning exon 8 to exon 10 containing either wild-type sequence or one of nine PHAII mutations was cloned and expressed in HEK293 cells, and the spliced RNA products were analysed. Whereas the wild-type sequence produces a properly spliced product containing all three exons, each of the mutants produces a predominant product that skips exon 9, joining exon 8 to exon 10 (Fig. 2c, d). This results in an in-frame 57 amino acid deletion (residues 403–459) in the segment linking the

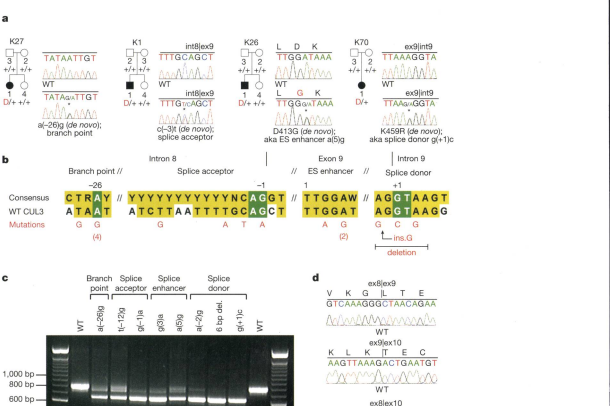

Figure 2 | Dominant *CUL3* mutations in PHAII kindreds cause skipping of exon 9. a, Representative kindreds demonstrating *CUL3* mutations, depicted as in Fig. 1 (all 17 kindreds are shown in Supplementary Fig. 6). int8, intron 8; ex9, exon 9; int9, intron 9. Positions are numbered relative to splice sites and the first base of the exonic splice (ES) enhancer. **b**, *CUL3* mutation locations. Consensus splicing sequences[18,28] and corresponding wild-type *CUL3* sequences are shown; invariant bases (green) and consensus homology (yellow) are indicated. Mutations are shown in red; recurrences are indicated by numbers. Ins.G, insertion of a G (guanine). **c**, Reverse transcription–polymerase chain reaction (RT–PCR) of spliced RNA. Wild-type *CUL3* constructs produce a single product including exons 8, 9 and 10 (844 bp); all nine mutants tested produce a predominant product that skips exon 9 (673 bp). **d**, Representative RT–PCR sequences. The wild-type construct produces complementary DNA with properly spliced junctions between exons 8–9 (top) and 9–10 (middle), whereas the mutant construct (splice donor g(+1)c) produces cDNA joining exon 8 to exon 10 (bottom).

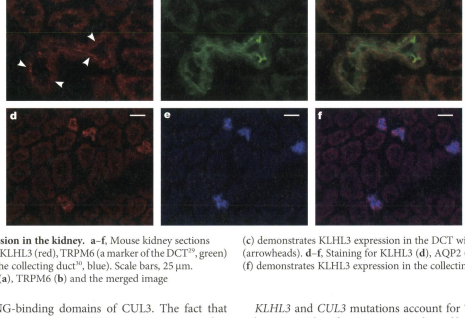

Figure 3 | *KLHL3* expression in the kidney. a–f, Mouse kidney sections stained with antibodies to KLHL3 (red), TRPM6 (a marker of the DCT[29], green) and AQP2 (a marker of the collecting duct[30], blue). Scale bars, 25 μm. **a–c**, Staining for KLHL3 (**a**), TRPM6 (**b**) and the merged image (**c**) demonstrates KLHL3 expression in the DCT with apical localization (arrowheads). **d–f**, Staining for KLHL3 (**d**), AQP2 (**e**) and the merged image (**f**) demonstrates KLHL3 expression in the collecting duct.

BTB-binding and RING-binding domains of CUL3. The fact that *CUL3* mutations phenocopy recessive *KLHL3* mutations suggests that they abrogate CUL3 function at KLHL3 targets.

As with PHAII caused by *WNK1* and *WNK4* mutations[1], virtually all patients with *KLHL3* and *CUL3* mutations have been treated with thiazide diuretics, inhibitors of the Na–Cl cotransporter (NCC), resulting in correction of phenotypic abnormalities. WNK4 regulates the activities of NCC[13,14,16], the epithelial Na^+ channel ENaC[17], and the K^+ channel ROMK[15], and is co-expressed with these proteins in the renal distal convoluted tubule (DCT) and collecting duct[11,19,20]. Staining mouse kidney sections with specific antibodies demonstrated that KLHL3 is predominantly expressed in the DCT and collecting duct, with apical localization in the DCT (Fig. 3). CUL3 is ubiquitously expressed and is in all nephron segments, with particularly high expression in the proximal tubule, but also in the DCT and collecting duct (Supplementary Fig. 7). These findings are consistent with both proteins having a role in the regulation of salt and electrolyte homeostasis in the distal nephron.

There are highly significant differences in phenotypic severity among PHAII patients with mutations in different genes (Table 1 and Supplementary Figs 1, 2 and Supplementary Table 4). Subjects with *CUL3* mutations presented at much younger ages than those with mutation in *KLHL3*, *WNK1* or *WNK4*, had significantly more severe hyperkalaemia and metabolic acidosis, and were far more likely to have hypertension before age 18 (others commonly develop hypertension at later ages). The majority of subjects with *CUL3* mutations demonstrated failure to thrive or growth impairment. These observations, in conjunction with the high rate of *CUL3 de novo* mutation, support impairment of reproductive fitness. Among the other mutant loci, there remain significant differences in disease severity (rank order recessive *KLHL3* > dominant *KLHL3* > *WNK4* > *WNK1*).

KLHL3 and *CUL3* mutations account for 79% of kindreds in our cohort. Gene identification was complicated by the combined effects of locus heterogeneity, two modes of transmission at one locus, and few informative meioses. Many so far unsolved Mendelian traits may have similar complexities. Use of control exomes as comparators for analysis of mutation burden may be broadly applicable to discovery of such loci.

The most parsimonious mechanism of *KLHL3* and *CUL3* mutations is that they abrogate ubiquitination of targets normally bound by KLHL3, activity that is required for normal modulation of renal salt, K^+ and H^+ handling in response to physiological challenge; this speculation will require biochemical verification. The fact that recessive mutations in *KLHL3* cause PHAII without other diverse effects implies either that KLHL3 targets are highly restricted to the renal salt and electrolyte pathway, or that loss of KLHL3 function at other targets can be compensated by other loci. BTB-kelch–CUL3 CRLs can act as dimers, with two substrate-binding domains capable of engaging the same target molecule[2]. This suggests a potential mechanism to explain dominant-negative effects of *KLHL3* and *CUL3* mutations.

CUL3-based CRLs participate in a wide range of critical cellular processes[8] via binding diverse BTB-domain-containing proteins[3,5]. *CUL3* mutations affecting all or many of these activities would undoubtedly produce very broad phenotypes. *CUL3* mutations in PHAII merely phenocopy the effects of loss of *KLHL3*, suggesting that they selectively abrogate function at KLHL3 targets. The stereotypic consequences of *CUL3* mutations, all deleting 57 amino acids in a region linking the BTB-binding and RING-binding domains, support such a specific effect. Consistent with this possibility, introduction of a flexible linker sequence to this region of CUL1 leaves substrate protein binding and ubiquitin polymerization intact, but nonetheless abolishes ubiquitination of a normal substrate[21].

Table 1 | PHAII phenotypes, stratified by genotype.

Mutant gene	No. of kindreds	No. of affecteds	Dx/Ref age*	K^+ (mM) (nl 3.5–5.0 mM)†	HCO_3^- (mM) (nl 22–28 mM)†	Hypertension at ≤age 18 (%)†
CUL3	17	21	9 ± 6	7.5 ± 0.9	15.5 ± 2.0	94
KLHL3 recessive	8	14	26 ± 14	6.8 ± 0.5	17.6 ± 1.5	14
KLHL3 dominant	16	40	24 ± 18	6.2 ± 0.6	17.2 ± 2.5	17
WNK4	5	15	28 ± 18	6.4 ± 0.7	20.8 ± 2.3	10
WNK1	2	23	36 ± 20	5.8 ± 0.8	22.4 ± 4.6	13

Dx/Ref age, age at diagnosis or referral. K^+, serum potassium; HCO_3^-, serum bicarbonate; nl, normal range. Hypertension at ≤age 18 (%), percentage of affected patients diagnosed with hypertension by age 18. Values for Dx/Ref age, K^+ and HCO_3^- are means ± standard deviations. Significance of differences among genotype classes was calculated by ANOVA (Dx/Ref age, K^+, HCO_3^-) or Fisher's exact test (hypertension).
* $P = 0.0002$.
† $P < 0.0001$.

Thiazide diuretics correct abnormalities in virtually all PHAII subjects; similar correction is seen in a mouse model of PHAII with either thiazides or genetic ablation of NCC[16]. These findings suggest that increased NCC activity is likely to be a common pathogenic mechanism. Co-expression of KLHL3 and CUL3 with NCC in the DCT, and evidence that NCC is ubiquitinated[22] is consistent with this notion. ROMK and the H^+ ATPase are respectively required for net renal K^+ secretion[23] and H^+ secretion[24] and are also likely targets, although their activity is expected to be decreased, rather than increased, in PHAII. Another thiazide-sensitive Na–Cl cotransport pathway in the collecting duct has recently been described, suggesting an additional potential target[25]. Whether a KLHL3–CUL3 CRL acts directly or indirectly on these targets, whether they alter delivery of NCC and other targets to, or retrieval from, the plasma membrane, and what upstream pathways regulate this activity is unknown. Similarly, whether KLHL3–CUL3 and WNKs operate within the same or different pathways is presently unknown; it is of interest that segments of NRF2 that interact with the kelch propeller domain of KEAP1 are highly acidic[9,26], akin to the domain of WNK4 that is mutated in PHAII[11].

These findings demonstrate previously unrecognized roles for KLHL3 and CUL3. Understanding the upstream regulators and downstream targets of KLHL3–CUL3 activity will provide further insight into the mechanisms underlying maintenance of blood pressure and electrolyte homeostasis in response to diverse environmental challenges.

METHODS SUMMARY

A cohort of 52 PHAII kindreds comprising 126 affected subjects was ascertained, characterized and recruited for study. Index cases of eleven kindreds were chosen for whole exome capture and sequencing, and novel variants were identified. Genes were prioritized for follow-up and subjected to Sanger sequencing of index cases of each kindred. Segregation of rare variants within kindreds was analysed. KLHL3 and CUL3 were localized in kidney by staining with specific antibodies and immunofluorescence microscopy. Effects of *CUL3* mutations on RNA splicing were studied by analysis of spliced products produced in mammalian cells.

Full Methods and any associated references are available in the online version of the paper at www.nature.com/nature.

Received 3 September; accepted 22 December 2011.
Published online 22 January 2012.

1. Kahle, K. T., Ring, A. M. & Lifton, R. P. Molecular physiology of the WNK kinases. *Annu. Rev. Physiol.* **70**, 329–355 (2008).
2. Lai, F. *et al.* Molecular characterization of *KLHL3*, a human homologue of the *Drosophila kelch* gene. *Genomics* **66**, 65–75 (2000).
3. Furukawa, M., He, Y. J., Borchers, C. & Xiong, Y. Targeting of protein ubiquitination by BTB-Cullin 3–Roc1 ubiquitin ligases. *Nature Cell Biol.* **5**, 1001–1007 (2003).
4. Prag, S. & Adams, J. C. Molecular phylogeny of the kelch-repeat superfamily reveals an expansion of BTB/kelch proteins in animals. *BMC Bioinformatics* **4**, 42 (2003).
5. Stogios, P. J., Downs, G. S., Jauhal, J. J., Nandra, S. K. & Prive, G. G. Sequence and structural analysis of BTB domain proteins. *Genome Biol.* **6**, R82 (2005).
6. Hudson, A. M. & Cooley, L. Phylogenetic, structural and functional relationships between WD- and kelch-repeat proteins. *Subcell. Biochem.* **48**, 6–19 (2008).
7. Zimmerman, E. S., Schulman, B. A. & Zheng, N. Structural assembly of cullin-RING ubiquitin ligase complexes. *Curr. Opin. Struct. Biol.* **20**, 714–721 (2010).
8. Sarikas, A., Hartmann, T. & Pan, Z. Q. The cullin protein family. *Genome Biol.* **12**, 220 (2011).
9. Lo, S. C., Li, X., Henzl, M. T., Beamer, L. J. & Hannink, M. Structure of the Keap1:Nrf2 interface provides mechanistic insight into Nrf2 signaling. *EMBO J.* **25**, 3605–3617 (2006).
10. Lifton, R. P., Gharavi, A. G. & Geller, D. S. Molecular mechanisms of human hypertension. *Cell* **104**, 545–556 (2001).
11. Wilson, F. H. *et al.* Human hypertension caused by mutations in WNK kinases. *Science* **293**, 1107–1112 (2001).
12. Choi, M. *et al.* K^+ channel mutations in adrenal aldosterone-producing adenomas and hereditary hypertension. *Science* **331**, 768–772 (2011).
13. Wilson, F. H. *et al.* Molecular pathogenesis of inherited hypertension with hyperkalemia: the Na–Cl cotransporter is inhibited by wild-type but not mutant WNK4. *Proc. Natl Acad. Sci. USA* **100**, 680–684 (2003).
14. Yang, C. L., Angell, J., Mitchell, R. & Ellison, D. H. WNK kinases regulate thiazide-sensitive Na-Cl cotransport. *J. Clin. Invest.* **111**, 1039–1045 (2003).
15. Kahle, K. T. *et al.* WNK4 regulates the balance between renal NaCl reabsorption and K^+ secretion. *Nature Genet.* **35**, 372–376 (2003).
16. Lalioti, M. D. *et al.* Wnk4 controls blood pressure and potassium homeostasis via regulation of mass and activity of the distal convoluted tubule. *Nature Genet.* **38**, 1124–1132 (2006).
17. Ring, A. M. *et al.* WNK4 regulates activity of the epithelial Na^+ channel *in vitro* and *in vivo*. *Proc. Natl Acad. Sci. USA* **104**, 4020–4024 (2007).
18. Fairbrother, W. G., Yeh, R. F., Sharp, P. A. & Burge, C. B. Predictive identification of exonic splicing enhancers in human genes. *Science* **297**, 1007–1013 (2002).
19. Bachmann, S., Bostanjoglo, M., Schmitt, R. & Ellison, D. H. Sodium transport-related proteins in the mammalian distal nephron—distribution, ontogeny and functional aspects. *Anat. Embryol. (Berl.)* **200**, 447–468 (1999).
20. Welling, P. A. & Ho, K. A comprehensive guide to the ROMK potassium channel: form and function in health and disease. *Am. J. Physiol. Renal Physiol.* **297**, F849–F863 (2009).
21. Zheng, N. *et al.* Structure of the Cul1–Rbx1–Skp1–F box^{Skp2} SCF ubiquitin ligase complex. *Nature* **416**, 703–709 (2002).
22. Ko, B. *et al.* RasGRP1 stimulation enhances ubiquitination and endocytosis of the sodium–chloride cotransporter. *Am. J. Physiol. Renal Physiol.* **299**, F300–F309 (2010).
23. Simon, D. B. *et al.* Genetic heterogeneity of Bartter's syndrome revealed by mutations in the K^+ channel, ROMK. *Nature Genet.* **14**, 152–156 (1996).
24. Karet, F. E. *et al.* Mutations in the gene encoding B1 subunit of H^+-ATPase cause renal tubular acidosis with sensorineural deafness. *Nature Genet.* **21**, 84–90 (1999).
25. Leviel, F. *et al.* The Na^+-dependent chloride-bicarbonate exchanger SLC4A8 mediates an electroneutral Na^+ reabsorption process in the renal cortical collecting ducts of mice. *J. Clin. Invest.* **120**, 1627–1635 (2010).
26. Tong, K. I. *et al.* Different electrostatic potentials define ETGE and DLG motifs as hinge and latch in oxidative stress response. *Mol. Cell. Biol.* **27**, 7511–7521 (2007).
27. Wang, Y. *et al.* MMDB: annotating protein sequences with Entrez's 3D-structure database. *Nucleic Acids Res.* **35**, D298–D300 (2007).
28. Zhang, M. Q. Statistical features of human exons and their flanking regions. *Hum. Mol. Genet.* **7**, 919–932 (1998).
29. Voets, T. *et al.* TRPM6 forms the Mg^{2+} influx channel involved in intestinal and renal Mg^{2+} absorption. *J. Biol. Chem.* **279**, 19–25 (2004).
30. Fushimi, K. *et al.* Cloning and expression of apical membrane water channel of rat kidney collecting tubule. *Nature* **361**, 549–552 (1993).

Supplementary Information is linked to the online version of the paper at www.nature.com/nature.

Acknowledgements We thank the PHAII subjects, their families, and the health care professionals whose participation made this study possible; S. Umlauf and the staff of the Yale Center for Genome Analysis; J. Santosuosso; H. Tirrell and the staff of Beckman Coulter Genomics; V. Klump, Y. Lu, U. Scholl and J. Zhou for providing reagents; W. Hill for artistic assistance with Fig. 1d; and E. Boyden, S. Boyden, L. Cooley and M. Hochstrasser for helpful discussions. This work was supported in part by the Leducq Transatlantic Network on Hypertension and grants from the National Institutes of Health (P30-DK079310 and UL1-RR024139).

Author Contributions L.M.B., M.C., K.A.C. and R.P.L. designed experiments and analysed data. L.M.B., C.J.N.-W. and I.R.T. performed experiments. A.F., H.R.T., G.C., M.L., R.D.G., B.A.S., A.P., M.J.V., M.E.D.F., S.A.S., M.G., F.E.K., J.R.T., J.R.S., K.M.K.-N., C.C.P., S.K.A., M.L.W., I.D.D., S.B.D., A.B., J.J.F., C.W.B., T.E.H., R.D.N., H.T., T.R.P.C., M.P., D.B., M.S., P.V., J.W.F., M.R., F.T., H.Z.A.-S., J.R., A.G.G. and B.G. recruited PHAII subjects and families. R.B. and S.M.M. directed the information technology and DNA sequencing infrastructure. L.M.B. and R.P.L. wrote the manuscript.

Author Information mRNA and protein sequences are available at NCBI under accession numbers NM_017415.2 and NP_059111.2 (KLHL3), NM_003590.3 and NP_003581.1 (CUL3); mutation data is available at dbSNP under batch accession 1056535. Reprints and permissions information is available at www.nature.com/reprints. The authors declare no competing financial interests. Readers are welcome to comment on the online version of this article at www.nature.com/nature. Correspondence and requests for materials should be addressed to R.P.L. (richard.lifton@yale.edu).

LETTER

doi:10.1038/nature10791

A novel sensor to map auxin response and distribution at high spatio-temporal resolution

Géraldine Brunoud[1], Darren M. Wells[2]*, Marina Oliva[1]*, Antoine Larrieu[2,3]*, Vincent Mirabet[1], Amy H. Burrow[4], Tom Beeckman[3], Stefan Kepinski[4], Jan Traas[1], Malcolm J. Bennett[2] & Teva Vernoux[1]

Auxin is a key plant morphogenetic signal[1] but tools to analyse dynamically its distribution and signalling during development are still limited. Auxin perception directly triggers the degradation of Aux/IAA repressor proteins[2–6]. Here we describe a novel Aux/IAA-based auxin signalling sensor termed DII-VENUS that was engineered in the model plant *Arabidopsis thaliana*. The VENUS fast maturing form of yellow fluorescent protein[7] was fused in-frame to the Aux/IAA auxin-interaction domain (termed domain II; DII)[8] and expressed under a constitutive promoter. We initially show that DII-VENUS abundance is dependent on auxin, its TIR1/AFBs co-receptors[4–6,8] and proteasome activities. Next, we demonstrate that DII-VENUS provides a map of relative auxin distribution at cellular resolution in different tissues. DII-VENUS is also rapidly degraded in response to auxin and we used it to visualize dynamic changes in cellular auxin distribution successfully during two developmental responses, the root gravitropic response and lateral organ production at the shoot apex. Our results illustrate the value of developing response input sensors such as DII-VENUS to provide high-resolution spatio-temporal information about hormone distribution and response during plant growth and development.

Central to auxin signalling is the ubiquitin- and proteasome-dependent degradation of Aux/IAA catalysed by the SCF-type E3 ubiquitin-ligase complexes $SCF^{TIR1/AFB1-5}$ (refs 2–6, 8). Aux/IAA repressors form heterodimers with transcription factors termed auxin response factors (ARFs)[9,10]. Auxin directly promotes the interaction between TIR1/AFBs auxin co-receptors and Aux/IAAs[5], thus recruiting Aux/IAAs to the SCF complex[3,6] and derepressing ARF-bound loci. This allows the transcription of target genes including most *Aux/IAA* genes, hence providing a negative feedback loop (Fig. 1a)[2,10]. The most widely used tools to monitor auxin distribution *in planta* are *DR5*-based auxin-inducible reporters whose promoter contains several ARF binding sites[11,12]. However, as an output of the auxin response pathway (Fig. 1a), reporter activity does not directly relate to endogenous auxin abundance but also reflects the contribution of a complex signalling pathway[2].

Monitoring the degradation of an Aux/IAA-based green fluorescent protein (GFP) reporter would provide a better target for an auxin sensor as its signal can be related more directly to hormone abundance (Fig. 1a)[3,5,6,13]. This has proved very challenging because Aux/IAA half-lives are often shorter than GFP maturation time[7,14–17]. To overcome this technical limitation, we fused the VENUS fast maturing yellow fluorescent protein (YFP)[7] to the auxin-interaction domain (termed domain II; DII)[8] from several Aux/IAA proteins and expressed these fusion proteins under the constitutive 35S promoter (Fig. 1b and Supplementary Fig. 1a, b). Confocal imaging of transgenic root apical tissues revealed similar fluorescence patterns but the strongest signal

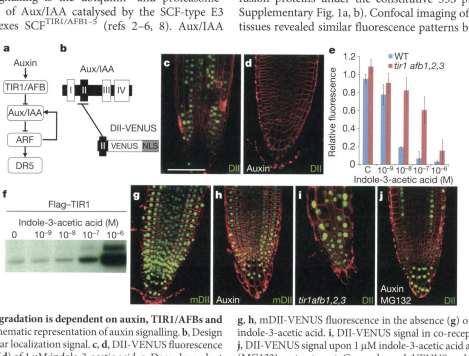

Figure 1 | DII-VENUS degradation is dependent on auxin, TIR1/AFBs and proteasome activity. a, Schematic representation of auxin signalling. **b**, Design of DII-VENUS; NLS, nuclear localization signal. **c**, **d**, DII-VENUS fluorescence in absence (**c**) or presence (**d**) of 1 μM indole-3-acetic acid. **e**, Dose-dependent degradation of DII-VENUS in wild-type and mutant roots. **f**, IAA28 domain II peptide pull-down assay with Flag–TIR1 in the presence of indole-3-acetic acid. **g**, **h**, mDII-VENUS fluorescence in the absence (**g**) or presence (**h**) of 1 μM indole-3-acetic acid. **i**, DII-VENUS signal in co-receptor quadruple mutant. **j**, DII-VENUS signal upon 1 μM indole-3-acetic acid and proteasome inhibitor (MG132) co-treatment. Green channel, VENUS; red channel, FM4-64. Scale bar, 50 μm. Error bars, s.d. (WT, $n = 2$; mutant, $n = 3$).

[1]Laboratoire de Reproduction et Développement des Plantes, CNRS, INRA, ENS Lyon, UCBL, Université de Lyon, 69364 Lyon, France. [2]Centre for Plant Integrative Biology, University of Nottingham, Sutton Bonington LE12 5RD, UK. [3]Department of Plant Systems Biology, VIB, Ghent University, B-9052 Gent, Belgium. [4]Centre for Plant Science, Faculty of Biological Sciences, University of Leeds, Leeds LS2 9JT, UK.

*These authors contributed equally to this work.

was obtained using domain II of the most stable Aux/IAA used, IAA28 (Fig. 1c and Supplementary Fig. 1c–f). We thus focused our analyses on this form of the sensor, henceforth called DII-VENUS.

We tested on root tissues the relationship between auxin, its response components and DII-VENUS in several independent ways. First, the DII-VENUS signal was sensitive in a dose-dependent fashion to exogenous auxin treatment (Fig. 1c–e). Second, the DII peptide interacted with its co-receptors TIR1 (Fig. 1f), AFB1 and AFB5 (ref. 18) in an auxin-dependent manner. Third, introducing a mutation in the domain II sequence of DII-VENUS (mDII-VENUS), that disrupts the interaction between Aux/IAA, auxin and the TIR1/AFBs[5], reduced the differential distribution of fluorescence (Fig. 1g; see below for description of pattern) and blocked its auxin-induced degradation (Fig. 1h). Fourth, DII-VENUS fluorescence was ubiquitously distributed in roots of the most strongly affected *tir1 afb1 afb2 afb3* quadruple mutant[4] (Fig. 1i) and the mutants were significantly less sensitive to auxin treatment (Fig. 1e). Fifth, disruption of ubiquitin-dependent breakdown of Aux/IAA proteins using proteasome inhibitors stabilized DII-VENUS and blocked its auxin-induced degradation (Fig. 1j and Supplementary Fig. 2). We conclude that DII-VENUS abundance is regulated by auxin via its receptors, consistent with the model for Aux/IAA degradation (Fig. 1a)[2]. We also demonstrated that DII-VENUS does not disrupt the activity of the auxin response machinery (Supplementary Fig. 3 and Supplementary Information). Hence, DII-VENUS directly reports, but does not interfere with, the input into the auxin signalling pathway.

We next took advantage of the simple cellular organization of the root apex to quantify the distribution of DII-VENUS fluorescence with cellular definition (Fig. 2a, b and Supplementary Fig. 4). Because the TIR1/AFB1-3 co-receptor distribution shows only limited variations in the root meristem region (except in the root cap; Supplementary Fig. 5a–d)[19], this will confer a homogeneous perception capacity. Hence, the spatial distribution of DII-VENUS fluorescence is likely to represent an inverted auxin distribution map in the root tip. This conclusion is further supported by the more homogeneous fluorescence distribution of mDII-VENUS (Fig. 2c and Supplementary Fig. 6) and by the complementary patterns of DII-VENUS and *DR5::VENUS* expression in the quiescent centre, columella and differentiating xylem cells (Fig. 2d, e)[21,20,23]. However, mDII-VENUS fluorescence distribution suggests a higher 35S promoter activity in the epidermis and cortex in the elongation zone and in the most external root cap cells (Fig. 2c and Supplementary Fig. 6). Lower expression of the TIR/AFBs is also expected to confer a lower sensitivity to auxin in the root cap (Supplementary Fig. 5a–d). In both cases, this will lead to an underestimation of auxin levels by DII-VENUS. Analyses of TIR/AFBs co-receptor distribution and of 35S promoter activity are thus essential to interpret the DII-VENUS pattern.

Even considering these biases (Supplementary Information), DII-VENUS quantification indicates that auxin levels are reproducibly higher in the first two tiers of columella cells and initials, the quiescent centre, the stele initials and early daughters and the differentiating xylem cells (Fig. 2b and Supplementary Fig. 4)[22]. The other cells in the root meristem have lower levels of auxin, with minima observed in the epidermis and cortex, but auxin levels significantly increased close to the start of the elongation zone. This increase occurs closer to the root tip in the epidermis and vasculature compared to the cortex (Fig. 2b). The DII-VENUS fluorescence map thus confirms the local maximum of auxin at the quiescent centre and in the columella cells[11] but also allows visualizing the distribution of auxin in the entire root tip. It also reveals a previously unsuspected auxin accumulation starting at the transition zone between the meristem and the elongation zone. These results are in partial agreement with measurements of auxin concentrations in root tissues obtained after cell sorting[23], the differences being possibly due to the higher resolution achieved using DII-VENUS.

We also detected differential distributions of DII-VENUS fluorescence in the vegetative shoot apical meristem (SAM), in the vascular tissues of the hypocotyl (Fig. 2f, g) and later during development in the inflorescence SAM and young floral meristems (Supplementary Fig. 7a–d)[18]. As in the root, reduced differential expression with mDII-VENUS, partly complementary *DR5::VENUS* patterns and distribution of TIR1/AFB1–3 co-receptors (Fig. 2h, i and Supplementary Fig. 5e–h) indicate that the distribution of DII-VENUS fluorescence is primarily controlled by auxin levels in the shoot apex (Supplementary Information)[18]. DII-VENUS is therefore able to report relative auxin distribution at high spatial resolution in various tissues and developmental stages. In addition, in both root and shoot tissues, DII-VENUS is degraded not only in cells where *DR5* is expressed but also in cells that do not express *DR5* (Figs 1c, 2a–f and Supplementary Fig. 7 and Supplementary Information)[18]. This observation demonstrates that the Aux/IAA-ARF signalling pathway contributes significantly to the definition of the *DR5* expression pattern.

To analyse the temporal resolution of the DII-VENUS sensor, we compared dynamic changes in DII-VENUS and *DR5::VENUS* signals

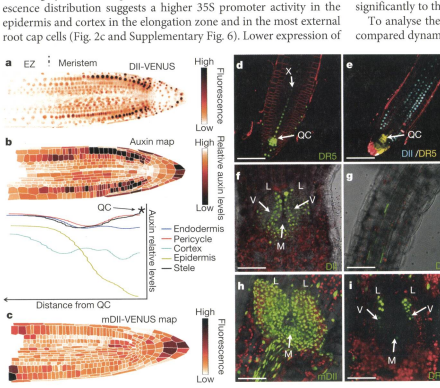

Figure 2 | DII-VENUS provides a sensor to map auxin distribution in plant tissues. a–d, Root meristematic tissues. **a**, **b**, DII-VENUS fluorescence (**a**) and corresponding map of relative auxin distribution (**b**; top) using the same look-up table. EZ, elongation zone. Tissue-specific changes in auxin levels along the root axis are shown (**b**; bottom). QC, quiescent centre. **c**, Fluorescence map of mDII-VENUS control. **d**, *DR5::VENUS*. X, xylem axis. **e**, DII-VENUS (blue) and *DR5::GFP* (yellow). **f–i**, DII-VENUS (**f**, **g**), mDII-VENUS (**h**) and *DR5::VENUS* (**i**) in the vegetative shoot apex (**f**, **h**, **i**) and hypocotyl (**g**). M, meristem; L, leaves; V, vasculature. Green or blue channel, VENUS; yellow channel in **e**, GFP; red channel, FM4-64 (**d**, **e**) or autofluorescence (**f–i**). In **f–i** the transmission channel has been added. Scale bars, 50 μm.

in roots following exogenous auxin treatment (Fig. 3a, b and Supplementary Movie 1). Time-lapse confocal imaging revealed that the DII-VENUS signal was rapidly lost from all root tissues, whereas the signal in untreated roots remained stable (Fig. 3a and Supplementary Movie 1). Quantification of VENUS fluorescence in the root tip showed that a reduction in the DII-VENUS signal was detected minutes after auxin addition and the signal was abolished within 60 min (Fig. 3b). In contrast, an increase in the *DR5::VENUS* signal was first detected only after 120 min (Fig. 3b). This delay is due to post-transcriptional processes, because quantitative reverse transcription-PCR (qRT–PCR) detected VENUS messenger RNA minutes after auxin treatment (Fig. 3b). We could further show that the DII-VENUS degradation kinetics upon auxin treatment is very similar in different root tissues, but is slower in the root cap (Supplementary Fig. 8). These results indicate similar auxin sensitivity throughout the root except for a lower sensitivity in the root cap, as already suggested by the distribution of the TIR/AFBs (Supplementary Fig. 5a–d). We also observed that the global dynamics of degradation of DII-VENUS was similar in the vegetative and inflorescence SAM, with a minimal fluorescence reached after 1 h (Fig. 3c and Supplementary Fig. 9). We conclude that DII-VENUS responds almost immediately and similarly to exogenous auxin application in various tissues. This observation strengthens our conclusion that DII-VENUS fluorescence is directly related to auxin levels in both shoot and root meristematic tissues but that co-receptor distribution needs to be considered.

Finally, we used DII-VENUS to follow changes in auxin distribution during developmental processes. Roots have been proposed to bend in response to gravity by accumulating auxin on the lower side of root apical tissues[21,24,25]. Consistent with this model, induction of the *DR5* reporter occurs after 1.5–2 h in the lateral root cap (LRC) and epidermis on the lower side of the root (Supplementary Fig. 10)[21]. By contrast, within 30 min of a 90° gravity stimulus the DII-VENUS signal was entirely lost in these tissues on the lower side, whereas fluorescence was stable on the upper side (Fig. 4a). A decrease in DII-VENUS fluorescence was also observed in the cortex and endodermis on both sides of the root and to a lesser extent in vascular tissues. Hence, DII-VENUS

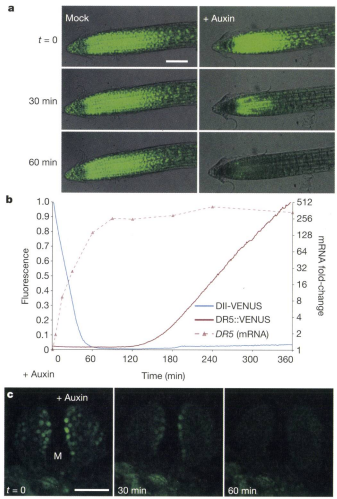

Figure 3 | DII-VENUS monitors changes in auxin response and distribution at high temporal resolution. **a**, Time-course of DII-VENUS fluorescence following either a mock or an auxin treatment (1 μM 1-naphthaleneacetic acid; NAA). **b**, Quantification of DII-VENUS and DR5::VENUS fluorescence and of *DR5::VENUS* mRNA levels in root apices treated with 1 μM NAA. **c**, Time-course of DII-VENUS fluorescence in the shoot apex upon 1 μM indole-3-acetic acid treatment; images are projections of 10 confocal serial sections. Green channel, VENUS. In **a** the transmission channel has been added. Scale bars, 50 μm.

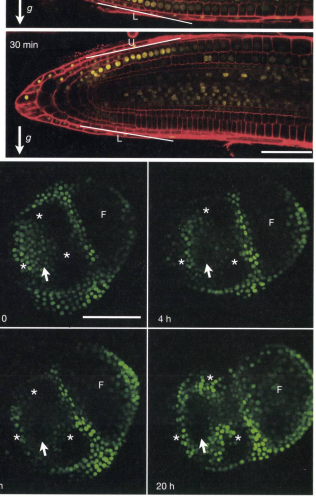

Figure 4 | DII-VENUS allows visualization of changes in auxin distribution during development. **a**, Changes in DII-VENUS fluorescence during a root gravitropic response. *g*, gravity vector; a line was drawn near equivalent cells in the LRC and epidermis on the lower (L) and upper (U) side. **b**, Auxin build-up during organ initiation at the shoot apex visualized using DII-VENUS; arrow, site of new organ initiation; asterisks, groups of nuclei showing notable changes in fluorescence; F, flower. Yellow or green channel, VENUS; red channel, propidium iodide. Scale bars, 50 μm.

indicates that the changes in auxin concentration are not restricted to the LRC and epidermis during the gravitropic response. We next used DII-VENUS to follow auxin-dependent organ initiation at the SAM (Fig. 4b)[26,27]. DII-VENUS allowed the visualization of the progressive build-up of auxin triggering the formation of a new organ (Fig. 4b). It also demonstrated significant redistribution of DII-VENUS fluorescence throughout the SAM, most probably reflecting the dynamics of auxin transport in the tissue[27]. Taken together, our observations demonstrate that, during both shoot and root development, DII-VENUS detects dynamic changes in endogenous auxin distribution and responses that are more complex than previously thought. By demonstrating that DII-VENUS and *DR5* fluorescence patterns are only partly complementary, we also provide evidence that the auxin signalling pathway has a key role in the spatial control of transcription in response to auxin during developmental processes. Finally, several other plant hormones have been shown to signal through degradation of key signalling regulators[28–30]. Our work provides the foundation for building synthetic signalling sensors for different hormones to explore their role during development.

METHODS SUMMARY

Generation and characterization of DII-VENUS reporter plants. Aux/IAA degron sequences[16] were fused to VENUS-NLS under the control of the 35S promoter (Supplementary Fig. 1) and recombined into gateway binary vector pH7m34GW (http://gateway.psb.ugent.be/). Plasmids were transformed into Col-0 plants by floral dipping.

Microscopy, live imaging and chemical treatments. All images were obtained using laser-scanning confocal microscope. Tissue organization was visualized using FM4-64, propidium iodide, transmission or chlorophyll autofluorescence. For live imaging of shoot meristems, plants were grown on the auxin transport inhibitor 1-*N*-naphthylphthalamic acid (NPA) to produce naked apices before transferring to a new medium without NPA. To generate maps of relative auxin distribution in the root meristem, a cellular grid was generated from a median optical section and for each cells fluorescence was extracted from the optical section cutting the nucleus at its most median part.

For analysis of chemically treated roots, 5-day-old DII-VENUS seedlings were transferred to media containing the chemicals at the stated concentration. For root live imaging, immediately following transfer, the seedlings were scanned every 2 to 5 min for 2 h. The fluorescence intensity over identical scanned portion of the root (corresponding approximately to the first 200 μM from the root tip) was extracted at each time point. For tissue-specific kinetics, fluorescence was extracted from groups of nuclei with nearly identical fluorescence in the different tissues. For the vegetative SAM, 5-day-old DII-VENUS seedlings were mounted in water after removing one cotyledon to allow observation of the vegetative shoot apex before treating with the stated concentration of auxin.

Pull-down assays. Pull-down assays were performed using a 35S:Flag-TIR1 line and biotinylated IAA28 peptide. The immunodetection of TIR1/AFB–Flag was performed with a 1:5,000 dilution of anti-Flag 2-peroxidase (HRP) antibody followed by chemiluminescent detection with ECL plus reagents.

Full Methods and any associated references are available in the online version of the paper at www.nature.com/nature.

Received 11 July; accepted 19 December 2011.
Published online 15 January 2012.

1. Friml, J. Auxin transport—shaping the plant. *Curr. Opin. Plant Biol.* **6,** 7–12 (2003).
2. Chapman, E. J. & Estelle, M. Mechanism of auxin-regulated gene expression in plants. *Annu. Rev. Genet.* **43,** 265–285 (2009).
3. Dharmasiri, N., Dharmasiri, S. & Estelle, M. The F-box protein TIR1 is an auxin receptor. *Nature* **435,** 441–445 (2005).
4. Dharmasiri, N. *et al.* Plant development is regulated by a family of auxin receptor F box proteins. *Dev. Cell* **9,** 109–119 (2005).
5. Tan, X. *et al.* Mechanism of auxin perception by the TIR1 ubiquitin ligase. *Nature* **446,** 640–645 (2007).
6. Kepinski, S. & Leyser, O. The *Arabidopsis* F-box protein TIR1 is an auxin receptor. *Nature* **435,** 446–451 (2005).
7. Shaner, N. C., Steinbach, P. A. & Tsien, R. Y. A guide to choosing fluorescent proteins. *Nature Methods* **2,** 905–909 (2005).
8. Greenham, K. *et al.* The AFB4 auxin receptor is a negative regulator of auxin signaling in seedlings. *Curr. Biol.* **21,** 520–525 (2011).
9. Ulmasov, T., Hagen, G. & Guilfoyle, T. J. ARF1, a transcription factor that binds to auxin response elements. *Science* **276,** 1865–1868 (1997).
10. Guilfoyle, T. J. & Hagen, G. Auxin response factors. *Curr. Opin. Plant Biol.* **10,** 453–460 (2007).
11. Sabatini, S. *et al.* An auxin-dependent distal organizer of pattern and polarity in the *Arabidopsis* root. *Cell* **99,** 463–472 (1999).
12. Ulmasov, T., Murfett, J., Hagen, G. & Guilfoyle, T. J. Aux/IAA proteins repress expression of reporter genes containing natural and highly active synthetic auxin response elements. *Plant Cell* **9,** 1963–1971 (1997).
13. Gray, W. M., Kepinski, S., Rouse, D., Leyser, O. & Estelle, M. Auxin regulates SCF^{TIR1}-dependent degradation of AUX/IAA proteins. *Nature* **414,** 271–276 (2001).
14. Ramos, J. A., Zenser, N., Leyser, O. & Callis, J. Rapid degradation of auxin/indoleacetic acid proteins requires conserved amino acids of domain II and is proteasome dependent. *Plant Cell* **13,** 2349–2360 (2001).
15. Zenser, N., Ellsmore, A., Leasure, C. & Callis, J. Auxin modulates the degradation rate of Aux/IAA proteins. *Proc. Natl Acad. Sci. USA* **98,** 11795–11800 (2001).
16. Dreher, K. A., Brown, J., Saw, R. E. & Callis, J. The *Arabidopsis* Aux/IAA protein family has diversified in degradation and auxin responsiveness. *Plant Cell* **18,** 699–714 (2006).
17. Abel, S., Oeller, P. W. & Theologis, A. Early auxin-induced genes encode short-lived nuclear proteins. *Proc. Natl Acad. Sci. USA* **91,** 326–330 (1994).
18. Vernoux, T. *et al.* The auxin signalling network translates dynamic input into robust patterning at the shoot apex. *Mol. Syst. Biol.* **7,** 508 (2011).
19. Parry, G. *et al.* Complex regulation of the TIR1/AFB family of auxin receptors. *Proc. Natl Acad. Sci. USA* **106,** 22540–22545 (2009).
20. Benková, E. *et al.* Local, efflux-dependent auxin gradients as a common module for plant organ formation. *Cell* **115,** 591–602 (2003).
21. Ottenschläger, I. *et al.* Gravity-regulated differential auxin transport from columella to lateral root cap cells. *Proc. Natl Acad. Sci. USA* **100,** 2987–2991 (2003).
22. Santuari, L. *et al.* Positional information by differential endocytosis splits auxin response to drive *Arabidopsis* root meristem growth. *Curr. Biol.* **21,** 1918–1923 (2011).
23. Petersson, S. V. *et al.* An auxin gradient and maximum in the *Arabidopsis* root apex shown by high-resolution cell-specific analysis of IAA distribution and synthesis. *Plant Cell* **21,** 1659–1668 (2009).
24. Boonsirichai, K., Guan, C., Chen, R. & Masson, P. H. Root gravitropism: an experimental tool to investigate basic cellular and molecular processes underlying mechanosensing and signal transmission in plants. *Annu. Rev. Plant Biol.* **53,** 421–447 (2002).
25. Boonsirichai, K., Sedbrook, J. C., Chen, R., Gilroy, S. & Masson, P. H. ALTERED RESPONSE TO GRAVITY is a peripheral membrane protein that modulates gravity-induced cytoplasmic alkalinization and lateral auxin transport in plant statocytes. *Plant Cell* **15,** 2612–2625 (2003).
26. Reinhardt, D. *et al.* Regulation of phyllotaxis by polar auxin transport. *Nature* **426,** 255–260 (2003).
27. Heisler, M. G. *et al.* Patterns of auxin transport and gene expression during primordium development revealed by live imaging of the *Arabidopsis* inflorescence meristem. *Curr. Biol.* **15,** 1899–1911 (2005).
28. Silverstone, A. L. *et al.* Repressing a repressor: gibberellin-induced rapid reduction of the RGA protein in *Arabidopsis*. *Plant Cell* **13,** 1555–1566 (2001).
29. Fu, X. & Harberd, N. P. Auxin promotes *Arabidopsis* root growth by modulating gibberellin response. *Nature* **421,** 740–743 (2003).
30. Santner, A. & Estelle, M. Recent advances and emerging trends in plant hormone signalling. *Nature* **459,** 1071–1078 (2009).

Supplementary Information is linked to the online version of the paper at www.nature.com/nature.

Acknowledgements We thank A. Erktan and C. Cellier for help with marker expression analysis; J. Neve, A. Miyawaki, M. Heisler and M. Estelle for providing the 35S::*Flag-TIR1* line, *VENUS* complementary DNA, DR5::VENUS plasmids and TIR/AFB GUS lines, respectively; the PLATIM for access to confocal microscopes; F. Parcy, O. Hamant, A. Boudaoud and P. Das for discussions. T.V. was supported by the Human Frontier Science Program Organization (CDA 0047/2007 HFSPO) and the Agence National de la Recherche (ANR-07-JCJC-0115 and EraSysBio+ iSAM). D.M.W., A.L. and M.J.B. acknowledge the support of the Biotechnology and Biological Sciences Research Council (BBSRC) and Engineering and Physical Sciences Research Council (EPSRC) funding to the Centre for Plant Integrative Biology (CPIB); BBSRC grants BB/F013981/1 and BB/F007418/1 to S.K.; BBSRC Professional Research Fellowship funding to D.M.W. & M.J.B.; and Belgian Scientific policy (BELSPO contract BARN) to A.L., T.B. and M.J.B.

Author Contributions T.V. designed the DII-VENUS tool. G.B., M.O. and T.V. engineered and characterized DII-VENUS transgenic lines. D.M.W., G.B., A.L. and V.M. quantified the spatial and temporal dynamics of DII-VENUS. A.H.B. did the pull-down assay. T.V. and M.J.B. designed the experiments with the help of T.B., S.K. and J.T. T.V. and M.J.B. analysed the data and wrote the paper. All authors discussed the results and commented on the manuscript.

Author information Seed for the lines described in this study have been deposited at the Nottingham *Arabidopsis* Stock Centre. Reprints and permissions information is available at www.nature.com/reprints. The authors declare no competing financial interests. Readers are welcome to comment on the online version of this article at www.nature.com/nature. Correspondence and requests for materials should be addressed to T.V. (teva.vernoux@ens-lyon.fr).

LETTER

doi:10.1038/nature10729

Adenylylation control by intra- or intermolecular active-site obstruction in Fic proteins

Philipp Engel[1]*†, Arnaud Goepfert[1,2]*, Frédéric V. Stanger[1,2], Alexander Harms[1], Alexander Schmidt[3], Tilman Schirmer[2] & Christoph Dehio[1]

Fic proteins that are defined by the ubiquitous FIC (filamentation induced by cyclic AMP) domain are known to catalyse adenylylation (also called AMPylation); that is, the transfer of AMP onto a target protein. In mammalian cells, adenylylation of small GTPases through Fic proteins injected by pathogenic bacteria can cause collapse of the actin cytoskeleton and cell death[1,2]. It is unknown how this potentially deleterious adenylylation activity is regulated in the widespread Fic proteins that are found in all domains of life and that are thought to have critical roles in intrinsic signalling processes. Here we show that FIC-domain-mediated adenylylation is controlled by a conserved mechanism of ATP-binding-site obstruction that involves an inhibitory α-helix (α_{inh}) with a conserved (S/T)XXXE(G/N) motif, and that in this mechanism the invariable glutamate competes with ATP γ-phosphate binding. Consistent with this, FIC-domain-mediated growth arrest of bacteria by the VbhT toxin of *Bartonella schoenbuchensis* is intermolecularly repressed by the VbhA antitoxin through tight binding of its α_{inh} to the FIC domain of VbhT, as shown by structure and function analysis. Furthermore, structural comparisons with other bacterial Fic proteins, such as Fic of *Neisseria meningitidis* and of *Shewanella oneidensis*, show that α_{inh} frequently constitutes an amino-terminal or carboxy-terminal extension to the FIC domain, respectively, partially obstructing the ATP binding site in an intramolecular manner. After mutation of the inhibitory motif in various Fic proteins, including the human homologue FICD (also known as HYPE), adenylylation activity is considerably boosted, consistent with the anticipated relief of inhibition. Structural homology modelling of all annotated Fic proteins indicates that inhibition by α_{inh} is universal and conserved through evolution, as the inhibitory motif is present in ~90% of all putatively adenylylation-active FIC domains, including examples from all domains of life and from viruses. Future studies should reveal how intrinsic or extrinsic factors modulate adenylylation activity by weakening the interaction of α_{inh} with the FIC active site.

In two Fic proteins, IbpA and VopS, that are translocated by pathogenic bacteria into host cells, the ubiquitous FIC domain has been shown to catalyse adenylylation[1–4]. The crystal structure of the effector domain IbpA(FIC2) in complex with its adenylylated host target Cdc42 has been reported[5] and a catalytic mechanism has been proposed[5,6]. IbpA- or VopS-mediated adenylylation of Rho-family GTPases abolishes downstream signalling in human cells and, thus, causes actin cytoskeleton collapse and cell death[1,2]. By contrast, overexpression of a human Fic protein with similar target specificity, HYPE, had only a marginal effect[1]. This suggests that the potentially deleterious adenylylation activity is tightly regulated in HYPE and probably in most of the almost 3,000 Fic proteins that are proposed to have important roles in intrinsic signalling processes in bacteria, archaea and eukaryotes.

VbhT is a bacterial Fic protein of the mammalian pathogen *B. schoenbuchensis*[7,8]. It is composed of an N-terminal FIC domain and a C-terminal BID domain (Fig. 1a). The BID domain facilitates protein translocation into mammalian or bacterial target cells through a type IV secretion system or conjugation machinery[9], respectively, but the target cell and functional role of VbhT are unknown. VbhT arrests growth when expressed in *Escherichia coli* (Fig. 1c and Supplementary Fig. 1a). Growth arrest is repressed by mutation of histidine to alanine (VbhT(H136A)) in the conserved FIC motif HXFX(D/E)GNGRXXR. In other Fic proteins, this signature motif has been shown to be essential for target protein adenylylation activity[1,2,10], therefore suggesting that toxicity is related to adenylylation of endogenous proteins. Indeed, wild-type VbhT, but not VbhT(H136A), catalysed *in vitro* adenylylation of a putative *E. coli* target protein of approximately 80 kilodaltons (kDa) (Fig. 1d). Furthermore, *E. coli* cells showed filamentation after expression of wild-type VbhT, but not of VbhT(H136A) (Supplementary Fig. 2). A similar phenotype has been described for what is thought to be a hyperactive mutant of the *E. coli* Fic protein[11]. Co-expression of VbhT with VbhA, encoded by the small open reading frame *vbhA*

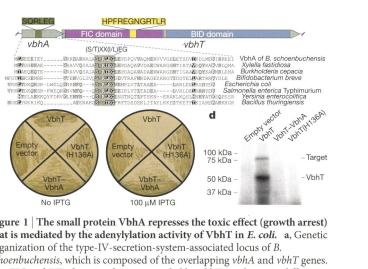

Figure 1 | The small protein VbhA represses the toxic effect (growth arrest) that is mediated by the adenylylation activity of VbhT in *E. coli*. **a**, Genetic organization of the type-IV-secretion-system-associated locus of *B. schoenbuchensis*, which is composed of the overlapping *vbhA* and *vbhT* genes. The FIC and BID domains that are encoded by *vbhT* are shown in different colours. Protein translations of the regions encoding the conserved motif of VbhA and the FIC motif of VbhT are depicted. **b**, Protein alignment of VbhA and a subset of the 158 homologues that are encoded upstream of *fic* loci in different bacteria (see also Supplementary Fig. 4). The most conserved region shows a (S/T)XX(I/L)EG consensus. Sequence accessions and strain designations are given in Supplementary Fig. 4. **c**, Growth of *E. coli* on lysogeny broth (LB) plates after IPTG-induced expression of different VbhT and VbhA constructs. Expression of VbhT shows a toxic effect, whereas bacterial growth is not affected when VbhT(H136A) is expressed or when VbhT and VbhA are co-expressed (VbhT–VbhA). All *E. coli* strains revealed normal growth without induction. Growth curve experiments in LB gave analogous results (Supplementary Fig. 1). **d**, Adenylylation assay with crude cell lysates of *E. coli* ectopically expressing the same constructs as in panel **c**.

[1]Focal Area Infection Biology, Biozentrum, University of Basel, CH-4056 Basel, Switzerland. [2]Core Program Structural Biology and Biophysics, Biozentrum, University of Basel, CH-4056 Basel, Switzerland. [3]Proteomics Core Facility, Biozentrum, University of Basel, CH-4056 Basel, Switzerland. †Present address: Department of Ecology and Evolutionary Biology, Yale University, New Haven, CT 06520-8106, USA. *These authors contributed equally to this work.

immediately upstream of *vbhT* (Fig. 1a), completely repressed VbhT toxicity, as shown by wild-type-like bacterial growth, normal cell morphology, and inhibition of VbhT-dependent adenylylation (Fig. 1 and Supplementary Figs 1a and 2). We also observed VbhT-mediated toxicity and its repression by VbhA in *B. schoenbuchensis*, the natural carrier of this toxin and antitoxin, and in the related species *Bartonella henselae* (Supplementary Fig. 3).

The inhibitory action of VbhA on the VbhT toxin, and the genetic organization of the respective genes in an operon are reminiscent of toxin–antitoxin modules that are found in many bacterial genomes, often associated with mobile genetic elements[12]. A comprehensive analysis of the upstream region of FIC-domain-encoding genes (PFAM pf02661) identified 158 bacterial *vbhA* homologues that probably function as antitoxins. Although the sequences are rather diverse, a central (S/T)XX(I/L)EG motif is conspicuous (Fig. 1b and Supplementary Fig. 4). The high-resolution (1.5 Å) crystal structure of VbhA in complex with the FIC domain of VbhT (VbhT(FIC)) (Supplementary Table 1) shows that VbhA is folded into three anti-parallel helices that tightly embrace VbhT(FIC) (Fig. 2a) with the N-terminal helix (α_{inh}), adopting a location that is analogous but distinct to that of the antitoxin Phd in its complex with Doc[13] (Supplementary Fig. 5). Doc is a Fic protein with a degenerate, probably adenylylation-incompetent FIC motif[14] that may have adopted another toxic activity (Supplementary Information, section 1). The VbhA antitoxin motif locates to the C-terminal part of α_{inh} and is positioned close to the putative ATP-binding site[10] at the N-cap of the helix that follows the active loop of VbhT(FIC). This suggests that the antitoxin competes with ATP binding. VbhA residues Ser 20 and Glu 24 of the inhibitory motif form a hydrogen bond and a salt bridge, respectively, with the conserved Arg147 of VbhT following the active loop.

Intriguingly, structural comparison with other bacterial Fic proteins of known fold (Fic proteins from *S. oneidensis* (SoFic)[14,15] and from *N. meningitidis* (NmFic)[14] (Fig. 2b, c), and from *Bacteroides theataiotaomicron* (BtFic)[14] and from *Helicobacter pylori* (HpFic)[14] (Supplementary Fig. 6)) reveals that a structural equivalent of α_{inh} can be part of the FIC domain fold itself. Moreover, these proteins also show the SXXXE(G/N) inhibitory motifs that are, with respect to the FIC active site, arranged exactly as in the VbhA-VbhT(FIC) complex. Along the polypeptide chain, however, these α_{inh} occur at two distinct locations either in the N-terminal part (SoFic and BtFic) or at the C terminus (NmFic and HpFic). Thus, Fic proteins containing α_{inh} can be grouped into three classes (Fig. 2d) depending on whether α_{inh} is provided by an interacting antitoxin (class I) or whether it is part of the FIC fold as an N-terminal helix (class II) or a *C*-terminal helix (class III).

To investigate the distribution of class II and class III Fic proteins, we predicted the structures of all PFAM FIC domain entries by homology modelling (Supplementary Information, section 1). Including the class I proteins that are identified above, two-thirds of all Fic proteins were classified (Fig. 2e and Supplementary Table 2), with a strong dominance of class II, the class to which human HYPE belongs (Supplementary Tables 3 and 4). The proportion of classified Fic proteins increases to 90% when considering only adenylylation-competent Fic proteins that are defined by compliance with the HXFX(D/E)GNGRXXR motif (Supplementary Text). This suggests co-evolution of catalytic and inhibitory function. The inhibition motifs that are derived from Psi-Blast (class I) and structural predictions (classes II and III) are shown in Fig. 2f with the overall consensus being (S/T)XXXE(G/N). The strict conservation of the glutamate is striking and indicates that the observed ionic interaction with the second arginine of the conserved FIC motif (Figs 2a–c) is crucial for inhibition. Phylogenetic distribution of class I

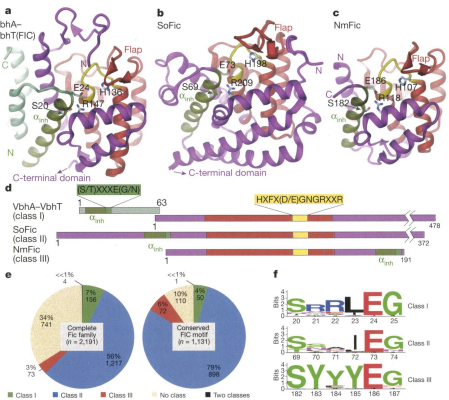

Figure 2 | Structures and classification of Fic proteins according to the position of the inhibitory motif along the polypeptide chain. Structures are shown in cartoon (FIC core as defined by PFAM, red; active site loop with histidine, yellow; inhibitory helix (α_{inh}) with SXXXE(G/N) motif, green) with important residues in full. **a**, Complex of VbhT(FIC) with antitoxin VbhA (green). **b**, SoFic (from *S. oneidensis*, PDB code 3EQX) with C-terminal domain omitted. **c**, NmFic (from *N. meningitidis*, PDB code 2G03). **d**, Linear organization of motifs in the proteins presented in panels **a**–**c**. **e**, Distribution of the three Fic protein classes for the entire family in the PFAM database (left) and the subset of Fic proteins with the conserved FIC motif HXFX[(D/E)GNGRXXR that is likely to convey adenylylation activity (right; see also Supplementary Information, section 1). **f**, Sequence profiles for the inhibition site of the three Fic protein classes.

and class III Fic proteins indicates that each is of monophyletic origin (Supplementary Fig. 7). Fic proteins with a degenerate FIC motif are dispersed over the tree, with the exception of the large cluster of Doc-like toxins. This suggests that there is recurrent degeneration of the conserved FIC motif with concomitant loss of adenylylation activity. Consistent with this, deterioration of the FIC motif seems to correlate with the absence of a recognizable inhibitory motif (Supplementary Fig. 7). Fic proteins with a degenerate FIC motif may display catalytic activities different from adenylylation, such as phosphocholination, as reported for the *Legionella pneumophila* effector AnkX[16].

Owing to our discovery of the prevalence of the inhibitory motif in Fic proteins, we carried out a detailed analysis of its functional and structural role. For this, NmFic (class III, Fig. 2c) was chosen, as it is the smallest active Fic family protein with known crystallization condition (Supplementary Table 1). As reported before[6], NmFic exhibits *in vitro* auto-adenylylation activity (Fig. 3d). The acceptor site was traced to Y183 of α_{inh} by mass spectrometry (Supplementary Information, section 1, and Supplementary Fig. 8). On the basis of the location of Y183 relative to the active site, auto-adenylylation is probably catalysed intermolecularly after partial unfolding or detachment of α_{inh}. Addition of *E. coli* lysate to NmFic did not reveal additional bands on the autoradiograph, and this indicated that there are no NmFic targets in *E. coli* or that the activity of NmFic is inhibited. The latter was shown to be correct as mutation of the inhibitory motif (S182A/E186A, NmFic(SE/AA)) resulted in transfer of radioactivity onto an ~80-kDa *E. coli* protein and enhanced auto-adenylylation with an additional acceptor site (Y188; Fig. 3d and Supplementary Fig. 9). Deletion of the entire α_{inh} helix (NmFic(Δ8)) led to similar target protein adenylylation, proving that the activity resides in the FIC domain core. However, only weak auto-adenylylation was apparent owing to the lack of the acceptor tyrosines in this deletion mutant (Fig. 3d and Supplementary Fig. 8c).

To investigate the inhibitory mechanism, crystals of NmFic proteins were soaked with the non-hydrolysable ATP analogue adenylyl imidodiphosphate (AMPPNP) (Supplementary Table 1). The NmFic–AMPPNP structure revealed nucleotide binding but with the γ-phosphate disordered (Fig. 3a). Notably, the orientation of the α-phosphate seems to be non-productive, as the position that is in line with the scissile Pα-Oβ bond is occluded by H107 and N113 (Supplementary Fig. 10a and Supplementary Movie). To reveal the situation in an inhibition-relieved mutant, the structure of NmFic(SE/AA) was determined to 3.0 Å (Supplementary Fig. 11). Electron density was lacking for α_{inh}, indicating disorder, whereas the nucleotide conformation was well defined. In the NmFic(Δ8)–AMPPNP structure, the same nucleotide conformation was observed (Fig. 3b) and, owing to its high resolution (1.7 Å), the structural basis for the observed relief of inhibition in these mutants became evident. Whereas the adenosine moiety adopts the same position as in the wild-type, the γ-phosphate of the nucleotide is bound to R118, occupying the same position as the carboxylate of the inhibitory E186 in the wild type. As a consequence, the α-phosphate is found to be re-oriented, and the new orientation permits in line attack of a target side chain onto the α-phosphorus to accomplish AMP transfer (Fig. 3c, Supplementary Fig. 10 and Supplementary Movie).

The exact role of the inhibitory glutamate was investigated further by mutagenesis of Fic proteins from the three regulatory classes. In wild-type NmFic, Cα and Cβ of the glutamate are close to the position that is attained by the γ-phosphate position in NmFic(Δ8) (Fig. 3c). Still, an E to G single point mutant may provide sufficient space and main-chain flexibility to allow γ-phosphate binding. Indeed, similar to NmFic(Δ8)and NmFic(SE/AA), the mutant NmFic(E186G) resulted in growth inhibition of *E. coli* (Supplementary Fig. 1b). Likewise, co-expression of VbhT(FIC) and VbhA(E24G)$_2$ as representatives for class I, caused *E. coli* growth defects (Supplementary Fig. 1a). We also included SoFic, a bacterial class II protein, in this analysis. Consistent with the effects of E to G single point mutants in NmFic and VbhA, mutant SoFic(E73G) revealed a negative effect on *E. coli* growth

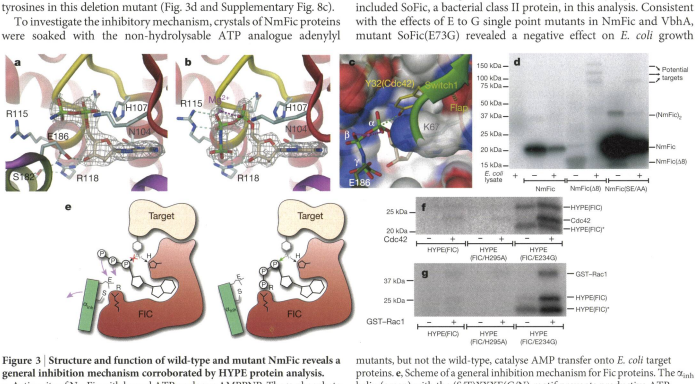

Figure 3 | Structure and function of wild-type and mutant NmFic reveals a general inhibition mechanism corroborated by HYPE protein analysis. **a**, Active site of NmFic with bound ATP analogue AMPPNP. The γ-phosphate seems to be disordered and has not been modelled. **b**, Active site of NmFic(Δ8) with bound AMPPNP and Mg^{2+}. The γ-phosphate occupies the position taken by E186 of the SXXXEG motif in the wild-type (as shown in **a**). Also shown are $2Fo-Fc$ maps that are contoured at 1.2σ and cover the ligands. **c**, Surface representation of the active site of NmFic(Δ8) with modifiable Y32 (yellow) of the Cdc42 switch I loop (green) in a position that is obtained from a superposition of the active site loops of NmFic over the IbpA(FIC2)–Cdc42 complex[2]. **d**, Autoradiography of an SDS gel after incubation of wild-type and mutant NmFic with [α-^{32}P]ATP in the presence or absence of *E. coli* lysate. The mutants, but not the wild-type, catalyse AMP transfer onto *E. coli* target proteins. **e**, Scheme of a general inhibition mechanism for Fic proteins. The α_{inh} helix (green) with the (S/T)XXXE(G/N) motif prevents productive ATP binding. It is only after dissociation of the helix that the ATP γ-phosphate attains the position close to a conserved arginine (indicated by "R") of the FIC motif. This is accompanied by reorientation of the α-phosphate to allow in-line attack of the target hydroxyl side chain after proton transfer to the active histidine as proposed before[6]. **f**, **g**, Autoradiography after incubation of HYPE(FIC) with α-^{32}P-ATP in the presence or absence of Cdc42 (**f**) or GST-tagged Rac1 (GST–Rac1) (**g**). HYPE(FIC/E234G) shows enhanced auto-adenylylation and target adenylylation. HYPE(FIC)* denotes a degradation product of HYPE(FIC).

(Supplementary Fig. 1c) and strongly enhanced auto-adenylylation (Supplementary Fig. 12). A similar marked effect on auto-adenylylation was observed after mutation of the corresponding residue in human HYPE (HYPE(FIC/E234G)), another class II protein (Fig. 3f, g). It is known that HYPE catalyses Cdc42 and Rac1 adenylylation[1,4]. The rather low adenylylation activity of wild-type HYPE on these substrates is markedly enhanced in the HYPE(FIC/E234G) mutant (Fig. 3f, g), demonstrating that the relief of inhibition by α_{inh} enhances not only auto-adenylylation but also AMP transfer onto bona fide protein targets.

From this study a general mechanism for the inhibition of the FIC-domain-mediated adenylylation has emerged that invokes a glutamate finger from α_{inh} to inter- or intramolecularly block part of the ATP binding site (Fig. 3e). Dissociation of the toxin–antitoxin complex (class I) or intramolecular loosening of the contact between α_{inh} and the FIC domain active site (classes II and III) allows ordered binding of the entire ATP moiety with the α-phosphate in an orientation that is productive for accepting an incoming target hydroxyl side chain.

Class I proteins might exert functions similar to the classical bacterial toxin–antitoxin modules[1,2], whereas class II and III Fic proteins seem to regulate intrinsic cellular functions that are related to physiological adaptation and cell homeostasis. Conservation of class II Fic proteins in all three kingdoms of life (Supplementary Table 2) emphasizes the important role of the regulatory mechanisms described here. How the adenylylation activity is activated by weakening the interaction of α_{inh} with the FIC active site in class II and class III Fic proteins is one of many important questions for future research. We also anticipate our study to be a starting point for rational approaches to modulate the adenylylation activities of Fic proteins—approaches that should aid in elucidating the diverse biological functions of these widespread signalling proteins.

METHODS SUMMARY

Toxicity experiments were performed with *E. coli* strain MG1655, which encodes an IPTG (isopropyl-β-D-thiogalactoside)-inducible T7 polymerase (strain AB472). Protein expression was controlled by the addition of either 100 μM IPTG (induction) or 1% glucose (repression). A PSI-BLAST search for homologues with VbhA of *B. schoenbuchensis* was conducted to identify Fic proteins belonging to class I. Class II and class III proteins were classified by structure predictions using the program HHpred[17]. We analysed all 2,189 proteins of the FIC PFAM family (pf02661, release 24). Adenylylation assays were carried out using bacterial crude cell lysates for VbhT constructs or purified proteins for NmFic, SoFic and HYPE constructs. For structure determination, VbhA and VbhT(FIC) were co-expressed in the BL21(DE3) strain of *E. coli*, and NmFic, SoFic(Δ8) and NmFic(SE/AA) in the BL21-A1 strain of *E. coli*. VbhA-VbhT(FIC) and NmFic were purified by affinity chromatography followed by size exclusion chromatography. An additional anion exchange chromatography step was performed for NmFic(Δ8)and NmFic(SE/AA). Diffraction data were collected at beamline X06SA of the Swiss Light Source. For NmFic(Δ8)and NmFic(SE/AA), we obtained phases by molecular replacement using the NmFic structure (PDB code 2G03) as a search model. The VbhA–VbhT(FIC) complex was solved by molecular replacement using a fragment of BepA (PDB code 2JK8).

Full Methods and any associated references are available in the online version of the paper at www.nature.com/nature.

Received 4 July; accepted 24 November 2011.
Published online 22 January 2012.

1. Worby, C. A. *et al.* The fic domain: regulation of cell signaling by adenylylation. *Mol. Cell* **34,** 93–103 (2009).
2. Yarbrough, M. L. *et al.* AMPylation of Rho GTPases by *Vibrio* VopS disrupts effector binding and downstream signaling. *Science* **323,** 269–272 (2009).
3. Roy, C. R. & Mukherjee, S. Bacterial FIC proteins AMP up infection. *Sci. Signal.* **2,** pe14 (2009).
4. Mattoo, S. *et al.* Comparative analysis of *Histophilus somni* immunoglobulin-binding protein A (IbpA) with other Fic domain-containing enzymes reveals differences in substrate and nucleotide specificities. *J. Biol. Chem.* **286,** 32834–32842 (2011).
5. Luong, P. *et al.* Kinetic and structural insights into the mechanism of AMPylation by VopS Fic domain. *J. Biol. Chem.* **285,** 20155–20163 (2010).
6. Xiao, J., Worby, C. A., Mattoo, S., Sankaran, B. & Dixon, J. E. Structural basis of Fic-mediated adenylylation. *Nature Struct. Mol. Biol.* **17,** 1004–1010 (2010).
7. Dehio, C. *et al. Bartonella schoenbuchii* sp. nov., isolated from the blood of wild roe deer. *Int. J. Syst. Evol. Microbiol.* **51,** 1557–1565 (2001).
8. Engel, P. *et al.* Parallel evolution of a type IV secretion system in radiating lineages of the host-restricted bacterial pathogen *Bartonella*. *PLoS Genet.* **7,** e1001296 (2011).
9. Schulein, R. *et al.* A bipartite signal mediates the transfer of type IV secretion substrates of *Bartonella henselae* into human cells. *Proc. Natl Acad. Sci. USA* **102,** 856–861 (2005).
10. Palanivelu, D. V. *et al.* Fic domain-catalyzed adenylylation: insight provided by the structural analysis of the type IV secretion system effector BepA. *Protein Sci.* **20,** 492–499 (2011).
11. Utsumi, R., Nakamoto, Y., Kawamukai, M., Himeno, M. & Komano, T. Involvement of cyclic AMP and its receptor protein in filamentation of an *Escherichia coli* fic mutant. *J. Bacteriol.* **151,** 807–812 (1982).
12. Engelberg-Kulka, H., Amitai, S., Kolodkin-Gal, I. & Hazan, R. Bacterial programmed cell death and multicellular behavior in bacteria. *PLoS Genet.* **2,** e135 (2006).
13. Garcia-Pino, A. *et al.* Doc of prophage P1 is inhibited by its antitoxin partner Phd through fold complementation. *J. Biol. Chem.* **283,** 30821–30827 (2008).
14. Kinch, L. N., Yarbrough, M. L., Orth, K. & Grishin, N. V. Fido, a novel AMPylation domain common to Fic, Doc, and AvrB. *PLoS ONE* **4,** e5818 (2009).
15. Das, D. *et al.* Crystal structure of the Fic (Filamentation induced by cAMP) family protein SO4266 (gi|24375750) from *Shewanella oneidensis* MR-1 at 1.6 Å resolution. *Proteins* **75,** 264–271 (2009).
16. Mukherjee, S. *et al.* Modulation of Rab GTPase function by a protein phosphocholine transferase. *Nature* **477,** 103–106 (2011).
17. Söding, J., Biegert, A. & Lupas, A. N. The HHpred interactive server for protein homology detection and structure prediction. *Nucleic Acids Res.* **33,** W244–W248 (2005).

Supplementary Information is linked to the online version of the paper at www.nature.com/nature.

Acknowledgements We thank T. Glatter for mass spectrometry analysis of samples at the Core Proteomics facility. We thank the staff of beamline X06SA of the Swiss Light Source for assistance with data acquisition. We are grateful to G. Pluschke for providing the genomic DNA of *Neisseria meningitidis*, the ASU Biodesign Institute for providing the plasmid enclosing the *Shewanella oneidensis* Fic protein and S. Mattoo and J. Dixon for providing the pET-GSTX plasmids enclosing HYPE and HYPE(H295A). We also thank D. Bumann and A. Boehm for providing plasmid pC10E and *E. coli* strain AB472, respectively. This work was supported by grants 3100-061777 and 3100-138414 from the Swiss National Science Foundation (to C.D. and T.S., respectively), and grant 51RT 0_126008 (InfectX) in the frame of the SystemsX.ch Swiss Initiative for Systems Biology (to C.D.).

Author Contributions P.E., F.V.S. and A.H. cloned recombinant plasmids. P.E. discovered and physiologically characterized VbhT–VbhA as a toxin–antitoxin module and carried out the bioinformatic analysis. A.G. expressed, purified and crystallized VbhA–VbhT(FIC), NmFic(SE/AA) and NmFic(Δ8), and determined their structures. F.V.S. expressed, purified and crystallized NmFic with AMPPNP and determined the structure. A.G. and A.H. performed the adenylylation assays. A.H. carried out the growth curve experiments. A.S. conducted the mass spectrometry analysis. All authors contributed to experimental design and data analysis. The manuscript was written by P.E., A.G., T.S. and C.D.

Author Information The atomic coordinates of VbhA–VbhT(FIC) and the complexes of NmFic, NmFic(SE/AA) and NmFic(Δ8) with AMPPNP have been deposited in the Protein Data Bank under accession codes 3SHG, 3S6A, 3SN9 and 3SE5, respectively. Reprints and permissions information is available at www.nature.com/reprints. The authors declare no competing financial interests. Readers are welcome to comment on the online version of this article at www.nature.com/nature. Correspondence and requests for materials should be addressed to C.D. (Christoph.Dehio@unibas.ch) or T.S. (Tilman.Schirmer@unibas.ch).

LETTER

doi:10.1038/nature10731

Cysteinyl leukotriene type I receptor desensitization sustains Ca^{2+}-dependent gene expression

Siaw-Wei Ng[1], Daniel Bakowski[1], Charmaine Nelson[1], Ravi Mehta[1], Robert Almeyda[2], Grant Bates[2] & Anant B. Parekh[1]

Receptor desensitization is a universal mechanism to turn off a biological response; in this process, the ability of a physiological trigger to activate a cell is lost despite the continued presence of the stimulus. Receptor desensitization of G-protein-coupled receptors involves uncoupling of the receptor from its G-protein or second-messenger pathway followed by receptor internalization[1]. G-protein-coupled cysteinyl leukotriene type I (CysLT1) receptors regulate immune-cell function and CysLT1 receptors are an established therapeutic target for allergies, including asthma[2]. Desensitization of CysLT1 receptors arises predominantly from protein-kinase-C-dependent phosphorylation of three serine residues in the receptor carboxy terminus[3]. Physiological concentrations of the receptor agonist leukotriene C_4 (LTC_4) evoke repetitive cytoplasmic Ca^{2+} oscillations, reflecting regenerative Ca^{2+} release from stores, which is sustained by Ca^{2+} entry through store-operated calcium-release-activated calcium (CRAC) channels[4]. CRAC channels are tightly linked to expression of the transcription factor *c-fos*[5], a regulator of numerous genes important to cell growth and development[6]. Here we show that abolishing leukotriene receptor desensitization suppresses agonist-driven gene expression in a rat cell line. Mechanistically, stimulation of non-desensitizing receptors evoked prolonged inositol-trisphosphate-mediated Ca^{2+} release, which led to accelerated Ca^{2+}-dependent slow inactivation of CRAC channels and a subsequent loss of excitation–transcription coupling. Hence, rather than serving to turn off a biological response, reversible desensitization of a Ca^{2+} mobilizing receptor acts as an 'on' switch, sustaining long-term signalling in the immune system.

The paradox of receptor desensitization is how long-term responses can be evoked if the receptor is inactivated. This is a particularly acute problem in immune cells, in which cell differentiation and clonal selection develop over hours in the continued presence of external cues.

Stimulation of rat basophilic leukaemia (RBL-1) cells with LTC_4, acting exclusively on CysLT1 receptors[7,8] (Supplementary Fig. 1), led to cytoplasmic Ca^{2+} signals (Fig. 1a) followed by robust expression of *c-fos* at both messenger RNA (Fig. 1b, c)[9] and protein levels (Fig. 1d, e). Maximal activation of CRAC channels with thapsigargin led to a similar increase in *c-fos* expression (Fig. 1b–e). Both LTC_4 and thapsigargin induce *c-fos* expression through the build-up of Ca^{2+} microdomains near open store-operated CRAC channels[4,5]. Thapsigargin led to a larger, more sustained Ca^{2+} signal than LTC_4 (Fig. 1a)[4,5] and the rate of Ca^{2+} entry through CRAC channels was approximately twofold more for thapsigargin than LTC_4 (Fig. 1f), consistent with patch-clamp recordings[7]. The similar increase in Ca^{2+}-dependent *c-fos* expression to LTC_4 and thapsigargin was therefore surprising, given the significant difference in CRAC channel activation.

We considered various explanations for why CysLT1 receptor activation and thapsigargin evoked similar *c-fos* levels despite marked differences in the extent of CRAC channel activation. These included: (1) CysLT1 receptors tapped into a different signalling mechanism linking CRAC channel microdomains to *c-fos* expression; (2) local Ca^{2+} entry through CRAC channels was larger after receptor activation because LTC_4 hyperpolarized the membrane potential; and (3) cytoplasmic Ca^{2+} and protein kinase C (PKC) interacted synergistically to drive gene expression in response to CysLT1 receptor activation. Evidence against these possibilities is presented in Supplementary Figs 2–4. Instead, gene expression showed high sensitivity to Ca^{2+} entry, enabling CysLT1 receptor activation to couple effectively to *c-fos* transcription (Supplementary Fig. 5), as well as rapidity and high gain. Combined, this ensures efficient gene expression to bursts of CRAC channel activity after physiological levels of receptor stimulation.

Experiments described in Fig. 1g and h revealed an important role for PKC in receptor-dependent gene expression. The structurally distinct PKC blockers G06983 and calphostin C abolished *c-fos* expression (Fig. 1g, h). PKC block had a marked effect on the Ca^{2+} signal evoked by agonist. Whereas cytoplasmic Ca^{2+} oscillations were routinely observed with LTC_4 (Fig. 1i), the response was converted into a large, single, slowly decaying Ca^{2+} spike after PKC inhibition (Fig. 1i, j). Acute stimulation with PMA in the absence of LTC_4 failed to induce significant *c-fos* expression (data not shown)[9], demonstrating that PKC activity per se was not sufficient to induce *c-fos* expression in these cells. The PKC inhibitors had no effect on thapsigargin-evoked *c-fos* expression (Fig. 1k) or cytoplasmic Ca^{2+} signals (Fig. 1l). Thapsigargin (2 μM) activates CRAC channels maximally (Supplementary Fig. 5) and, by blocking SERCA pumps (which can be located near CRAC channels[10]), reduces the decay of Ca^{2+} gradients radiating from the plasma membrane. It is possible that other non-receptor-dependent stimuli, which raise local Ca^{2+} levels less effectively than 2 μM thapsigargin, might activate *c-fos* in a manner dependent on basal PKC activity, but this activity would be unusual in that it is not stimulated acutely by PMA in the presence of submaximal CRAC channel activation (Supplementary Fig. 4).

In RBL cells, exposure to the phorbol ester PMA for several hours downregulates several PKC isozymes[11]. Using this protocol, we found that *c-fos* expression was substantially reduced in response to CysLT1 receptor stimulation (Fig. 1m), whereas no significant reduction was seen when thapsigargin was used instead (Fig. 1m) or when inactive 4α-phorbol replaced PMA (data not shown). Similar to PKC blockers, the Ca^{2+} signal to LTC_4 was prolonged after PKC downregulation (Fig. 1n). This prolonged Ca^{2+} signal did not reflect a change in Ca^{2+} clearance mechanisms (Supplementary Fig. 6); instead, it is characteristic of loss of receptor desensitization, particularly for CysLT1 receptors, in which desensitization is mediated predominantly by PKC[3] and prevention of desensitization leads to broader Ca^{2+} signals[12]. Inhibition of CysLT1 receptor desensitization is predicted to lead to greater inositol trisphosphate ($InsP_3$) production and hence more extensive Ca^{2+} store emptying. Several findings are consistent with this. First, Ca^{2+} release to LTC_4 lasted approximately five times longer when PKC was blocked than in control cells (Fig. 2a, expanded in inset). Second, the amount of Ca^{2+} remaining within the stores, measured as the ionomycin-sensitive Ca^{2+} response[13], was substantially less after activation of CysLT1 receptors in the presence of PKC block than in control cells (Fig. 2a). Third, $InsP_3$ production, measured using the green fluorescent protein–pleckstrin homology

[1]Department of Physiology, Anatomy and Genetics, University of Oxford, Parks Road, Oxford OX1 3PT, UK. [2]Department of Ear-Nose-Throat Surgery, John Radcliffe Hospital, Oxford OX3 9DH, UK.

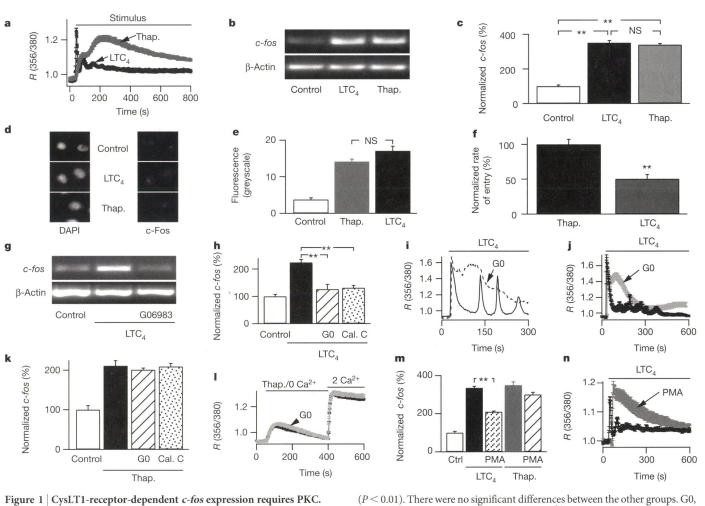

Figure 1 | CysLT1-receptor-dependent *c-fos* expression requires PKC. **a**, Averaged Ca^{2+} signals to LTC_4 and thapsigargin (Thap.) are compared (>50 cells per graph). *R* (356/380), ratio of fluorescence measured at 356 and 380 nm. **b**, *c-fos* expression is compared between control (non-stimulated), 160 nM LTC_4- and 2 μM thapsigargin-stimulated cells. Stimulus was present for 8 min. **c**, Histograms show averaged responses from three independent experiments. LTC_4 and thapsigargin groups were different from control ($P < 0.001$), but not from one another ($P > 0.3$; analysis of variance (ANOVA)). **d**, Cells stained with antibody against c-Fos protein. DAPI, 4′,6-diamidino-2-phenylindole. **e**, Aggregate data are compared ($n > 20$ per bar). Thapsigargin and LTC_4 groups were different from control ($P < 0.001$) but not from one another ($P = 0.11$). **f**, Ca^{2+} entry rate was measured after readmission of Ca^{2+} to cells stimulated with LTC_4 or thapsigargin in Ca^{2+}-free solution (*$P < 0.01$). **g**, G06983 (1 μM; 10 min pre-treatment) suppresses LTC_4-induced *c-fos* expression. **h**, Histogram comparing the effects of PKC blockers. LTC_4 control group (LTC_4 in the absence of PKC block) was different from the other groups ($P < 0.01$). There were no significant differences between the other groups. G0, G06983. Cal. C, calphostin C. **i**, Single-cell Ca^{2+} signals to LTC_4 are compared for the conditions shown. **j**, Averaged data are compared (>45 cells for each condition). **k**, Histogram showing *c-fos* expression to thapsigargin in the presence of PKC blockers. All thapsigargin-treated groups were significantly different from control ($P < 0.001$) but were not significantly different from one another. **l**, Ca^{2+} signals to thapsigargin are unaffected by PKC block. 0 Ca^{2+}, Ca^{2+}-free external solution; 2 Ca^{2+}, external solution containing 2 mM Ca^{2+}. **m**, Downregulation of PKC (PMA; 500 nM, 24 h) reduces LTC_4- but not thapsigargin-induced *c-fos* expression (data from four independent experiments). All stimulated groups were significantly different from control ($P < 0.01$). For LTC_4 the PMA group was different from the LTC_4 control ($P < 0.01$). For thapsigargin, the PMA groups was not different from the thapsigargin control ($P = 0.07$). Ctrl, control. **n**, PKC downregulation alters the LTC_4-evoked Ca^{2+} signal. Error bars show data ± s.e.m. NS, not significant.

(GFP–PH) construct[14], increased to a greater extent when PKC was inhibited (Fig. 2b).

Cytoplasmic Ca^{2+} inhibits CRAC channels through mechanisms of fast and slow inactivation[15]. The prolonged Ca^{2+} release evoked by LTC_4 in the presence of non-desensitizing receptors could therefore inactivate CRAC channels to suppress agonist-evoked gene expression. In support of this, accumulation of the slow Ca^{2+} chelator EGTA in the cytoplasm rescued gene expression to CysLT1 receptor activation in the presence of PKC block (Fig. 2c, d). Ca^{2+}-dependent fast inactivation of CRAC channels is unlikely to contribute here because (1) it is unaffected by the slow chelator EGTA[16,17], which reversed the inhibitory effects of PKC block (Fig. 2c, d), and (2) the rate and extent of fast inactivation were unaltered by CysLT1 receptor activation in the presence of PKC downregulation (Fig. 3a). Instead, Ca^{2+}-dependent slow inactivation is likely to be the dominant mechanism because (1) it too is suppressed by cytoplasmic EGTA[18,19], (2) the Ca^{2+} dependence of slow inactivation has a dissociation constant (K_d) of ~0.5 μM and full block occurs at ~1 μM (Fig. 3b), which is similar to the peak Ca^{2+} rise evoked by LTC_4 in the presence of PKC inhibitors or following downregulation of PKC (0.87 ± 01 μM), and (3) Ca^{2+}-dependent slow inactivation develops with a time course similar to the duration of the prolonged Ca^{2+} rise caused by LTC_4 following loss of PKC activity[18,19].

If prolonged Ca^{2+} release to non-desensitizing CysLT1 receptors leads to slow inactivation of CRAC channels, then development of a calcium-release-activated calcium current (I_{CRAC}) to a subsequent stimulus should be impaired. Pre-activation of CysLT1 receptors reduced I_{CRAC} evoked by thapsigagin but only in the presence of PKC block (Fig. 3c). No such inhibitory effect was seen when cells were dialysed with a strongly buffered Ca^{2+}-containing pipette solution, which prevents the development of slow inactivation (Fig. 3d). Increasing the time between the termination of Ca^{2+} release and

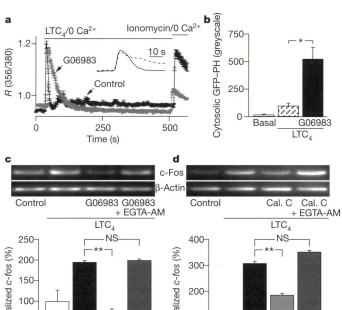

Figure 2 | Gene expression to non-desensitizing CysLT1 receptors is rescued by preventing a cytoplasmic Ca^{2+} rise. a, Stimulation with LTC_4 in the presence of G06983 evokes a more sustained Ca^{2+} release response, and this leads to more extensive store depletion (measured through the extent of Ca^{2+} release evoked by 5 μM ionomycin). Both LTC_4 and ionomycin were applied in Ca^{2+}-free external solution. Inset compares the kinetics of Ca^{2+} release. **b**, Cytosolic GFP–PH levels, a measure of $InsP_3$ levels, rise when CysLT1 receptors are stimulated in the presence of G06983. **c**, Top, loading cells with the Ca^{2+} chelator EGTA prevents loss of gene expression to agonist when PKC is blocked. Bottom, aggregate data from five independent gels are summarized. **d**, As in **c**, but calphostin C was used to block PKC instead. Bottom, aggregate data from three independent gels are summarized. Error bars show data ± s.e.m. NS, not significant.

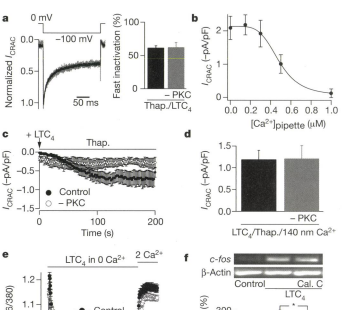

Figure 3 | Ca^{2+}-dependent slow inactivation underlies suppression of c-Fos expression to non-desensitizing CysLT1 receptors. a, Ca^{2+}-dependent fast inactivation is unaffected by non-desensitizing receptors (labelled −PKC). Cells were stimulated with LTC_4 (160 nM) before breaking in with a pipette solution containing thapsigargin and buffered Ca^{2+} (140 nM) and fast inactivation was measured within 60 s of break-in. **b**, Dependence of Ca^{2+}-dependent slow inactivation on patch pipette Ca^{2+} concentration. pA, picoamperes; pF, picofarads. $[Ca^{2+}]_{pipette}$, concentration of Ca^{2+} in pipette. **c**, Stimulation of non-desensitizing receptors with LTC_4 before break-in significantly reduced the size of I_{CRAC} that developed in response to dialysis with thapsigargin in weak buffer (0.2 mM EGTA). **d**, As in **c**, but cells were dialysed with a pipette solution containing strong Ca^{2+} buffer (10 mM EGTA, 140 nM free Ca^{2+}). **e**, Store-operated Ca^{2+} entry recovers partially by increasing the time interval between Ca^{2+} release and subsequent Ca^{2+} entry. **f**, *c-fos* expression to non-desensitizing receptor stimulation is rescued partially when Ca^{2+} entry occurs several minutes after Ca^{2+} release has reached completion. **g**, c-Fos expression in human nasal mast cells after CysLT1 receptor activation is suppressed by PKC inhibition. **h**, Aggregate data are compared (12–17 cells per bar; three patients each). Error bars show data ± s.e.m. NS, not significant.

subsequent store-operated Ca^{2+} entry should enable some recovery from Ca^{2+}-dependent slow inactivation and this should partially rescue gene expression. When Ca^{2+} influx was evoked a few minutes after Ca^{2+} release, significant, albeit incomplete, rescue of Ca^{2+} entry (Fig. 3e) and *c-fos* transcription (Fig. 3f) occurred in cells stimulated with LTC_4 in the presence of PKC inhibition. Hence, allowing CRAC channels time to recover from Ca^{2+}-dependent inactivation results in partial rescue of agonist-driven gene expression.

Our attempts to express the PKC-insensitive CysLT1 receptor, in which S313, S315 and S316 had been mutated to alanines, were thwarted by the difficulty of expressing these receptors[3], although in a few cells we observed that Ca^{2+} oscillations to LTC_4 were less frequent (3.1 ± 0.5 versus 5.4 ± 0.4, 4 and 6 cells, respectively) and the initial spike was a little broader (~1.25-fold) than mock-transfected cells.

To place our findings in a physiological context, we turned to the human nasal polyp, which is rich in mast cells[20]. The polyp and associated nasal mucosa are largely self-contained, providing an excellent 'quasi *in vivo* human system'. Mast cells from polyps, acutely isolated from patients undergoing surgery, respond to LTC_4 and express functional CRAC channels[7,8]. Stimulation with LTC_4 activated c-Fos protein expression in mast cells isolated from polyps (Fig. 3g) and this was reduced by pre-treatment with either calphostin C or G06983 (Fig. 3h). PKC inhibitors had no inhibitory effect when thapsigargin was used instead.

Western blots revealed the presence of Ca^{2+}-dependent PKC-α, -β and -ζ isozymes[11,21] but only faint expression of PKC-δ and -ε (Fig. 4a). Overnight PMA exposure significantly reduced PKC-α and -β expression, but not PKC-ζ (Fig. 4a, b). Their weak expression made PKC-δ and -ε difficult to quantify. Confocal microscope studies confirmed robust expression of PKC-α, -β and -ζ (Fig. 4c), with barely detectable levels of PKC-δ and -ε (data not shown). Overnight PMA exposure significantly reduced PKC-α and -β but not -ζ at the cellular level (Fig. 4d). Knockdown of PKC-α using a targeted short interfering RNA (siRNA) approach (Fig. 4e) resulted in a broadening of the first Ca^{2+} oscillation evoked by LTC_4, indicative of less receptor desensitization, and fewer Ca^{2+} oscillations in each cell (Supplementary Fig. 7). Knockdown of PKC-β had a much weaker effect on the Ca^{2+} oscillations (Supplementary Fig. 7). Knockdown of PKC-α or PKC-α plus -β simultaneously, but not PKC-β alone, reduced LTC_4-driven

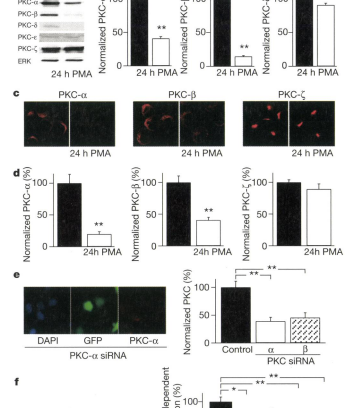

Figure 4 | PKC-α regulates CysLT1 receptor-driven *c-fos* transcription. **a**, Expression of PKC-α, -β and -ζ (western blot) is shown in control cells and cells exposed to PMA for 24 h. **b**, Quantification of data from three independent experiments, as in **a**. **c**, Confocal microscope images of PKC expression for the conditions shown. Cells were fixed before analysis. Original magnification, ×100. **d**, Quantification of images from experiments, as in **c**. **e**, siRNA against PKC-α or -β significantly reduces corresponding protein expression. Left, DAPI staining of nuclei; middle, GFP expression (indicating transfection); and right, PKC-α expression after siRNA-mediated knockdown. Right, aggregate data from four experiments are depicted. Both siRNA groups were different from control ($P < 0.005$). Error bars show data ± s.e.m. NS, not significant. **f**, Knockdown of PKC-α, -β and PKC-α plus -β on LTC_4-dependent *c-fos* expression. Data are compared with mock-transfected cells. For comparison, 24 h exposure to PMA is included. All treated groups were significantly different from the LTC_4 control (black bar) group except siRNA PKC-β knockdown ($P > 0.1$). PKC-α plus -β and 24 h PMA groups had $P < 0.01$; PKC-α group had $P < 0.05$. Error bars show data ± s.e.m. NS, not significant.

c-fos expression to an extent similar to that seen after overnight PMA treatment (Fig. 4f). Stimulation of non-G-protein-coupled FCεRI antigenic receptors in RBL-2H3 cells activates *c-fos* expression primarily through PKC-δ and -ε[22]. Although it is possible that these PKC isoforms also contribute to gene expression under our conditions, our results nevertheless suggest a major role for PKC-α in G-protein-coupled-receptor desensitization, and thus coupling to the nucleus.

Collectively, our findings reveal a counterintuitive function for desensitization of a phospholipase-C-coupled receptor. Rather than terminating a response, homologous receptor desensitization is essential for maintaining excitation–transcription coupling. Desensitization of CysLT1 receptors is mediated principally by PKC-dependent phosphorylation[3]. Prevention of receptor desensitization through either acute block or degradation of PKC or after knockdown of PKC-α all led to loss of Ca^{2+}-dependent gene expression, despite potentiation of Ca^{2+} release to agonist. Mechanistically, the prolonged Ca^{2+} release phase accelerated Ca^{2+}-dependent slow inactivation of CRAC channels, resulting in loss of Ca^{2+} entry. Because Ca^{2+} microdomains near open CRAC channels drive *c-fos* expression, the decline in CRAC channel activity abolishes excitation–transcription coupling. The interval between Ca^{2+} oscillations after CysLT1 receptor activation is ~25 s (ref. 4). Because $InsP_3$ has a short half-life in the cytoplasm (~1 s)[23], receptor desensitization will presumably lower $InsP_3$ levels during the interspike interval. Store refilling will occur quickly and CRAC channel activity will be transient after CysLT1 receptor stimulation. The short duration of Ca^{2+} release and thus Ca^{2+} entry, determined by receptor desensitization, will ensure Ca^{2+}-dependent slow inactivation does not develop, as this inhibitory mechanism requires a sustained Ca^{2+} rise for several seconds. It is therefore the kinetics of receptor desensitization and recovery from desensitization within a highly Ca^{2+} sensitive and high-gain system that ensures bursts of store-operated Ca^{2+} entry occur that are sufficient for the activation of *c-fos* expression, without the build-up of the Ca^{2+}-dependent slow inactivation pathway that would abolish the response.

METHODS SUMMARY

Cultured RBL-1 cells and acutely isolated human nasal polyps were prepared as described previously[7]. Transfection with siRNA constructs was achieved using the AMAXA system. Patch-clamp recordings and cytoplasmic Ca^{2+} measurements followed standard methods[5]. RT–PCR, western blotting and confocal microscopy were carried out as described previously[6]. Error bars are s.e.m.

Full Methods and any associated references are available in the online version of the paper at www.nature.com/nature.

Received 8 April; accepted 23 November 2011.
Published online 9 January 2012.

1. Pierce, K. L., Premont, R. T. & Lefkowitz, R. J. Seven-transmembrane receptors. *Nature Rev. Mol. Cell Biol.* **3,** 639–650 (2002).
2. Funk, C. D. Leukotriene modifiers as potential therapeutics for cardiovascular disease. *Nature Rev. Drug Discov.* **4,** 664–672 (2005).
3. Naik, S. *et al.* Regulation of cysteinyl leukotriene type 1 receptor internalization and signaling. *J. Biol. Chem.* **280,** 8722–8732 (2005).
4. Di Capite, J., Ng, S.-W. & Parekh, A. B. Decoding of cytoplasmic Ca^{2+} oscillations through the spatial signature drives gene expression. *Curr. Biol.* **19,** 853–858 (2009).
5. Ng, S.-W., Nelson, C. & Parekh, A. B. Coupling of Ca^{2+} microdomains to spatially and temporally distinct cellular responses by the tyrosine kinase Syk. *J. Biol. Chem.* **284,** 24767–24772 (2009).
6. Foletta, V. C., Segal, D. H. & Cohen, D. R. Transcriptional regulation in the immune system: all roads lead to AP-1. *J. Leukoc. Biol.* **63,** 139–152 (1998).
7. Di Capite, J. L., Shirley, A., Nelson, C., Bates, G. & Parekh, A. B. Intercellular calcium wave propagation involving positive feedback between CRAC channels and cysteinyl leukotrienes. *FASEB J.* **23,** 894–905 (2009).
8. Di Capite, J., Nelson, C., Bates, G. & Parekh, A. B. Targeting CRAC channels and leukotriene receptors provides a novel combination strategy for treating nasal polyposis. *J. Allergy Clin. Immunol.* **124,** 1014–1021 (2009).
9. Stephan, V., Seibt, A., Koerholz, D. & Wahn, V. Expression of mRNA for the proto-oncogene c-fos in rat basophilic leukemia cells. *Cell. Signal.* **9,** 65–70 (1997).
10. Jousset, H., Frieden, M. & Demaurex, N. STIM1 knockdown reveals that store-operated Ca^{2+} channels located close to sarco/endoplasmic Ca^{2+} ATPases (SERCA) pumps silently refill the endoplasmic reticulum. *J. Biol. Chem.* **282,** 11456–11464 (2007).
11. Ozawa, K. *et al.* Ca^{2+}-dependent and Ca^{2+}-independent isozymes of protein kinase C mediate exocytosis in antigen-stimulated rat basophilic RBL-2H3 cells. Reconstitution of secretory responses with Ca^{2+} and purified isozymes in washed permeabilized cells. *J. Biol. Chem.* **268,** 1749–1756 (1993).
12. Deshpande, D. A. *et al.* PKC-dependent regulation of the receptor locus dominates functional consequences of cysteinyl leukotriene type 1 receptor activation. *FASEB J.* **21,** 2335–2342 (2007).
13. Bird, G. S. & Putney, J. W. J. Capacitative calcium entry supports calcium oscillations in human embryonic kidney cells. *J. Physiol.* **562,** 697–706 (2005).
14. Stauffer, T. P., Ahn, S. & Meyer, T. Receptor-induced transient reduction in plasma membrane $PtdIns(4,5)P_2$ concentration monitored in living cells. *Curr. Biol.* **8,** 343–346 (1998).
15. Parekh, A. B. & Putney, J. W. J. Store-operated calcium channels. *Physiol. Rev.* **85,** 757–810 (2005).
16. Zweifach, A. & Lewis, R. S. Rapid inactivation of depletion-activated calcium current (ICRAC) due to local calcium feedback. *J. Gen. Physiol.* **105,** 209–226 (1995).

17. Fierro, L. & Parekh, A. B. Fast calcium-dependent inactivation of calcium release-activated calcium current (CRAC) in RBL-1 cells. *J. Membr. Biol.* **168,** 9–17 (1999).
18. Zweifach, A. & Lewis, R. S. Slow calcium-dependent inactivation of depletion-activated calcium current. *J. Biol. Chem.* **270,** 14445–14451 (1995).
19. Parekh, A. B. Slow feedback inhibition of calcium release-activated calcium current by calcium entry. *J. Biol. Chem.* **273,** 14925–14932 (1998).
20. Takasaka, T., Kaku, Y. & Hozawa, K. Mast cell degranulation in nasal polyps. *Acta Otolaryngol. Suppl.* **430,** 39–48 (1986).
21. Ozawa, K., Yamada, K., Kazanietz, M. G., Blumberg, P. M. & Beaven, M. A. Different isozymes of protein kinase C mediate feedback inhibition of phospholipase C and stimulatory signals for exocytosis in RBL-2H3 cells. *J. Biol. Chem.* **268,** 2280–2283 (1993).
22. Razin, E., Szallasi, Z., Kazanietz, M. G., Blumberg, P. M. & Rivera, J. Protein kinases C-β and C-ε link the mast cell high-affinity receptor for IgE to the expression of c-fos and c-jun. *Proc. Natl Acad. Sci. USA* **91,** 7722–7726 (1994).
23. Kasai, H. & Petersen, O. H. Spatial dynamics of second messengers: IP_3 and cAMP as long-range and associative messengers. *Trends Neurosci.* **17,** 95–101 (1994).

Supplementary Information is linked to the online version of the paper at www.nature.com/nature.

Acknowledgements This work was supported by Medical Research Council grant support to A.B.P. S.-W. N. held a BBSRC-Glaxo-Smith-Kline studentship. We thank G. Miesenboeck and J. Putney for comments on the manuscript.

Author Contributions S.-W.N. performed and analysed Ca^{2+} measurements, RT–PCR, western blots and siRNA knockdown. D.B. performed and analysed patch-clamp recordings. C.N. carried out immunocytochemistry. R.M. helped with Ca^{2+} measurements. R.A. and G.B. supplied human nasal polyps. A.B.P. carried out some patch-clamp experiments, discussed the results, supervised the project and wrote the paper.

Author Information Reprints and permissions information is available at www.nature.com/reprints. The authors declare no competing financial interests. Readers are welcome to comment on the online version of this article at www.nature.com/nature. Correspondence and requests for materials should be addressed to A.B.P. (anant.parekh@dpag.ox.ac.uk).

LETTER

doi:10.1038/nature10743

Structures of cytochrome P450 17A1 with prostate cancer drugs abiraterone and TOK-001

Natasha M. DeVore[1] & Emily E. Scott[1]

Cytochrome P450 17A1 (also known as CYP17A1 and cytochrome P450c17) catalyses the biosynthesis of androgens in humans[1,2]. As prostate cancer cells proliferate in response to androgen steroids[2,3], CYP17A1 inhibition is a new strategy to prevent androgen synthesis and treat lethal metastatic castration-resistant prostate cancer[4], but drug development has been hampered by lack of information regarding the structure of CYP17A1. Here we report X-ray crystal structures of CYP17A1, which were obtained in the presence of either abiraterone, a first-in-class steroidal inhibitor recently approved by the US Food and Drug Administration for late-stage prostate cancer[5], or TOK-001, an inhibitor that is currently undergoing clinical trials[4,6]. Both of these inhibitors bind the haem iron, forming a 60° angle above the haem plane and packing against the central I helix with the 3β-OH interacting with aspargine 202 in the F helix. Notably, this binding mode differs substantially from those that are predicted by homology models and from steroids in other cytochrome P450 enzymes with known structures, and some features of this binding mode are more similar to steroid receptors. Whereas the overall structure of CYP17A1 provides a rationale for understanding many mutations that are found in patients with steroidogenic diseases, the active site reveals multiple steric and hydrogen bonding features that will facilitate a better understanding of the enzyme's dual hydroxylase and lyase catalytic capabilities and assist in rational drug design. Specifically, structure-based design is expected to aid development of inhibitors that bind only CYP17A1 and solely inhibit its androgen-generating lyase activity to improve treatment of prostate and other hormone-responsive cancers.

CYP17A1 is a membrane-bound dual-function monooxygenase with a critical role in the synthesis of many human steroid hormones[1]. The 17α-hydroxylase activity of CYP17A1 is required for the generation of glucocorticoids such as cortisol, but both the hydroxylase and 17,20-lyase activities of CYP17A1 are required for the production of androgenic and oestrogenic sex steroids (Supplementary Fig. 1). CYP17A1 is an important target for the treatment of breast and prostate cancers that proliferate in response to oestrogens and androgens[2,3]. In the absence of structural information, CYP17A1 inhibitors have been designed that are thought to bind the cytochrome P450 haem iron[4], but it has been difficult to rationalize or predict other structural features that are critical for effective and selective CYP17A1 inhibition. In addition, structural information is important for understanding 17-hydroxylase deficiencies and may also improve our understanding of polycystic ovary disease[2]. We determined the structures of human CYP17A1 when bound to two clinically relevant CYP17A1 inhibitors (Supplementary Fig. 2). Abiraterone is the active form of a prodrug that was recently approved by the US Food and Drug Administration for metastatic prostate cancer[5,6] and is under investigation for breast cancer[6]. TOK-001 is currently undergoing clinical trials for prostate cancer[4].

A truncated, His-tagged version of the human CYP17A1 protein was generated from a synthetic complementary DNA that was engineered to remove the single amino-terminal transmembrane helix, and this CYP17A1 was expressed in *Escherichia coli*. The resulting CYP17A1 was membrane bound and so it was solubilized with detergent before purification. This CYP17A1 binds abiraterone (17-(3-pyridyl)androsta-5,16-dien-3β-ol) (Fig. 1a) and TOK-001 (17-(1H-Benzimidazol-1-yl)androsta-5,16-dien-3β-ol) with decreases in absorbance at 402 nm and increases in absorbance at 424 nm, consistent with nitrogen binding to the haem iron (type II interaction) with dissociation constant (K_d) values of <100 nM (Fig. 1a, inset). Similar titrations with the substrates progesterone (Fig. 1b) and pregnenolone revealed decreases in absorbance at 419 nm and increases in absorbance at 385 nm, which is indicative of the ligand displacing water from the haem (type I interaction). CYP17A1 binds pregnenolone (K_d <100 nM) more tightly than progesterone (K_d 229 ± 14 nM; Fig. 1b, inset). We found that full-length enzyme[10] had a similar k_{cat} and three-fold higher Michaelis constant (k_{cat} 1.31 ± 0.03 min^{-1}, K_m 11.4 ± 0.7 μM) compared to the truncated form (k_{cat} 1.31 ± 0.03 min^{-1}, K_m 3.7 ± 0.3 μM). The half-maximum inhibitory concentration (IC_{50}) values for abiraterone (201 ± 1 nM) were lower than for TOK-001 (503 ± 1 nM) (Fig. 1c). Thus, truncated human CYP17A1 is a functional enzyme in terms of ligand binding, catalytic function and inhibition.

Both structures with abiraterone (2.6 Å) and TOK-001 (2.4 Å) demonstrate the characteristic cytochrome P450 fold (Fig. 2a) and have four very similar protein copies in each asymmetric unit

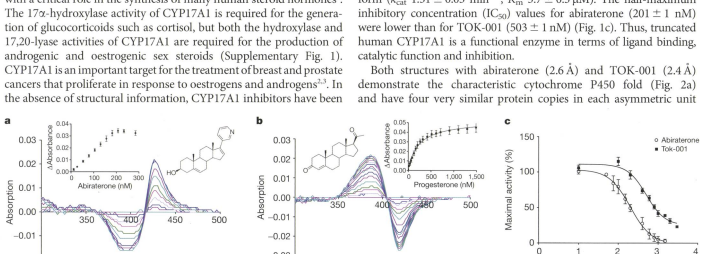

Figure 1 | Function of CYP17A1 and inhibition by clinical compounds. **a**, CYP17A1 titration with abiraterone (10–274 nM) yields progressive shifts in the ultraviolet–visible difference spectrum that indicate nitrogen binding to haem iron. **b**, Similar titration with progesterone (10–1535 nM) indicates water displacement from the haem iron. **c**, IC_{50} of abiraterone (circles) and TOK-001 (squares) for progesterone 17α-hydroxylation.

[1]Department of Medicinal Chemistry, 1251 Wescoe Hall Drive, University of Kansas, Lawrence, Kansas 66045, USA.

(Supplementary Table 1). Consistent with spectral binding data, abiraterone and TOK-001 bind with the nitrogen of the C17 pyridine or benzimidazole, respectively, forming a coordinate covalent bond with the haem iron (Fig. 2b, d). The steroidal cores of these inhibitors rise at an angle of 60° above the haem plane, directed between the F and G helices (Fig. 2b, d), and essentially overlap with each other (Fig. 2f). The unsubstituted α-face packs flat against the I helix where G301, A302 and adjacent residues form a highly complementary hydrophobic planar surface (Fig. 2b). The 3β-OH groups of abiraterone (Fig. 2b) and TOK-001 (Fig. 2d) hydrogen bond with N202 in the F helix (~2.6 Å and ~2.4 Å, respectively).

Although inhibitors occupy the majority of the enclosed active site, the void extends beyond these ligands in several directions. First, the active site wall nearest the inhibitor β-face is not as complementary to the steroid core as to the α-face. The C18 and C19 methyl groups project towards a crevice between the B′ helix, the β4 loop and the loop following the F helix (Fig. 2b). Only three side chains of the cavity wall come within 4 Å of C18 or C19. The cavity wall facing the β-face of abiraterone or TOK-001 is primarily lined with hydrophobic atoms of A105, S106, A113, F114, I206, L209, V236 and V482 (Fig. 2c), but there are two notable exceptions. R239 and D298 extend from the G and I helices, respectively, to orient their basic and acidic termini towards C6. These two polar side chains flank a substantial extension of the active site void adjacent to C6. Second, in the abiraterone structure there is unfilled space in the active site cavity adjacent to the pyridine ring bordered by V366, A367, I371 and V483 (Fig. 2c), and this volume is occupied by benzimidazole in the TOK-001 structure (Fig. 2e). Last, the most substantial active site cavity extension is from the 3β-OH of the inhibitors over the top of helix I and along the underside of helices F and G. This cavity is mostly lined by hydrophobic residues (I198, L243 and F300), but its 'roof' is bordered by several polar F and G helix residues (Y201, N202 and R239; Fig. 2c) that interact with, or are located near, water molecules in this region. The overall cavity containing TOK-001 is similar to that observed when abiraterone is bound, except that the available void volume over helix I is slightly smaller (Fig. 2e).

The single direct hydrogen bond between inhibitors and the protein is part of a larger hydrogen bonding network. In the abiraterone complex this network involves N202, E305, several conserved water molecules, R239, the backbone carbonyl of G297 and, in some molecules, Y201 (Fig. 3). Although Y201 is not within hydrogen bonding distance to these waters for molecules A and B, the side chain rotates slightly towards abiraterone in molecules C and D to interact with one or both of the water molecules. TOK-001 has a very similar hydrogen bonding network (Supplementary Fig. 3). These interactions are strongly reminiscent of the interactions that are conserved in the androgen, oestrogen, glucocorticoid, mineralocorticoid and progesterone receptors[11] (Fig. 4a, b). In each receptor, the 3β-OH or 3-keto group of steroids binds within a deep receptor pocket and forms hydrogen bonds with a glutamine or glutamate, an arginine and often a conserved water

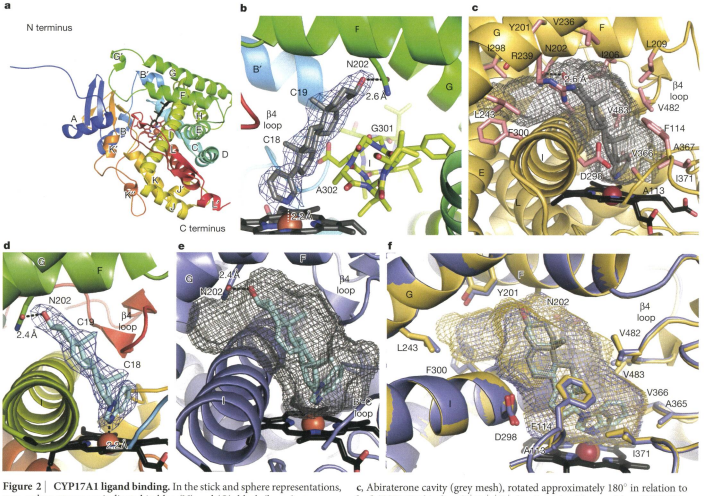

Figure 2 | CYP17A1 ligand binding. In the stick and sphere representations, non-carbon atoms are indicated in blue (N), red (O), black (haem), grey (abiraterone), cyan (TOK-001) and by a dark red sphere (Fe). **a**, A coloured representation of the CYP17A1–abiraterone structure, from the N terminus (blue) to the C terminus (red). **b**, Abiraterone binds ($2|F_o|-|F_c|$ density at 1σ; blue mesh) at an angle of approximately 60° from haem against helix I (yellow). **c**, Abiraterone cavity (grey mesh), rotated approximately 180° in relation to **b**. **d**, TOK-001 binding ($2|F_o|-|F_c|$ density at 1σ, blue mesh). **e**, TOK-001 cavity (grey mesh). **f**, Abiraterone structure (yellow) superimposed on TOK-001 structure (purple) with respective voids (mesh). The B′ helix has been removed from panels **c**–**f** so that it is possible to view the ligands.

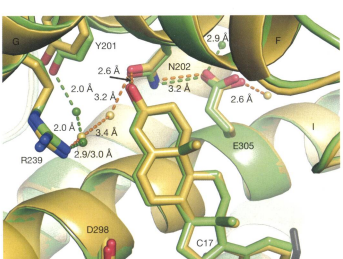

Figure 3 | Hydrogen bond network with abiraterone. CYP17A1 has a hydrogen bonding network at the top of the active site that interacts with abiraterone. Molecules A and B (yellow), and C and D (green) have slightly different networks, with the main difference being the involvement of Y201. Water molecules are indicated by small spheres. Hydrogen bonds are represented by dashed lines and the distances between them are indicated.

molecule. These interactions are critical for ligand recognition by hormone receptors[12] and may also contribute to CYP17A1 selectivity for pregnenolone, progesterone and their 17α-hydroxy derivatives. Notably, TOK-001 is both a CYP17A1 inhibitor and androgen receptor antagonist[13], and the similarity of these binding modes is probably the reason for this dual mechanism of action.

Orientations of the native CYP17A1 substrates are of substantial value in understanding the function of this enzyme. Pregnenolone and progesterone were docked into the CYP17A1–abiraterone structure modelled as the Fe(IV)=O (compound I) catalytic state. Progesterone maintained the N202 hydrogen bond. The distances from C17 and C16 to the catalytic oxygen were 3.7 Å and 3.9 Å, respectively, distances that are consistent with the experimentally observed major 17α-OH and minor 16α-OH progesterone metabolites. The pregnenolone 3β-OH hydrogen was also bonded to N202 and the C17 atom was 3.6 Å from the Compound I oxygen (Supplementary Fig. 4). However, the active site topology may be altered in the presence of substrates and this is an important area for further investigation.

CYP17A1 can be compared to three other P450 enzymes that are involved in steroidogenesis or cholesterol metabolism with reported steroid complex structures: CYP19A1 (aromatase)[14], CYP11A1 (cholesterol side-chain cleavage enzyme)[15] and CYP46A1, a cholesterol 24-hydroxylase[16]. Although all four enzymes maintain the canonical cytochrome P450 fold, CYP19A1, CYP11A1 and CYP46A1 orient steroids in the opposite direction from CYP17A1 so that the steroid ligands are positioned over the K–L loop directed towards the β1 sheet (as shown for CYP11A1 in Fig. 4c) instead of oriented towards helices F and G.

More than 50 CYP17A1 mutations have been identified, and most of these were identified in patients with 17-hydroxylase deficiencies. The biochemical effects of many clinical mutations can be rationalized by examining the CYP17A1 structure (Supplementary Fig. 5 and Supplementary Table 2). Mutations R96W, R125Q, H373D/N and R440H/C all alter residues that directly interact with the haem propionates and probably disrupt haem binding, resulting in the complete loss of activity that was observed[17–22]. Mutations E305G, R347H/C, R358Q and R449A eliminate only the lyase activity of CYP17A1[23–25]. E305 forms a hydrogen bond to N202 in the active site, indicating a role in substrate positioning, whereas the other residues are on the proximal face of the protein (Supplementary Fig. 5), and this is consistent with their proposed role in cytochrome b_5 binding[23,26], which promotes lyase activity. Finally, reduction of the minor 16α-hydroxyprogesterone metabolite is reported for the artificial mutation A105L[27], consistent with its location in the active site facing the β-face where the additional bulk may reduce the steroid movement within the active site.

Abiraterone and TOK-001 have several features that make them effective inhibitors of CYP17A1: first, a heterocyclic nitrogen that coordinates to the haem iron; second, a planar α-face to pack against the I helix; and third, hydrogen bonding interactions of 3β-OH with conserved polar residues in a hydrogen binding network. These structures provide a model for the binding of substrates and other inhibitors that is very different from binding orientations that have previously been proposed by homology modelling and docking studies and from structures that have been demonstrated in other steroid-metabolizing cytochrome P450 enzymes. Perhaps most importantly, the cavity that is observed is not bilobed as predicted by many modelling studies[28,29]. CYP17A1 interactions with these inhibitors are instead more reminiscent of steroid binding to steroid receptors, and this may be the origin of the TOK-001 dual mechanism of action. Thus, these structures contribute to a better understanding of the function and inhibition of CYP17A1 in a way that should substantially benefit the apprehension of enzyme dysfunction in clinical disease and enable structure-based drug design of CYP17A1 inhibitors for treating hormone-responsive cancers, particularly prostate cancer.

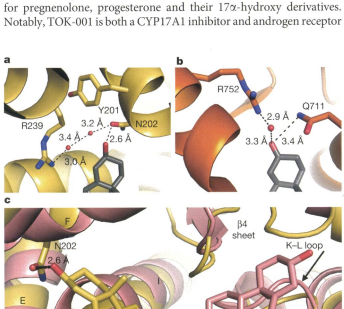

Figure 4 | CYP17A1 compared to the androgen receptor and CYP11A1. **a**, The hydrogen bonding network near the abiraterone 3β-OH involves N202, R239 and conserved waters. **b**, The androgen receptor (PDB 3L3X) has a similar hydrogen bond network with R752, Q711 and several waters that interact with the dihydrotestosterone ketone. **c**, The structure of CYP17A1 with abiraterone (yellow) superimposed on the structure of CYP11A1 with 20,22-dihydroxycholesterol (PDB 3NA0, pink). This shows that there are markedly different steroid orientations between the two structures.

METHODS SUMMARY

A synthetic cDNA for human CYP17A1 was modified to delete residues 2–19, substitute the hydrophilic sequence Arg 20-Arg 21-Cys 22-Pro 23 with Ala 20-Lys 21-Lys 22-Thr 23 and add a carboxy-terminal four-histidine tag (Supplementary Fig. 6) before cloning into the pCWori$^+$ plasmid and overexpression in *Escherichia*

coli JM109 cells. Protein was purified by nickel affinity, cation exchange and size exclusion chromatography. Abiraterone was synthesized (see Methods). Binding affinities were determined using an ultraviolet–visible spectral shift assay. Progesterone 17α-hydroxylation was evaluated using HPLC separation and ultraviolet detection. For crystallography, inhibitors were included throughout purification. Crystals were grown from CYP17A1 (30 mg ml^{-1}) complexed with inhibitor using hanging-drop vapour diffusion to equilibrate against 30% PEG 3350, 0.175 M Tris, pH 8.5, 0.30 M ammonium sulphate and 3% glycerol. Diffraction data were collected and phased by molecular replacement. Iterative model building and refinement generated the final model. Substrates were docked using Surflex-Dock.

Full Methods and any associated references are available in the online version of the paper at www.nature.com/nature.

Received 12 May; accepted 30 November 2011.
Published online 22 January 2012.

1. Miller, W. L. & Auchus, R. J. The molecular biology, biochemistry, and physiology of human steroidogenesis and its disorders. *Endocr. Rev.* **32,** 81–151 (2011).
2. Attard, G., Reid, A. H., Olmos, D. & de Bono, J. S. Antitumor activity with CYP17 blockade indicates that castration-resistant prostate cancer frequently remains hormone driven. *Cancer Res.* **69,** 4937–4940 (2009).
3. Yap, T. A., Carden, C. P., Attard, G. & de Bono, J. S. Targeting CYP17: Established and novel approaches in prostate cancer. *Curr. Opin. Pharmacol.* **8,** 449–457 (2008).
4. Vasaitis, T. S., Bruno, R. D. & Njar, V. C. CYP17 inhibitors for prostate cancer therapy. *J. Steroid Biochem. Mol. Biol.* **125,** 23–31 (2011).
5. de Bono, J. S. *et al.* Abiraterone and increased survival in metastatic prostate cancer. *N. Engl. J. Med.* **364,** 1995–2005 (2011).
6. Molina, A. & Belldegrun, A. Novel therapeutic strategies for castration resistant prostate cancer: inhibition of persistent androgen production and androgen receptor mediated signaling. *J. Urol.* **185,** 787–794 (2011).
7. Auchus, R. J., Geller, D. H., Lee, T. C. & Miller, W. L. The regulation of human P450c17 activity: relationship to premature adrenarche, insulin resistance and the polycystic ovary syndrome. *Trends Endocrinol. Metab.* **9,** 47–50 (1998).
8. Attard, G. *et al.* Phase I clinical trial of a selective inhibitor of CYP17, abiraterone acetate, confirms that castration-resistant prostate cancer commonly remains hormone driven. *J. Clin. Oncol.* **26,** 4563–4571 (2008).
9. Brodie, A., Njar, V., Macedo, L. F., Vasaitis, T. S. & Sabnis, G. The Coffey Lecture: steroidogenic enzyme inhibitors and hormone dependent cancer. *Urol. Oncol.* **27,** 53–63 (2009).
10. Imai, T. *et al.* Expression and purification of functional human 17α-hydroxylase/17,20-lyase (P450c17) in *Escherichia coli*. Use of this system for study of a novel form of combined 17α-hydroxylase/17,20-lyase deficiency. *J. Biol. Chem.* **268,** 19681–19689 (1993).
11. Huang, P., Chandra, V. & Rastinejad, F. Structural overview of the nuclear receptor superfamily: insights into physiology and therapeutics. *Annu. Rev. Physiol.* **72,** 247–272 (2010).
12. Pereira de Jésus-Tran, K. *et al.* Comparison of crystal structures of human androgen receptor ligand-binding domain complexed with various agonists reveals molecular determinants responsible for binding affinity. *Protein Sci.* **15,** 987–999 (2006).
13. Vasaitis, T. *et al.* Androgen receptor inactivation contributes to antitumor efficacy of 17α-hydroxylase/17,20-lyase inhibitor 3β-hydroxy-17-(1H-benzimidazole-1-yl)androsta-5,16-diene in prostate cancer. *Mol. Cancer Ther.* **7,** 2348–2357 (2008).
14. Ghosh, D., Griswold, J., Erman, M. & Pangborn, W. Structural basis for androgen specificity and oestrogen synthesis in human aromatase. *Nature* **457,** 219–223 (2009).
15. Mast, N. *et al.* Structural basis for three-step sequential catalysis by the cholesterol side chain cleavage enzyme CYP11A1. *J. Biol. Chem.* **286,** 5607–5613 (2011).
16. Mast, N. *et al.* Crystal structures of substrate-bound and substrate-free cytochrome P450 46A1, the principal cholesterol hydroxylase in the brain. *Proc. Natl Acad. Sci. USA* **105,** 9546–9551 (2008).
17. Dhir, V. *et al.* Steroid 17α-hydroxylase deficiency: Functional characterization of four mutations (A174E, V178D, R440C, L465P) in the CYP17A1 gene. *J. Clin. Endocrinol. Metab.* **94,** 3058–3064 (2009).
18. Rosa, S. *et al.* Clinical, genetic and functional characteristics of three novel CYP17A1 mutations causing combined 17α-hydroxylase/17,20-lyase deficiency. *Horm. Res. Paediatr.* **73,** 198–204 (2010).
19. Katsumata, N., Ogawa, E., Fujiwara, I. & Fujikura, K. Novel CYP17A1 mutation in a Japanese patient with combined 17α-hydroxylase/17,20-lyase deficiency. *Metabolism* **59,** 275–278 (2010).
20. Ergun-Longmire, B. *et al.* Two novel mutations found in a patient with 17α-hydroxylase enzyme deficiency. *J. Clin. Endocrinol. Metab.* **91,** 4179–4182 (2006).
21. Sahakitrungruang, T., Tee, M. K., Speiser, P. W. & Miller, W. L. Novel P450c17 mutation H373D causing combined 17α-hydroxylase/17,20-lyase deficiency. *J. Clin. Endocrinol. Metab.* **94,** 3089–3092 (2009).
22. Biason-Lauber, A. *et al.* 17α-hydroxylase/17,20-lyase deficiency as a model to study enzymatic activity regulation: role of phosphorylation. *J. Clin. Endocrinol. Metab.* **85,** 1226–1231 (2000).
23. Lee-Robichaud, P. *et al.* The cationic charges on Arg347, Arg358 and Arg449 of human cytochrome P450c17 (CYP17) are essential for the enzyme's cytochrome b_5-dependent acyl-carbon cleavage activities. *J. Steroid Biochem. Mol. Biol.* **92,** 119–130 (2004).
24. Gupta, M. K., Geller, D. H. & Auchus, R. J. Pitfalls in characterizing P450c17 mutations associated with isolated 17,20-lyase deficiency. *J. Clin. Endocrinol. Metab.* **86,** 4416–4423 (2001).
25. Tiosano, D. *et al.* Metabolic evidence for impaired 17α-hydroxylase activity in a kindred bearing the E305G mutation for isolate 17,20-lyase activity. *Eur. J. Endocrinol.* **158,** 385–392 (2008).
26. Auchus, R. J., Lee, T. C. & Miller, W. L. Cytochrome b_5 augments the 17,20-lyase activity of human P450c17 without direct electron transfer. *J. Biol. Chem.* **273,** 3158–3165 (1998).
27. Swart, A. C., Storbeck, K. H. & Swart, P. A single amino acid residue, Ala 105, confers 16α-hydroxylase activity to human cytochrome P450 17α-hydroxylase/17,20 lyase. *J. Steroid Biochem. Mol. Biol.* **119,** 112–120 (2010).
28. Haider, S. M., Patel, J. S., Poojari, C. S. & Neidle, S. Molecular modeling on inhibitor complexes and active-site dynamics of cytochrome P450 C17, a target for prostate cancer therapy. *J. Mol. Biol.* **400,** 1078–1098 (2010).
29. Jagusch, C. *et al.* Synthesis, biological evaluation and molecular modelling studies of methylenimidazole substituted biaryls as inhibitors of human 17α-hydroxylase-17,20-lyase (CYP17). Part I: heterocyclic modifications of the core structure. *Bioorg. Med. Chem.* **16,** 1992–2010 (2008).

Supplementary Information is linked to the online version of the paper at www.nature.com/nature.

Acknowledgements X-ray data were collected at the Stanford Synchrotron Radiation Lightsource (SSRL). The SSRL Structural Molecular Biology Program is supported by the US Department of Energy Office of Biological and Environmental Research and by the US National Institutes of Health (NIH), National Center for Research Resources, Biomedical Technology Program and the National Institute of General Medical Sciences. We thank C.-J. Liu and the University of Kansas (KU) Center of Biomedical Research Excellence (COBRE) Center for Cancer Experimental Therapeutics for synthesizing abiraterone (NIH RR030926), M. R. Waterman for the full-length CYP17A1 construct, J. Wang for assistance with the Fe(v)=O construct used in docking and A. Skinner and J. Aubé for manuscript suggestions. This research was funded by the NIH through the KU COBRE Center for Protein Structure and Function (NIH RR17708) and GM076343.

Author Contributions N.M.D. engineered, expressed, characterized, purified and crystallized CYP17A1 under the direction of E.E.S. N.M.D. and E.E.S. jointly performed X-ray diffraction experiments, solved and refined the structures, and wrote the manuscript. N.M.D. performed the docking studies of CYP17A1.

Author Information Atomic coordinates and structure factors for the reported crystal structures have been deposited with the Protein Data Bank under the accession codes 3RUK for CYP17A1 with abiraterone and 3SWZ for CYP17A1 with TOK-001. Reprints and permissions information is available at www.nature.com/reprints. The authors declare no competing financial interests. Readers are welcome to comment on the online version of this article at www.nature.com/nature. Correspondence and requests for materials should be addressed to E.E.S. (eescott@ku.edu).

CORRECTIONS & AMENDMENTS

CORRIGENDUM

doi:10.1038/nature10817

The unusual γ-ray burst GRB 101225A from a helium star/neutron star merger at redshift 0.33

C. C. Thöne, A. de Ugarte Postigo, C. L. Fryer, K. L. Page, J. Gorosabel, M. A. Aloy, D. A. Perley, C. Kouveliotou, H. T. Janka, P. Mimica, J. L. Racusin, H. Krimm, J. Cummings, S. R. Oates, S. T. Holland, M. H. Siegel, M. De Pasquale, E. Sonbas, M. Im, W.-K. Park, D. A. Kann, S. Guziy, L. Hernández García, A. Llorente, K. Bundy, C. Choi, H. Jeong, H. Korhonen, P. Kubánek, J. Lim, A. Moskvitin, T. Muñoz-Darias, S. Pak & I. Parrish

Nature **480**, 72–74 (2011).

The Acknowledgements of this Letter should have included the following line: "We thank A. J. Castro-Tirado for help in obtaining the data from the BTA 6-m telescope and comments on an early draft." This has been added to the PDF and HTML versions online.

CORRIGENDUM

doi:10.1038/nature10788

A reserve stem cell population in small intestine renders *Lgr5*-positive cells dispensable

Hua Tian, Brian Biehs, Søren Warming, Kevin G. Leong, Linda Rangell, Ophir D. Klein & Frederic J. de Sauvage

Nature **478**, 255–259 (2011).

In this Letter, two additional references[32,33], which described stem-cell organization in the intestinal crypt, should have been cited after the first sentence of the main text: "Two types of stem cells have been described in the small intestine based on location and cycling dynamics[1–4,32,33]." The references and their citations have been added to the PDF and HTML versions.

32. Potten, C. S., Gandara, R., Mahida, Y. R., Loeffler, M. & Wright, N. A. The stem cells of small intestinal crypts: where are they? *Cell Prolif.* **42**, 731–750 (2009).
33. Bjerknes, M. & Cheng, H. The stem-cell zone of the small intestinal epithelium. I. Evidence from Paneth cells in the adult mouse. *Am. J. Anat.* **160**, 51–63 (1981).

CAREERS

TURNING POINT Bioinformatician's career benefits from good timing **p.123**

NON-PROFIT SECTOR Despite job growth, research posts are under pressure **p.123**

NATUREJOBS For the latest career listings and advice **www.naturejobs.com**

COLUMN

Global collaboration

Mastering scientific protocols is only half the battle when it comes to conducting a clinical study in another country, says **Andrew Fung**.

In 2010, I began work on a project to create a new type of malaria test. I wanted to diagnose the disease using saliva, with an inexpensive test that looked, felt and tasted like chewing gum, rather than through the conventional blood sample. I had first proposed the idea in an effort to impress at an interview for a postdoctoral position. To my great delight, it gained funding from the Grand Challenges Explorations programme of the Bill & Melinda Gates Foundation in Seattle, Washington. I was aiming to land a job designing medical devices, but ended up with a grant for a blue-skies idea.

Had I bitten off more than I could chew? I was a postdoc at the University of California, Los Angeles (UCLA), at the time, and Los Angeles has few malaria patients. How would I confirm the prevalence of the malaria-causing parasite's proteins in saliva? I would have to go overseas and, crucially, I would have to build a collaborative group of experts whose skills complemented my own.

Successfully managing this collaborative, international clinical study required not only the right team, but also careful planning, dealing with regulations and adapting to unexpected circumstances in a different culture. I learned that it takes more than a creative idea and bench experience to guide a project to its intended destination.

ASSEMBLE RESEARCH ALLIES

I had training in protein detection, an essential skill for analysing samples in the field, but needed help to run a clinical study in a malaria-endemic region. A friend and mentor — Theodore Moore, the clinical director of the Pediatric Blood and Marrow Transplant Program at UCLA — shared my interest in making new medical tools for developing communities. In 1989, as a senior medical student, Moore had started to volunteer for relief efforts around the world. He ended up training medical professionals in countries from southern Africa to the Middle East. I wanted Moore on the team because of his professional expertise and his sympathy for the cause.

BELLE MELLOR

I also needed access to malaria patients, and a partner to handle field operations. During Moore's medical missions in the Philippines, he had befriended just the right person: Daniel Horton, then administrator of the Palawan Baptist Hospital (PBH), which he had helped to establish. During his 36 years in rural Palawan, the province with the highest incidence of malaria in the Philippines, Horton had seen more malaria patients than he could remember. He knew how to improvise under unexpected conditions, and could help us to navigate the local culture. Moore and Horton had ▶

▶ strengths in areas that were my weaknesses.

At our kick-off meeting, we agreed on the objectives and timeline of our work, drawing up an overall strategy and specific contingency plans. This is the best time to flag up foreseeable disruptions, address potential ethical problems and agree on how to share data and intellectual property. In our case, setting a general order of authorship before pouring effort into the collaborative melting pot gave us a smooth working relationship, free from surprise competition.

My advice is to make sure that the group meets in person before you start, especially if lead members haven't worked together before. Moore was familiar with the PBH and UCLA and coordinated all our efforts, but I didn't meet Horton or his team until we arrived in Palawan for the fieldwork. A pre-emptive visit to the hospital would have helped us to spot some lurking problems with site logistics and the availability of lab ware. Teleconferences should be saved for short communications and status updates.

ADAPT YOUR MATERIALS AND METHODS

When researchers are working internationally, experimental methods need to be adapted to the infrastructure of the host facility. For example, our original protocols recommended storing saliva at −80 °C. But ultra-low-temperature freezers weren't an option at the PBH, which has public electricity for just half the day, so we redesigned our approach to use a domestic freezer. Horton's researchers at the PBH also refitted their lab with a combination of electrical outlets at 120 volts and 220 volts so that we could use equipment from the United States in their hospital.

The climate affected our materials and processes. Reactions at room temperature have an entirely different behaviour in a tropical environment at 34 °C than in one where the normal temperature is around 25 °C. By using dry reagents stored in a desiccator, we kept protocols portable and stable. Because we would eventually transfer those protocols to Horton's team, we got other operators to reproduce our experiments in a few different labs, to anticipate possible hiccups.

"International partnerships are as much about people as they are about science."

Some basic materials may be difficult to find abroad. The hospital ended up stocking 40 litres of distilled water just for our chemicals, much more than they typically kept on hand. Will your reagents need a low-temperature supply chain? Team members who flew from Los Angeles carried perishable reagents in temperature-controlled boxes in checked baggage. At the PBH, we crushed ice to keep our working samples chilled using a domestic appliance for making halo-halo, a local fruit dessert.

Timing and logistics were crucial. Although my grant lasted for one year, the seasonal nature of malaria gave us only three months in which to collect samples. Early on, we ruled out shipping specimens from the Philippines to the United States for analysis, because of the high cost and legal barriers. That meant we had to transport chemicals and instruments overseas for fieldwork. Whether you choose to travel with these materials as passenger baggage or to ship them ahead as cargo, arranging their passage can be less than straightforward.

Customs carnets can be very convenient documents for arranging temporary import of scientific equipment: they act as merchandise passports, allowing simplified, tax-free customs procedures. Unfortunately, many countries, including the Philippines, do not accept carnets.

To find the best alternative, we sought guidance from a logistics officer for the International Medical Corps, a global organization for humanitarian relief based in Santa Monica, California. He made sure that we prepared meticulous packing lists and an official letter of intent designating our materials solely for academic research. By being detailed about what we were shipping and clear about our purpose, we could apply for authorization to import before we arranged for transit.

Because the PBH was not a licensed importer, we had to work with a door-to-door international forwarder and its clearing agent in Manila. The agent caught us off guard with a very high and unjustified quote for customs handling and brokerage. But with help from a friend who was chief customs officer in Manila, we ended up with a proper quote at a fraction of the original fee, and a personal escort through airport customs. Whatever import method you choose, you should make sure that you know what to expect at customs clearance in every country you have to go through. To avoid falling victim to price gouging, get quotes from more than one vendor. If anything seems grossly out of place, someone is probably not complying with local laws.

REGULATORY CHALLENGES

Logistics will get your boxes onto site, but the work that the scientists do there will be governed by myriad regulations. International collaborations involving clinical medical research require oversight from multiple institutional review boards (IRBs) charged with the protection of human subjects. Each review board has specific requirements for the protocol and consent forms.

To learn how to get through this often long and iterative process of approval most efficiently, Moore met with representatives from the IRBs of both UCLA and the PBH, as well as other experienced investigators. They explained best practice for international collaborations — cooperating with local government, upholding the institutions' integrity, writing protocols to prioritize patient safety — and aspects unique to UCLA. By working with the decision-makers from the start, we got protocols approved on the first pass.

Sometimes institutional approval isn't enough. Make sure to include local-government officials in your regulatory team, to head off authorities who may scrutinize your project for financial gain. As we prepared to enrol our first patients at the PBH, a member of a Philippines environmental and cultural heritage group told Horton that the study needed its permission to proceed, implying that a bribe of some sort was necessary. We felt our collective arm being twisted.

"In research, as in health, an ounce of prevention is worth a pound of cure."

Moore had already sent information about our study to Abraham Mitra, the governor of Palawan. When he and Horton sat down in Mitra's office and explained our circumstances, the governor was taken aback. "This is about malaria," he said. "What does it have to do with the environment?" A phone call was made and the problem evaporated. With written endorsement from the Provincial Health Office, we were clear of further regulatory obstacles. It never hurts to have friends inside the system.

WATCH OUT FOR UNEXPECTED TWISTS

In research, as in health, remember that an ounce of prevention is worth a pound of cure. Nevertheless, no amount of risk management — whether pertaining to technical uncertainty, complex logistics or impenetrable regulations — guarantees a smooth operation. We experienced some extra bumps first hand.

The oil company Pilipinas Shell Petroleum has operations in Palawan, and its social-development arm had partnered with the provincial government from 1999 onwards to launch a major anti-malaria campaign. Just before our study, their programme increased insecticide spraying, distributed bed nets and opened a new central clinic not far from the PBH. The timing of these interventions markedly reduced the number of malaria cases seen at the PBH, which could have jeopardized the project. We had to extend the enrolment period by several months to get enough people for our pilot study, and still ended up with fewer than we had expected.

International partnerships are as much about people as they are about science. They open unique avenues for discovery by empowering scientists to explore beyond their accustomed borders. So above all, enjoy the adventure. Granted, it is a risky enterprise, but one full of professional reward and personal satisfaction. ■

Andrew Fung *is a postdoc in the electrical and computer engineering department at the University of Waterloo in Ontario, Canada.*

TURNING POINT
Ewan Birney

EMBL-EBI

Ewan Birney helped to assemble the genetic database for the international Human Genome Project. In April, he will become an associate director at the European Molecular Biology Laboratory's European Bioinformatics Institute (EBI) in Hinxton, UK, where he has worked since 2000.

How did you launch your scientific career?
I was always drawn to biology. I went to Eton College, UK, a secondary school that has links with Cold Spring Harbor Laboratory (CSHL) in New York. Between school and university, it is traditional in England to take a 'gap year'. So I did an internship at the CSHL, which had a big effect on me. Working at an institution headed by James Watson, one of the key people involved in deciphering the structure of DNA, was probably one of the biggest reasons I went into science.

Describe the most significant turning point in your career.
I was a graduate student at the Wellcome Trust Sanger Institute in Hinxton, and was involved in the Human Genome Project from 1999 to 2000, when everything went crazy because of the competition between public and private efforts to sequence the genome. There was a constant push to release results. The Sanger was a major sequencing centre, and I had to grow up scientifically very quickly — learning to solve problems and get results — on account of the pace of discovery and the constant changes in technology. I effectively skipped the postdoc phase. I am sure I will never experience an atmosphere like that again. It was intensely demanding: every two weeks the team needed to create a new tool, or provide key information to show that we were on top of things.

What was your biggest accomplishment there?
In the final push of the Human Genome Project in 2000, we created Ensembl, a web browser for genetic information. We worked like idiots for two years to develop it. A huge amount of what we did fell on a few people who could understand databases and bioinformatics. Ensembl now holds genetic information from more than 60 species and a lot of tools for analysis — all freely available.

What will be your managerial focus at the EBI?
In 2006 I handed off Ensembl, because at some point, you have to trust people to improve what you've begun. It is wrenching to let go of something you've helped to create. But you have to if you want it to live. That requires a lot of coaching and mentoring of those taking over the project. Hiring excellent people, setting up situations for them to succeed in and coaching and mentoring them will be key parts of my new position.

How did you come to bioinformatics?
Bioinformatics is just a word to describe part of modern data-intensive molecular biology. Ever since a senior scientist advised me to learn the C programming language when I was at the CSHL, I've used whatever methods or tools I can find. Very early on, I adapted a programme to scan databases of expressed sequence tags, short bits of DNA that help to identify genes. I continue to teach myself programming and statistics. In general, I think about what problems I would like to address, what theories are out there and what computational or mathematical approaches might work. For instance, some colleagues mentioned that combinatorial mathematics might be a good way to understand genome assembly. At first I didn't understand how, but I finally got it, then went back to the maths textbooks and refined my approach.

What's the secret of your success?
I just really enjoy doing science. And that has helped me to get through some difficult times, when I've pushed myself and others perhaps too hard. The other thing that leads to success is trusting collaborators and the people you hire; I think that, often, we don't put enough trust in the scientists around us and it hinders progress. I am very lucky to be a part of the EBI and to be moving into such a central role. I enjoy nearly everything about it — although there are one or two meetings I could do without. ■

INTERVIEW BY PAUL SMAGLIK

CANADA

Pension values shrink

Some Canadian academics will have to increase contributions to their pension plans as a consequence of the recession, says the Canadian Association of University Teachers (CAUT) in Ottawa, which represents faculty members at about 70 public institutions. Neil Tudiver, CAUT's assistant executive director of collective bargaining, says that the economic downturn has decreased the value of faculty pension accounts. Provincial regulations call for reductions to public universities' costs, forcing institutions to consider plan adjustments to make up the shortfall. Tudiver says that pension contributions for affected plans will rise by 2% on average.

NON-PROFIT SECTOR

Uncertain prospects

Tightening of federal support for US science is creating a mixed employment outlook for academic researchers, says the author of *Holding the Fort: Nonprofit Employment during a Decade of Turmoil*. The report, released on 18 January, found that employment in the US non-profit sector grew by an average of 2.1% each year from 2000 to 2010, despite the recession; growth in education alone was 2.6%. Although universities and health care saw some of the biggest job increases, a slowdown in federal funding is placing a strain on academic research, suggests Lester Salamon, a policy expert at Johns Hopkins University in Baltimore, Maryland, and lead author of the report. Salamon predicts a shift to private sources of research funding, including industry.

UNITED STATES

Postdoc stipend grows

For the second year running, postdocs funded through US National Institutes of Health (NIH) traineeships will receive a 2% stipend increase. In 2011, 6,686 postdocs received the stipend. The NIH announced the increase on 20 January for trainees — including undergraduates, PhD students and postdocs — who receive the Ruth L. Kirschstein National Research Service Award (NRSA). Entry-level NRSA stipends still fall short of the US$45,000 advocated by the US National Postdoc Association (NPA) in Washington DC; last year, an informal NPA survey of 74 US institutions found that 35 of them base their postdoc salaries on the NRSA, which increased by 1% in 2010.

naturejobs

European Head Office, London naturejobs@nature.com

The Macmillan Building, 4 Crinan Street, London N1 9XW, UK
Tel: +44 (0) 20 7843 4961 Fax: +44 (0) 20 7843 4996

European Manager:
Nils Moeller, +44 (0) 20 7843 4953 n.moeller@nature.com

Southwest UK/RoW:
Emma Hare, +44 (0) 20 7843 4944 e.hare@nature.com

Northeast UK/Ireland:
Matthew Ward, +44 (0) 20 7014 4059 m.ward@nature.com

France/Switzerland/Belgium:
Julie Aramburu, +44 (0) 20 7843 4994 j.aramburu@nature.com

Scandinavia/Spain/Portugal/Italy:
Megan Ball, +44 (0) 20 7843 4973 m.ball@nature.com

North Germany/The Netherlands/Eastern Europe:
Kristin Doelling, +44 (0) 20 7843 4970 k.doelling@nature.com

South Germany/Austria:
Maria Kubalova, +44 (0) 20 7014 4084 m.kubalova@nature.com

Natureevents:
Matthew Clare, +44 (0) 20 7014 4015 m.clare@nature.com

Business Development Manager, Middle East:
Jon Giuliani, +44 (0) 20 7843 4922 j.giuliani@nature.com

USA Head Office, New York naturejobs@us.nature.com

75 Varick Street, 9th Floor, New York, NY 10013-1917
Tel: +1 800 989 7718 Fax: +1 800 989 7103

US Sales Manager:
Ken Finnegan, +1 212 726 9248 k.finnegan@us.nature.com

Japan Head Office, Tokyo

Chiyoda Building, 2–37 Ichigayatamachi, Shinjuku-ku, Tokyo 162-0843
Tel: +81 3 3267 8751, Fax: +81 3 3267 8746

Asia-Pacific Sales & Business Development Manager:
Yuki Fujiwara, +81-3-3267-8765 y.fujiwara@natureasia.com

Business Development Manager, Greater China/Singapore:
Gloria To, +852 2811 7191 g.to@natureasia.com

India

3a, 4th Floor, DLF Corporate Park, Gurgaon, 122 002, India

Advertisement Sales:
Vikas Chawla, +91 1242881057 v.chawla@nature.com

THE CHINESE UNIVERSITY OF HONG KONG

Dean of the Faculty of Science

Founded in 1963, The Chinese University of Hong Kong is a forward-looking and vibrant university, aspiring to be acknowledged regionally and internationally as a first-class comprehensive research university. With a team of over 2,000 full-time teaching and research staff, the University offers a broad spectrum of programmes up to PhD level in various disciplines organized under eight Faculties (viz. Arts, Business Administration, Education, Engineering, Law, Medicine, Science and Social Science). In 2011-12, undergraduate and postgraduate enrolment in publicly-funded programmes reaches 11,300 and 3,100 respectively (*http://www.cuhk.edu.hk*).

The Faculty of Science comprises four Departments: Chemistry, Mathematics, Physics, and Statistics, and two Schools: Chinese Medicine and Life Sciences, and also offers a number of multidisciplinary and interfaculty programmes. The Faculty has 300 full-time teaching and research staff, 1,740 undergraduate students and more than 490 postgraduate research students. Detailed information on the Faculty is available at *http://www.cuhk.edu.hk/sci/*.

The University now invites applications and nominations of qualified candidates for the Deanship of the Faculty. The Dean will be a member of the University senior management team reporting to the University Council via the Vice-Chancellor/President or the Provost. As the academic and executive head of the Faculty, the Dean will provide academic leadership and discharge administrative responsibilities in respect of academic, staff, financial and student matters.

Candidates should be academics with established scholarship appropriate for appointment at Professor level in an academic department, with an appreciation of the breadth of research and educational developments in the fields relevant to the Faculty. They should have demonstrated capability for academic leadership and management at an appropriate level in higher education institutions, long-term vision for the development of the Faculty, and excellent interpersonal and communication skills.

Salary and fringe benefits for the post will be highly competitive, commensurate with qualifications and experience.

Please send applications/nominations under confidential cover, with the post marked, to the Search Committee for the Dean of the Faculty of Science, c/o Provost's Office, The Chinese University of Hong Kong, Shatin, N.T., Hong Kong [fax: (852) 3943 1462; e-mail: *SCDeanship-Sc@aab.cuhk.edu.hk*]. All applications/nominations will be treated in strict confidence. The Personal Information Collection Statement will be provided upon request.

Consideration of applications/nominations will continue until the post is filled. The University reserves the right to fill the post by invitation.

JP221263R

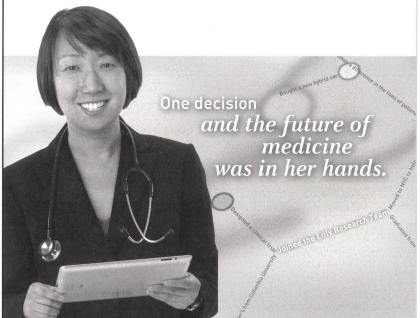

LILLY IS AN EQUAL OPPORTUNITY EMPLOYER.

Eli Lilly & Company: ***New Lilly China R&D Center in Shanghai***

Biology and Chemistry Leadership Openings for Group Leader and Lab Head Positions

Eli Lilly and Company has an established diabetes franchise with the strategy to commercialize first-in-class and best-in-class treatments to address unmet medical needs. As an integral part of our R&D investment, Lilly has recently established the Lilly China Research & Development Center (LCRDC) in Shanghai, China. The new center will focus primarily on discovering new medicines to treat diabetes and its complications with the aim of improving the health of diabetes patients across the world.

We are seeking seasoned scientific leaders in biology and chemistry who will be involved in building a world class research organization and who are interested in career development opportunities in China. Requirements include PhD degree and/or MD degree with postdoctoral research experience in relevant fields or at least 5 years of drug hunting experience in metabolic diseases. Strong track record of achievements, excellent communication skills and the ability to work in a team are essential for all positions.

We offer competitive compensation packages and benefits, and provide workforce training and development opportunities.

For application, please send resume and cover letter to YANG_HUI_HY@LILLY.COM

Be connected. Be inspired. **Be a catalyst.**

Visit lilly.com/careers

Lilly

US21126P

HJKRI–Hunter James Kelly Research Institute

University at Buffalo
The State University of New York

Assistant/Associate Professor Positions
SMBS-School of Medicine & Biomedical Sciences

The Hunter James Kelly Research Institute invites outstanding scientists with a Ph.D., M.D. or equivalent degree to apply for two tenure-track positions. We seek basic or physician-scientists who use innovative approaches to explore myelin, its diseases, or associated neurodegeneration. Examples might include non-rodent genetic models, dynamic imaging, metabolism/energetics, proteomics, epigenetics, computational biology or translational research. The ideal candidate will come from a successful post-doctoral or young faculty experience, and establish an original, active and NIH-funded research program and teach graduate students.

New faculty receive dual appointments in HJKRI and in a basic science or clinical department within the UB-SMBS; a generous start-up package; and laboratory space in the NYS Center of Excellence in Bioinformatics and Life Sciences, located on the Buffalo Niagara Medical Campus adjacent to the Roswell Park Cancer Institute and the Hauptman-Woodward Institute. HJKRI is supported by UB, the Hunter's Hope Foundation and NYS; and benefits from an interdisciplinary scientific environment, and integrated basic and clinical research arms. Biomedical research at UB is fostered by Ph.D. programs in each basic science department; Neuroscience and Genetics graduate groups; and core facilities including next-gen sequencing, genetically modified organisms and high-end computational facilities in the NYS Center of Excellence. Expansion of the UB downtown campus, including a multi-story Clinical and Translational Research Center, aims to bring new clinical and basic science programs together in a stimulating environment.

Applications online only. Please submit CV, description of research accomplishments/plans, and three references at UB Jobs https://www.ubjobs.buffalo.edu Posting Number: 1200057. Please address all inquiries to Lawrence Wrabetz, Director HJKRI, at lwrabetz@buffalo.edu.

U at B is an Equal Opportunity/Affirmative Action Employer

NW221083R

MoveAhead

Change your future and become part of Abbott's success in one of the following roles:

Senior Histopathologist – Req # 102754BR

Seeking a Sr. Histopathologist to join the *In Vivo* Tumor Biology team to support the IHC needs of multiple small molecule and biologics programs and drive the strategy for translational biomarker development.

Requirements:

MD and/or DVM (board certification is highly desired) or PhD in a relevant field with 5-8 years experience. Must have 3+ years experience in IHC, antibody selection and optimization of IHC protocols. Strong pathology experience is required; clinical pathology and digital pathology experience with relevant cancer biology research background is highly preferred. Leadership skills, strong research and industry experience, good interpersonal skills, ability to direct or lead technical studies, strong communication (excellent verbal and written skills) and teamwork skills are required.

Senior Scientist/Principal Research Scientist –

(2 positions available: Req # 98284BR/Req # 93371BR)

The incumbent will be responsible for identification and validation of novel cancer targets, developing assay infrastructure and biology strategy toward discovery of compounds for promising targets, and championing such projects toward clinical proof of concept. The individual must have solid and multi-faceted experience in cancer biology (cell cycle, cell death, DNA repair, cancer metabolism, epigenetics, signal transduction, etc). Strong communication and teamwork skills are essential.

Requirements:

Ph.D. in Cell/Mol Biology or related with 2 years post-graduate experience in cancer biology is required. Demonstrated scientific achievements, i.e., strong publication and/or patent record. Proficiency in standard biochemical, cellular and molecular techniques; ability to guide the development of novel target candidates; develop and maintain appropriate *in vitro* assays to guide SAR studies; interact with cross-functional teams to facilitate lead advancement; critically evaluate relevant scientific data and apply this knowledge to research efforts; contribute substantially to the overall research strategies; continually implement and validate novel research approaches to advance project goals; communicate results to multi-disciplinary teams; publish in peer-reviewed journals. The position grade level will be filled commensurate with experience.

Abbott is at the forefront of cancer research in discovering and developing novel treatments that offer a new approach to cancer therapy. Our strong pipeline includes signal transduction inhibitors as well as first in class agents that target angiogenesis, metastasis and resistance to apoptosis. Abbott's oncology franchise extends beyond pharmaceutical research to provide a range of health care products, from supportive care products for pain management, to diagnostic tests for the detection of cancer.

We invite you to apply online at www.abbottcareers.com and search for the desired Req #.

An equal opportunity employer, Abbott welcomes and encourages diversity in our workforce.

NW220844R

MUSC
MEDICAL UNIVERSITY *of* SOUTH CAROLINA

MEDICAL UNIVERSITY OF SOUTH CAROLINA

PROFESSOR AND CHAIR

DEPARTMENT OF BIOCHEMISTRY AND MOLECULAR BIOLOGY

The Medical University of South Carolina College of Medicine invites applications and nominations for the position of PROFESSOR AND CHAIR of its Department of Biochemistry and Molecular Biology. Applicants must possess a PhD and/or MD, a distinguished record of scientific research and extramural funding, administrative and leadership skills, and a commitment to education and academic excellence. The selected individual will report directly to the Dean of the College of Medicine and will be expected to foster new areas of research within the department while supporting and enhancing current research strengths.

The Medical University of South Carolina is in the midst of an exciting period of growth with recent NCI designation for the Hollings Cancer Center, a CTSA award, two new research buildings, and new clinical outreach facilities under construction. This is an outstanding opportunity for the right candidate in a city known for its enviable quality of life. Nominations and inquiries may be directed to Peter Kalivas, PhD, Chair, Biochemistry Chair Search Committee, in care of Jennifer Nall at nallj@musc.edu.

Interested individuals should submit a letter of interest, curriculum vitae, and the names and contact information of three references via the MUSC employment website at https/www.jobs.musc.edu, requisition ID# 047955.

MUSC is an equal opportunity employer, promoting workplace diversity.

NW221260R

HEINRICH HEINE
UNIVERSITÄT DÜSSELDORF

Heinrich Heine University has more than 20 000 students in five faculties: the faculties of law, medicine, arts and humanities, mathematics and natural sciences, and economics. It supports close interdisciplinary cooperations on a regional and international level.

JÜLICH
FORSCHUNGSZENTRUM

With a staff of 4 700, Forschungszentrum Jülich – a member of the Helmholtz Association – is one of the large interdisciplinary research centres in Europe and stands for the next generation of key technologies. Work with us on the grand challenges in the fields of health, energy & environment, and information technology, as well as on the many and varied tasks of research management.

Forschungszentrum Jülich is seeking an internationally respected scientist in a joint procedure with Heinrich Heine University Düsseldorf for the position of

DIRECTOR (W 3)

of Molecular Biophysics (ICS-5) at the Institute of Complex Systems

The Institute of Complex Systems works at the interface between biology, physics and chemistry and bridges the gaps between research into soft matter, structural biology and cell physics in the Helmholtz BioSoft programme.

The successful candidate will be an internationally respected scientist in the field of structural biology and conduct basic research in biology or biomedicine. The focus of his/her work will be on the application and development of modern cryo-electron microscopy (preferably structural analysis of individual particles, tomography, diffraction in two-dimensional protein lattices) and/or the application of coherent X-ray radiation (e.g. PETRA III and X-FELs in Hamburg). The future director will bring together the scientific areas of atomic-resolution structural biology and integrative cell biology in an attractive and future-oriented concept.

In accordance with the "Jülich Model", the successful applicant will also be appointed professor (grade W3) in Physical Biology at the Faculty of Mathematics and Natural Sciences of Heinrich Heine University Düsseldorf. Active participation in existing and proposed research collaborations of the two institutions is expected, as well as a contribution (2 hours a week per semester) to the biology and biochemistry courses.

Prerequisites for the position are a university degree in science or medicine, a Habilitation or equivalent scientific achievements, experience in leading a scientific team, as well as in the acquisition of third-party funds and in teaching.

The implementation of equal opportunities is a cornerstone of staff policy in Forschungszentrum Jülich and Heinrich Heine University Düsseldorf. Applications from women are therefore particularly welcome.

We also welcome applications from disabled persons.

Forschungszentrum Jülich has a dual career service, and both Jülich and Heinrich Heine University Düsseldorf are members of the Dual Career Network Rhineland. More information at **www.fz-juelich.de/dualcareer**

Applications including the appropriate documents should be submitted, **preferably by email**, by 30 March 2012 to

Board of Directors of Forschungszentrum Jülich GmbH
52425 Jülich
Germany
berufungen@fz-juelich.de

More information is available at **www.fz-juelich.de** or from Prof. Willbold (+49 2461 61-2100 or d.willbold@fz-juelich.de).

W220730R

UNIVERSITY OF CAMBRIDGE

A world of opportunities
www.cam.ac.uk/jobs/

Post-Doctoral Research Associate

Department of Genetics
£27,428 - £35,788 pa
Limit of tenure: Two years from date of appointment.

Applications are invited for a Postdoctoral Researcher to join an interdisciplinary research group and participate in a European Research Council (ERC) funded project on the dynamics of gene expression during stem cell differentiation. You should have experience in biological image analysis and knowledge of software tool development, with a focus on usability, and an interest in working with experimentalists. Knowledge of microscopy will be an advantage.

Applications, which should consist of a completed CHRIS/6 application form (Parts I and II) - see http://www.admin.cam.ac.uk/offices/hr/forms/chris6/ - a full CV and covering letter describing your research interests, should be sent to Ms R Baglow, Dept of Genetics, Downing St, Cambridge CB2 3EH. e-mail: jobs@gen.cam.ac.uk

Quote reference: PC12592, Closing date: 20 February 2012.

The University values diversity and is committed to equality of opportunity.

U221282R

You don't have to look this hard to find a job with Naturejobs.

nature jobs
making science work

"When trying to recruit good scientists for such a remote institutions like ours, in the Canary Is., the high visibility and wide-range exposure that Naturejobs provides has been crucial. I'm very happy to have international candidates who applied to our position from places ranging between St. Petersburg and Cincinnati. Thanks a lot!"

Eduardo Salido, MD, PhD,
Hospital Universitario de Canarias

nature jobs

The University of Edinburgh

The University of Edinburgh is an exciting, vibrant, research led academic community offering opportunities to work with leading international academics whose visions are shaping tomorrow's world.

Chair of Chemistry
Crum Brown Chair of Chemistry
Forbes Chair of Organic Chemistry

The University invites applications from world-leading Chemists for one of three prestigious Chairs. The Chair of Chemistry and the Crum Brown Chair of Chemistry are available in any area of Chemistry but we are seeking to make one appointment in Theoretical & Computational Chemistry. The Forbes Chair will be in Organic Chemistry. These appointments will be located in the School of Chemistry, which, together with St Andrews' School of Chemistry, forms EaStCHEM, the strongest Chemistry Research School in Scotland and amongst the very best Chemistry Schools in the UK. The School has strength and breadth in fundamental research, strong interactions with industry and world class research support facilities.

The School of Chemistry at Edinburgh holds a Silver Athena SWAN award, in recognition of excellence in science, engineering and technology employment in higher education relating to supporting women in science.

Salary Scale: Within the Professorial Scale

Apply online, view further details or browse more jobs at our website. Alternatively, telephone the recruitment line on 0131 650 2511. Ref: 3015258N. Closing date 31 March 2012.

Committed to Equality and Diversity

The University of Edinburgh is a charitable body, registered in Scotland, with registration number SC005336.

www.jobs.ed.ac.uk

U221265R

Imperial College London

Division of Molecular Biosciences/
Department of Life Sciences

Lecturers in Structural Biology of Large Macromolecular Complexes (2 posts)

Salary: £43,350 - £48,400 p.a.

Imperial College London invites applicants to apply for two Lectureship positions in the area of structural biology within the Division of Molecular Biosciences. A strategic research aim of the Division is to address the challenges of integrating structural biology research of individual components with the visualisation of macromolecular complexes *in vivo*. We are particularly interested in recruiting individuals with a track record in using electron microscopy to study large macromolecular complexes and/or using electron tomography to visualise macromolecular complexes in cells to complement and integrate existing structural biology research. Imperial College London has excellent facilities including state-of-the-art electron microscopy facilities as well as a dynamic interdisciplinary research environment. The successful candidate will have an outstanding publication record in structural biology research and a demonstrated ability in directing internationally competitive independent research. They would also be expected to contribute to undergraduate and postgraduate teaching.

Our preferred method of application is online via our website http://www3.imperial.ac.uk/employment (please select "Job Search" then enter the job title or vacancy reference number, **NS 2012 110 DPN**, into "Keywords"). **Please note you must submit an application form for our posts not just a CV, if you do not fill in an application form, your application will not be considered.** For any queries about the application process please contact Kasia Pearce, e-mail: k.pearce@imperial.ac.uk

Closing date: 29 February 2012.

Committed to equality and valuing diversity. We are also an Athena Bronze SWAN Award winner and a Stonewall Diversity Champion.

Stonewall DIVERSITY CHAMPION

U221273R

THE UNIVERSITY OF ALABAMA AT BIRMINGHAM

Department of Biochemistry and Molecular Genetics
University of Alabama at Birmingham
Schools of Medicine and Dentistry
NMR Faculty Positions

Faculty positions (tenure track junior and senior faculty and/or tenured senior faculty) are available for outstanding investigators with extensive experience in the application of High-Field NMR Spectroscopy to study the structural biology of proteins of significance in human diseases. Structural biology areas of interest include, but not limited to, stem cell biology, virology, glycobiology, cancer cell biology, membrane proteins, immunology, and drug discovery and design. Nationally competitive salaries, start-up packages and space allocations, as well as complete access to the Central Alabama High-Field NMR Facility consisting of a new state-of-the-art Bruker 850 MHz NMR system with a cryoprobe and lower NMR field systems, will be offered to the successful candidates. Preference will be given to NIH funded investigators. UAB is a highly interactive environment with strong basic and clinical science programs and Research Centers. Birmingham is a beautiful and affordable city with many cultural attractions. Applicants should send a C.V., a summary of research interests and the names of three references before February 29th, 2012 to:

Dr. Tim Townes
Chairman, Department of Biochemistry and Molecular Genetics
University of Alabama at Birmingham
Kaul Genetics Building, Room 502
720 20th Street South
Birmingham, AL 35294
Email: ttownes@uab.edu

UAB is an Equal Opportunity /Affirmative Action Employer committed to fostering a diverse, equitable and family-friendly environment in which all faculty and staff can excel and achieve work/life balance irrespective of ethnicity, gender, faith and sexual orientation. UAB also encourages applications from individuals with disabilities and veterans.

NW221028R

Group Leaders: MRC-Laboratory for Molecular Cell Biology, UCL, London, UK

The MRC Laboratory for Molecular Cell Biology is seeking to appoint two new group leaders. Situated in the heart of the University College London campus in the centre of London, this modern research institute (www.ucl.ac.uk/lmcb) has an exceptional record in cell biology research, excellent resources, and outstanding facilities, together with strong links to UCL's life and physical sciences departments and clinical facilities.

We will be seeking young or established investigators who are interested in solving fundamental questions in cell biology. The primary selection criterion will be scientific excellence but candidates with advanced imaging backgrounds, expertise in mathematical approaches to cell biology or systems-based approaches are encouraged to apply. Research areas in synergy with our existing research programmes, which include strengths in organelle biology, cell number, shape and polarity, virology and neurobiology, will also be an advantage.

Substantial core funding for salaries and consumables will be available to the successful candidates. You should hold a PhD, MD or equivalent and exhibit an excellent track record of previous publications with a clear potential for independent research. The appointments are likely to be at the tenure track level, although a more senior appointment will be considered for a suitably experienced candidate.

The positions will remain open until filled; however, expressions of interest received by 29th February 2012 will be given priority in the initial selection process.

Informal enquiries can be addressed to Mark Marsh:
m.marsh@ucl.ac.uk

Expressions of interest should include a cover letter and full CV, an outline of current research interests (1 page) and a proposal for future research (up to 2 pages), along with the names and addresses of three referees who will be willing to provide a reference, and should be emailed to i.karney@ucl.ac.uk or sent to I Karney, MRC-LMCB, UCL, Gower Street, London, WC1E 6BT, UK.

U221284R

LMU LUDWIG-MAXIMILIANS-UNIVERSITÄT MÜNCHEN

FACULTY OF CHEMISTRY AND PHARMACY

The **Faculty of Chemistry and Pharmacy** of the Ludwig-Maximilians-Universität München (LMU) invites applications for a

Full Professorship (W3) for Biophysical Chemistry

commencing on 1 April 2013.

The successful candidate is expected to represent the field of Biophysical Chemistry in research and the field of Physical Chemistry in teaching.

The position will play a key role in the development of quantitative and mechanistic investigations of chemical and biological systems, and complements existing research activities at the LMU. The newly appointed professor will be active in method development, e.g., in the areas of spectroscopy and/or superresolution microscopy, and collaborate with research groups in chemistry, physics and biology. Active participation in the local research networks, including the Excellence Clusters "Center for Integrated Protein Science Munich" (CIPSM) and "Nanosystems Initiative Munich" (NIM) is highly desirable.

Prerequisites for this position are a university degree, a doctoral degree, teaching skills at university level and a post-doctoral degree (Habilitation) or equivalent qualification that may have been gained outside the university or may consist in a junior professorship.

Candidates for this position should be aged 52 or under at the time of appointment. Exceptions thereto may be considered in the case of outstanding candidates.

The LMU is an equal opportunity employer and aims to increase the number of female faculty members. Therefore, applications from female candidates are explicitly encouraged.

Disabled candidates with essentially equal qualifications will be given preference.

The LMU supports dual career couples.

Information concerning equality of treatment may be obtained through the women's representative of the faculty (Martina.Rueffer@cup.uni-muenchen.de).

Please submit your application comprising a curriculum vitae, documentation of academic degrees and certificates, a research summary with three to five relevant publications, a summary of teaching activities as well as a list of publications in printed and electronic form (on CD) to the **Dean of the Faculty of Chemistry and Pharmacy, Ludwig-Maximilians-Universität, Butenandtstr. 5-13, 81377 Munich, Germany**, email: Dekanat@cup.uni-muenchen.de, no later than **31 March 2012**.

W221091R

ETH

Eidgenössische Technische Hochschule Zürich
Swiss Federal Institute of Technology Zurich

Professor of Animal Physiology

The Institute of Agricultural Sciences (www.ias.ethz.ch) of the Department of Environmental Systems Science (www.usys.ethz.ch) at ETH Zurich invites applications for a Professorship in Animal Physiology. The new Professor will be responsible for developing a leading research and teaching program in physiology of livestock species oriented around understanding metabolic function and control mechanisms. The approach should be integrative, encompassing genetic, molecular, cellular and organismal levels with a goal of improving the efficiency of nutrient utilisation.

The Professorship's primary research topics might include: characterizing interactions among metabolic pathways and the underlying mechanisms (metabolomics concept) as well as their regulation by genetic and environmental factors; exploring metabolic adaptive capabilities and limitations, stress responses and coping mechanisms that affect adaptation of high genetic merit animals as well as animals exposed to harsh environments, including different climate change scenarios; relating metabolic processes to the regulation of energy and protein utilization as well as metabolic partitioning (including research in energy homeostasis).

Following the World Food System focus of the Department, the Professorship is expected to express a global view of the problems coming along with food scarcity and climate change and to help in developing solutions. The new Professor will be able to hire several staff and will have access to state of the art experimental and analytical equipment. She or he will be expected to teach undergraduate level courses (in German or English) and graduate level courses (in English) covering both basic and advanced Animal Physiology.

Please apply online at **www.facultyaffairs.ethz.ch.** Your application should include your curriculum vitae, a list of publications, and a statement of your research and teaching interests. The letter of application should be addressed **to the President of ETH Zurich, Prof. Dr. Ralph Eichler. The closing date for applications is 30 April 2012.** ETH Zurich is an equal opportunity and affirmative action employer. In order to increase the number of women in leading academic positions, we specifically encourage women to apply. ETH Zurich is further responsive to the needs of dual career couples and qualifies as a family friendly employer.

W221040R

Small cog, big machine?
Jobs that make a difference.
Each week. *Naturejobs*.
naturejobs

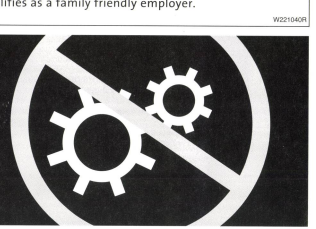

UNIVERSITY OF OXFORD

www.ox.ac.uk/jobs

Mathematical, Physical and Life Sciences Division

SILVER
Athena SWAN
Charter for Women in Science

Professorship of Zoology

Department of Zoology in association with Jesus College

Start date: 1 October 2012 or as soon as possible thereafter.

The post is one of five established professorships in the Department. The appointee will be expected to engage in internationally outstanding research; provide leadership in a particular area of biological sciences; develop a vigorous externally-funded research programme; and teach aspects of the subject at undergraduate and postgraduate level. The Department of Zoology recently celebrated its 150th anniversary, and although it maintains its historic name its research programmes have expanded to include the ecology and evolution of animals, bacteria, viruses and ecosystems. The Department has research strengths in evolution, ecology, animal behaviour, conservation, development and disease biology, spanning all levels of analysis from molecules to ecosystems (see http://www.zoo.ox.ac.uk). The Professorship is open to applicants from any field of biological science research, although preference will be given to candidates whose research aligns with the Department's strengths mentioned above and with research priorities of major funding agencies.

Please see the further particulars on the website at **http://www.ox.ac.uk/about_the_university/jobs/fp/** for more details about the post and for full instructions before making an application. Applications, including a covering letter and full CV, and naming three referees should be received no later than Monday 12 March 2012, by Dr Gwen Booth, Personnel Officer, Senior Appointments (email: professorships@admin.ox.ac.uk). If you have a query about how to apply, please contact Mrs Elaine Eastgate email: professorships@admin.ox.ac.uk; tel: +44 (0)1865 280189.

Applications are particularly welcome from women and black and minority ethnic candidates, who are under-represented in academic posts in Oxford.

Committed to equality and valuing diversity

U221239R

NYSCF The New York Stem Cell Foundation

Request for Applications

The New York Stem Cell Foundation Innovator Program is now accepting proposals for high-risk, high-reward projects exploring the therapeutic potential of human stem cells.

The NYSCF - Robertson Investigator Awards in Translational Stem Cell Research
$1.5M USD over 5 years
Open to junior faculty across the US, Canada, and the UK

Application deadline: March 30, 2012
View the full RFA at www.nyscf.org/stemcell

NYSCF is pleased to congratulate the 2011 class of NYSCF - Robertson Stem Cell Investigators:

Paola Arlotta, PhD
Harvard University

Ravindra Majeti, MD, PhD
Stanford University

Gabsang Lee, PhD
Johns Hopkins University School Of Medicine

NYSCF The New York Stem Cell Foundation

NW221307A

Epigenesys

SEVENTH FRAMEWORK PROGRAMME

EpiGeneSys Open Call 2012 for young PIs and SMEs
"Research Integrating Systems Biology and Epigenetics" (RISE)

Submission deadline for application: March 15th, 2012, 17h00 CET.

The Network of Excellence "EpiGeneSys" (FP7) strives to unite the fields of epigenetics and systems biology. The network's inter-disciplinary research programme addresses fundamental epigenetic mechanisms in quantitative terms in order to model and predict how the balance between maintenance and erasure of epigenetic information varies in specific contexts.

This open competitive call will further expand the network, by integrating young researchers and research-oriented small or medium sized enterprises (SMEs) through a 3-year research grant of 150,000€ (50,000 € per annum) and full network membership.

EpiGeneSys offers membership to young teams from the fields of Systems Biology (3 - 6 teams) and Epigenetics (3 - 6 teams):

Systems biology applicants' research interests should explore computational and mathematical analysis of epigenetic mechanisms, modelling and algorithmic development for studies involving novel epigenomic experiments and/or a collaborative approach towards joint research with experimentalists within or outside of EpiGeneSys. The network seeks expertise in a wide range of computational and quantitative approaches and encourages incorporation of new methodologies and analytical techniques to the epigenetics field.

Epigenetics applicants' proposals should apply systems biology tools to solve epigenetic questions, and are expected to work at the interface of biological, computational, and/or engineering sciences to produce data relevant to mathematical analyses and modelling of epigenetic processes.

PI applicants must have been independent for 3 years and hold a position in an institute eligible for funding via FP7 for the duration of the three-year grant.

EpiGeneSys offers membership to 2 small or medium sized enterprises (SMEs):

SMEs should explain how they would expand and strengthen EpiGeneSys's goal of forging a durable link between epigenetics and systems biology. Proposals focusing on acquisition, storage, modelling and integration of epigenetics data and on novel visualisation and user-guided analysis of massive biological datasets are strongly encouraged. SME applicants must be eligible for funding via FP7 and fit in the EC definition of an SME.

For detailed information, guidelines and submission of proposals go to

www.epigenesys.eu

W220979R

NYSCF The New York Stem Cell Foundation

Request for Applications

The New York Stem Cell Foundation Innovator Program is now accepting proposals for high-risk, high-reward projects exploring fundamental areas of developmental, cellular, cognitive, and behavioral neuroscience.

The NYSCF - Robertson Investigator Awards in Neuroscience
$1.5M USD over 5 years
Open to junior faculty across the US, Canada, and the UK
Proposals do not need to be related to stem cells

Application deadline: March 30, 2012
View the full RFA at www.nyscf.org/neuro

NYSCF is pleased to congratulate the 2011 inaugural class of NYSCF - Robertson Neuroscience Investigators:

Ed Boyden, PhD
Massachusetts Institute of Technology

Gaby Maimon, PhD
The Rockefeller University

Takaki Komiyama, PhD
University of California, San Diego

Christopher Gregg, PhD
University of Utah

NYSCF The New York Stem Cell Foundation

NW221076A

REPROGRAPHICS: CTT, London E17 6BU UK and **The Charlesworth Group,** Wakefield, UK.
PRINTED BY: William Gibbons & Sons Ltd, UK; **Publishers Press,** Lebanon Junction, Ky, USA and **Obun Printing Co. Inc,** Tokyo, Japan

Skolkovo Tech

Skolkovo Institute of Science and Technology

The Skolkovo Institute of Science and Technology (SkTech)
and The Massachusetts Institute of Technology (MIT) announce Round One:

Call for International Research Center Proposals

White Paper Deadline: **March 13, 2012**
Invitations to Submit Full Proposal: **April 14, 2012**
Research Awards Announced: **June 30, 2012**

Research Center Proposals:
US $6 million to US $12 million
per center, per year for up to five years

Planning Award Proposals:
US $30,000 for up to one year

Biomedical
Energy
Information
Nuclear
Space

SkTech is a new graduate research university in Russia, launching in collaboration with MIT and the Skolkovo Foundation. SkTech aims to create a pioneering interdisciplinary model for graduate education and research; integrating teaching, research, innovation and entrepreneurship.

Up to 15 research centers will be formed at SkTech. Each research center will be a collaboration among SkTech and both a non-Russian and a Russian participant, and will function as an interdisciplinary international research initiative.

This Call for Proposals is open to Russian and non-Russian universities and research institutions with significant research and educational capacity.

Full details at:
web.mit.edu/SkTech/rc-call

Contact us at:
SkTech-rc-call@mit.edu

SkTech/MIT
INITIATIVE

Skolkovo Tech

Skolkovo Institute of Science and Technology

The Skolkovo Institute of Science and Technology (SkTech)
and The Massachusetts Institute of Technology (MIT) announce Round One:

Call for Proposals Information Workshop

February 9-10, 2012
Massachusetts Institute of Technology
Cambridge, Massachusetts, USA

- Information Sessions
- Team Building Workshops
- Panel Discussions
- Proposal Development Clinics

Research Center Proposals:
US $6 million to US $12 million
per center, per year for up to five years

Planning Award Proposals:
US $30,000 for up to one year

Biomedical
Energy
Information
Nuclear
Space

SkTech is a new graduate research university in Russia, launching in collaboration with MIT and the Skolkovo Foundation. SkTech aims to create a pioneering interdisciplinary model for graduate education and research; integrating teaching, research, innovation and entrepreneurship.

Up to 15 research centers will be formed at SkTech. Each research center will be a collaboration among SkTech and both a non-Russian and a Russian participant, and will function as an interdisciplinary international research initiative.

This Call for Proposals is open to Russian and non-Russian universities and research institutions with significant research and educational capacity.

Full details at:
web.mit.edu/SkTech/rc-call

Contact us at:
SkTech-rc-call@mit.edu

SkTech/MIT
INITIATIVE

NW22128BA

a nature conference

Nature Genetics and the *Journal of Investigative Dermatology* present:

Dermatogenetics

The conference will cover genetic variation, gene expression and cellular mechanisms in this shared area of exceptional interest to basic researchers, biopharma and translational medicine. Lectures and posters are invited in all areas of the field and sessions including: complex dermatological diseases, stem cells and skin cancer, development and regeneration, melanoma and pigmentation, monogenic skin disorders and epigenetics and gene expression.

February 9-12, 2012
JW Marriott Marquis Miami
Miami, FL, USA

KEYNOTE SPEAKERS:
Raphael Kopan
Fiona Watt

SPEAKERS:

Allan Balmain	**Andrzej Dlugosz**	**Anthony Oro**
Greg Barsh	**David Fisher**	**Dennis Roop**
Regina Betz	**Nick Hayward**	**Yardena Samuels**
David (Tim) Bishop	**Valerie Horsley**	**Julie Segre**
Natalia Botchkareva	**Birgitte Lane**	**Eli Sprecher**
Anne Bowcock	**Robert Lavker**	**Richard Spritz**
Pierre Coulombe	**Jianjun Liu**	**Xue Zhang**
James Elder	**Sarah Millar**	

ORGANIZERS:
Myles Axton (*Nature Genetics*, USA)
Angela Christiano (Columbia University, USA)
John McGrath (King's College London, UK)
Irwin McLean (University of Dundee, UK)

Artwork by: Daniel Kohn

For more information and to register, visit:
www.nature.com/natureconferences/dg2012

nature genetics

JOURNAL OF INVESTIGATIVE DERMATOLOGY

THE SOCIETY FOR INVESTIGATIVE DERMATOLOGY, INC.

EUROPEAN SOCIETY FOR DERMATOLOGICAL RESEARCH ESDR

INZ16199E

a nature conference

European Materials Research Society and *Nature Materials* present:

Frontiers in Materials: Spintronics

The purpose of the workshop is to provide an overview of the most interesting developments in the field of spintronics, a technology that aims at controlling the electron spin beside the electron charge and that could provide efficient electronic devices with potentially new functionalities. The meeting will consist of a number of invited talks covering the most recent achievements from both a fundamental and a technological perspective.

May 13, 2012
Congress Center (Palais des Congrès)
Strasbourg, France

SPEAKERS:

Albert Fert
Hideo Ohno
Jairo Sinova
Laurence Molenkamp
Theo Rasing
Manuel Bibes
Gerrit Bauer
Jon Slaughter

ORGANIZERS:

Vincent Dusastre (*Nature Materials*, U.K.)
Rodrigo Martins (Faculty of Science and Technology, New University of Lisbon, Portugal)
Francesco Priolo (Department of Physics and Astronomy, University of Catania, Italy)
Fabio Pulizzi (*Nature Materials*, U.K.)

ADVISERS:

Tomas Jungwirth (Inst. of Physics ASCR Prague, CZ, and Univ. of Nottingham, U.K.)
Andrew Kent (Department of Physics, New York University, USA)

For more information and to register visit:

www.nature.com/natureconferences/spin12

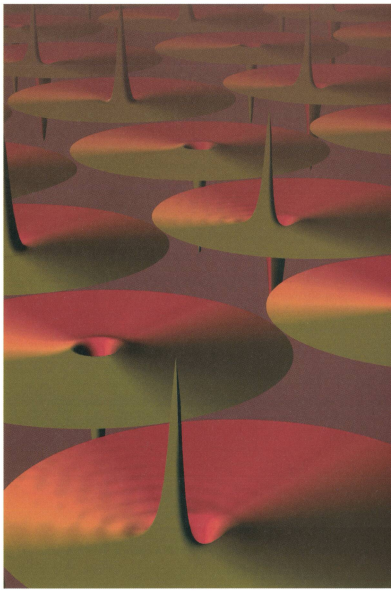

E-MRS

nature materials

IN217950E

a nature conference

Nature Reviews Immunology presents:

Resolving Inflammation: Mechanisms and Drug Discovery

Infl ammation is a primordial response that protects against infection and restores damaged tissue. In general, an inflammatory response is initiated within minutes of sensing a threat and, if all is well, resolves within hours or days. By contrast, chronic inflammation persists for weeks, months or even years. It is this breakdown in resolution of an otherwise beneficial immune response that leads to chronic inflammatory diseases.

This conference will bring together scientists and clinicians from academia and industry to provide, through presentations and discussion sessions, a comprehensive overview of the crucial endogenous checkpoints necessary for mounting a limited, yet effective, inflammatory response.

April 1-3, 2012
Keble College, Oxford, UK

SPEAKERS AND MODERATORS

Abul Abbas
Helen Braley-Mullen
Gordon Brown
Chris Buckley
Edward Fisher
Dmitry Gabrilovich
Derek Gilroy
Siamon Gordon
Gerry Graham
Peter Henson
Stephen Holgate
Tracy Hussell
Toby Lawrence
Alberto Mantovani
Diane Mathis
David Mosser
Allan Mowat
Carl Nathan
Luke O'Neill
Mauro Perretti
Fiona Powrie
John Savill
Anthony Segal
Charles Serhan
Brigitta Stockinger
Paul-Peter Tak
Kevin Tracey
Shannon Turley
Herman Waldmann
John Wallace
Cara Williams

ORGANIZERS:
Olive Leavy (*Nature Reviews Immunology*, UK)
Derek Gilroy (University College London, UK)

For more information and to register visit:
www.nature.com/natureconferences/rimdd12

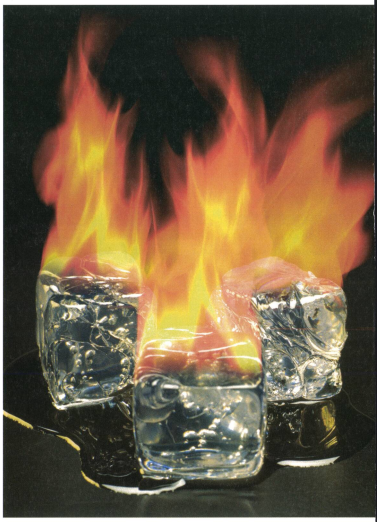

nature REVIEWS IMMUNOLOGY

IN218348E

natureevents directory 2012

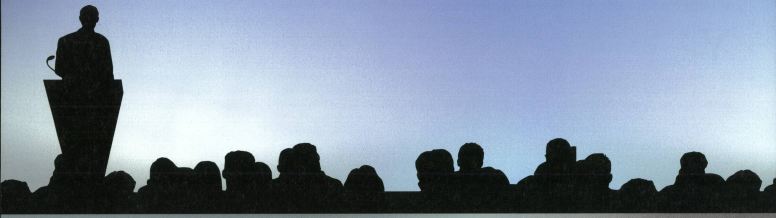

There is no substitute for face-to-face.

No resource connects you with networking opportunities like the *Natureevents Directory.*

The 2012 *Natureevents Directory* is now available, packed with valuable information covering a complete range of scientific events, conferences and courses from around the world. Begin planning your conference attendance today, visit the *Natureevents Directory* at natureevents.com!

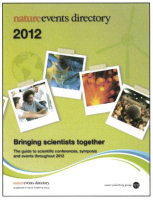
natureevents directory
2012
Bringing scientists together
The guide to scientific conferences, symposia and events throughout 2012

Stay up-to-date with the latest events throughout the year at **natureevents.com**

WORDS AND MUSIC

A performance of note.

BY RONALD D. FERGUSON

Yeah, you got me, fair and square. I didn't think you'd recognize me. I am the government translator, the guy who lurks off the shoulder of Space Systems' chief negotiator and whispers connotations, corrections and culpability in case the computer renders too literal a verdict on Utmano phrasing. I've got nothing to do with speakos. Talk with the programmers for input–output problems.

I hope you're recording this, because it will be my only interview. Please, just a few questions, so quit yelling. I'll tell the story, and then I go home. Understood?

Here's what happened. The meeting began with the formal greeting …

Example? You want to know what the Utmano said? Do you speak Utmano? Oh, the literal translation into English? Right. Let me see …

It is beautiful weather we shall be having tomorrow wasn't it?

That's not the literal translation of the Utmano greeting, but that's as close as I'm likely to get on a Tuesday. Today is Wednesday? No, I can't do better today. Of course, the literal translation isn't what the Utmano meant. From the variations of pitch within the context of the meeting, my best interpretation is:

We should complete negotiations successfully tomorrow based on the current tolerant atmosphere and previously adopted ground rules.

The computer's translation was close, possibly better based on pitch and less accurate where context was important. Diphthong? No pitch, like I said. Intonation would be a reasonable description. Thai is the human intonation language that comes to mind, but Utmano is like intonation on steroids. Spoken Utmano must be sung.

No, I don't think an Utmano looks like a whale. That's uncalled for.

Speak Utmano? Unaided, I cannot speak Utmano. My base vocabulary is okay, and I might squeeze out a few words, but the Utmano tonal range is 14 octaves. They have some vocabulary modifiers well above 20,000 hertz, which is likely to make your neighbour's dog bark. Humans have a more limited range. I use a synthesizer to …

Human range? Oh, I don't know. If you watch old videos, Julie Andrews had a four-octave range, Mariah Carey perhaps five, but most people can't do that. I certainly can't. I'm good at listening to the symphony that Utmano call speech. I'm not Mozart, but I have a good ear, and training as a professional musician.

No, Julie Andrews. You know, *The Sound of Music*. Okay?

Symphony? Each Utmano has a double set of vocal chords and can sound two notes at once. An Utmano can sing harmony with itself. The Utmano divide an octave into 32 parts. That's why we rely on computers and Fourier analysis …

No. I understand your question, but Utmano translation doesn't compare well to translations among human languages. The Utmano language has a peculiar view of tense, you know, past, present, future, in its sentences — well maybe not sentences, but the complete-thought communication structure. Psychologists claim that the Utmano have a lingering, vivid, recent memory combined with a mild prescience that blends with their perception of the 'now'. It sounds like gobbledegook, but they claim that the Utmano idea of the present spans from the middle of last week to a couple of hours from now.

In translating from English to Greek, or French, or whatever Earth language you pick, we have the advantage of common human experiences. Humans share uncommonly little with the Utmano.

➲ **NATURE.COM**
Follow Futures on Facebook at:
go.nature.com/mtoodm

No. I'm not making excuses. I accept the blame for missing any subtle nuance, but the Utmano response was undocumented. Google the literature, and the only violent reactions are for personal insults …

I'll stick to the topic. I repeat for the record. Intonation is not a critical characteristic of most human languages, but to the Utmano, a change in pitch is an essential communication detail.

Look, I've got to go. I need to finish this interview. I can't give any details of the ongoing negotiations, because those are secret. I can confirm the official report. Yes, I know the report is short. Do you have a copy? Okay, I'll read it for those in the back.

"Chief Negotiator Simon Mann died today when he bade farewell to the Utmano Ambassador. A focused eruption of sonic energy homogenized Dr Mann's brain. With no hope for recovery, his family directed he be removed from life support."

You heard that the sonic energy was a blast of rage from the Utmano Ambassador? No. I cannot confirm that. Yes, I was there, but appearances aren't always reality.

Yes, I was told that Dr Mann practised a few phrases in Utmano. No, I didn't coach him. I was never asked to coach him. Besides, I use the very tedious process of keyboarded voice modulation when I speak Utmano. Dr Mann wasn't a musician, and I wouldn't know how to coach him. I certainly didn't know that Dr Mann planned to speak in Utmano or I would have advised against it.

What? John Kennedy at the Berlin Wall, the '*Ich bin ein Berliner*' speech? Yeah, I've seen the newsreel. No, I don't think Kennedy said 'I'm a jelly doughnut.' No, I don't know whether Dr Mann planned to run for elected office.

Negotiations? Negotiations will resume in two weeks, once we are well past the Utmano concept of the present. No, I don't believe that is 'pout time' or 'holding a grudge.'

One last question? Okay, you, in the back. Did Dr Mann make a mistake? All I've got is my humble opinion, not as a translator, but as a musician.

Like many tone-deaf amateurs, he thought he could sing. ■

Ronald D. Ferguson *has decided that writing fiction is more fun than writing college textbooks. He lives with his wife and five feral cats on two acres of the Texas Hill Country.*

JACEY

6,000 Recombinant Human Proteins

More Assays! Better Assays!

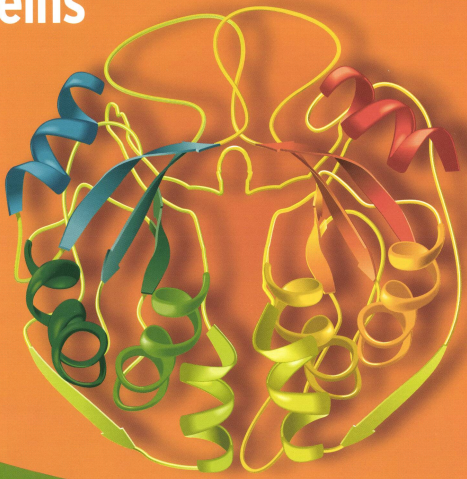

The Largest Collection of Mammalian Cell-Derived Proteins

Protein functional studies

Compound screening

Immunogens for antibody production

Assay standards: ELISA, Mass Spec, and more

Human MTOR protein activity verified in a kinase assay

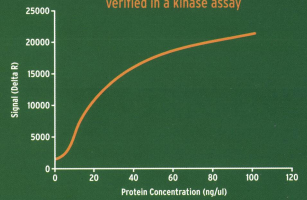

origene.com/protein

ORIGENE
Your Gene Company

Cancer
Development
Endocrinology
Glycobiology
Immunology
Neuroscience
Proteases
Signal Transduction
Stem Cells

R&D Systems Specialized Tools for Cancer Research

Cancer is a disease of cellular dysfunction involving a range of biological activities that promote unregulated proliferation. To help advance the understanding of this complex disease, R&D Systems offers an expansive selection of quality products, including **high performance antibodies, proteins, ELISAs, & arrays,** for investigating various cancer-related factors. Every product from R&D Systems undergoes rigorous quality control testing to ensure industry leading reliability.

Angiogenesis

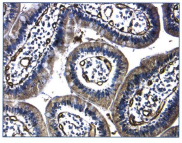

Angiopoietin-2 (Catalog # AF623)
Human Gastrointestinal Cancer Tissue

Epithelial to Mesenchymal Transition

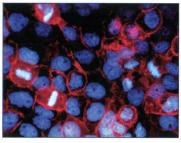

E-Cadherin (Catalog # AF648)
Human Epidermoid Carcinoma Cells

Cancer Biomarkers

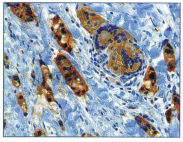

BRCA1 (Catalog # MAB22101)
Human Breast Cancer Tissue

Inflammation

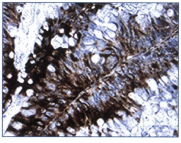

EMAP-II (Catalog # AF1910)
Human Colon Cancer Tissue

Growth Factor/Receptor Signaling

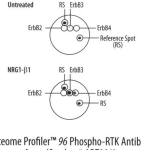

Proteome Profiler™ 96 Phospho-RTK Antibody Array (Catalog # ARZ001)
MDA-MB-453 Cell Line

Cancer Stem Cells

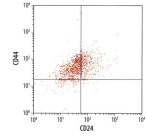

MagCellect CD24⁻CD44⁺ Breast Cancer Stem Cell Isolation Kit (Catalog # MAGH111)
MCF-7 Cell Line

For more information visit our website at www.RnDSystems.com/go/Cancer

For research use only. Not for use in diagnostic procedures.

R&D Systems, Inc. www.RnDSystems.com
R&D Systems Europe, Ltd. www.RnDSystems.co.uk
R&D Systems China Co., Ltd. www.RnDSystemsChina.com.cn

R&D SYSTEMS®